uOttawa

L'Université canadienne
Canada's university

FACULTÉ DES ÉTUDES SUPÉRIEURES ET POSTOCTORALES

uOttawa

L'Université canadienne
Canada's university

FACULTY OF GRADUATE AND POSDOCTORAL STUDIES

Frédéric Tessier

AUTEUR DE LA THÈSE / AUTHOR OF THESIS

Ph.D. (Physics)

GRADE / DEGREE

Department of Physics

FACULTÉ, ÉCOLE, DÉPARTEMENT / FACULTY, SCHOOL, DEPARTMENT

Modelling of electrokinetic phenomena involving confined polymers: applications to DNA separation and electroosmotic flow control

TITRE DE LA THÈSE / TITLE OF THESIS

Gary Slater

DIRECTEUR (DIRECTRICE) DE LA THÈSE / THESIS SUPERVISOR

CO-DIRECTEUR (CO-DIRECTRICE) DE LA THÈSE / THESIS CO-SUPERVISOR

EXAMINATEURS (EXAMINATRICES) DE LA THÈSE / THESIS EXAMINERS

Christopher James Backhouse

Xiaoyi Bao

Javier Giorgi

David Sinclair

Gary W. Slater

LE DOYEN DE LA FACULTÉ DES ÉTUDES SUPÉRIEURES ET POSTDOCTORALES /
DEAN OF THE FACULTY OF GRADUATE AND POSTDOCORAL STUDIES

Modelling of electrokinetic phenomena involving confined polymers: applications to DNA separation and electroosmotic flow control

Frédéric Tessier
B.Sc. Université de Montréal 1996
M.Sc. Simon Fraser University 1999

THESIS SUBMITTED IN PARTIAL FULFILLMENT
OF THE REQUIREMENTS FOR THE DEGREE OF
DOCTOR OF PHILOSOPHY IN PHYSICS

UNIVERSITY OF OTTAWA

Your file Votre référence
ISBN: 978-0-494-15050-4
Our file Notre référence
ISBN: 978-0-494-15050-4

SUMMARY

Microfluidic and nanofluidic technology is revolutionizing experimental practices in analytical chemistry, molecular biology and medicine. Indeed, the development of systems of small dimensions for the processing of fluids heralds the miniaturization of traditional, cumbersome laboratory equipment onto robust, portable and efficient microchip devices (similar to the electronic microchips found in computers). Moreover, the conjunction of scale between the smallest man-made device and the largest macromolecules evolved by Nature is fertile ground for the blooming of our knowledge about the key processes of life. In fact, the conjunction is threefold, because modern computational resources also allow us to contemplate a rather explicit modelling of physical systems between the nanoscale and the microscale. In the five articles comprising this thesis, we present the results of computer simulations that address specific questions concerning the operation of two different model systems relevant to the development of small-scale fluidic devices for the manipulation and analysis of biomolecules. First, we use a Bond-Fluctuation Monte Carlo approach to study the electrophoretic drift of macromolecules across an entropic trap array built for the length separation of long, double-stranded DNA molecules. We show that the motion of the molecules is consistent with a simple balance between electric and entropic forces, in terms of a single characteristic parameter. We also extract detailed information on polymer deformation during migration, predict the separation of topoisomers, and investigate innovative ratchet driving regimes. Secondly, we present theoretical derivations, numerical calculations and Molecular Dynamics simulation results for an electrolyte confined in a capillary of nanoscopic dimensions. In particular, we study the effectiveness of neutral grafted polymer chains in reducing the magnitude of electroosmotic flow (fluid flow induced by an external electric field). Our results constitute the first independent, quantitative verification of theoretical scaling predictions for the coupling between grafted macromolecules and electroosmotic flow. Such simulations will contribute to the rationalization of the existing empirical knowledge about flow control with polymer coatings.

SOMMAIRE

Les technologies microfluidiques et nanofluidiques ont amorcé, depuis quelques années, une véritable révolution dans le domaine de la chimie analytique, de la biologie moléculaire et de la médecine. En effet, l'avènement de systèmes pouvant servir à la manipulation de fluide à petite échelle annonce une ère de miniaturisation, et nous verrons bientôt l'encombrant équipement du laboratoire traditionnel faire place à des microsystèmes analytique robustes, portatifs, et efficients (ressemblant aux puces électroniques que l'on retrouve dans les ordinateurs). De plus, la conjonction d'échelle entre les plus petits dispositifs créés par l'Homme et les plus grandes macromolécules construites par l'évolution naturelle offre un terrain fertile pour l'accroissement de nos connaissances à propos des processus essentiels au développement et au maintien de la vie. En fait, la conjonction est triple, car les ressources informatiques modernes nous permettent aussi de modéliser à un niveau de détail appréciable des systèmes physiques mésoscopiques. Dans les cinq articles qui constituent cette thèse, nous présentons des résultats de simulations portant sur deux systèmes d'intérêt pour le développement de dispositif fluidiques à petite échelle, en vue de la manipulation et de l'analyse d'entités biomoléculaires. Dans un premier temps, nous utilisons un algorithme Monte Carlo nommé *Bond Fluctuation* pour étudier l'électrophorèse de macromolécules à travers une série de trappes entropiques, destiné à la séparation de longues molécules d'ADN double brin en fonctions de leur taille. Nous démontrons que la migration des molécules concorde plutôt bien avec un modèle théorique simple caractérisé par un seul paramètre, et basé sur une compétition entre forces électriques et entropiques. Nous obtenons également une image détaillée de la déformation des polymères en fonction de leur déplacement, nous offrons une prédiction quant à la séparation de topoisomères, et nous traitons de nouveaux régimes d'entraînement de type *ratchet*. Dans un deuxième temps, nous étudions de façon théorique, numérique, et par simulation de dynamique moléculaire, le cas d'un électrolyte confiné dans un capillaire nanoscopique. En particulier, nous considérons l'efficacité de polymères neutres greffés quant à la réduction du flux électroosmotique (un type de flux soutenu par un champ électrique externe). Nos résultats constituent la première vérification quantitative indépendante des prédictions théoriques à propos du couplage entre macromolécules greffées et flux électroosmotique. Ce genre de recherche mènera à une rationalisation des vastes connaissances empiriques reliées au contrôle de flux par revêtement de polymères.

STATEMENT OF ORIGINALITY

As far as I am aware, the work reported in this thesis is innovative. I developed the original research ideas and composed all the articles presented herein, with critical input from my supervisor, Gary W. Slater. The first of the five articles also includes Josée Labrie as a co-author, because my Monte Carlo computer program evolved from her code. In its initial form, the article also included two-dimensional simulation results obtained by Josée, but these were dropped in the publication process for the sake of conciseness. I wrote the entire Molecular Dynamics simulation program for the production of data for the last two articles, in occasional collaboration with Martin Kenward and Steve Guillouzic. My implementation is also largely inspired by authoritative textbooks on the subject, in particular *Computer Simulation of Liquids* by Allen and Tildesley and *The Art of Molecular Dynamics* by Rapaport. My research results offer evidence to support existing theoretical predictions pertaining to electrokinetic phenomena involving confined polymers, and in some cases they reveal new, previously unreported effects.

ACKNOWLEDGEMENTS

I am deeply indebted to my supervisor Gary W. Slater for his sound scientific guidance, his generosity in all respects, as well as his unrelenting, most engaging enthusiasm and optimism during the course this work. I also thank my friends for their abiding encouragement. In particular, I would like to acknowledge the assistance of my immediate colleagues in the research group over the years, namely Jean-François, Martin, Michel, Laurette, Steve, Tatek, Yannick, Martin B., Eric, Sébastien, Owen, Sorin, Simona, Josée, Marc, Katerina, Justin, Claude and Sylvain. Their contributions have ranged from stimulating discussions to the critical revision of manuscripts, to the occasional supply of comestibles. I should also not forget to mention insightful comments by professors Béla Joós and Ivan L'Heureux. I am grateful to my parents, my sister, and the members of my extended family for their sustained confidence in my ability to carry out this enterprise. Finally, I extend my profound gratitude to my wife Nelly for her love, support, and patience throughout the completion of my doctoral studies, as well as for her skill in editing the final version of the thesis.

LIST OF ACRONYMS

2D	Two Dimensions, Two-Dimensional
3D	Three Dimensions, Three-Dimensional
AC, ac	Alternating Current
ATP	Adenosine Triphosphate
BF	Bond Fluctuation
bp	Base Pair
CE	Capillary Electrophoresis
DC, dc	Direct Current
DH	Debye-Hückel
DLVO	Derjaguin-Landau-Verwey-Overbeek
DNA	Deoxyribonucleid Acid
DPD	Dissipative Particle Dynamics
dsDNA	Double-stranded Deoxyribonucleid Acid
EDL	Electric Double-Layer
ELFSE	End-Labelled Free-Solution Electrophoresis
ENIAC	Electronic Numerical Integrator And Computer
EOF	Electroosmotic Flow
ET	Entropic Trapping
FCC	Face-Centered Cubic
FENE	Finitely Extensible Non-Linear Elastic
FJC	Freely-Jointed Chain
FORTRAN	Formula Translation (Programming language)
ISI	Institute For Scientific Information
kbp	Kilobase Pairs
LJ	Lennard-Jones
MANIAC	Mathematical And Numerical Integrator And Computer
MC	Monte Carlo
mcs	Monte Carlo Step
MD	Molecular Dynamics
MEMS	Microelectromechanical Systems
μTAS	Micro-Total-Analysis System

NEMD	Non-equilibrium molecular dynamics
NIH	National Institutes Of Health
NS	Navier-Stokes
NSERC	Natural Sciences And Engineering Council Of Canada
NVT	Number Volume Temperature
RW	Random Walk, Rice And Whitehead (Chapter 6)
PB	Poisson-Boltzmann
PBC	Periodic Boundary Conditions
PBE	Poisson-Boltzmann Equation
PDMS	Polydimethylsiloxane
PTFE	Polytetrafluoroethylene
SI	Système International
SAW	Self-Avoiding Walk
SNP	Single-Nucleotide Polymorphism
ssDNA	Single-Stranded Deoxyribonucleid Acid
US	United States
VV	Velocity-Verlet
WCA	Weeks-Chandler-Andersen
ZIFE	Zero-Integrated-Field Electrophoresis

Table of contents

1

Introduction

Nanotechnology

The prefix *nano* derives from the Latin *nanus* or its Greek equivalent *nanos*, meaning *dwarf*, although further etymology is obscure. Its earliest recorded usage in English are found in the words *nanophanerophyte* (borrowed from French and designating a shrub between 25 centimeters and 2 meters in height) and *nanoplankton* (borrowed from German and designating the smallest unicellular plankton organisms), with the obvious intent to convey the vague meaning of *very small* [1]. It formally acquired its precise scientific meaning in 1960, at the *Onzième Conférence Générale des Poids et Mesures*, when it was definitely adopted to mean $10^{-9}\times$ when adjoined to a measurement unit in the new International System of Units, or SI, for *Système International*: nanometer (nm), nanosecond (ns), nanogram (ng), etc. [2, 3]. The word *technology*, on the other hand, is built from the Greek roots *techne* (craft) and *logia* (discourse), and is understood in the broad encompassing sense of "the scientific study of the practical or industrial arts" [4]; "technology is the application of knowledge (scientific, engineering, and/or otherwise) to achieve practical results" [5].

Nanotechnology therefore refers to "the branch of technology that deals with dimensions and tolerances of 0.1 to 100 nanometers" [6], i.e., the length scale of atoms and molecules (the size of one water molecule is about 0.3 nm, for example). However, the exciting prospects of manipulating individual atoms and molecules have led to much abuse of the prefix *nano* to secure a share of new dedicated research funding, e.g., the US$3.7 billion released for 2005–2008 under the *21st Century Nanotechnology Research and Development Act* signed by the United States government in December

2003 [7]. Roger Smith, the head of the Materials Science Department at Oxford University, even jokingly suggests that *nano* "comes from the verb which means *to seek research funding*" [8]. Venture capital and commercial interests also exacerbate the hype, as the market for nano-based products is expected to grow from about US$13 billion in 2004 to more than US$500 billion in 2010 [9, 10]. It is perhaps a sign that I fall victim to the general enthralment for nanotechnology that I choose to open this thesis with a section entitled as such, but in earnest I do report in later chapters on the study of truly nanoscopic systems, i.e., electrolytes and polymers confined in pores a few nanometers in size.

The organization of matter on an ever decreasing scale has preoccupied scientists of all epochs, but the original formulation of ideas concerning the directed and purposeful handling of matter at the nanoscale is often attributed to the famous physicist Richard P. Feynman. On December 29th, 1959, he presented a popular talk at the annual meeting of the American Physical Society entitled "There's plenty of room at the bottom: an invitation to enter a new field of physics" [11]:

> "I would like to describe a field, in which little has been done, but in which an enormous amount can be done in principle. (...) Furthermore, a point that is most important is that it would have an enormous number of technical applications. What I want to talk about is the problem of manipulating and controlling things on a small scale. (...) It is a staggeringly small world that is below. In the year 2000, when they look back at this age, they will wonder why it was not until the year 1960 that anybody began seriously to move in this direction. (...)
>
> At the atomic level, we have new kinds of forces and new kinds of possibilities, new kinds of effects. The problems of manufacture and reproduction of materials will be quite different. (...) The principles of physics, as far as I can see, do not speak against the possibility of maneuvring things atom by atom. It is not an attempt to violate any laws; it is something, in principle, that can be done; but in practice, it has not been done because we are too big."

In a recent review published in the journal bearing the euphemistic title *Small*, George M. Whitesides marks an interesting distinction between two *flavours* of nanotechnology [12]. The first, *evolutionary* nanotechnology, is already "in the robust health of early childhood" and refers to the further miniaturization of current micrometer-scale technology (e.g., the semiconductor industry already produces transistors with 90 nm components and oxides only 1.2 nm thick) or to existing products that rely on nanoscale features (e.g., those of material science and chemistry). The second, rather more thrilling, *revolutionary* nanotechnology, is emerging from fundamentally new science that exploits properties of matter unique to the nanoscale: novel electronics based on quantum dots; new nanostructured materials based on carbon nanotubes; true molecular design based on the

manipulation of individual atoms. However, this new nanoscience remains for the moment confined to the university laboratory workbench. The advent of journals gathering advances in nanoscale science across all disciplines into a common forum, e.g., the American Chemical Society's *Nanoletters*, the Institute of Physics's *Nanotechnology* and the *Virtual Journal of Nanoscale Science and Technology*, is a tribute to the convergence of ideas in the field, but also a sure sign that novel nanoscience has not yet matured into actual technologies. It is not clear how much of it will, or how fast the transition will occur, but as best put by Whitesides: "where there is smoke, there will eventually be fire; that is, where there is enough new science, important new technologies will eventually emerge" [12].

There are significant hurdles to the advancement of science, let alone the development of reliable technologies, at the nanometer scale. Despite nanoscale systems being simpler (in the sense that they involve a relatively small number of constituents), their characterization and analysis is often more complicated because one cannot rely on average bulk properties; in other words, one cannot invoke a thermodynamic limit and, ultimately, has to leap from a continuum, macroscopic description to an explicit but intractable n-body problem. Physical phenomena at the nanoscale can also be downright counterintuitive to classically trained scientists and engineers. For example, thermal motion becomes dominant (the thermal velocity of a water molecule at room temperature is almost 650 m/s), the second law of thermodynamics can be violated on time scales relevant to operation of nanomachines [13], and surface effects can overwhelm bulk material properties. From this perspective it might seem incredible that nanotechnology could work at all! But it undoubtedly does, for life itself relies on intricate nanomachinery. As aptly turned around by the renowned evolutionary biologist Richard Dawkins in his book "Climbing Mount Improbable" [14], it is rather organisms of our dimension that constitute *gigatechnology*. The nanometer range is the natural home of molecules, and all of life's elementary processes — information storage and replication, metabolic transactions, mechanical transduction — thus occur on this molecular scale. Indeed, Nature had to *invent* a wide array of amazing structures in order to evolve cells and eventually more complex organisms: DNA to hold genetic code (the organism's *construction program*), proteins for metabolic functions such as the catalysis of favourable chemical reactions, microtubules and motor proteins for intracellular transport and organism-scale movement, etc. From this alternate perspective, it is incredible that *gigatechnology* could work at all! Feynman had already alluded to the intimate connection between nanoscience and biology in another passage of his 1959 presentation [11]:

> "The biological example of writing information on a small scale has inspired me to think of something that should be possible. Biology is not simply writing information; it is doing something about it. A biological system can be exceedingly small. Many of the

> cells are very tiny, but they are very active; they manufacture various substances; they walk around; they wiggle; and they do all kinds of marvellous things — all on a very small scale. (...) I am, as I said, inspired by the biological phenomena in which chemical forces are used in repetitious fashion to produce all kinds of weird effects (one of which is the author)."

That life is rooted in nanoscale mechanisms is certainly another strong incentive for the development of nanotechnology. The idea of using nanoscopic pores for the sequencing of DNA molecules [15–28], initially formulated in 1996 by Kasianowicz, Brandin, Branton and Deamer [29], is a telling illustration of future prospects for nanoscale biotechnology. The idea is to thread long flexible double-stranded DNA segments through a natural or synthetic pore only about 2 nm in diameter and to measure the strand length with current monitoring techniques, or even read the DNA sequence directly with a minuscule detector integrated into the pore (see Figure 1.1). Estimates for the attainable throughput of a single such pore are in the range of a million nucleotides per second

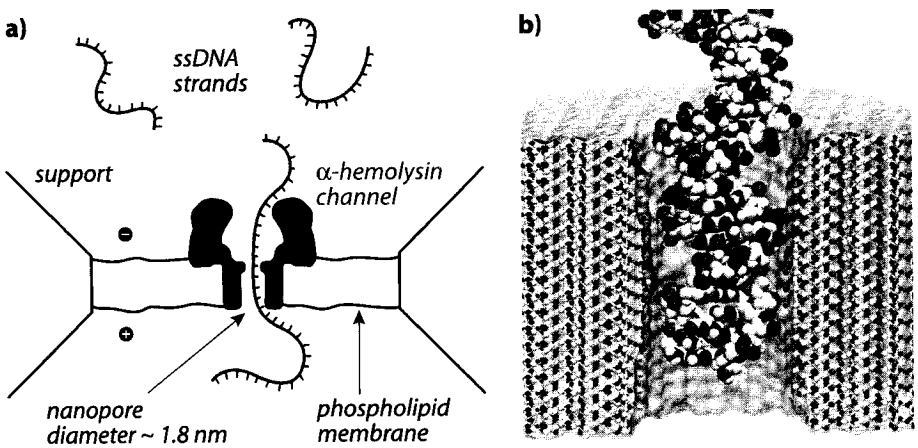

FIGURE 1.1 **a)** A natural nanopore for high-speed genetic sequencing: an electric field forces negatively charged single-stranded DNA molecules to slither through an α-hemolysin protein channel. Because the pore diameter is commensurate with that of the DNA strand, the current between the two electrolyte reservoirs on either side of the suspended lipid bilayer is blocked during DNA passage. The duration of the current blockade gives an indication of strand length, and if different bases featured different current signatures, one could in principle infer the DNA sequence. Reproduced with permission from Reference 17, copyright (2001) by the American Physical Society. **b)** Atomistic computer simulation of a double-stranded DNA molecule passing through a small bore inside a wall of Si_3N_4. There are significant advantages to using synthetic nanopores: they are tunable, robust, and compatible with solid-state electronics, raising hopes to integrate sensors in the vicinity of the pore for direct reading of the DNA sequence. Image courtesy of A. Aksimentiev [30].

[17, 25, 27], so assuming that detection is possible at such speeds, sequencing the three billion bases of the human genetic code would require less than an hour, a far cry from the 13 years spent on this task by the Human Genome Project using modern sequencing methods [31–33]. Many groups today join efforts (*compete*, really) to build nanopore-based sequencing devices, but given the difficulties implied by the rich dynamical behaviour of nanoscale systems, sequencing DNA in nanopores with single nucleotide resolution has not yet been achieved.

Microfluidic technology

In stark contrast with nanometer-scale technology, technology at the scale of the micrometer (10^{-6} m, or μm) is quite tangible, and over the last four decades it has practically invaded our world. One only has to think of the ubiquitous electronic microchip, used to store information at ever increasing density and process it at ever increasing speed, to be convinced that modern technology has a firm foothold on the micrometer landscape. Perhaps even more convincing is the development over the last 20 years of microelectromechanical systems (MEMS) — essentially micrometer-scale machines — constructed using microlithography techniques initially elaborated for silicon in the microelectronics industry. MEMS rely on electric and mechanical interactions of microscopic moving parts to carry out useful tasks, usually with higher precision and on shorter timescales than their macroscopic equivalents. Mass-produced micromachined accelerometers and gyroscopes used for automotive safety (e.g., the deployment of an airbag during a car collision or the dynamic adjustment of suspension to ensure vehicle stability) epitomize the reality of microscale mechanical engineering [34, 35].

The advent of microfluidic devices, which allow for the transport and manipulation of minute amounts of fluid in microchannel manifolds, offers yet another example of the amazing progeny of microfabrication techniques [36]. Instead of filling the etched regions of a substrate with a metal or a semiconductor to create pathways for electric signals, one can simply seal the etched void to build microscopic pipes and reservoirs, and eventually assemble a network of basic fluidic components to form a complex microflow system. But whereas silicon and glass are excellent materials for electronic devices and MEMS, they are not necessarily ideal for microfluidic systems: leak proof valves usually rely on a compliant material, and some fluidic applications may rely on delicate channel surface properties that are incompatible with silicon processing techniques. For this reason, microfluidics has sponsored the use of new soft material substrates, such as the popular elastomer polydimethylsiloxane (PDMS), and new soft fabrication techniques [37]. The field of microfluidics promises to do

for chemical and biochemical analysis what the microelectronics industry has done for computing: the miniaturization of room-size equipment into low-cost, portable, integrated devices. While it is true that the transistor is the fundamental building block of computers, it is really the invention of the integrated circuit that heralded the computer revolution. In a similar fashion, while various sensors and actuators are the basic components of a fluidic system, it is their integration into a microscopic *laboratory* that holds fantastic scientific and industrial prospects. This ultimate goal is often embodied in the designations *lab-on-a-chip* and *micro-total-analysis system* (μTAS). The comparison between microelectronics and microfluidics is more than a useful analogy: fluidic circuits were apparently built as an alternative to vacuum tubes and solid state devices in the 1960s and, more recently, researchers have built microfluidic memories and flux stabilizers [38].

A stunning example of the progress toward integrated analytical systems is the microfluidic *processor* built and operated by Quake and co-workers in 2002, shown in Figure 1.2. This device contains 2056 microvalves and is capable of performing automated chemical assays by loading and mixing sub-nanolitre amounts of fluid, i.e., volumes less than $(0.1\,\mathrm{mm})^3$, in 256 individually addressable reaction chambers, and then recover the reaction products [39, 40]. Microchemical reactors in large parallel integration have in fact already revolutionized combinatorial chemistry, a brute force approach to the synthesis and screening of new compounds in search of specific properties, with immediate applications to drug design [41, 42]. Three immediate advantages of microfluidic laboratories are an increased analysis speed (through both shorter time per analysis and massive parallelism), a reduction in reagent consumption and costs, and the inherent mechanical stability of monolithic systems [36]. Less obvious benefits are the high heat and mass transfer rates attainable in microchannels (on account of the large surface-to-volume ratio), which imply that chemical reactions can be carried out under conditions that are more uniform (allowing better characterization of the reaction environment) but also more aggressive (allowing higher reaction yields) [41].

Given the current thrust behind genomics, the development of microfluidic technology is also in large part motivated by the analysis of biological entities, and in particular by the sequencing and analysis of DNA molecules. Again, the integration of the many steps typically involved in genetic sample preparation and detection — cell culture, cell isolation, cell lysis, nucleic acid purification, amplification and finally detection — onto a single, automated microchip offers key advantages. In a 2004 review article, Lagally and Mathies estimate that the time required for a complete analysis cycle could thus be reduced from days to minutes [43]. They also note that integration eliminates much of the external contamination since the sample is not exposed to the open environment between the

various steps. Hence it is not surprising that the development of integrated bioanalytical systems is currently the subject of intense research. However, the critical analysis stage of DNA length detection and sequence recognition has received most of the early attention and was the first to be transposed to microscale devices, in the form of DNA hybridization arrays or via the miniaturization of widespread capillary gel electrophoresis methods. In the latter approach, an external electric field forces DNA strands to migrate through a gel matrix, and this effective *obstacle course* reduces the mobility of the strands in a length-dependent way, hence separation is achieved. But the ability to microfabricate separation systems offers more than a mere scaling down of existing experimental methods. Indeed, one can now design different *obstacle courses* practically at will and thus modulate the mobility of DNA molecules in novel and useful ways. Geometrical features inside a microchannel

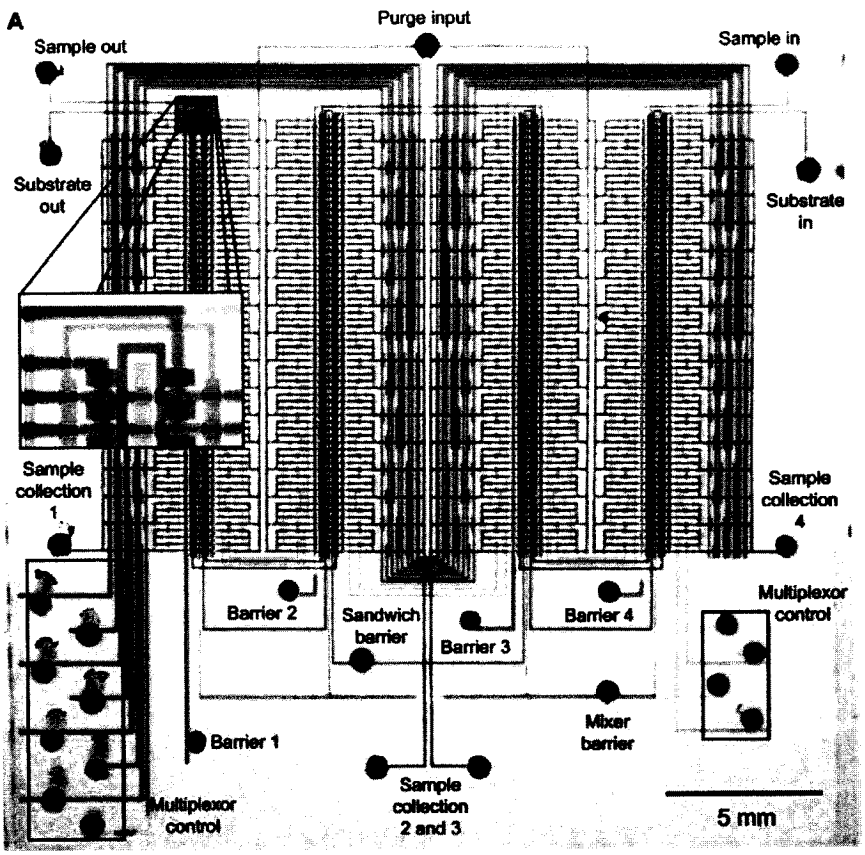

FIGURE 1.2 Optical micrograph of a microfluidic comparator chip built by Quake *et al.* [39]. The content of each of the 256 reaction chambers can be accessed independently and mixed with that of another chamber via a set of 2056 elastomeric valves. In this image, the various inputs have been loaded with dyes to reveal the elements of the fluidic logic. Reprinted with permission from Reference 39, copyright (2002) AAAS.

can effectively replace gel fibres, as clearly demonstrated by the Craighead Research Group from Cornell University with their *artificial gel* structure in the form of an array of narrow posts, pictured in Figure 1.3 [44, 45]. It is interesting to note that such microfabricated structures can not only serve as chip-based DNA separation devices, but they also allow for direct observation of single DNA molecules in well-defined environments. This provides better insight into the fundamentals of the separation process than that afforded by mean-field type parameters, e.g., the mean pore size, typically invoked to characterize disorded media such as gels. The open dialogue thus established between experiment and theory can guide the development of new, more realistic models.

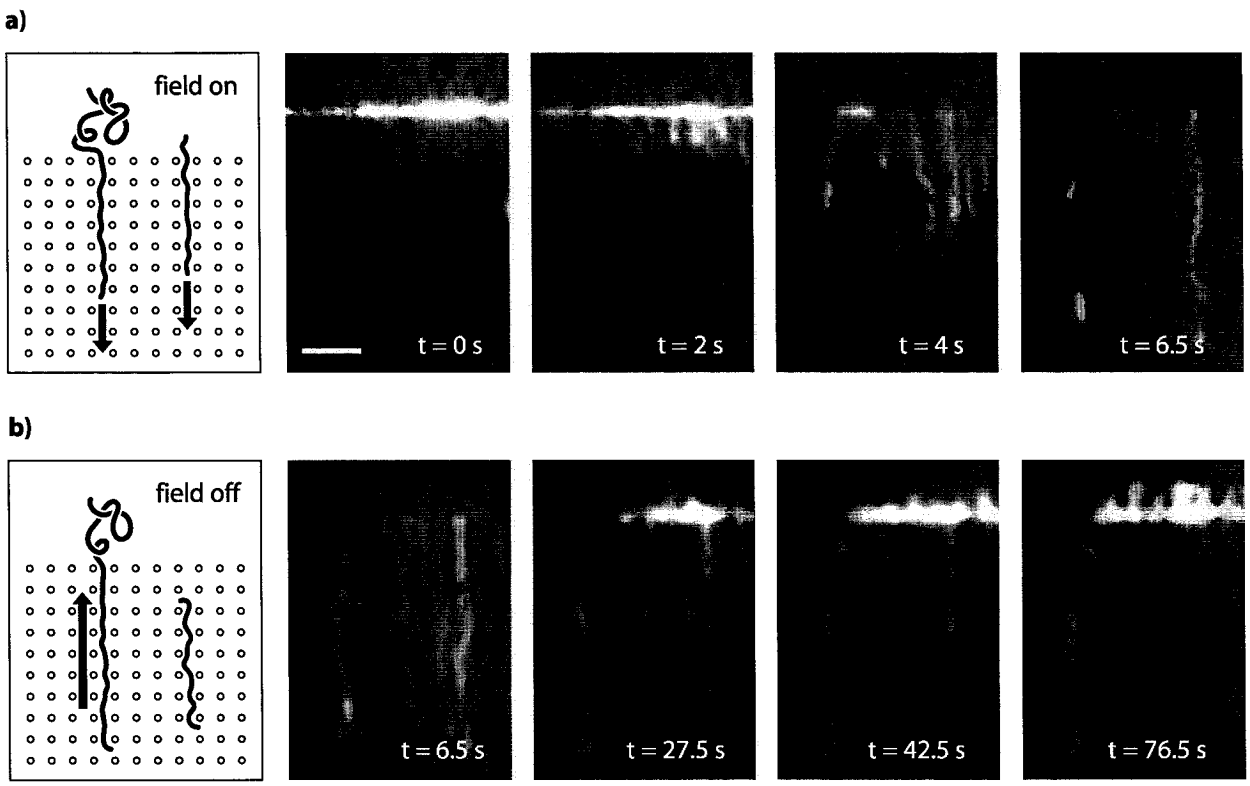

FIGURE 1.3 DNA molecules in the artificial gel structure built by the Craighead Research Group, using microlithography techniques [44]. The scale bar in the $t = 0\,\mathrm{s}$ frame represents $5\,\mu\mathrm{m}$. **a)** From $t = 0\,\mathrm{s}$ to $t = 6.5\,\mathrm{s}$, an electric field is applied to allow the DNA molecules to overcome the entropic barrier and enter a pillar-dense region, where they must elongate between the pillars (separated by about 100 nm, but not visible in these photographs). **b)** When the field is turned off at $t = 6.5\,\mathrm{s}$, molecules that have completely entered the pillar region remain there, but the other molecules experience a recoil and retract in the entropically more favourable pillar-free region. Reproduced with permission from Reference 44, copyright (2002) by the American Physical Society.

Lagally and Mathies point out another interesting avenue for genetics in microfluidic environments: single-cell DNA analysis [43]. A typical mammalian cell encloses a volume of roughly $(10\,\mu\mathrm{m})^3$, and the dilution of its content into a conventional analysis volume of about $1\,\mathrm{mm}^3$ reduces a million times the concentration of any one of its DNA strands, to a scant $10^{-18}\mathrm{mol/L}$. This is at least three orders of magnitude lower than that required by the most sensitive nucleic acid detection methods, hence DNA sequencing is normally based on a large population of cells to ensure that enough DNA is harvested for proper detection. The ability to study the genetic content of a single cell within a microscopic analysis volume, which has already been demonstrated [46], could yield precious information about gene expression and variation within cell populations, and clarify the origin and consequences of such cellular-level phenotypic and genetic polymorphism.

For all of the advantages outlined above, and more, microfluidic technology and its integration with readily available electronic data storage and signal processing components holds tremendous potential. The emergence of low cost, mass-produced lab-on-a-chip systems is bound to profoundly transform our society by revolutionizing experimental practices in chemical synthesis and analysis, bioanalytical science, and *a fortiori* in medical diagnostics (e.g., point-of-care blood sample analysis with a *blood-on-a-chip* system [47]).

Thesis rationale

The work reported in this thesis pertains to computer simulations of polymers in microfluidic and nanofluidic channels, and is geared more specifically towards the modeling of phenomena relevant to DNA analysis technologies. Simulation is generally regarded as a very useful research tool in bridging the gap between theory and experiment [48–51], and its relevance is only enhanced by the miniaturization of the studied systems. Indeed, computational resources available today allow us to perform detailed atomistic or molecular simulations at length and time scales approaching those of the smallest man-made devices (nanoscience encourages the lazy computational physicist: don't design simulations to handle larger systems, wait for engineers to build smaller ones). The mesoscale range (between 10^{-9} and 10^{-6} meters) is a fertile ground for the growth of a strong symbiosis between experimental and computational science.

The original motivation behind this work is well summarized in an excerpt from my original Ph.D. project proposal submitted to the Natural Sciences and Engineering Research Council of Canada for the post-graduate scholarship competition (my translation, from French):

> "Our goal is to develop, over the next few years, a complete numerical model of [capillary electrophoresis]. It is nowadays possible to carry out Molecular Dynamics simulations involving over 100 000 molecules on high-performance computers. Within three years, we can probably handle millions of molecules on personal workstations. It therefore becomes possible to model [capillary electrophoresis] at the molecular level, an exciting possibility we wish to explore right away. We are not aware of any other research group which has undertaken this ambitious project.
>
> We will thus develop a model that accounts for: i) interactions between analytes and capillary surfaces; ii) the presence of polymers (or gel) in solution; iii) interactions with counter-ions; iv) solvent flow, eventually; v) the external electric field; vi) electroosmotic effects near the walls; vii) Joule heating effects; viii) the parabolic temperature profile in the conduit; and any other effects typical of microfluidic systems."

Although consistent in spirit with our original plan, the content of Chapters 2 and 3 is notably absent from this rather precise road map. At the outset of this degree, a novel electrophoretic microchannel built by the Craighead Research Group captured our attention [52]. The efficient separation of large DNA strands in this device relies on the entropic trapping phenomenon: the electrophoretic motion of DNA molecules drifting in solution is hindered by periodic narrow constrictions, and longer strands are found to elute faster. This rather counterintuitive experimental finding fuelled a certain controversy regarding the existence of DNA-surface interactions or hydrodynamic flow inside the channel, and immediately prompted us to investigate the issue with a computer simulation model, depicted in Figure 1.4a. Our results confirmed that the proposed model for the separation mechanism could account for the observed elution order of the molecules.

Following this success, and realizing that the microchannel in question could easily be turned into a geometrical ratchet (see page 29), or used under pulsed-field ratchet conditions, we set out to characterize such novel operating regimes. This became the first 3D example of Slater, Guo and Nixon's original and widely recognized idea concerning *entropic ratchets* published in *Physical Review Letters* in 1997 and cited more than 40 times by other groups since [53]. We showed that a judicious choice of ratcheting parameters could yield bi-directional transport according to molecular-size; moreover, we uncovered a previously unreported "resonance" phenomena that can be used to optimize the performance of electrophoretic devices based on entropic trapping.

After this excursion in the simulation of microchannel electrophoresis, we returned to the original goal set out in the Ph.D. project proposal. We developed a large-scale Molecular Dynamics program for the simulation of polymers in solution that explicitly accounts for hydrodynamic and electrostatic interactions, temperature gradients, the presence of polymer chains, fluid-solid surface interactions, and electroosmotic flow (EOF). In fact, during the course of this work, we decided to

focus our simulation efforts more specifically on the phenomenon of EOF itself, and on its modulation with grafted polymer chains, as depicted in Figure 1.4b. This is of great relevance for modern electrophoresis technology because polymer coatings are routinely employed on an empirical basis to control EOF in capillary electrophoresis, despite the lack of a fundamental understanding of the process. The only (and timely) theoretical publication on the subject by Harden, Long and Ajdari in 2001 [54] certainly motivated us further in this direction, as it offered detailed predictions for the coupling between the EOF and polymer coatings with which to compare our simulation results (presented in Chapters 5 and 6). Finally, our theoretical work on the Poisson-Boltzmann equation (Chapter 4) also derives from early EOF simulation results which clearly indicated the inadequacy of the bulk approximation in closed, high surface-to-volume ratio electrolyte systems. While this point had been addressed before in the context of mean-field models for colloid suspensions, our treatment is *a priori* unburdened by linearization concerns and is certainly more accessible to the electrophoresis community.

This thesis is a collection of research articles published in leading scientific journals over the course of my Ph.D., with additional contributions to collaborative publications highlighted in the appendices. The remainder of this chapter is devoted to introducing some basic concepts on which this work is founded but that are only briefly mentioned, if at all, in subsequent chapters, since they are generally considered common knowledge among the intended audience of the publications.

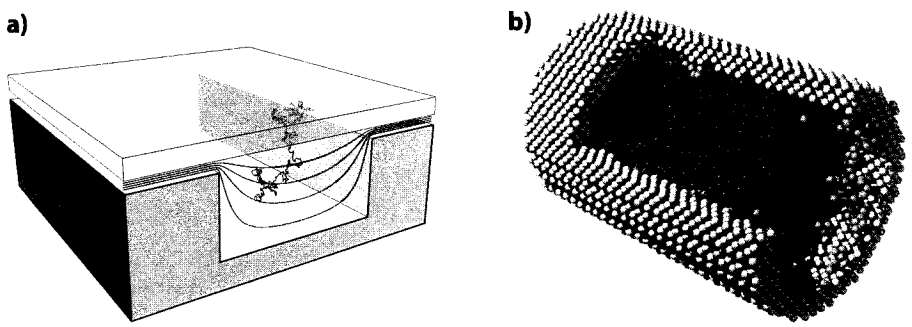

FIGURE 1.4 **a)** A snapshot from a lattice Monte Carlo simulation of the entropic trap array device built by the Craighead Research Group for the separation of long DNA molecules, as detailed in Chapter 2. A 600-monomer molecule is shown here, just about to escape from the trap via the narrow constriction, under the pull of an external electric field (the field lines are shown in red). **b)** A snapshot from a Molecular Dynamics simulation of electroosmotic flow control with a polymer coating in a nanoscopic capillary, as detailed in Chapters 5 and 6 (with sections removed to reveal all the components). Water is shown in blue, wall atoms in grey, positive ions in red, negative ions in black, and grafted polymer chains in yellow.

Polymers

The word *polymer* literally means *many parts*, and refers to a substance composed of large molecules, each one constructed from the repetition of a basic chemical unit, or *monomer*. These units are linked together by strong covalent bonds to form long, usually flexible, linear chains, although more exotic arrangements, such as stars or other branched topologies, are also possible. This thesis deals almost exclusively with linear polymers, except for a short mention of loops and knots at the end of Chapter 2. The number of monomers in the chain, or *degree of polymerization*, is usually quite large (e.g., up to 10^5 in polystyrene), hence such molecules are generally referred to as *macromolecules*. Figure 1.5 provides schematic representations of a specific macromolecule, polytetrafluoroethylene, commonly known under the commercial name Teflon®, at two different levels of magnification. Although the word *polymer* formally designates a substance composed of macromolecules, in polymer physics it is usually taken to designate the individual macromolecule itself, and we will follow this usage.

It is interesting to learn that the word *polymeric* was first used by the great Swedish chemist Jöns J. Berzelius as early as 1832, at a time when the structure of even the simplest chemical com-

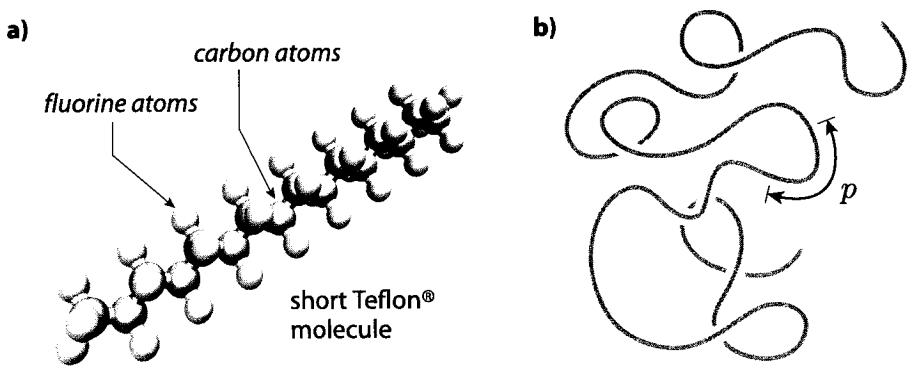

FIGURE 1.5 **a)** A short segment of polytetrafluoroethylene (PTFE), composed of 16 carbon atoms, in cyan, each bearing two fluorine atoms, in white (except the end carbons which bear three fluorines). In principle, there is no limit to the number of monomers that can be linked together, and it is thus possible to form very long macromolecules. Here all the monomers are aligned in a straight line, but at finite temperature there is some rotational freedom between monomers, hence the molecule is usually flexible. **b)** A schematic representation of what a long PTFE molecule comprising thousands of monomers might look like, from a distance. The flexibility of a macromolecule is usually characterized by its *persistence length*, p, which can be regarded as the arc length over which the "memory" of the chain direction is lost.

pounds was still a matter of debate (Berzelius also coined the term *protein* and introduced the modern chemical nomenclature and notation) [55, 56]. Historically, the very high molar masses of polymeric substances confounded chemists. For example, a polymeric starch from the Easter Lily has a molar mass of 250 *tonnes* per mole [57], which is roughly 14 million times that of water! With caution, and even though "the rules of chemical valency, even in their most primitive form, anticipate the occurrence of macromolecular structures" [58], such substances were for a long time considered to be giant aggregates of smaller molecular species. Not until 1920 did the German physical chemist Hermann Staudinger put forth the bold concept of true macromolecules, in the sense of being held together by strong covalent bonds. His ideas were initially mocked but came to be accepted within only ten years, on the basis of accumulating experimental evidence. The first journals and learned societies dedicated to polymers appeared just before 1950, and the 1953 Nobel prize in chemistry was awarded to Staudinger "for his discoveries in the field of macromolecular chemistry" [59].

We often associate polymers with industrial plastics, so common today, and we thus tend to forget that natural polymers also abound. Although the invention of the first synthetic polymer material by Leo H. Baekeland in 1906 did set in motion a huge industry, naturally occurring polymers existed and were put to technological use long before. Perhaps the most remarkable example is that of natural rubber, which is essentially coagulated latex tapped from the Hhevé tree. The French geologist de la Condamine, in a 1751 report on his travels to South America (where he was sent on a famous three-man expedition to measure the length of a degree of meridian at the equator), recounts that the Maya already harvested the substance to waterproof footwear and even fashion elastic water bottles, and they had presumably been doing so for hundreds of years. Rubber was eventually imported to Europe, where it actually got its English name in 1770, when E. Nairne, the owner of a artist's shop, discovered its effectiveness in *rubbing* away pencil marks on paper (the French name *caoutchouc*, on the other hand, is thought to derive from the original Mayan expression *caa o-chu* meaning *weeping wood*). The material found widespread applications in industry, particularly after 1839 when Goodyear resolved the problem of its tackiness by the serendipitous overnight discovery of *vulcanization*, eight years in trying. Natural rubber rapidly became a precious commodity, and the sharp increase in its trade price between 1908 and 1910 certainly fostered the emergence of the synthetic rubber industry. [55, 57, 56]

Polymers also play a central role in biology—so many roles, in fact, as to basically form the whole cast of life: macromolecules account for about 90% by weight of the total organic matter in a cell [60]. The most remarkable *biopolymer* is without question deoxyribonucleic acid, or DNA, a

macromolecule that actually holds, in coded form, the set of instructions to build any given living organism. Strictly speaking, a DNA molecule is composed of two macromolecules, called *strands*, intertwined to form the famous double-helix structure, uncovered through X-ray diffraction by Franklin, Watson and Crick in 1953 [01–07]. However, the stability of the double-stranded form, due to both the helical structure and the strong hydrogen bonding between the two strands, is such that we usually speak of double-stranded DNA (dsDNA) as one molecular entity. It is possible to separate the two strands by physical or chemical means to obtain two single-stranded DNA molecules (ssDNA).

The detailed structure of DNA, shown in Figure 1.6, is more involved than that of the simple polymer shown in Figure 1.5 but it nevertheless arises from a repetition of basic chemical units. Each strand is composed of a sugar-phosphate backbone to which are attached, every 0.34 nm, one of four bases: adenine (A), thymine (T), cytosine (C) or guanine (G). These bases have the singular property of forming two complementary pairs. The atomic disposition in A and T bases are such that they *fit* well when facing each other, forming two hydrogen bonds (sharing two electrons); however, neither fits well with either C or G. Likewise, facing C and G bases form a rather stable base pair

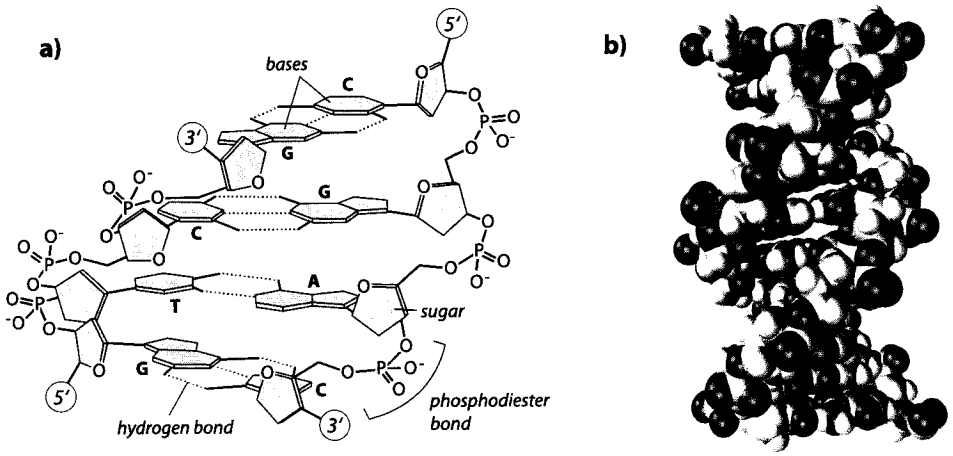

FIGURE 1.6 **a)** The organization of a double-stranded DNA molecule: the two strands, running in opposite directions, are composed of a sugar-phosphate backbone, with each ribose ring bearing one of the four bases adenine (A), thymine (T), cytosine (C) or guanine (G). The atomic geometry of the bases is such that every A faces a T, and every C faces a G. Reproduced with permission from Reference 01, copyright (1989) Garland Science/Taylor & Francis LLC. **b)** A space-filled atomic representation of one turn of the DNA double-helix, or 10 DNA base pairs, that is, about 3.4 nm. Carbon atoms are shown in cyan, hydrogen in white, oxygen in red, nitrogen in blue, and phosphorus in green. The size of the spheres in this picture is a good measure of the relative atomic size of each element.

with three hydrogen bonds. Hence, the two strands in a DNA molecule are exact complements: every A on one strand faces a T on the other and the same is true for the C–G pair. And therein lies Nature's trick to allow self-replication, one of the key ingredients of life. Since the two strands are complementary, two exact copies of one original dsDNA molecule can be reconstructed from the two separated strands; this is what occurs during cell division to allow each daughter cell to inherit a complete copy of the genetic code. We use the word *code* because a small part of the sequence of bases in DNA (only about 1% in humans) is read by intricate intra-cellular machinery, and ultimately translated into various chains of amino acids to form all the proteins needed by an organism. DNA molecules can be amazingly long: the human genome consists of approximately 3 billion base pairs divided into 46 compactly wound microscopic segments (paired in 23 *chromosomes*), but even that pales in comparison to the longest genome on record, that of the lung fish, which stands at about 139 billion base pairs [57] (so perhaps we should call it the *long* fish). The largest human chromosome is roughly 245 million base pairs long, and has a contour length of 85 millimeters. The total nuclear DNA in one adult human would thus measure about 10 billion kilometers if unwound into a straight line (i.e., almost 70 times the distance between the Earth and the Sun), but amounts to only about 30 grams!

Model representations

The single most defining characteristic of polymers in regards to their physical properties is that they are long, flexible objects: in solution, they adopt convoluted conformations such as the one shown in Figure 1.5b, on page 12. The atomic or *local* structure of polymers, e.g., that in Figure 1.5a, is the business of chemistry (or, rather, quantum physics; all natural sciences boil down to physics, right?), and does not differ much from that of small molecules. In fact, experimental methods to probe polymers on that scale, e.g., infrared and Raman spectroscopy or nuclear magnetic resonance, are essentially the same as those used to probe simple chemical compounds [68]. Knowledge of what goes on at the monomer level is of course crucial to the construction of a macromolecule by chemical means (a process called *polymerization*), but generally it has little influence on the overall physical properties of the completed chain taken as a whole; however, the polymer physicist is concerned precisely with the molecular-scale, *global* properties of polymers. From the perspective offered in Figure 1.5b, he or she intently discounts the chemical details to extract universal features common to a large class of polymers [68]. This point of view is remarkably well emphasized in the Nobel lecture of Paul J. Flory, the recipient of the 1974 Nobel prize in chemistry[58]:

> "It is noteworthy that the chemical bonds in macromolecules differ in no discernible respect from those in monomeric compounds of low molecular weight. The same rules of valency apply; the lengths of the bonds, e.g., C–C, C–H, C–O, etc., are the same as the corresponding bonds in monomeric molecules within limits of experimental measurement. This seemingly trivial observation has two important implications: first, the chemistry of macromolecules is coextensive with that of low molecular substances; second, the chemical basis for the special properties of polymers that equip them for so many applications and functions, both in nature and in the artifacts of man, is not therefore to be sought in peculiarities of chemical bonding but rather in their macromolecular constitution, specifically, in the attributes of long molecular chains."

The universal attributes of polymers are topology-dependent *emergent properties* that cannot, in fact, be predicted from an atomistic model, however refined (more generally, the disconnect between local and global scale phenomena is actually a profound question in physics, and has recently prompted two physicists [69] to regard it as a fundamental obstacle to the formulation of a *Theory of Everything*).

The irrelevance of monomer-level details affords us, in turn, some flexibility of our own in choosing a representation for the basic unit of a model polymer. The only important criterion is that we ultimately recover the thread-like appearance of Figure 1.5b when we combine a large number of units. In the language of critical phenomena, various model representations of polymers are equivalent in the long-chain limit (akin to the thermodynamic limit in statistical mechanics) when they belong to the same universality class, and the polymer physicist is ultimately interested in the critical exponents and other such universal properties of polymer chains. Some of the most common *coarse-grained* models of macromolecules, shown in Figure 1.7, exploit this point of view. The *freely-jointed chain model* (FJC) in Figure 1.7a is probably the simplest way to account for the global features of a long thread-like object. It amounts to an immaterial random walk (RW) that is conceived to trace the conformation of the macromolecule, and it depends on just two parameters: the number of steps N and the step size a. In fact, since the global properties of polymers are insensitive to the local chain structure, we can even use a *lattice random walk*, as in Figure 1.7b. A lattice approach is particularly well suited for computational studies, since integer operations in a computer are significantly faster than floating-point ones; it is for this reason that simulations in Chapter 2 are lattice-based. To determine the detailed dynamic properties of a polymer chain, it is convenient to choose a model that takes into account the actual motion of the individual parts of the chain. A popular choice is the *bead-spring model*, represented in Figure 1.7c, wherein beads are connected together with simple springs; this resembles the perspective adopted in the Molecular Dynamics simulations of Chapters 5 and 6. [70, 71]

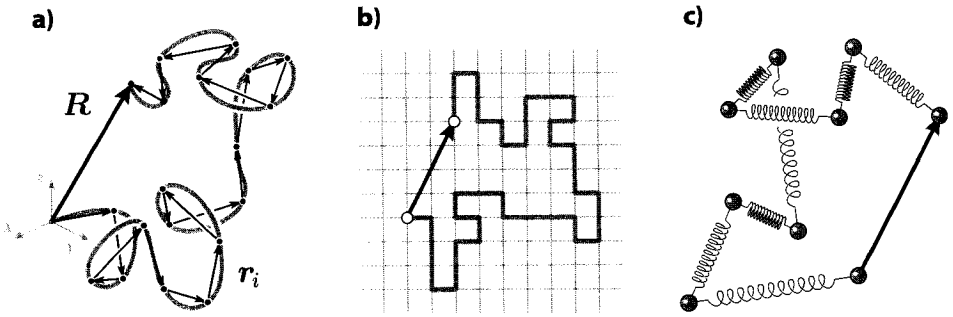

FIGURE 1.7 **a)** The freely-jointed chain model of polymers consists in a random walk, shown here in three dimensions. Any given walk is constructed from a set of N randomly oriented vectors $\{\boldsymbol{r}_i\}$, each one of length a, adding up to the end-to-end vector $\boldsymbol{R}$. Each walk is imagined to correspond to a particular spatial conformation of the polymer molecule. **b)** The lattice random walk model, shown here in two dimensions, is more efficient for computer simulations because it can be implemented using integer arithmetic. **c)** The bead-spring model can be used to calculate some dynamic properties of macromolecules; the springs between the beads embody the entropic elasticity of polymer chain segments.

Polymer coil size

In the FJC picture of Figure 1.7a, a macromolecule can reach any of its possible conformations at no cost in energy and, since each one is *a priori* equiprobable, we can obtain some basic physical properties of isolated polymer molecules from a simple ensemble averaging procedure. For example, to address the question "what is the physical extent of a macromolecule?", we pick a representative measure for the size of one conformation, and average its value over all possible conformations. But what is the best representative measure for the size of one conformation? We could consider the total walk distance $L = Na$, i.e., the contour length of the molecule, but this is not very representative because most conformations are quite convoluted and thus occupy a space of typical extent much smaller than L. Upon looking at Figure 1.7a, we see that the end-to-end vector $\boldsymbol{R}$ of the RW, i.e., the net displacement, provides a much better measure of chain size. Since the directions of individual steps are not correlated here, it is easy to calculate the mean square value $\langle R^2 \rangle$ for a RW of N steps by averaging over all the possible walks:

$$\langle R^2 \rangle = \left\langle \sum_{i=1}^{N} \sum_{j=1}^{N} \boldsymbol{r}_i \cdot \boldsymbol{r}_j \right\rangle = \left\langle \sum_{i=1}^{N} r_i^2 \right\rangle = Na^2 , \tag{1.1}$$

and we can therefore write the characteristic size of a FJC as

$$\tilde{R} \equiv \langle R^2 \rangle^{1/2} = N^{1/2} a . \tag{1.2}$$

The exponent in Equation 1.2 is an example of the universal properties discussed above; it is the same for a large class of simple RWs, provided that $N \gg 1$. The local details (e.g., the size of individual steps) only influences the proportionality constant in Equation 1.2, not the exponent. Even if, more realistically, we specify values for the azimuthal angle θ and the polar angle ϕ between successive steps in the RW, we still find, in the large N limit,

$$\langle R^2 \rangle = Na^2 \left(\frac{1+\cos\theta}{1-\cos\theta} \right) \left(\frac{1+\langle\cos\phi\rangle}{1-\langle\cos\phi\rangle} \right) \equiv Nb^2 , \tag{1.3}$$

and the scaling relation $\tilde{R}^{1/2} \sim N^{1/2}$ still holds [71]; we merely have a FJC with an effective bond length b. In fact, the universal character of the scaling exponent allows us to calculate this effective bond length for any chain in terms of its physical size and its maximal extension $R_{\max}$:

$$\frac{\langle R^2 \rangle}{R_{\max}} = \frac{Nb^2}{Nb} = b . \tag{1.4}$$

The bond length b is called the statistical segment length, or *Kuhn length*, and physically it corresponds to the distance along the chain contour over which correlations between tangent vectors of the polymer coil essentially vanish (formally, it corresponds to twice the persistence length of the chain). In the case of an unconstrained RW, of course, $b = a$.

Another good measure of the polymer coil size is the radius of gyration, R_{g}, which corresponds to the second moment of the distribution of mass around the center of mass of the coil (the name derives from the fact that the moment of inertia of a uniform body of mass m is simply mR_{g}^2):

$$R_{\mathrm{g}}^2 = \frac{1}{n} \sum_{i=0}^{n} \langle \, (\boldsymbol{R}_i - \boldsymbol{R}_{\mathrm{cm}})^2 \, \rangle = \frac{1}{2n^2} \sum_{i=0}^{n} \sum_{j=0}^{n} \langle \, (\boldsymbol{R}_i - \boldsymbol{R}_j)^2 \, \rangle , \tag{1.5}$$

where $\boldsymbol{R}_i$ is the position of the i^{th} vertex in the walk (with $\boldsymbol{R}_0$ at the origin), and $\boldsymbol{R}_{\mathrm{cm}}$ is the location of the center-of-mass of the chain. A short calculation [71] for the RW model yields

$$R_{\mathrm{g}} = \frac{N^{1/2} a}{\sqrt{6}} , \tag{1.6}$$

and we find that R_{g} also scales as $N^{1/2}$. This is another useful characteristic of a universal approach: quantities that represent the same physical reality, here the coil size, necessarily scale in the same way (in the long chain limit); differences are found only in the prefactors. Caution is warranted in the interpretation of $\tilde{R}$ or R_{g} as the size of a polymer molecule, because these radii somehow suggest the picture of a sphere. This image is incorrect for polymers. First, individual polymers in solution are typically not compact objects, e.g., the RW in Figure 1.7a is evidently not akin to

a solid sphere. Secondly, as already predicted by Werner Kuhn in 1934 [72], the instantaneous conformation of a polymer is far from spherically symmetric. On the contrary, the average shape of a random coil is that of an elongated ellipsoid [72–74]; one set of experimental measurements of DNA revealed aspect ratios of about 4:2:1 (but the elongation direction is arbitrary so upon averaging over all conformations we find, of course, spherical symmetry). Finally, the typical fluctuations in the size of polymer are very large: the standard deviation in the values of R are on the order of R itself (this is referred to as the lack of self-averaging).

Up to now we have considered all possible RWs without any concern for the fact that some walks actually cross over themselves, i.e., they visit the same site many times in the lattice picture of Figure 1.7b. We have thus established what is called an *ideal* chain model. Physically, a *real* chain cannot self-intersect because of the tight chemical bonds between sequential monomers, and a realistic model should account for the *excluded volume interactions* that arise when different parts of the molecule come in contact. Mathematically, a real polymer therefore corresponds to a self-avoiding walk (SAW), the properties of which are at the outset very difficult to calculate because there is no simple way to "flag" forbidden conformations, so to speak, and disregard them in the calculations of averages. Nevertheless, Flory developed an ingenious mean field argument to arrive at the scaling prediction $\tilde{R} \sim N^{3/5} b$ for real chains in three dimensions [71, 70]. Generically, we write the characteristic size $\tilde{R}$ of a polymer coil as

$$\tilde{R} \sim N^{\nu} b\,, \tag{1.7}$$

where ν, the *Flory exponent*, can be expressed in terms of the dimensionality d of the space in which the RW is embedded:

$$\nu = \frac{3}{d+2}\,. \tag{1.8}$$

The formula is exact for $d = 1$, $d = 2$, and $d = 4$; for $d = 3$ it turns out to be remarkably accurate (but only fortuitously so, according to de Gennes) [68]. Real chains in two and three dimensions are thus swollen compared to their ideal counterpart, which makes sense because compact conformations are more likely to lead to excluded volume interactions. Renormalization group theory has allowed physicists, in the 1970s, to calculate the precise numerical value $\nu \approx 0.588$ in three dimensions, hence Flory's approximation $\nu \approx 0.6$ is accurate within about 2% and is sufficient for most practical applications [75, 68].

We have also forgone, up to this point, discussing the interactions between the monomers and the large number of solvent molecules that surround the polymer in dilute solution. In a *good* solvent,

such interactions are not unfavourable energetically compared to monomer-monomer interactions, so the chain follows the scaling of a SAW, and $\nu \approx 3/5$. In the opposite case, in a *bad* solvent, the monomers "dislike" the solvent molecules and the chain adopts a more compact conformation to minimize contact with the solvent; in the extreme case it condenses into a globule, hence in that case $\nu = 1/3$. The interesting intermediate case called the Θ solvent occurs when the monomer-solvent interactions are "not particularly friendly but polite", such that the tendency of monomers to group together just offsets the excluded volume contribution to yield the ideal scaling $\nu = 1/2$. Since the strength of the monomer-solvent interactions is modulated by temperature, we also speak of the Θ temperature, and the mean-field theory that explores these issues in detail is called the Flory-Huggins theory. All the simulations reported in this thesis correspond to good solvent conditions. [71]

Entropic elasticity

We have already stated at the beginning of this section that the most defining aspect of macromolecules is that they are long, flexible objects. More formally, we say that they are *entropic* objects. The entropy S is simply a measure of the number of different states available to a physical system and, given the vast number of conformations of a macromolecule, the physical properties of polymers are mostly determined by entropy (as are those of an ideal gas, in which there are no interaction energies). For example, consider pulling on the ends of the polymer in Figure 1.7a to move them apart. If we stay well below the complete extension limit, we are not stretching the chemical bonds of the molecule at all; we are simply forcing the end-to-end vector $\boldsymbol{R}$ to take on a specific value. But since the number of distinct RWs in a given direction increases with decreasing end-to-end distance R (see Equation 1.9 below), and that every which walk is *a priori* equiprobable, the chain will naturally tend to adopt a conformation that reduces R (physically, solvent molecules colliding with the polymer create kinks in its conformation which tend to reduce R). We will therefore feel an *entropic restoring force* acting against our efforts to stretch the coil, and in first approximation we can regard the overall polymer coil as an *entropic spring*. Moreover, since in thermodynamics entropy is conjugate with temperature, increasing the latter will magnify the entropic effects and increase the restoring force of the polymer (collisions with surrounding solvent molecules are more violent and the formation of kinks is promoted). This is why oil pools together in a hot pan, and why a rubber band — a network of connected polymer chains — stretched under constant load contracts when it is heated. Remarkably, the latter observation, and the converse one of stretch-induced heating, were already reported for natural rubber by Gough as early as 1805 [55].

We can calculate the entropy and the strength of the entropic restoring force of a macromolecule, in the context of the ideal chain model, by calculating the total number of possible different RWs that have a specific end-to-end vector $\boldsymbol{R}$. The binomial probability distribution for the net displacement in a RW of N steps of size b quickly approaches a Gaussian distribution of zero mean and variance $2Nb^2$ when $N \gg 1$. For a RW in three dimensions, the $N/3$ steps in each of the three spatial directions are independent, so we have the following distribution for the number of walks of total displacement $\boldsymbol{R}$:

$$\Omega(\boldsymbol{R}) = \Omega_0 \exp\left(-\frac{3R^2}{2Nb^2}\right), \tag{1.9}$$

where Ω_0 is a normalization constant independent of R. The entropy associated with a given vector $\boldsymbol{R}$ is then, by definition,

$$S(\boldsymbol{R}) = k_{\mathrm{B}} \ln \Omega(\boldsymbol{R}) = k_{\mathrm{B}} \ln \Omega_0 - \frac{3k_{\mathrm{B}}R^2}{2Nb^2}. \tag{1.10}$$

Given that the moderate stretching considered here does not significantly affect the internal energy E of the molecule, we may calculate the magnitude of the entropic restoring force $F_{\mathrm{S}}(R)$ directly from the Helmholtz free energy $A \equiv E - TS$:

$$F_{\mathrm{S}}(R) = -\frac{\partial A}{\partial R} = T\frac{\partial S}{\partial R} = \frac{3k_{\mathrm{B}}T}{Nb^2}R. \tag{1.11}$$

We thus find that energy is required to deform a polymer chain, and that the entropic force associated with the deformation indeed increases with temperature. According to Equation 1.11, a polymer molecule under moderate deformation essentially behaves like a harmonic spring of force constant

$$k_{\mathrm{s}} = \frac{3k_{\mathrm{B}}T}{Nb^2} = \frac{3k_{\mathrm{B}}T}{\tilde{R}^2}, \tag{1.12}$$

and this identification forms the basis of entropic elasticity. Although we have focused on the ideal chain in the derivation above, the same general scaling holds for real chains as well, i.e.,

$$k_{\mathrm{s}} \sim \frac{3k_{\mathrm{B}}T}{\tilde{R}^2} \sim \frac{3k_{\mathrm{B}}T}{N^{2\nu}b^2}, \tag{1.13}$$

hence excluded volume interactions *soften* the entropic spring since $2\nu > 1$ for real chains. Scaling concepts can be used to derive beautiful predictions for different phenomena that involve deformations, such as the stretching, adsorption and confinement of polymers [68]. The question of chain confinement is particularly important in this thesis: the periodic translocation of DNA macromolecules through narrow constrictions in the Craighead device modeled in Chapter 2 incurs a significant decrease in entropy which is proportional to the confined portion of the polymer

chain (entropy is an extensive property). The constrictions therefore act as *entropic barriers* which hinder the motion of the molecules, and the device is referred to as an array of *entropic traps*.

Electrokinetic phenomena

The work in this thesis is aimed at modeling phenomena that involve either the motion of a charged macromolecule in solution (Chapters 2 and 3) or the motion of an electrolyte past a charged surface (Chapters 4–6). These fall under the general category of *electrokinetic* phenomena which, broadly defined, encompass all the electric and hydrodynamic effects manifested in the relative motion of bodies and ionic solutions [76]. In this section we review some fundamentals of electrokinetics and, given the implied presence of a fluid phase, we shall begin with the basic principles of hydrodynamics before considering the motion of charged objects in solution.

Hydrodynamics

Liquids are distinguished from dilute gases by the importance of collisional processes and short-range correlations, and from solids by the lack of long-range order [77]. The number of atoms or molecules in a macroscopic liquid sample is of course very large (there are approximately 10^{22} molecules in $1\,\mathrm{cm}^3$ of water), so hydrodynamics is derived using a continuum picture wherein the discrete nature of the fluid is hidden in differential fluid volumes, or fluid *elements*. These are envisioned large compared to the molecular scale but small compared to the flow scale, so that all macroscopic observables of the fluid can be regarded as continuous functions. However, simulation results in Chapter 6 show that, in fact, a continuum description is warranted in surprisingly small fluid volumes since molecular correlations typically decay within about five molecular diameters. The continuum approximation is common in physics, e.g., in the elasticity theory of solids, but in the case of fluids it is more complicated because one cannot neglect collisional processes (as in an ideal gas model, in which collisions are disregarded) nor the large-scale migration of individual molecules (as in the harmonic theory of solids, where each constituent atom oscillates around a fixed position) [77]. The governing equation for the velocity field $\boldsymbol{v}$ of a fluid can nevertheless be derived by applying Newton's Second Law to a fluid element:

$$\rho \frac{d\boldsymbol{v}}{dt} = \boldsymbol{f} + \boldsymbol{\nabla}\cdot\boldsymbol{\sigma}\,, \tag{1.14}$$

where ρ is the local density of the fluid, $\boldsymbol{f}$ comprises all the body forces per unit volume (e.g., gravitational, electric, etc.) and $\boldsymbol{\nabla}\cdot\boldsymbol{\sigma}$ is a vector of components $\partial\sigma_{ij}/\partial x_j$ (the derivatives of the

stress tensor elements σ_{ij}) that embodies the forces acting on the surface of each fluid element. The derivative on the left-hand side of Equation 1.14 is the total time derivative and accounts for the movement of fluid elements in space, i.e., we are using the Lagrangian picture.

To carry the analysis further, we have to supplement Equation 1.14 with constitutive relations that establish the basic physical properties of the fluid elements, e.g., their mechanical response upon deformation. For a fluid that is both incompressible (or, more accurately stated, one in which the density remains constant) and Newtonian (an isotropic fluid in which shear stresses are linear in the strain rate; the case of most simple liquids), Equation 1.14 reduces to

$$\rho\left(\frac{\partial}{\partial t}+\boldsymbol{v}\cdot\boldsymbol{\nabla}\right)\boldsymbol{v}=-\boldsymbol{\nabla}p+\eta\boldsymbol{\nabla}^2\boldsymbol{v}+\boldsymbol{f}\,, \tag{1.15}$$

where η is the viscosity coefficient of the fluid and p is the local pressure. The criterion for a constant-density flow can be stated quantitatively in terms of the characteristic ratio of the flow speed to the speed of sound in the fluid (the Mach number), which should remain small compared to unity [76, 78]. Equation 1.15 is known as the *Navier-Stokes* (NS) equation for an incompressible fluid, and it describes the dynamical behaviour of fluids and gases under a large variety of conditions. It was first derived by the French engineer Claude-Louis Navier in 1822 and more or less independently some years later by the Irish mathematician George Stokes. It is reported that Navier actually had no conception of shear stress and that he arrived at the proper equations by reasoning, albeit incorrectly, on the nature of inter-molecular forces [79]. It is also slightly ironic that he should be remembered not as the notorious bridge engineer that he was (he formulated the theory of suspension bridges), but for an equation describing what flows under them. The properties of the NS equation remain ill-understood to this day; the Clay Mathematics Institute even offers, within its millennium problems competition, a prize of US$1 million to whoever answers an open question regarding the existence of smooth solutions (the precise formulation of the question covers a few pages and can be obtained from the Institute) [80]. The widespread applications of the NS equation, e.g., in aerodynamics, has in recent years spawned the field of computational fluid dynamics, devoted to finding its solutions numerically, in non-trivial situations.

It often proves useful to cast equations in dimensionless form in order to isolate the parameters that really control the physics of the problem. For example, we can rewrite the free, steady state NS equation (disregarding the partial time derivative and the body force terms for the moment) in terms of the scaled velocity $\boldsymbol{v}^\star=\boldsymbol{v}/v_0$ and the scaled positions $x_i^\star=x_i/l_0$, where v_0 and l_0 are the

characteristic velocity and dimension of the flow:

$$(\boldsymbol{v}^\star \cdot \boldsymbol{\nabla}^\star)\boldsymbol{v}^\star = -\boldsymbol{\nabla}^\star p^\star + \left(\frac{\eta}{l_0 v_0 \rho}\right) \boldsymbol{\nabla}^{\star 2} \boldsymbol{v}^\star , \tag{1.16}$$

with $p^\star \equiv p/v_0^2\rho$ being a normalized pressure. In this form, we see that the flow characteristics depend only on $p^\star$ and the value of the dimensionless *Reynolds number*

$$\mathrm{Re} \equiv \frac{l_0 v_0 \rho}{\eta} , \tag{1.17}$$

hence for the same normalized pressure two hydrodynamic flows will behave in similar ways if their Reynolds numbers are the same; this similarity has major practical implications, e.g., in testing aerodynamic flow around a large-scale structure such as a plane using a small-scale maquette. The Reynolds number gives the ratio of inertial and viscous forces; above a certain critical value, inertia dominates and the flow tends to become turbulent. This critical value depends on the geometry of the system; in circular pipes, the transition from non-turbulent (laminar) flow to turbulent flow occurs at $\mathrm{Re} \approx 2000$ [81]. It is interesting in the context of this thesis to consider the Reynolds number for the case of water in a microfluidic channel, i.e., for $l_0 = 10^{-4}\,\mathrm{cm}$, $\rho = 1\,\mathrm{g/cm^3}$ and $\eta = 10^{-2}\,\mathrm{g/(cm \cdot s)}$. We find $\mathrm{Re} = v_0/(100\,\mathrm{cm/s})$, hence for practical flow speeds the Reynolds number is much less than the critical value, i.e., inertia plays a negligible role compared to viscous forces, and liquid flow always remains laminar in microchannels (actually, this poses a problem if one wants to mix fluids at this scale). The Reynolds number can be used to classify all types of flows, e.g., the movement of the Earth's crust corresponds to $\mathrm{Re} \sim 10^{-20}$, and that of a large passenger jet to $\mathrm{Re} \sim 10^9$ [82, 83]. There exists a number of other dimensionless parameters to characterize hydrodynamic phenomena: Strouhal, Froude, Peclet, Prandtl, Schmidt and Lewis numbers, but these do not come into play in the context of this thesis [78].

Charged objects in solution

Solids typically acquire a net surface charge when placed in contact with an aqueous medium, via a variety of possible mechanisms (thankfully, for otherwise dissolved particles would aggregate and precipitate out of solution; our own bodies would be subject to a fatal phase separation!). For example, when glass comes in contact with water (at neutral pH), protons dissociate from surface silanol groups and are released in solution, leaving behind a negatively charged surface (a dynamic exchange of protons with the solution is established, so in equilibrium the surface charge depends on the pH and the salt concentration). In turn, the charged surface attracts mobile ions of opposite

charge present in the solution, and the formation of a cloud of *counterions* ensues; from a distance, the object is shielded by the counterions and appears neutral, as expected. Note that in the context of this discussion we usually think of small solid particles suspended in the electrolyte (i.e., gravitational forces are negligible compared to thermal agitation). The layer of counterions is often conceptually divided into an adsorbed component, the *Stern* layer, and a diffuse component, the *Debye* layer, hence it is often called the *electric double layer*; however for our purpose this distinction is not very important. [84–88]

The distribution of ions in the diffuse layer is determined by a balance between electrostatic and thermal energies, so at the level of mean-field theory it is described self-consistently by a combination of the Poisson and Boltzmann equations. With k referring to each one of n ionic species present in the solution, the Poisson-Boltzmann (PB) equation is:

$$\nabla^2\phi = -\frac{e}{\epsilon}\sum_{k=1}^{n} c_k z_k \mathrm{e}^{-ez_k\phi/k_\mathrm{B}T}\,, \tag{1.18}$$

where ϕ is the electric potential, ez_k and c_k are the charge and bulk concentration of ion species k, respectively, ϵ is the electric permittivity of the fluid, k_B is the Boltzmann constant and T is the absolute temperature. Note that in the article presented in Chapter 4, we apply the PB equation to a closed nanoscopic capillary in which there is no bulk fluid phase; then the c_k cannot be taken as the ionic concentration of the electrolyte, which significantly complicates the problem. If the absolute value of $ez_k\phi/k_\mathrm{B}T$ remains well below unity throughout the region of interest, we can invoke the *Debye-Hückel approximation*, which amounts to linearizing Equation 1.18:

$$\nabla^2\phi \approx \left(\sum_{k=1}^{n}\frac{c_k z_k^2 e^2}{\epsilon k_\mathrm{B}T}\right)\phi \equiv \kappa^2\phi\,. \tag{1.19}$$

The precise solution of Equation 1.19 depends on the geometry of the problem, of course, but in any case the form of the equation implies an exponential decrease of the potential away from the surface, with a characteristic decay length given by κ. The inverse of this important quantity, $\lambda_\mathrm{D} \equiv \kappa^{-1}$, is called the Debye length and gives a measure of the extent of the diffuse layer in the solution. In the following subsections, we consider the motion imparted by an external electric field to either an electrolyte or to a particle suspended in solution. These electrokinetic processes go by the names of *electroosmosis* and *electrophoresis*, respectively, but they are the manifestation of essentially the same phenomenon, viewed from a reference frame attached to the solid surface or to the quiescent fluid far away from the surface. Of course, only the relative motion of the surface and the electrolyte is really significant in the end.

Electroosmosis

Let us consider an external field of magnitude E applied to the system depicted in Figure 1.8a, parallel to the surface, and toward the right. Since there is a net charge in the diffuse layer, the fluid there will be set in motion and, by viscous coupling, will eventually drag the bulk of the solution into a uniform flow. Assuming there are no pressure gradients, we can solve the NS equation for the x-component of the fluid velocity field. We take $\partial \boldsymbol{v}/\partial t = 0$ because we are considering a steady-state regime, and $\boldsymbol{v} \cdot \boldsymbol{\nabla} \boldsymbol{v} = 0$ because the velocity field is oriented along the x-axis and is independent of x (by symmetry), to obtain:

$$\nabla^2 v = -\frac{E\rho_e}{\eta} = \frac{\epsilon E \nabla^2 \phi}{\eta}\,, \tag{1.20}$$

where ρ_e is the net charge density, and ϕ is the electric double-layer potential from the PB equation. By integrating twice, we determine that the magnitude of the fluid velocity far away from the surface is given by the so-called *Helmholtz-Smoluchowski* value

$$v_0 = -\frac{\epsilon E \zeta}{\eta}\,. \tag{1.21}$$

We have introduced here the zeta-potential, ζ, which is just the value of ϕ at the position of the shear plane, i.e., where the velocity of the fluid vanishes at the interface (it can differ from the surface potential on account of the Stern layer). Within electroosmotic flow (EOF), shear is located almost entirely inside the Debye layer and the velocity profile away from the surface does not depend on position, as indicated in Figure 1.8a; this is usually referred to as a *plug flow*. Historically, the discovery of electroosmosis is credited to Ferdinand F. Reuss who showed in 1809 that under the influence of an electric field, water migrates through porous clay membranes. This is an instance of EOF, although that was not recognized at the time [85, 78].

Electrophoresis

We now turn to the situation depicted in Figure 1.8b, where an external electric field is applied to the suspended particle. Because the field imparts motion to both the charged sphere and the mobile ions in the Debye layer, and since the two are hydrodynamically coupled, this problem is in general rather complicated. However, we can gain some insight by investigating two simple limits. When the size of the object is much smaller than the Debye length ($\lambda_{\mathrm{D}} \gg R$), we can consider the system as a charged sphere drifting through a neutral fluid under the action of a total force QE (where Q is the total charge of the sphere). Recalling that the Stokes friction on a sphere of radius R in a fluid

of viscosity η is given by $6\pi\eta R$, the electrophoretic velocity of the sphere in this limit is simply

$$v = -\frac{QE}{6\pi\eta R}. \tag{1.22}$$

In the opposite limit (when $\lambda_D \ll R$), we may consider the spherical surface as locally flat and, choosing a reference frame attached to the sphere, we simply change the sign in expression 1.21 for EOF and we write, directly,

$$v = \frac{\epsilon E\zeta}{\eta}. \tag{1.23}$$

The similarity between electroosmosis and electrophoresis in this limit was in fact used by Smoluchowski in 1903 to derive Equation 1.23, which allows for experimental measurements of ζ by direct observation. Notably, the balance between driving and friction forces in the small λ_D limit occurs *locally* at every point on the surface, so the electrophoretic velocity in this case is *independent of the body's shape and size*. Taking a small leap, we understand that this explains the experimental observation that DNA strands in free-solution migrate electrophoretically with the same velocity,

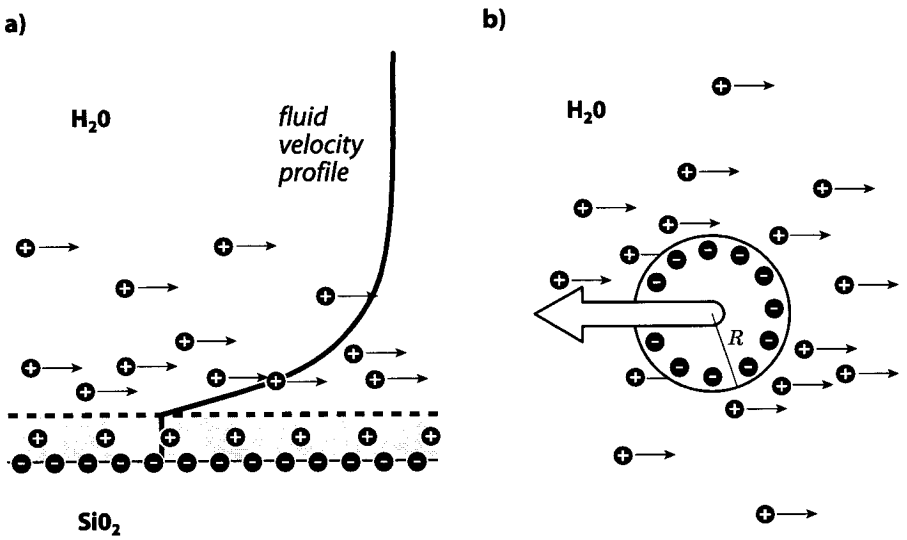

FIGURE 1.8 **a)** Electroosmotic flow occurs when counterions in the diffuse layer near a charged surface (above the fixed Stern layer) are set in motion by an electric field. In steady-state, the bulk of the solution assumes a flat velocity profile (plug flow). **b)** Electrophoresis refers to the migration of colloidal particles under the influence of an electric field. When $\lambda_D \gg R$ (imagine there are no positive ions in the diagram), the velocity of the particle is simply given by the ratio of the electric force (large white arrow) and the hydrodynamic friction. When $\lambda_D \ll R$ (imagine that the positive ions are all very close to the particle), the situation can be mapped onto that of panel (a), on the left. Note that the electric field lines curve around a dielectric, so the force arrows on the positive ions in this picture should really follow the spherical shape.

irrespective of their length (except for very small DNA molecules, typically shorter than 400 base pairs; see Figures 7 and 8 in Reference 89). Of course, a DNA molecule is not a solid object, but the preceding analysis applies because under typical conditions the Debye length is much smaller than the DNA random-coil size. Counterions in solution flow through the DNA coil during electrophoresis, and again the balance between the driving and friction forces occurs locally along the chain, independently of its conformation. [88]

This *free-draining* property of DNA is most unfortunate because sorting of DNA strands according to their length happens to lie at the heart of genetic sequencing. A very interesting, if not downright candid review of the historical development of electrophoresis sequencing technology over the last 65 years has been published recently by Righetti [90]. Briefly, the approach is as follows. We place multiple copies of a given ssDNA molecule in a solution containing the bases A, T, C and G, as well as polymerase enzymes that can *reconstruct* complete dsDNA molecules using the individual bases. But we also add to the mix a small portion of A*, which is an A base modified chemically to be radioactive or fluorescent and to inhibit further polymerization. The enzymes thus repolymerize dsDNA molecules up to the point where, by chance, an A* is inserted instead of an A. We then chemically cut the dangling ssDNA portions and in the end we obtain a solution of dsDNA molecules of various lengths corresponding to all the positions of the A base in the original molecule. Upon separating these A*-terminated dsDNA strands by length, it is possible to determine these positions (alternatively, we could measure the length of the ssDNA segments). The same can be done with modified bases T*, C* and G*; if each one is labelled with a distinct feature, e.g., fluorophores of different colours, the reading of all four bases can be carried out simultaneously in a single experiment. The automatization of this process allowed the Human Genome Project to be completed years ahead of schedule [31–33]. But, as stated above, the electrophoretic velocity of DNA is independent of molecular size, hence conventional length separation techniques rely on gels as a retarding medium during electrophoresis: larger molecules have more difficulty migrating through the constricted space between gel fibres, so they elute more slowly and separation is achieved. However, gels are impractical in microscale capillaries, so other separation methods are envisaged for microfluidic electrophoresis devices. The simulations in Chapters 2 and 3 model a gel-free entropic trap microchannel designed for the length separation of very long dsDNA molecules (although not at the single base pair resolution). Incidentally, the free-draining property of DNA allows us to use an efficient computational model for our simulations: we can disregard the fluid completely and use a simple biased RW to recover the free-draining character of the macromolecule.

Ratchets

Everybody knows what a *ratchet* is (from the ancient French *rochet*), if only the wrench variety, depicted in Figure 1.9a; the mechanism inside the wrench converts the bi-directional motion of the handle into the unidirectional rotation of the bolt. Generally, a ratchet is *a device which rectifies fluctuations into net directional motion*. Mechanically, it is a straightforward system (pun intended), but we cannot readily transpose our intuition regarding its operation to a scale where thermal fluctuations become significant. For example, one may infer that a miniature ratchet, wherein the hand in Figure 1.9a is replaced by random thermal movement, can extract work spontaneously from heat energy, in obvious contradiction with the Second Law of thermodynamics. Coincidentally, I shall again quote Feynman here. In his 1953 Lectures on Physics [91], he revives the ratchet and pawl system, shown in Figure 1.9b (and already envisioned by Smoluchowski in 1912 [92]), for his insightful discussion of the Second Law:

> "In this chapter we discuss the ratchet and pawl, a very simple device which allows a shaft to turn only one way. The possibility of having something turn only one way requires some detailed and careful analysis, and there are some very interesting consequences. (...)
>
> Let us try to invent a device that will violate the Second Law of Thermodynamics, that is, a gadget that will generate work from a heat reservoir with everything at the same temperature. Let us say we have a box of gas at a certain temperature, and inside there is an axle with vanes in it. (See [Figure 1.9b] but take $T_1 = T_2 = T$, say). Because of the bombardments of gas molecules on the vane, the vane oscillates and jiggles. All we have to do is to hook onto the other end of the axle a wheel which can turn only one way — the ratchet and pawl. Then when the shaft tries to jiggle one way, it will not turn, and when it jiggles the other, it will turn. Then the wheel will slowly turn, and perhaps we might even tie a flea onto a string hanging from a drum on the shaft, and lift the flea! Now let us ask if this is possible. According to Carnot's hypothesis, it is impossible. But if we just look at it, we see, *prima facie*, that it seems quite possible. So we must look more closely."

Feynman goes on to explain why, despite the obvious asymmetry, no useful work can be extracted from such a contraption: when everything is held at the same temperature, the probability of the pawl being lifted by a random thermal fluctuation and letting the ratchet skip backward is equal to that of the ratchet moving forward, and no net motion is produced. In an electric analogue, Brillouin showed that a diode cannot rectify the random current fluctuations in a closed circuit to produce a finite voltage, for the same reason [93]. Amazingly, chemists have recently built a molecular-size equivalent of the ratchet and pawl device, and they indeed find that it exhibits no net

rotation [94–96]. A functional ratchet and pawl would in fact constitute a mechanical equivalent of a *Maxwell demon*, a hypothetical being of molecular dimension capable of sorting fast and slow molecules to generate a thermal gradient from initial isothermal conditions [97].

However, advances in molecular biology have revealed two disturbing facts in this respect: first, the energies involved in the operation of the cell's machinery are comparable to thermal energies and, secondly, a significant number of key cellular mechanisms rely on motor proteins that travel in a directed fashion along rigid filaments (kinesins and dyeins on tubulin, and myosins on actin) [98]. The emergence of refined experimental techniques over the last 20 years has allowed for the observation of isolated protein–filament complexes and has forced physicists to reconsider ratchet motion as the acting principle behind biomolecular motors. But given the arguments presented

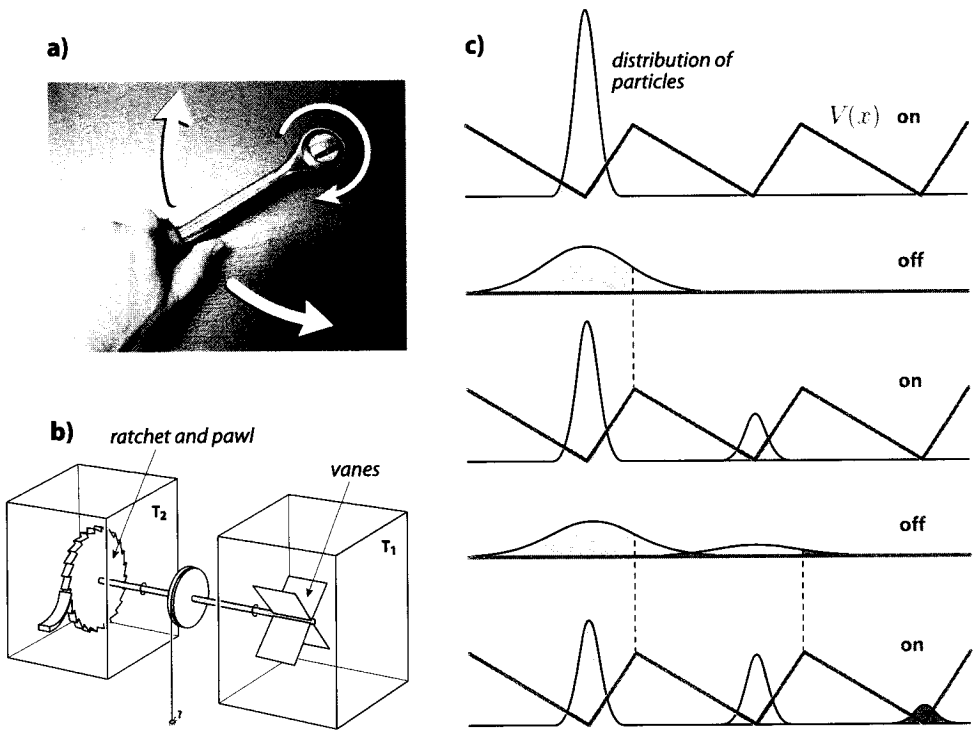

FIGURE 1.9 **a)** The mechanism inside a ratchet wrench rectifies the bi-directional rotation of the handle into a net rotation of the bolt. **b)** The ratchet and pawl system used by Feynman to discuss the meaning of the Second Law of thermodynamics, as discussed in the text. Reproduced from Reference 91. **c)** The flashing ratchet in action. When the asymmetric potential $V(x)$ is turned on, the suspended particles concentrate in the potential wells. When the field is turned off, the particles diffuse symmetrically and a portion of them diffuse enough to fall into the next well on the right when $V(x)$ is turned back on: there is a net transport of particles.

above, how can unidirectional motion arise in the *vibrant community* of molecules inside a cell? How can fluctuations be rectified to generate useful work? In the slightly Freudian formulation of Magnasco and Slotovitzky: "We are, in some sense, made of demons"! [97].

In a seminal 1993 paper (there have been about 1300 articles on ratchets published since, and almost 500 citations of this one paper, according to the ISI citation index [99]), Magnasco established that, in fact, rectification of thermal fluctuations *is* possible if: 1) there is an asymmetry in the system and 2) there are long time correlations in the fluctuations, i.e., there is non-white noise. These two conditions are satisfied in biomolecular motors: the filaments are asymmetric by construction, and the exclusive binding of a single ATP molecule in the stepping of the motor provides long time correlations [100]. Devices that rectify motion based on this principle are termed *thermal* or *Brownian* ratchets. Another type of ratchet, the *fluctuating* or *flashing* ratchet, proposed in 1992 by Ajdari and Prost and implemented experimentally two years later by Rousselet *et al.* [101], lends itself to a convincing visual representation of the ratchet effect, as depicted in Figure 1.9c. A sawtooth potential $V(x)$ is periodically applied to particles suspended in solution. During the "field off" period, the particles diffuse symmetrically, but during the following "field on" period, particles migrate on average to the right, because of the local asymmetry in $V(x)$. Moreover, since the diffusion coefficient decreases with particle size, smaller particles will migrate faster in such a ratchet, and the device can be used to separate species according to molecular size, as most clearly demonstrated by Bader *et al.* [102–104]. Ratchet mechanisms are certain to inspire the design of synthetic nanoscale motors that remain highly efficient even when surrounded by thermal agitation.

I will not dwell much further on the general concepts surrounding ratchets. At any rate, it proves difficult to say anything original on the subject following Riemann's colossal 209 page review [92] covering in great detail the history, the basic principles and the numerous versions of ratchet systems in diverse fields of physics; the 784 references contained therein should fill the appetite of the most curious reader! But of course, I cannot fail to mention the important concept of *entropic ratchets* contributed in 1997 by Slater, Guo and Nixon [53], as it ties in directly with the simulations reported in Chapter 3. Slater *et al.* showed that steric interactions with the walls in an asymmetric channel can themselves be considered as an asymmetric potential and drive ratchet motion. More importantly, they realized that the height and the degree of asymmetry of steric potential barriers are directly modulated by the internal entropy of polymers. While steric constraints are inefficient at rectifying the motion of small spherical hard objects, they are quite efficient at rectifying the motion of macromolecules. Since internal entropy is proportional to polymer length, this discovery has

direct applications in separation science. The goal of the work presented in Chapter 3 was to apply ratcheting idea to an *existing* microfluidic DNA separation device (itself inspired by the work of Slater *et al.*). We verified that both temporal asymmetries in the driving field and spatial asymmetries in the channel structure can lead to rectified electrophoretic migration. Following the idea of Slater *et al.*, we also showed how an additional bias yields bi-directional motion according to molecular size.

Monte Carlo simulations

Monte Carlo simulation methods were used long before the advent of the electronic computer; the name simply refers to the use of random numbers in generating synthetic data sets that can be used to obtain a statistical approximation of an exact calculation. In that sense, Lazzerini's 1901 calculation of π based on throws of a needle according to Buffon's theorem, Lord Kelvin's study of collision processes based on thousands of random trajectories generated by his assistant [48], or Fermi's use of statistical sampling techniques to arrive at his "to good to be true" predictions of experimental results in the 1930s [105], are all worthy of the *Monte Carlo* designation .

A simple example illustrates the concept of statistical sampling [48]. Consider throwing a dart randomly at a square dartboard on which a circle is drawn, and say that we record the total number of throws (*trials*) as well as the number of times the dart falls inside the circle (*hits*). After a large number of throws, we can estimate the area of the disk enclosed by the circle by multiplying the area of the board and the ratio of the number of hits to the number of trials. By increasing the number of throws, we can in principle increase the accuracy of the estimate indefinitely. To spare some time, and one's arm, we can implement this hit-and-miss technique in the form of a computer program which quickly generates a large number of random coordinates (x, y) for the location of the dart. This is in fact the *Hello World* program of Monte Carlo simulation, but it already highlights the importance of choosing a robust random-number generator: correlations in successive trial coordinates will affect the precision and limit the accuracy of the estimate. Computer-generated random numbers are usually drawn from a pseudo-random, deterministic sequence based on modulo integer arithmetic, and great care must be exercised to minimize correlations in the sequence, a subject treated at length in the literature [106, 107]. Today, the best compromise between randomness and computational speed is probably afforded by the Mersenne Twister algorithm which has a long repeat period of $2^{19937}-1$ and is equidistributed in 623 dimensions [108].

Of course, the shape drawn on the board in the foregoing simple example need not be a circle. Conceptually, we can extend the method to measure the space enclosed by any shape, i.e., calculate integrals, in an arbitrary number of dimensions (provided we have a criterion to discriminate between hits and misses). This immediately suggests that Monte Carlo methods can be useful in statistical physics, where the macroscopic physical properties of a system can be calculated from averages over an ensemble of microstates. Mathematically, if ω represents a state in the vast phase space Ω of all possible microstates of a given system and ψ is some physical property of the system, then the equilibrium measured value of ψ corresponds to the average

$$\langle \psi \rangle = \int_{\Omega} \psi(\omega)\, \rho(\omega)\, d\omega\,, \tag{1.24}$$

where $\rho(\omega)$ is the probability density for the appropriate thermodynamic ensemble. For definiteness, let us consider the canonical ensemble (for a system in contact with a heat reservoir at temperature T), for which $\rho(\omega) = \exp\left(-U(\omega)/k_{\mathrm{B}}T\right)$, with $U(\omega)$ the total energy of the microstate ω. By statistical sampling, we can approximate the value of $\langle \psi \rangle$ from a large set of n randomly generated states $\{\omega_i\}$:

$$\langle \psi \rangle \approx \frac{1}{n} \sum_{i=1}^{n} \psi(\omega_i)\, \mathrm{e}^{-U(\omega_i)/k_{\mathrm{B}}T}\,. \tag{1.25}$$

However, Equation 1.25 is still impractical to address physical problems because the exponential factor is typically negligible except in a very small region of the phase space Ω (in the dart throwing analogy, the circle drawn on the board is very small). The chances of randomly picking a state ω_i that even contributes to the sum are very slim. Ideally, we would instead generate a set of states $\{\omega_i^\star\}$ which are *already distributed according to* $\exp\left(-U(\omega_i^\star)/k_{\mathrm{B}}T\right)$; the value of $\langle \psi \rangle$ is then easily computed:

$$\langle \psi \rangle \approx \frac{1}{n} \sum_{i=1}^{n} \psi(\omega_i^\star)\,. \tag{1.26}$$

This is referred to as *importance sampling* and it is much more efficient than a uniform sampling approach (it corresponds to throwing darts only near the small circle on the dartboard). But there is *a priori* nothing trivial about generating a properly distributed set of states $\{\omega_i^\star\}$.

Metropolis algorithm

In 1953, Nicholas Metropolis and co-workers at the Los Alamos National Laboratory in the United States published an elegant method to generate a Markovian sequence of states $\{\omega_i^\star\}$ precisely distributed according to a canonical distribution [109]. Starting from a given state ω_0, their algorithm prescribes the following steps to generate the next state in the sequence:

1) generate a *trial* state ω_1 and compute $\Delta U = U(\omega_1) - U(\omega_0)$;

2) if $\Delta U \leq 0$, accept ω_1 as the new state;

3) if $\Delta U > 0$, accept ω_1 with a probability $\mathrm{e}^{-\Delta U/k_\mathrm{B}T}$;

4) if ω_1 is not accepted, record ω_0 as a *new* state.

This algorithm ensures detailed balance between the different states, which is a sufficient (but not necessary) condition to achieve a canonical distribution [110]. The *Metropolis algorithm* above is the culmination of the ideas of mathematicians John von Neumann and Stanislaw Ulam at Los Alamos in the 1940s on reviving statistical sampling techniques using the ENIAC and the MANIAC, the world's first electronic supercomputers. To show that the prefix "super" here is quite relative, Rosenbluth and Rosenbluth reported in a 1954 article [111] that a Metropolis Monte Carlo simulation in which 256 rigid spheres were each moved 100 times demanded 150 hours of computing time, whereas on a modern personal workstation a similar calculation requires only 0.01 second! Incidentally, Metropolis is also the one who coined the term *Monte Carlo* to designate statistical sampling methods, by his own account "a suggestion not unrelated to the fact that Stan [Ulam] had an uncle who would borrow money because he 'just had to go to Monte Carlo'" [105]. The Metropolis algorithm is quite generic and has found applications well outside of physics. It is now considered one of the 10 most influential algorithms in science and engineering (alongside the FORTRAN compiler and the Fast Fourier Transform) [112, 113], and the American Physical Society every year awards the Nicholas Metropolis prize to honour outstanding doctoral research in computational physics [114].

Bond fluctuation method

The Monte Carlo approach is well-suited to the modeling of polymers which, as discussed above, are complicated topological objects. For example, it is difficult to account for volume exclusion analytically, but in a Monte Carlo scheme one can simply change the conformation of the polymer slowly, monomer by monomer, and simply reject monomer moves that violate volume exclusion constraints. The most efficient algorithms use a lattice representation of the polymer (Figure 1.7b, on page 17) since the program can in this case be implemented almost entirely with integer operations. In a lattice Monte Carlo simulation a *monomer* is usually thought to represent approximately one Kuhn length of the actual polymer, and a trial move corresponds to moving a monomer in a random direction on the lattice.

In Chapter 2, we use the *Bond Fluctuation* (BF) method to model the behaviour of DNA molecules inside a microfluidic entropic trap array. This is a lattice-based method that, as the name implies,

allows the length of the bonds between successive monomers in the chain to fluctuate, slightly. It was introduced in 1988 by Carmesin and Kremer to address some flaws in simpler, fixed bond length schemes, namely non-ergodicity and the impossibility to handle branched topologies [115]. The essential principle in the BF method in two dimensions is to associate with each monomer four lattice sites that define a unit square on the lattice. The two simple, monomer-level rules that each site can belong to one and only one monomer at a time, and that the bond length remains shorter than four lattice units, automatically ensure that volume exclusion constraints are satisfied (see Chapter 2 for more details). Fluctuations in the bond length are not unrealistic, physically, because the coarse-grained Kuhn length typically represents a long sequence of chemical bonds which may adopt many different conformations [115]. The model can be extended to three dimensions by associating with each monomer the eight lattice sites forming a unit cube. The set of allowed bond lengths in this case is more difficult to determine than in the two-dimensional case because the topology is more rich, but it was derived by Deutsch and Binder in 1990 [116]. The contribution of an external field or other potential is easily included in a BF model by means of a Metropolis test on each monomer move, given that the energy associated with each site is known. This is the technique we used in our simulations of the Craighead microfluidic DNA separation device in Chapter 2, by solving for the electric potential at every site on the BF lattice, taking into account the curvature of the field lines. Figure 1.4a, on page 11, shows a 600 monomer macromolecule during a BF simulation.

Molecular Dynamics simulations

The basic precept of Molecular Dynamics (MD) is rather simple and consists in integrating the equations of motion of classical mechanics numerically using small but finite time increments δt. Given a set of n "particles" (coarse-grained molecules or even individual, realistic atoms) with masses $\{m_i\}$, coordinates $\{\boldsymbol{r}_i\}$ and momenta $\{\boldsymbol{p}_i\}$, these equations can be written as:

$$\frac{\partial \boldsymbol{r}_i}{\partial t} = \frac{\boldsymbol{p}_i}{m_i}, \tag{1.27}$$

$$\frac{\partial \boldsymbol{p}_i}{\partial t} = \boldsymbol{F}_i + \boldsymbol{F}_{i,\text{ext}} = -\boldsymbol{\nabla}_i U(\boldsymbol{r}_i) + \boldsymbol{F}_{i,\text{ext}}, \tag{1.28}$$

where $\boldsymbol{F}_i$ and $\boldsymbol{F}_{i,\text{ext}}$ are the internal and external forces exerted on particle i, respectively, and $U(\boldsymbol{r}_i)$ is the total potential energy of the system (assuming that it only depends on the positions of the particles). The notation employed here is deceptively compact: Equation 1.27 and Equation 1.28 represent $6n$ coupled first-order differential equations, and solving them analytically to obtain the

functions $\boldsymbol{r}_i(t)$ and $\boldsymbol{p}_i(t)$ is a formidable task, even for very modest values of n. Numerically, however, the integration can easily be carried out for an arbitrarily large number of individual particles, in practice limited only by the available computer memory and computational time. A significant advantage of MD is that the successive sets of value $\{\boldsymbol{r}_i, \boldsymbol{p}_i\}$ generated during the integration describe the physical motion of the particles, realistically. We can thus use MD *simulations* to extract detailed information about the dynamics of the system on a timescale almost as short as δt, as well as thermodynamic properties by averaging over a large number of independent system states, or *samples*, collected over a large enough time interval (assuming that the system is ergodic, i.e., that each point in phase space is *a priori* equiprobable).

The first MD simulations were implemented almost as soon as computers became available in the 1950s. The pioneering work of Alder and Wainwright [117, 118] on condensed systems of hard disks and spheres, and that of Rahman [119], Verlet and others [120–123] using continuous interaction potentials quickly ushered physicists into an era of "computer experiments". The usefulness of the approach initially rested on the fact that the basic bulk properties of simple condensed-matter systems can be obtained from a relatively small number of individual constituents (a few hundred) through the use of periodic boundary conditions. But modern computational resources allow for the modeling of systems involving billions of particles, i.e., approaching practical dimensions, *a fortiori* since what is considered practical continues to shrink in size below the micrometer scale (e.g., a cube of silicon $0.1\,\mu\mathrm{m}$ in size contains *just* 50 billion atoms). Simulations of material fracture by Abraham and co-workers are particularly convincing in this regard [124, 125].

Velocity Verlet algorithm

There are many ways in which to carry out the numerical integration of the equations of motion 1.27 and 1.28, and there exists vast literature on the technicalities involved, the pitfalls to avoid, etc. [48–51]. Here we will simply state the *Velocity Verlet* (VV) integration algorithm that we use in our MD simulations (Chapters 5 and 6). In terms of positions $\{\boldsymbol{r}_i\}$, velocities $\{\boldsymbol{v}_i\}$ and accelerations $\{\boldsymbol{a}_i\}$, the VV algorithm prescribes the following pseudo-code operations to advance the state of the system over a short time interval δt:

$$\boldsymbol{r}_i \leftarrow \boldsymbol{r}_i + \boldsymbol{v}_i\,\delta t + \boldsymbol{a}_i\,\delta t^2/2\,, \tag{1.29}$$

$$\boldsymbol{v}_i \leftarrow \boldsymbol{v}_i + \boldsymbol{a}_i\,\delta t/2\,, \tag{1.30}$$

$$\boldsymbol{a}_i \leftarrow -\boldsymbol{\nabla}_i U(\boldsymbol{r}_i)/m_i + \boldsymbol{F}_{i,\mathrm{ext}}/m_i\,, \tag{1.31}$$

$$\boldsymbol{v}_i \leftarrow \boldsymbol{v}_i + \boldsymbol{a}_i\,\delta t/2\,. \tag{1.32}$$

The updating of accelerations in the third step above is, by far, the most time consuming operation because it involves calculating the interactions between all particles. We usually assume that a sum of pair interaction energies $U_{ij} = U(\boldsymbol{r}_i, \boldsymbol{r}_j)$ is a sufficiently good approximation of the total potential energy, but this still implies $\mathcal{O}(n^2)$ calculations; and even though interaction cut-offs and neighbour lists strategies can reduce this to $\mathcal{O}(n)$ calculations, every interaction calculation involves many operations. In their authoritative 1987 textbook, Allen and Tildesley praise the VV algorithm: "its numerical stability, convenience and simplicity make it perhaps the most attractive method to date", and in a recent presentation, Allen bluntly announced that another popular method, the Gear predictor-corrector algorithm, is now officially "dead" when it comes to the simulation of large systems [48, 126]. Note that the half time step decomposition in Equations 1.29–1.32 is not necessarily optimal; using the elegant Liouville operator formalism, Omelyan *et al.* showed in 2002 that a third-order VV algorithm is in fact more accurate *and* faster [127].

Temperature measurement

Measuring the overall temperature of a system in an equilibrium MD simulation is straightforward because we can invoke the equipartition theorem, which states that every independent quadratic degree of freedom in the generalized Hamiltonian contributes $k_\mathrm{B}T/2$ to the total energy of the system [128, 129]. Since typically the momenta only enter the Hamiltonian through the kinetic energy, we can deduce the temperature directly from the particle velocities:

$$k_\mathrm{B}T = \frac{1}{3n}\left\langle \sum_{i=1}^{n} m_i v_i^2 \right\rangle, \tag{1.33}$$

where the angled brackets indicate a thermodynamic average (over a large number of samples in the simulation). Strictly speaking, we should discount three degrees of freedom here because the total momentum is conserved in MD, but this correction scales as n^{-1} and is negligible compared to thermal fluctuations of order $n^{-1/2}$, when n is large. Equation 1.33 can also serve to estimate the local temperature at a given point in space by restricting the sum to particles inside a small volume around that point.

However, measuring the temperature is not so simple in a Non-Equilibrium Molecular Dynamics (NEMD) simulation, when an external force imparts motion to the particles, e.g., the EOF induced by the external electric field in Chapters 5 and 6. In this case, the momenta of the particles are not independent and we cannot use them directly in the equipartition theorem. In applying Equation 1.33 we must instead consider the so-called *peculiar* velocities of the particles, i.e., with the net

drift contribution removed[130]. *Obviously*, the uniform center-of-mass motion of a body does not affect its temperature! Well, actually this last statement is not as obvious as it seems. The question has non-trivial implications in the relativistic interpretation of thermodynamics. Planck and Einstein pondered on the issue as early as 1907 and concluded that a body would appear *colder* to observers travelling at relativistic speeds. But in 1963, a physicist by the coincidental name of Ott concluded that the body would on the contrary appear *hotter*, and thus ignited a controversy [131–136] which is not settled to this day [137, 138]. The convincing argument that a system at the triple-point of its phase diagram (e.g., a mixture of ice, water and water vapour) should appear as such to all inertial observers seems to imply quite directly that temperature is a Lorentz invariant, but a definitive formal proof remains elusive. Landsberg and Matsas even claimed recently that it is impossible to establish a manifestly covariant formulation of thermodynamics [139, 140]. Of course, these considerations are purely academic because in the context of our simulations relativity is completely irrelevant; but it is interesting to explore the wider implications of a seemingly obvious statement.

The calculation of peculiar velocities is simple enough if all the particles in the system experience the same drift: we simply subtract the drift velocity from all the velocities (this case is not very interesting, since we normally perform simulations in the center-of-mass frame of reference anyway). We can extend this idea to systems in which there are gradients in the net velocity by discounting the drift component of the particles separately in appropriate regions, e.g., thin cylindrical shells for a Poiseuille flow in a tube. However this is not very satisfying conceptually, it is geometry-dependent, and it is not appropriate for flows involving ions or large macromolecules [141]; there are at least two better ways to measure the temperature of a NEMD system. The first is to define a local temperature by introducing a co-moving frame of reference for each particle and considering the *relative* velocity of neighbouring particles (particles that lie within a given short range):

$$k_{\mathrm{B}}T(\boldsymbol{r}_i) = \frac{\sum_{j=1}^{n} w(r_{ij})\, m_{ij}(\boldsymbol{v}_i - \boldsymbol{v}_j)^2}{3\sum_{j=1}^{n} w(r_{ij})}, \tag{1.34}$$

where $T(\boldsymbol{r}_i)$ is the local temperature associated with the i-th particle, r_{ij} is the distance between particles i and j, $w(r_{ij})$ is a short-ranged cut-off function, and $m_{ij} \equiv m_i m_j/(m_i + m_j)$ is the reduced mass of particles i and j [142]. The value of $T(\boldsymbol{r}_i)$ can then be handled as any other discretely sampled physical property of the system.

An even better way to solve the issue in NEMD simulations is to use an expression for the temperature that simply *does not involve the velocities of the particles at all.* That this is possible should come as no surprise (when the contributions of positions and momenta to the system's Hamiltonian

are separable). After all, the positional equivalent of the equipartition theorem, the virial theorem $-\langle r_i F_i \rangle = k_B T$, is such an expression. But unfortunately the virial expression is not compatible with periodic boundary conditions and it is therefore generally useless in MD simulations. The idea, instead, is to start from the fundamental thermodynamic definition of temperature,

$$\frac{1}{T} = \left.\frac{\partial S}{\partial E}\right|_V \tag{1.35}$$

(where S, E and V are the entropy, internal energy and volume of the system, respectively), and proceed to derive a practical expression for $\partial S/\partial E$ in a microcanonical context—quite a task! Rugh initially published such a formal derivation [143], but we should credit Butler, Ayton, Jepps and Evans [144, 145] for making it accessible to computational physicists. I will not relay here the detailed proofs which can be found in the original papers, but simply quote the central result of interest from a simulation perspective:

$$\frac{1}{k_B T} = \frac{\left\langle -\sum_{i=1}^{n} \boldsymbol{\nabla}_i \cdot \boldsymbol{F}_i \right\rangle}{\left\langle \sum_{i=1}^{n} F_i^2 \right\rangle} . \tag{1.36}$$

Importantly, Jepps *et al.* have shown that this *configurational temperature* expression is valid for periodic, canonical, and MD ensembles [145]. It is also interesting to note that the expression can be used to verify the temperature in canonical Monte Carlo simulations, in which there is no kinetic information at all [144]. Finally, the summations in Equation 1.36 can be restricted to particles in a small region of space to yield a local value of the temperature [141]. In our EOF simulations we used Equation 1.36 to validate values calculated with Equation 1.34, but in the production of final data we only used the latter because it is more efficient (it does not involve the calculation of forces).

Temperature control

MD simulations are usually performed under constant temperature conditions. Not only is this a useful physical context, but temperature control alleviates concerns about the slight errors in the discrete integration algorithm and the finite precision of computer arithmetic, thereby allowing for longer time steps. Moreover, in a NEMD context, it is crucial to remove the energy continuously pumped into or out of the system by external forces. Temperature control in MD is always effected *artificially* by a thermostatting method that mimics the coupling of the system with a heat reservoir; unless we include the whole reservoir in the simulation! Difficulties in controlling temperature are similar to those encountered in measuring it, but they are compounded by the fact that we must also modify the dynamics of the particles to keep the temperature in line with a target value.

Many different *thermostats* have been suggested over the years: the simplest method probably consists in periodically rescaling the particle velocities to satisfy the equipartition relation [146, 147]; in a similar vein, the Andersen thermostat involves the periodic random resampling of particle velocities from a Maxwell distribution at the target temperature [148]; the Gaussian thermostat imposes an isothermal constraint directly on the equations of motion [149, 150]; the Nosé-Hoover thermostat introduces in the Hamiltonian one extra degree of freedom that serves as a global feedback of the temperature on the particle velocities [151–154]; the popular Berendsen thermostat introduces a global coupling between all the particles and a heat reservoir, via a temperature-dependent velocity rescaling factor [155]; finally, the Langevin thermostat couples the motion of every particle to the heat reservoir through friction and stochastic forces (as in the Langevin equation) [156, 157]; and there are probably a variety of lesser known schemes. However, the aforementioned thermostatting techniques are not readily amenable to NEMD simulations because they do not account for the possibility that the particles may have a net drift velocity. Some schemes can be recuperated by operating on peculiar velocities, but the approach then suffers from the same drawbacks mentioned above for temperature measurement. It is also possible to restrict the application of a traditional thermostat to particles in a stationary phase of the system (e.g., the solid walls in a confined flow simulation, as in Chapter 5), but this limits the magnitude of the external force and may allow important temperature gradients to develop in the system.

A particularly elegant NEMD thermostatting solution has emerged from the development of Dissipative Particle Dynamics (DPD), a simulation technique based on "soft" particles to model fluids on mesoscopic length and time scales [158, 159]. It was recently realized that the DPD thermostatting method is in fact completely independent of the form of the inter-particle potential and is thus perfectly legitimate in standard MD as well [157]. In a spirit similar to the calculation of the local temperature in Equation 1.34, the DPD thermostat couples the *relative* velocities of pairs of neighbouring particles to a heat reservoir, via a Langevin approach. Since the algorithm explicitly conserves momentum and is strictly local, hydrodynamic interactions are preserved [160]. Soddeman, Dünweg and Kremer probably give one of the clearest exposition of the MD application of the DPD thermostat [157]; explicitly, the equations of motion are written as:

$$\frac{\partial \boldsymbol{r}_i}{\partial t} = \frac{\boldsymbol{p}_i}{m_i}, \tag{1.37}$$

$$\frac{\partial \boldsymbol{p}_i}{\partial t} = \boldsymbol{F}_i + \boldsymbol{F}_{i,\mathrm{ext}} + \sum_{j \neq i}^{n} \boldsymbol{F}_{ij}^{\mathrm{D}} + \sum_{j \neq i}^{n} \boldsymbol{F}_{ij}^{\mathrm{R}}. \tag{1.38}$$

The added dissipative force $\boldsymbol{F}_{ij}^{\mathrm{D}}$ and random force $\boldsymbol{F}_{ij}^{\mathrm{R}}$ are defined in terms of the unit vector $\hat{\boldsymbol{r}}_{ij}$ joining particles i and j, the relative velocity $\boldsymbol{v}_{ij} \equiv (\boldsymbol{v}_i - \boldsymbol{v}_j)$ and a cut-off function $w(r_{ij})$ which vanishes beyond a short distance:

$$\boldsymbol{F}_{ij}^{\mathrm{D}} = -\xi\, w(r_{ij})\, (\hat{\boldsymbol{r}}_{ij} \cdot \boldsymbol{v}_{ij})\, \hat{\boldsymbol{r}}_{ij} \tag{1.39}$$

$$\boldsymbol{F}_{ij}^{\mathrm{R}} = \alpha\, w(r_{ij})\, \vartheta_{ij} \hat{\boldsymbol{r}}_{ij} \delta t^{-1/2}\,, \tag{1.40}$$

where ϑ_{ij} is a Gaussian white-noise variable of zero mean and unit variance (chosen independently for each particle pair and at every time step). The origin of the $\delta t^{-1/2}$ factor in Equation 1.40 comes from the Dirac delta function in time in the definition of ϑ_{ij} and is discussed clearly by Groot and Warren [161]. The DPD thermostat parameters are the friction coefficient ξ and the noise strength, α and the two are related to respect the fluctuation-dissipation theorem:

$$\alpha^2 = 2k_{\mathrm{B}}T\xi\,. \tag{1.41}$$

Since both $\boldsymbol{F}_{ij}^{\mathrm{D}}$ and $\boldsymbol{F}_{ij}^{\mathrm{R}}$ are anti-symmetric with respect to the exchange of the indices i and j, it is clear that momentum is conserved locally. The DPD thermostat is easy to implement in an existing MD program because it only requires the addition of new local forces; it is used to control the temperature of the fluid in the EOF simulations reported in Chapter 6.

The development of efficient thermostats for NEMD simulations is still actively pursued by many research groups, and promising solutions continue to surface. Lowe suggested to combine the DPD thermostat idea with an Andersen resampling of relative velocities [162], and Stoyanov and Groot recently proposed to combine this new Lowe-Andersen thermostat with a modified Nosé-Hoover scheme to obtain an efficient algorithm which, very interestingly, allows for the tuning of some key hydrodynamic parameters [142]. There is, of course, no single best thermostat for all situations, and having many robust options to choose from is certainly a boon for the future of MD simulations.

Presentation of the thesis

This thesis is composed of five articles published or submitted for publication (pending peer review) in scientific journals during the course of my Ph.D. degree. Below is a list of these articles, with a few additional notes.

1) F Tessier, J Labrie, GW Slater. *Electrophoretic separation of long polyelectrolytes in submolecular-size constrictions: a Monte Carlo study.* **Macromolecules 35**, 4791–4800 (2002).

After introducing the operating principle of the entropic trap array for the separation of long DNA strands, we present the BF computational model, establish the correspondence between the simulations and real physical units, mention the implementation of the realistic electric field lines, and discuss some physical elements that are omitted in our approach. We then review the theoretical entropic barrier model proposed by the Craighead group to explain the observed electrophoretic mobility of DNA in the array, and discuss our simulation results in detail: the chain mobility as a function of chain size and field intensity, the molecular conformations, the separation of topoisomers, the resolution of the device, the critical hernia nucleation size and the trapping time. Most significantly, we find that the latter two quantities indeed depend on the inverse of the electric field strength, as suggested by the model. This article has up to now been cited six times by other groups [99].

2) F Tessier, GW Slater. *Strategies for the separation of polyelectrolytes based on non-linear dynamics and entropic ratchets in a simple microfluidic device.* **App. Phys. A 75**, 285–291 (2002).

For our contribution to this special issue of *Applied Physics A* dedicated to ratchets, we decided to report on a practical implementation of an entropic ratchet, i.e., in three dimensions and for an existing device. We quickly review the entropic trap array device from the previous article and the concept of entropic ratchet introduced by Slater *et al.* in 1997. We then describe our method to investigate ratchet regimes, which consists in fitting the electrophoretic mobility results obtained in the previous article with analytical functions, and extrapolating the low-frequency response of the system. We study ratcheting schemes based on either temporal or spatial asymmetries, and we confirm that a bias in the driving field can yield bi-directional motion according to molecular size. We also present explicit simulation results that support our predictions. Finally, we consider the finite frequency operating regime and uncover a previously unreported "resonance" phenomenon in the transport of long macromolecules through an array of entropic traps. This special issue of *Applied Physics A* as a whole has been cited many times, and our contribution has up to now been specifically cited in two publications other than our own.

3) F Tessier, GW Slater. *Effective Debye length in closed nanoscopic systems: a competition between two length scales.* **Submitted to Electrophoresis** (2005).

Early results of MD simulations for the distribution of ions in a closed nanoscopic channel (an NVT ensemble) clearly indicated that the bulk boundary conditions typically invoked in solving the PB equation are inadequate for closed, high surface-to-volume ratio electrolyte systems. We decided to look into this problem and found useful analytical approximations for the effective salt density of the electrolyte. Although it can be argued that closed systems are not very relevant experimentally, Molecular Dynamics simulations are usually carried out

in the NVT ensemble and results are often interpreted in contrast with classical continuum theory. There is a need to discuss the effects of surface counterions in nanofluidic systems, and we feel that our concise treatment clarifies the issue.

4) F Tessier, GW Slater. *Control and quenching of electroosmotic flow with end-grafted polymer chains* ***Macromolecules 38***, 6752–6754 (2002).

   This short communication briefly announces early results from our Molecular Dynamics simulations of EOF and control of EOF using grated polymer chains, results which manifestly generated interest when presented at various conferences. The format is intentionally concise. After introducing key concepts, we give some details on our methodology, and then address the precise question: "in what measure can neutral polymer chains grafted on the capillary surface reduce the magnitude of the EOF flow, and can they quench it altogether?" Simulations indicate that grafted polymer chains are efficient at reducing, even practically quenching the EOF at modest coating densities.

5) F Tessier, GW Slater. *Modulation of electroosmotic flow strength with end-grafted polymer chains in a nanochannel.* ***Submitted to Macromolecules*** (2005).

   This last article is a more elaborated, quantitative report of our MD simulations results for EOF and EOF control with neutral grafted chains. We introduce the issue and the related theory more broadly, and we provide detailed information on the various aspects of our simulation method: the basic algorithm, the nature of the capillary wall, the implementation of electrostatic interactions, the form of polymer molecules, and our thermostatting approach. The results are divided in three sections. First, we discuss the equilibrium situation (no external field) and show that ionic concentrations agree quite well with the prediction of the full, self-consistent integration of the PB equation (as discussed in our paper on the effective Debye length). Hence, continuum mean-field theory is useful even in nanofluidic systems. Secondly, we show that the simulation velocity profile during steady-state EOF (with no polymer coating) is very close to the profile predicted by theory, but that the agreement nevertheless cloaks a significant increase in the fluid viscosity near the wall. Finally, we report on the overall EOF velocity as a function of polymer length and grafting density, and we show that our simulation results are consistent with the theoretical predictions of Harden, Long and Ajdari [54].

Other contributions

In the course of my Ph.D. studies, I contributed to articles published by the group, and I also presented the results of my work at various conferences in Canada and abroad. Below is a summary of these research related activities, in chronological order. In the case of publications, my specific contributions have been highlighted in the Appendices at the end of the thesis, as indicated.

Publications

1) GW Slater, C Desruisseaux, SJ Hubert, JF Mercier, J Labrie, J Boileau, F Tessier, MP Pépin. *Theory of DNA Electrophoresis: A look at some current challenges.* ***Electrophoresis 21***, 3873-3887 (2000).
See **APPENDIX A.**

2) GW Slater, S Guillouzic, MG Gauthier, JF Mercier, M Kenward, LC McCormick, F Tessier. *Theory of DNA Electrophoresis (~1999–2002 1/2): A Review.* ***Electrophoresis 23***, 3791–3816 (2002).
See **APPENDIX B.**

3) GW Slater, Y Gratton, M Kenward, LC McCormick, F Tessier. *Deformation, stretching and relaxation of single polymer chains: fundamentals and examples.* ***Soft Materials 1***, 365–391 (2003). Also published as a chapter in *Soft Materials: Structure and Dynamics,* Marangoni and Dutcher Eds., Marcel Dekker, New York (2004).
See **APPENDIX C.**

Conference presentations

1) F Tessier, GW Slater. *Migration of Long Polyelectrolytes in a Structured Microfluidic Channel.* ***American Physical Society March Meeting***, Minneapolis, United States (2000).

2) F Tessier, GW Slater. *Separation of polymeric topoisomers in a microchannel device: a Monte Carlo study.* ***American Physical Society March Meeting***, Seattle, United States (2001).

3) F Tessier, GW Slater. *Separation of polymeric topoisomers in a microchannel device: a Monte Carlo study.* ***University/Industry Opportunities in Polymer Physics***, Guelph, Canada (2001).

4) F Tessier, GW Slater. *Separation of long polyelectrolytes in a molecular-size microfluidic channel with periodic constrictions: a Monte Carlo study.* ***US National Congress on Computational Mechanics***, Dearborn, United States (2001).

5) F Tessier, GW Slater. *Separation of long polyelectrolytes in a microfluidic channel with constrictions: a Monte Carlo study.* ***Modeling and Simulation of Microsystems***, San Juan, Puerto Rico (2002).

6) GW Slater, M Kenward, F Tessier. *Computer simulations of polymers and polymer dynamics in confined environments and microfluidic devices.* ***Materials Management Ontario: Partnerships 2002***, Toronto, Canada (2002).

7) F Tessier, GW Slater. *Molecular Dynamics simulations of electroosmotic flow in nanofluidic capillaries.* ***American Physical Society March Meeting***, Austin, United States (2003).

8) M Kenward, F Tessier, S Guillouzic, Y Tatek, Y Gratton, GW Slater. *Molecular Dynamics Simulations of Polymers in Microenvironments.* ***17th Annual International Symposium on High Performance Computing.***, Sherbrooke, Canada (2003).

9) F Tessier, GW Slater. *Control of electroosmotic flow in a nanofluidic channel using grafted polymer chains.* ***Neumann Institut für Computing Winter School***, Bonn, Germany (2004).

10) F Tessier, GW Slater. *Control of electroosmotic flow in a nanofluidic channel using grafted polymer chains.* ***American Physical Society March Meeting***, Montreal, Canada (2004).

11) GW Slater, F Tessier. *Control of electroosmotic flow in a nanofluidic channel using grafted polymer chains.* ***American Physical Society March Meeting***, Los Angeles, United States (2005).

References

[1] "nano–". *Online Oxford English Dictionary*, **http://www.oed.com** (accessed 31 August 2005).

[2] Résolution 12. *Résolutions de la Onzième Conférence Générale des Poids et Mesures*, **http://www.bipm.fr/jsp/fr/ListCGPMResolution.jsp?CGPM=11** (accessed 31 August 2005).

[3] NIST. *International System of Units*, **http://physics.nist.gov/cuu/Units/** (accessed 31 August 2005).

[4] "technology". *Online Oxford English Dictionary*, **http://www.oed.com** (accessed 31 August 2005).

[5] "technology". *Wikipedia*, **http://en.wikipedia.org/wiki/technology** (accessed 31 August 2005).

[6] "nanotechnology". *Online Oxford English Dictionary*, **http://www.oed.com** (accessed 31 August 2005).

[7] National Nanotech Initiative. *Funding*, **http://www.nano.gov/html/about/funding.html** (accessed 31 August 2005).

[8] The Economist. *Small wonders*, **http://www.economist.com/printedition/PrinterFriendly.cfm?Story_ID=3494722** (accessed 31 August 2005).

[9] BusinessWeek Online. *The business of nanotech*, **http://www.businessweek.com/magazine/content/05_07/b3920001_mz001.htm** (accessed 31 August 2005).

[10] National Science Foundation. *Societal implications of nanoscience and nanotechnology*, **http://www.wtec.org/loyola/nano/NSET.Societal.Implications/** (accessed 3 September 2005).

[11] RP Feynman. *There's plenty of room at the bottom: an invitation to enter a new field of physics*, **http://www.zyvex.com/nanotech/feynman.html** (accessed 31 August 2005).

[12] GM Whitesides. *Nanoscience, nanotechnology, and chemistry*, **Small 1**, 172–179 (2005).

[13] GM Wang, EM Sevick, E Mittag, DJ Searles, DJ Evans. *Experimental demonstration of violations of the Second Law of thermodynamics for small systems and short time scales*, **Phys. Rev. Lett. 89**, 050601 (2002).

[14] R Dawkins. *Climbing Mount Improbable*. W. W. Norton, New York (1996).

[15] A Meller, L Nivon, E Brandin, J Golovchenko, D Branton. *Rapid nanopore discrimination between single polynucleotide molecules*, **Proc. Nat. Acad. Sci. USA 97**, 1079–1084 (2000).

[16] JJ Kasianowicz, SE Henrickson, M Misakian, HH Weetall, B Robertson. *Applications for DNA transport in a single nanopore*, **Biophys. J. 80**, 339A–339A (2001).

[17] A Meller, L Nivon, D Branton. *Voltage-driven DNA translocations through a nanopore*, **Phys. Rev. Lett. 86**, 3435–3438 (2001).

[18] A Meller, D Branton. *Single molecule measurements of DNA transport through a nanopore*, **Electrophoresis 23**, 2583–2591 (2002).

[19] DW Deamer, D Branton. *Characterization of nucleic acids by nanopore analysis*, **Acc. Chem. Res. 35**, 817–825 (2002).

[20] J Nakane, M Akeson, A Marziali. *Evaluation of nanopores as candidates for electronic analyte detection*, **Electrophoresis 23**, 2592–2601 (2002).

[21] A Meller. *Dynamics of polynucleotide transport through nanometer-scale pores*, **J. Phys. Cond. Matt. 15**, R581–R607 (2003).

[22] JJ Nakane, M Akeson, A Marziali. *Nanopore sensors for nucleic acid analysis*, **J. Phys. Cond. Matt. 15**, R1365–R1393 (2003).

[23] JJ Kasianowicz. *Nanopores—flossing with DNA*, **Nature Materials 3**, 355–356 (2004).

[24] BJ Polk, M Bernard, JJ Kasianowicz, M Misakian, M Gaitan. *Microelectroplating silver on sharp edges toward the fabrication of solid-state nanopores*, **J. Electrochem. Soc. 151**, C559–C566 (2004).

[25] P Chen, JJ Gu, E Brandin, YR Kim, Q Wang, D Branton. *Probing single DNA molecule transport using fabricated nanopores*, **Nano Letters 4**, 2293–2298 (2004).

[26] A Aksimentiev, JB Heng, G Timp, K Schulten. *Microscopic kinetics of DNA translocation through synthetic nanopores*, **Biophys. J. 87**, 2086–2097 (2004).

[27] JB Heng, C Ho, T Kim, R Timp, A Aksimentiev, YV Grinkova, S Sligar, K Schulten, G Timp. *Sizing DNA using a nanometer-diameter pore*, **Biophys. J. 87**, 2905–2911 (2004).

[28] AJ Storm, C Storm, JH Chen, H Zandbergen, JF Joanny, C Dekker. *Fast DNA translocation through a solid-state nanopore*, **Nano Letters 5**, 1193–1197 (2005).

[29] JJ Kasianowicz, E Brandin, D Branton, DW Deamer. *Characterization of individual polynucleotide molecules using a membrane channel*, **Proc. Nat. Acad. Sci. USA 93**, 13770–13773 (1996).

[30] A Aksimentiev. ***http://www.ks.uiuc.edu/~alek/*** (accessed 3 September 2005).

[31] *Human Genome Project*, ***http://www.ornl.gov/sci/techresources/Human_Genome/home.shtml*** (accessed 31 August 2005).

[32] International Human Genome Sequencing Consortium. *Initial sequencing and analysis of the human genome*, **Nature 409**, 860–921 (2001).

[33] JC Venter et al. *The sequence of the human genome*, **Science 291**, 1304–1351 (2001).

[34] N Yazdi, F Ayazi, K Najafi. *Micromachined inertial sensors*, **Proc. IEEE 86**, 1640–1659 (1998).

[35] Analog Devices. *MEMS and sensors*, ***http://www.analog.com/en/cat/0,2878,764,00.html*** (accessed 31 August 2005).

[36] J Khandurina, A Guttman. *Bioanalysis in microfluidic devices*, **J. Chromatography A 943**, 159–183 (2002).

[37] SR Quake, A Scherer. *From micro- to nanofabrication with soft materials*, **Science 290**, 1536–1540 (2000).

[38] A Groisman, M Enzelberger, SR Quake. *Microfluidic memory and control devices*, **Science 300**, 955–958 (2003).

[39] T Thorsen, SJ Maerkl, SR Quake. *Microfluidic large-scale integration*, **Science 298**, 580–584 (2002).

[40] C Hansen, SR Quake. *Microfluidics in structural biology: smaller, faster... better*, **Curr. Opin. Struc. Bio. 13**, 538–544 (2003).

[41] KF Jensen. *Microreaction engineering—is small better?*, **Chem. Eng. Sci. 56**, 293–303 (2001).

[42] S Borman. *The many faces of combinatorial chemistry*, **Chem. Eng. News 81**, 45–56 (2003).

[43] ET Lagally, RA Mathies. *Integrated genetic analysis microsystems*, ***J. Phys. D* 37**, R245–R261 (2004).

[44] SWP Turner, M Cabodi, HG Craighead. *Confinement-induced entropic recoil of single DNA molecules in a nanofluidic structure*, ***Phys. Rev. Lett.* 88**, 128103 (2002).

[45] M Cabodi, SWP Turner, HG Craighead. *Entropic recoil separation of long DNA molecules*, ***Anal. Chem.* 74**, 5169–5174 (2002).

[46] JW Hong, V Studer, G Hang, WF Anderson, SR Quake. *A nanoliter-scale nucleic acid processor with parallel architecture*, ***Nature Biotech.* 22**, 435–439 (2004).

[47] M Toner, D Irimia. *Blood-on-a-chip*, ***Annu. Rev. Biomed. Eng.* 7**, 7–103 (2005).

[48] MP Allen, DJ Tildesley. *Computer simulation of liquids*. Oxford University Press, New York (1987).

[49] JM Haile. *Molecular Dynamics simulations: elementary methods*. John Wiley & Sons, New York (1992).

[50] DW Heermann. *Computer simulation methods in theoretical physics, 2^{nd} ed.* Springer-Verlag, Berlin (1990).

[51] DC Rapaport. *The art of Molecular Dynamics*. Cambridge University Press, Cambridge (1995).

[52] J Han, SW Turner, HG Craighead. *Entropic trapping and escape of long DNA molecules at submicron size constriction*, ***Phys. Rev. Lett.* 83**, 1688–1691 (1999).

[53] GW Slater, HL Guo, GI Nixon. *Bidirectional transport of polyelectrolytes using self-modulating entropic ratchets*, ***Phys. Rev. Lett.* 78**, 1170–1173 (1997).

[54] JL Harden, D Long, A Ajdari. *Influence of end-grafted polyelectrolytes on electro-osmosis along charged surfaces*, ***Langmuir* 17**, 705–715 (2001).

[55] H Morawetz. *Polymers: the origins and growth of a science*. Dover Publications, New York (1985).

[56] TI Williams. *A biographical dictionary of scientists*. John Wiley & Sons, London (1969).

[57] H Elias. *Mega Molecules*. Sringer-Verlag, Berlin (1987).

[58] Nobel Foundation. *Paul J. Flory — Nobel lecture*, ***http://nobelprize.org/chemistry/laureates/1974/flory-lecture.html*** (accessed 1 September 2005).

[59] Nobel Foundation. *The Nobel Prize in chemistry 1953*, ***http://nobelprize.org/chemistry/laureates/1953/*** (accessed 1 September 2005).

[60] B Alberts et al. *Molecular biology of the cell, 2^{nd} ed.* Garland Publishing, New York (1989).

[61] RE Franklin, RG Gosling. *Molecular configuration in sodium thymonucleate*, ***Nature* 171**, 740–741 (1953).

[62] RE Franklin, RG Gosling. *Evidence for 2-chain helix in crystalline structure sodium deoxyribonucleate*, ***Nature* 172**, 156–157 (1953).

[63] JD Watson, FHC Crick. *A structure for deoxyribose nucleic acid*, ***Nature* 171**, 737–738 (1953).

[64] JD Watson, FHC Crick. *Genetical implications of the structure of deoxyribonucleic acid*, ***Nature* 172**, 964–967 (1953).

[65] F Crick. *The double-helix: a personal view*, ***Nature* 248**, 766–769 (1974).

[66] A Klug. *Rosalind Franklin and the double helix*, ***Nature* 248**, 787 (1974).

[67] B Maddox. *The double helix and the 'wronged heroine'*, **Nature 421**, 407–408 (2003).

[68] P de Gennes. *Scaling concepts in polymer physics*. Cornell University Press, Ithaca (1979).

[69] RB Laughlin, D Pines. *The Theory of Everything*, **Proc. Nat. Acad. Sci. USA 97**, 28–31 (2000).

[70] M Doi, SF Edwards. *The theory of polymer dynamics*. Oxford Science Publications, New York (1986).

[71] I Teraoka. *Polymer solutions: an introduction to physical properties*. John Wiley & Sons, New York (2002).

[72] C Haber, SA Ruiz, D Wirtz. *Shape anisotropy of a single random-walk polymer*, **Proc. Nat. Acad. Sci. USA 97**, 10792–10795 (2000).

[73] B Maier, JO Radler. *Shape of self-avoiding walks in two dimensions*, **Macromolecules 34**, 5723–5724 (2001).

[74] M Bishop, JHR Clarke. *Investigation of the end-to-end distance distribution function for random and self-avoiding walks in 2 and 3 dimensions*, **J. Chem. Phys. 94**, 3936–3942 (1991).

[75] E Brezin, J Zinnjustin, JC Le Guillou. *Renormalization of the nonlinear σ model in $2+\epsilon$ dimensions*, **Phys. Rev. D 14**, 2615–2621 (1976).

[76] VG Levich. *Physicochemical hydrodynamics*. Prentice-Hall, Englewood Cliffs (1962).

[77] J Hansen, IR McDonald. *Theory of simple liquids, 2^{nd} ed.* Academic Press, San Diego (1986).

[78] RF Probstein. *Physicochemical hydrodynamics*. John Wiley & Sons, New York (1994).

[79] The MacTutor history of mathematics archive. *Navier*, ***http://www-groups.dcs.st-and.ac.uk/~history/Mathematicians/Navier.html*** (accessed 1 September 2005).

[80] Clay Mathematics Institute. *Navier-Stokes Equation*, ***http://www.claymath.org/millennium/Navier-Stokes_Equations/*** (accessed 1 September 2005).

[81] JJ Tuma. *Handbook of physical calculcations*. McGraw-Hill, New York (1976).

[82] Physics hypertextbook. *Flow Regimes*, ***http://hypertextbook.com/physics/matter/turbulence/*** (accessed 1 September 2005).

[83] E Guyon, J Hulin, L Petit. *Hydrodynamique physique*. Inter Éditions et CNRS Éditions, Paris (1994).

[84] J Israelachvili. *Intermolecular & surface forces, 2^{nd} ed.* Academic Press, London (1992).

[85] WB Russel, DA Saville, WR Schowalter. *Colloidal dispersions*. Cambridge University Press, Cambridge (1989).

[86] RK Iler. *The chemistry of silica*. John Wiley & Sons, New York (1979).

[87] SH Behrens, DG Grier. *The charge of glass and silica surfaces*, **J. Chem. Phys. 115**, 6716–6721 (2001).

[88] JL Viovy. *Electrophoresis of DNA and other polyelectrolytes: physical mechanisms*, **Rev. Mod. Phys. 72**, 813–872 (2000).

[89] NC Stellwagen, C Gelfi, PG Righetti. *The free solution mobility of DNA*, **Biopolymers 42**, 687–703 (1997).

[90] PG Righetti. *Electrophoresis: the march of pennies, the march of dimes*, **J. Chromatography A 1079**, 24–40 (2005).

[91] RP Feynman, RB Leighton, M Sands. *The Feynman lectures on physics, vol. 1*. Addison-Wesley, Reading (1963).

[92] P Reimann. *Brownian motors: noisy transport far from equilibrium*, **Phys. Rep. 361**, 57–265 (2002).

[93] L Brillouin. *Can the rectifer become a thermodynamical demon?*, **Phys. Rev. 78**, 627–628 (1950).

[94] TR Kelly, JP Sestelo, I Tellitu. *New molecular devices: in search of a molecular ratchet*, **J. Organic Chem. 63**, 3655–3665 (1998).

[95] TR Kelly, H De Silva, RA Silva. *Unidirectional rotary motion in a molecular system*, **Nature 401**, 150–152 (1999).

[96] JV Hernandez, ER Kay, DA Leigh. *A reversible synthetic rotary molecular motor*, **Science 306**, 1532–1537 (2004).

[97] MO Magnasco, G Stolovitzky. *Feynman's ratchet and pawl*, **J. Stat. Phys. 93**, 615–632 (1998).

[98] F Jülicher, A Ajdari, J Prost. *Modeling molecular motors*, **Rev. Mod. Phys. 69**, 1269–1281 (1997).

[99] ISI Web of Knowledge. *Web of Science citation index*, **http://www.isiknowledge.com** (accessed 2 September 2005).

[100] MO Magnasco. *Forced thermal ratchets*, **Phys. Rev. Lett. 71**, 1477–1481 (1993).

[101] J Rousselet, L Salome, A Ajdari, J Prost. *Directional motion of brownian particles induced by a periodic asymmetric potential*, **Nature 370**, 446–448 (1994).

[102] JS Bader, RW Hammond, SA Henck, MW Deem, GA McDermott, JM Bustillo, JW Simpson, GT Mulhern, JM Rothberg. *DNA transport by a micromachined brownian ratchet device*, **Proc. Nat. Acad. Sci. USA 96**, 13165–13169 (1999).

[103] RW Hammond, JS Bader, SA Henck, MW Deem, GA McDermott, JM Bustillo, JM Rothberg. *Differential transport of DNA by a rectified brownian motion device*, **Electrophoresis 21**, 74–80 (2000).

[104] JS Bader, MW Deem, RW Hammond, SA Henck, JW Simpson, JM Rothberg. *A brownian-ratchet DNA pump with applications to single-nucleotide polymorphism genotyping*, **App. Phys. A 75**, 275–278 (2002).

[105] N Metropolis. *The beginning of the Monte Carlo method*, **Los Alamos Sci. 15**, 125–130 (1987).

[106] DE Knuth. *The art of computer programming, vol. 2: seminumerical algorithms, 2nd ed.* Addison-Wesley, Reading (1981).

[107] WH Press, SA Teukolsky, WT Vetterling, BP Flannery. *Numerical recipes in C: the art of scientific computing, 2nd ed.* Cambridge University Press, Cambridge (1992).

[108] M Matsumoto, T Nishimura. *Mersenne twister: a 623-dimensionally equidistributed uniform pseudo-random number generator*, **ACM Trans. Model. Comp. Sim. 8**, 3–30 (1998).

[109] N Metropolis, AW Rosenbluth, MN Rosenbluth, AH Teller. *Equation of state calculations by fast computing machines*, **J. Chem. Phys. 21**, 1087–1092 (1953).

[110] WW Wood, FR Parker. *Monte Carlo equation of state of molecules interacting with the Lennard-Jones potential. I. A supercritical isotherm at about twice the critical temperature*, **J. Chem. Phys. 27**, 720–733 (1957).

[111] MN Rosenbluth, AW Rosenbluth. *Further results on Monte Carlo equations of state*, **J. Chem. Phys. 22**, 881–884 (1954).

[112] J Dongarra, F Sullivan. *The top 10 algorithms*, **Comp. Sci. & Eng. 2**, 22–23 (2000).

[113] I Beichl, F Sullivan. *The Metropolis algorithm*, **Comp. Sci. & Eng. 2**, 65–69 (2000).

[114] American Physical Society. *Nicholas Metropolis award for outstanding doctoral thesis work in computational physics*, ***http://www.aps.org/praw/metropol/*** (accessed 2 September 2005).

[115] I Carmesin, K Kremer. *The bond fluctuation method: a new effective algorithm for the dynamics of polymers in all spatial dimensions*, ***Macromolecules* 21**, 2819–2823 (1988).

[116] HP Deutsch, K Binder. *Interdiffusion and self-diffusion in polymer mixtures: a Monte Carlo study*, ***J. Chem. Phys.* 94**, 2294–2304 (1991).

[117] BJ Alder, TE Wainwright. *Studies in Molecular Dynamics. I. General method*, ***J. Chem. Phys.* 31**, 459–466 (1959).

[118] BJ Alder, TE Wainwright. *Phase transition for a hard sphere system*, ***J. Chem. Phys.* 27**, 1208–1209 (1957).

[119] A Rahman. *Correlations in the motion of atoms in liquid argon*, ***Phys. Rev.* 136**, A405–A411 (1964).

[120] L Verlet. *Computer "experiments" on classical fluids. I. Thermodynamical properties of Lennard-Jones molecules*, ***Phys. Rev.* 159**, 98–103 (1967).

[121] L Verlet. *Computer "experiments" on classical fluids. II. Equilibrium correlation functions*, ***Phys. Rev.* 165**, 201–214 (1968).

[122] J Hansen, L Verlet. *Phase transistions of the Lennard-Jones system*, ***Phys. Rev.* 184**, 151–161 (1969).

[123] D Levesque, L Verlet. *Computer "experiments" on classical fluids. III. Time-dependent self-correlation functions*, ***Phys. Rev. A* 2**, 2514–2528 (1970).

[124] FF Abraham, R Walkup, HJ Gao, M Duchaineau, TD De la Rubia, M Seager. *Simulating materials failure by using up to one billion atoms and the world's fastest computer: brittle fracture*, ***Proc. Nat. Acad. Sci. USA* 99**, 5777–5782 (2002).

[125] FF Abraham, R Walkup, HJ Gao, M Duchaineau, TD De la Rubia, M Seager. *Simulating materials failure by using up to one billion atoms and the world's fastest computer: work-hardening*, ***Proc. Nat. Acad. Sci. USA* 99**, 5783–5787 (2002).

[126] NIC winter school, Gustav-Stresemann-Institut, Bonn, Germany. *Computational soft matter: from synthetic polymers to proteins* (29 February – 6 March 2004).

[127] IP Omelyan, IM Mryglod, R Folk. *Optimized Verlet-like algorithms for Molecular Dynamics simulations*, ***Phys. Rev. E* 65**, 056706 (2002).

[128] F Reif. *Fundamentals of statistical and thermal physics*. McGraw-Hill, Boston (1965).

[129] RK Pathria. *Statistical Mechanics, 2nd ed.* Butterworth-Heinemann, Oxford (1996).

[130] DJ Evans, GP Morriss. *Statistical mechanics of nonequilibrium liquids*. Academic Press, London (1990).

[131] RK Pathria. *Lorentz transformation of thermodynamic quantities*, ***Proc. Phys. Soc.* 88**, 791–799 (1966).

[132] PT Landsberg. *Special relativistic thermodynamics*, ***Proc. Phys. Soc.* 89**, 1007–1016 (1966).

[133] NG van Kampen. *Relativistic thermodynamics of moving systems*, ***Phys. Rev.* 173**, 295–301 (1968).

[134] VH Hamity. *Relativistic thermodynamics*, ***Phys. Rev.* 187**, 1745–1752 (1969).

[135] CK Yuen. *Lorentz transformation of thermodynamic quantities*, ***Am. J. Phys.* 38**, 246–252 (1970).

[136] PT Landsberg. *Thought experiment to determine the special relativistic temperature transformation*, ***Phys. Rev. Lett.*** **45**, 149–150 (1980).

[137] I Avramov. *Relativity and temperature*, ***Russian J. Phys. Chem.*** **77**, S179–S182 (2003).

[138] GA de Parga, B López-Carrera, F Angulo-Brown. *A proposal for relativistic transformations in thermodynamics*, ***J. Phys. A*** **38**, 2821–2834 (2005).

[139] PT Landsberg, GEA Matsas. *Laying the ghost of the relativistic temperature transformation*, ***Phys. Lett. A*** **223**, 401–403 (1996).

[140] PT Landsberg, GEA Matsas. *The impossibility of a universal relativistic temperature transformation*, ***Physica A*** **340**, 92–94 (2004).

[141] J Delhommelle, DJ Evans. *Configurational temperature profile in confined fluids. I. Atomic fluid*, ***J. Chem. Phys.*** **114**, 6229–6235 (2001).

[142] SD Stoyanov, RD Groot. *From Molecular Dynamics to hydrodynamics: a novel galilean invariant thermostat*, ***J. Chem. Phys.*** **122**, 114112 (2005).

[143] HH Rugh. *Dynamical approach to temperature*, ***Phys. Rev. Lett.*** **78**, 772–774 (1997).

[144] BD Butler, O Ayton, OG Jepps, DJ Evans. *Configurational temperature: verification of Monte Carlo simulations*, ***J. Chem. Phys.*** **109**, 6519–6522 (1998).

[145] OG Jepps, G Ayton, DJ Evans. *Microscopic expressions for the thermodynamic temperature*, ***Phys. Rev. E*** **62**, 4757–4763 (2000).

[146] LV Woodcock. *Isothermal Molecular Dynamics calculations for liquid salts*, ***Chem. Phys. Lett.*** **10**, 257–261 (1971).

[147] JQ Broughton, GH Gilmer, JD Weeks. *Constant pressure Molecular Dynamics simulations of the* $2D$ r^{-12} *system: comparison with isochores and isotherms*, ***J. Chem. Phys.*** **75**, 5128–5132 (1981).

[148] HC Andersen. *Molecular-Dynamics simulations at constant pressure and/or temperature*, ***J. Chem. Phys.*** **72**, 2384–2393 (1980).

[149] DJ Evans, WG Hoover, BH Failor, B Moran, AJC Ladd. *Non-equilibrium Molecular-Dynamics via Gauss principle of least constraint*, ***Phys. Rev. A*** **28**, 1016–1021 (1983).

[150] DJ Evans, GP Morriss. *The isothermal/isobaric Molecular Dynamics ensemble*, ***Phys. Lett. A*** **98**, 389–489 (1983).

[151] S Nosé. *A unified formulation of the constant temperature Molecular-Dynamics methods*, ***J. Chem. Phys.*** **81**, 511–519 (1984).

[152] S Nosé. *A Molecular-Dynamics method for simulations in the canonical ensemble*, ***Mol. Phys.*** **52**, 255–268 (1984).

[153] WG Hoover. *Canonical dynamics – equilibrium phase-space distributions*, ***Phys. Rev. A*** **31**, 1695–1697 (1985).

[154] S Nosé. *An extension of the canonical ensemble Molecular-Dynamics method*, ***Mol. Phys.*** **57**, 187–191 (1986).

[155] HJC Berendsen, JPM Postma, WF van Gunsteren, A Dinola, JR Haak. *Molecular-Dynamics with coupling to an external bath*, ***J. Chem. Phys.*** **81**, 3684–3690 (1984).

[156] T Schneider, E Stoll. *Molecular-Dynamics study of a 3-dimensional one-component model for distortive phase-transitions*, ***Phys. Rev. B*** **17**, 1302–1322 (1978).

[157] T Soddemann, B Dünweg, K Kremer. *Dissipative Particle Dynamics: a useful thermostat for equilibrium and nonequilibrium Molecular Dynamics simulations*, **Phys. Rev. E 68**, 046702 (2003).

[158] PJ Hoogerbrugge, JMVA Koelman. *Simulating microscopic hydrodynamic phenomena with Dissipative Particle Dynamics*, **Europhys. Lett. 19**, 155–160 (1992).

[159] P Espanol, P Warren. *Statistical mechanics of Dissipative Particle Dynamics*, **Europhys. Lett. 30**, 191–196 (1995).

[160] P Espanol. *Hydrodynamics from Dissipative Particle Dynamics*, **Phys. Rev. E 52**, 1734–1742 (1995).

[161] RD Groot, PB Warren. *Dissipative particle dynamics: bridging the gap between atomistic and mesoscopic simulation*, **J. Chem. Phys. 107**, 4423–4435 (1997).

[162] CP Lowe. *An alternative approach to Dissipative Particle Dynamics*, **Europhys. Lett. 47**, 145–151 (1999).

2

Electrophoretic separation of long polyelectrolytes in submolecular-size constrictions: a Monte Carlo study

F Tessier, J Labrie, GW Slater. *Macromolecules* **35**, 4791 (2002)

Macromolecules **2002,** *35,* 4791−4800 **4791**

Electrophoretic Separation of Long Polyelectrolytes in Submolecular-Size Constrictions: A Monte Carlo Study

Frédéric Tessier, Josée Labrie, and Gary W. Slater*

Department of Physics, University of Ottawa, 150 Louis-Pasteur, Ottawa, Ontario, Canada K1N 6N5

Received June 18, 2001; Revised Manuscript Received March 8, 2002

ABSTRACT: We use a bond-fluctuation Monte Carlo method to study the motion of long polyelectrolytes inside an array of microscopic entropic traps. The molecules are pulled through the array by an electric field and forced into submolecular-size constrictions between the larger trap regions. We numerically solve the Laplace equation inside the structure to obtain realistic field lines for our simulations. We find that the mobility of the molecules *increases* with molecular size and that the size-separation mechanism relies mainly on the overall deformation of the molecules as they approach the narrow constrictions. We also investigate specific aspects of the separation mechanism, namely the conformational behavior of the molecule, the hernia nucleation process, and the trapping time statistics as a function of molecular size and field strength. Our simulation results for the mobility, the critical hernia nucleation size, the mean trapping time, and the resolution are consistent with the experimental data and model previously published by Han et al.[1,2] Finally, we predict that such microfluidic structures could be used to separate topoisomers bearing the same molecular size.

I. Introduction

Microscopic devices that can detect, sort, purify, or otherwise manipulate individual particles, molecules, or even cells are bound to revolutionize molecular sciences, offering an unprecedented level of control in experimental settings. Molecular biology, in particular, will greatly benefit from such devices, not only because of the widespread interest in the analysis of biomolecules but also because large biomolecules are conveniently commensurate in size to the resolution of current microfabrication technologies. The growing thrust behind genomics is also pressing the need for more efficient ways to separate DNA fragments by size (a task pertinent to both gene mapping and sequencing); hence, many groups are currently working on the confection of micromachined separation systems that can outperform traditional gel electrophoresis methods. Proposed devices include sieves in the form of microscopic arrays of posts that mimic gel fibers,[3−5] Brownian rectifiers in the form of ratchets or asymmetric arrays of obstacles,[6−12] single-molecule sizing devices,[13] and entropic trapping systems.[1,2,14]

In this article we focus our attention on a microscopic entropic trap array recently fabricated by Han et al. and used for the separation of double-stranded DNA (dsDNA) fragments in the tens of kilobase pairs (kbp) range.[1,2] This array consists of a small channel with periodic constrictions etched on a silicon wafer, as depicted in Figure 1. The channel is about 1 μm across, and dsDNA molecules of a comparable size are pulled through the structure by a "low-intensity" electric field. The narrow constrictions, less than 0.1 μm across, hinder this motion, and longer molecules are found to advance *faster* overall than shorter ones. Questions pertaining to the origin and optimization of this rather counterintuitive size selectivity prompted us to investigate, through Monte Carlo simulations, the separation mechanisms at play in this device, where entropic forces prevail. Our results will show that longer molecules indeed have a higher mobility than shorter ones and that the separation process relies mostly on the overall size and deformation of the molecules as they travel through the channel. Furthermore, simulations enable us to investigate molecular behavior on the local scale, which can then be compared with theory. Overall, our conclusions agree with experimental data and the simple theoretical model proposed by Han et al.[1]

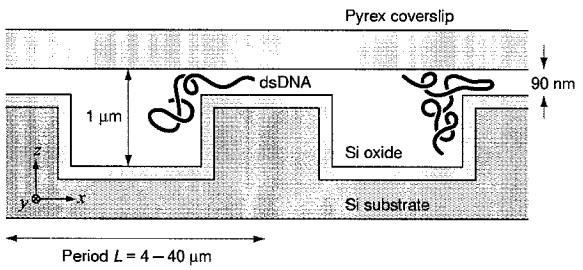

Figure 1. Schematic transverse cut of the microchannel device we are studying in this article (adapted from Han et al.[1]). Here the driving electric field is oriented toward the left so the (negatively charged) DNA strands migrate toward the right.

Before we present the outcome of our simulations, we briefly review our computational approach and some theoretical considerations. At the outset we should stress that the goal of this work is to characterize the generic mode of operation of the device and not to fit specific experimental data. We thus attempt to model the system in some level of detail to ensure that we operate in the appropriate regime and that we can establish a reliable qualitative correspondence with experiments, but we are not concerned with quantitative discrepancies that do not affect the nature of the separation process. Given its simple geometry, the structure studied in this article stands as a model pore-constriction system; hence, our results are also relevant in other contexts where macromolecules (i.e., flexible molecules with large internal conformational entropy)

* Corresponding author: e-mail gslater@science.uottawa.ca.

10.1021/ma0110406 CCC: $22.00
Published on Web 05/03/2002

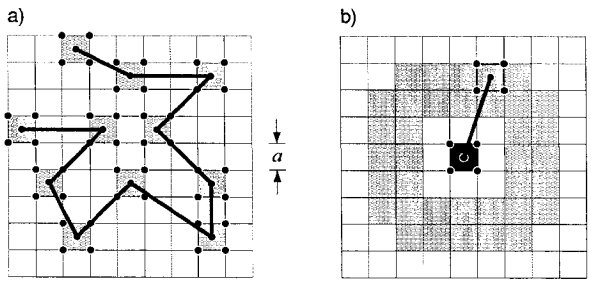

Figure 2. Bond fluctuation algorithm in two dimensions: (a) a sample walk on the bond fluctuation lattice, where each monomer occupies four lattice sites, and (b) the 36 allowed bond vectors between two successive monomers, the first of which is represented by the black square at the origin and the second one by a shaded square. This algorithm can be generalized in 3D, in which case each monomer occupies 8 lattice sites and there are 108 allowed bond vectors.

are forced through narrow slits or between large pores in a chemical gel.

II. Method

A. The Molecule and Its Dynamics. All the simulations reported in this article are based on the bond-fluctuation (BF) algorithm. This algorithm has been described in detail[15,16] and has been used extensively in polymer simulations, so we only recall its main characteristics. The simulation space is divided in unit cells so as to form an orthogonal lattice, and the macromolecule is represented by a chain of N effective monomers, each occupying 2^d lattice sites (where d is the dimensionality of space) to cover one unit cell (Figure 2a). A given lattice site can only belong to one monomer at a time in order to account for excluded volume interactions, and the bond vector connecting two successive monomers is constrained to a predefined set, chosen so as to avoid bond crossing; there are respectively 36 and 108 allowed bond vectors in 2D (Figure 2b) and 3D. In our case, each monomer also carries an effective electric charge q since we model a polyelectrolyte.

The motion of the chain is generated from local elementary moves: for each trial move, we randomly select a monomer and attempt to move it randomly by one lattice unit (which we denote by $a = 1$) along one of the axis directions. Provided that volume exclusion and bond constraints are respected, the move is accepted upon success of a Metropolis test[17] for the change in the electrostatic energy of the monomer (see below). The elementary time unit of the simulation is given by one Monte Carlo step (mcs), defined as N trial moves.

B. The Microchannel Device. The structure of the device sketched in Figure 1 is incorporated in the simulation by means of occupied lattice sites forming walls that match the device geometry. We use the lattice shown in Figure 3, with periodic boundary conditions (PBC) along the x and y directions. For conciseness, we refer to the large regions of the channel as *wells* and the constriction regions as *gaps*. We consider molecules with a radius of gyration (R_g) that is larger than half the gap size (so that there is trapping) yet smaller than half the well size (so that the molecule is not deformed between traps). If we assume that the average bond length in the simulations (roughly $2.8a$) is comparable to the persistence length of dsDNA (50 nm, or about 0.150 kbp), then we have $a \approx 20$ nm, hence our channel

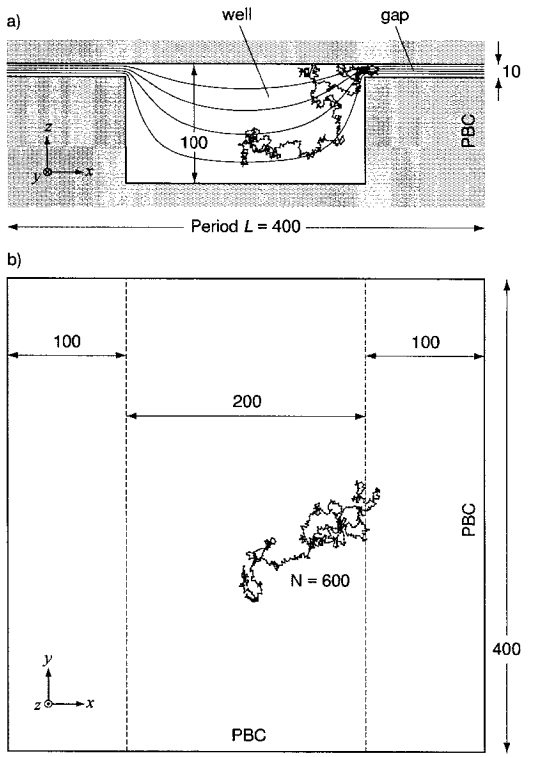

Figure 3. (a) A transverse (or xz) view of the lattice used for the 3D simulation of the microchannel device and (b) a top (or xy) view of the same system. The electric field lines are shown in the transverse view, and a sample molecule with $N = 600$ monomers is included. The dimensions of the lattice are all given in units of the lattice spacing ($a = 1$).

measures 2 μm across with a gap size of 200 nm, and it has a period L of 8 μm. The simulated chains vary in size from $N = 50$ to $N = 600$ effective monomers, which corresponds to dsDNA molecules ranging from 7 to 90 kbp. These numbers are all quite comparable to the dimensions reported by Han et al.[1]

We apply a potential difference ΔV_0 across the period L of our channel to model the driving electric field. The walls of the channel are considered perfect insulators, and we solve the Laplace equation numerically to obtain the local potential V on every lattice site. (We actually solve for the potential on a refined grid, and we take V as the average over the lattice cell of volume a^3 surrounding each site.) The resulting field lines are sketched in Figure 3a, and we verify that the electric field is stronger in the gap than in the well by a factor close to the ratio of the well size to the gap size, as it should. The Metropolis weight associated with the move of a monomer bearing a charge q is then simply given by $\exp(-q\delta V/k_B T)$, where δV is the potential difference between the two adjacent lattice sites involved, k_B is Boltzmann's constant, and T is the absolute temperature. The calculated potential drop across the periodic boundary in x is adjusted by ΔV_0 to obtain seamless field lines between successive sections of the periodic channel. Throughout this article, the strength of the applied field is always given in terms of the global dimensionless variable $\epsilon = q\Delta V_0 a/Lk_B T$. The field strength at the geometrical center of the gap is thus $\epsilon_{gap} \approx 1.8\epsilon$, whereas at the center of the well it is $\epsilon_{well} \approx 0.2\epsilon$.

C. Some Physical Elements That Are Omitted. We do not include solvent molecules in our simulations,

Macromolecules, Vol. 35, No. 12, 2002 Long Polyelectrolytes **4793**

so explicit hydrodynamic interactions are neglected. Nevertheless, the free-draining electrophoretic property of polyelectrolytes is conveniently preserved in the Monte Carlo approach. However, the physical origin of this free-draining property is absent from our model, as it lies in the friction exerted locally on the chain by surrounding counterions. It is also important to keep in mind that the entropic forces that slow down (or trap) the DNA molecules at the well–gap interface are effectively mechanical forces that affect the free-draining properties of the polyelectrolyte, as discussed by Long et al. in a recent series of key articles.[18–21] These subtle effects are clearly not part of our model. (In fact, we are not aware of any Monte Carlo computer simulation study that currently addresses this issue.) One known effect is to reduce the magnitude of the mechanical force required to pin a polyelectrolyte in an electric field.[18,19] In our case, this implies that we underestimate by a factor $\approx L/R_g \sim N^{2/5}$ the field intensity needed to overcome the entropic potential barrier. However, we do not expect the basic trapping and detrapping mechanisms to be qualitatively affected by this discrepancy.

We do not consider the electroosmotic flow (EOF), and there is no otherwise imparted flow field inside the device; experimentally, the EOF is apparently quenched by the use of a high ionic strength buffer.[1] We obviously ignore intermolecular interactions as we simulate only one chain at a time, but modest polyelectrolyte concentrations are reported to only slightly affect the mobility and the separation capability of the device.[2] Apart from strict volume exclusion, we disregard interactions between the molecules and the walls of the channel, which are assumed perfectly flat and otherwise neutral. We neglect the bending energy of the macromolecule (however, our monomers already replace roughly one dsDNA persistence length) as well as the electrostatic repulsion between the charged monomers, although both of these aspects could play a role during trapping, when parts of the chain are typically highly bent and quite compact. Finally, we should mention that the bond-fluctuation algorithm implies rather bulky "monomers"; indeed, one effective monomer measures about 20 nm on a side (and, as mentioned previously, represents or replaces ≈150 bp), whereas the width of dsDNA for example is 10 times smaller. The algorithm can thus lead to spurious finite-size effects, especially in the limit of narrow passages such as in the channel gap. This is why we did not attempt to study even stronger confinement using this algorithm. The gap confinement studied here is fully consistent with that investigated experimentally.[1,2]

III. Theory

The mobility of the polyelectrolytes inside the channel is the physical quantity that can be best compared with available experimental data.[1,2] We recall that the electrophoretic mobility μ is defined through

$$v = \mu E \tag{1}$$

where v is the mean velocity of the molecule and $E = \Delta V_0/L$ is the global magnitude of the applied electric field. In a separation device, the mobility is typically a function of both field strength (E) and molecular size (N). In the simulations we obtain μ from v/ϵ and throughout this article we always present the mobility in terms of the dimensionless ratio μ/μ_0, where μ_0 is the mobility of a chain in free solution (no constraint). Note that μ_0 is practically independent of chain length and field strength for free-draining polyelectrolytes; hence, we regard it as a constant.

To explain the observed mobility of DNA in their microdevice, Han et al. have constructed a simple kinetic model,[1] which we briefly review here. They suggest that DNA escapes from the entropic trap by way of small hernias entering the high-field region inside the gap. (Such hernias are seen in Figure 3a,b, for example.) The escape of the whole chain is iniated once a hernia venturing inside the gap reaches a critical distance x_c, at which point the hernia simply pulls the chain through; i.e., it helps the chain overcome the entropic barrier. When a length x of DNA enters the gap longitudinally, the decrease in electrical potential energy is proportional to x^2E, while the increase in entropic free energy is proportional to xT (since conformational entropy is an extensive molecular property). The net free energy change caused by the hernia is thus $\Delta F \sim xT - x^2E$. This function reaches a maximum $\Delta F_{max} \sim T^2/E$, which represents the activation barrier for the escape of the molecule from the trap. This maximum occurs at a critical insertion length

$$x_c \sim T/E \sim 1/\epsilon \tag{2}$$

which can also be regarded as the critical hernia nucleation size (since a hernia reaching that size basically keeps growing). For moderate field intensities, the mean trapping time τ_{trap} can then be written in terms of the corresponding Boltzmann weight as

$$\tau_{trap} = \tau_0 \exp(\Delta F_{max}/k_B T) = \tau_0 \exp(\epsilon_0/\epsilon) \tag{3}$$

where ϵ_0 is independent of field strength and molecular size. The prefactor τ_0 on the other hand may depend on both E and N. According to eq 3, the molecules cannot escape from the trap without the help of an applied field, as the trapping time becomes infinite when the magnitude of the driving electric field vanishes. This is not completely realistic since the molecule could eventually diffuse out of the trap, but it is certainly reasonable over the time scale of our simulations.

Sebastian and Paul have developed a more detailed theory to treat the problem of a long macromolecule crossing a free energy barrier in one dimension.[22] The outcome of their calculations is consistent with the analysis above, and from their results we deduce that τ_0 should be proportional to $1/(N\sqrt{E})$ when escape occurs via hernia nucleation. If the molecule enters the gap head or tail first, then τ_0 should be independent of N, but this process is rare when N becomes large. Note, however, that the model they use implies that all monomers along the chain can simultaneously participate in the nucleation of hernias; hence, that the rate of escape is proportional to N.

The model reviewed here assumes that the hernias enter the gap longitudinaly, i.e., completely extended along the field direction. This may not be realistic when the field is weak since the entropic elasticity of the inserted hernia may exceed the electric forces acting on it, in which case it would retain a random coil conformation. We can easily generalize the model to take this aspect into account. For a contour length s inserted inside the gap, the entropic contribution remains proportional to sT, but the potential energy contribution now becomes proportional to $s^{1+\nu}E$ for a chain that extends over a distance s^ν inside the gap. (We can take

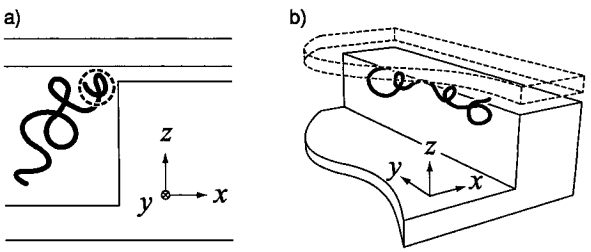

Figure 4. (a) If the molecule does not have the time to deform, only the monomers in the entrance blob close to the gap (represented by dashed circle) determine the escape dynamics; thus, increasing the chain length does not affect the escape process. (b) In this 3D view, we see how the molecule may deform and align itself along the gap axis; many escape blobs can then participate concurrently in the escape of the molecule.

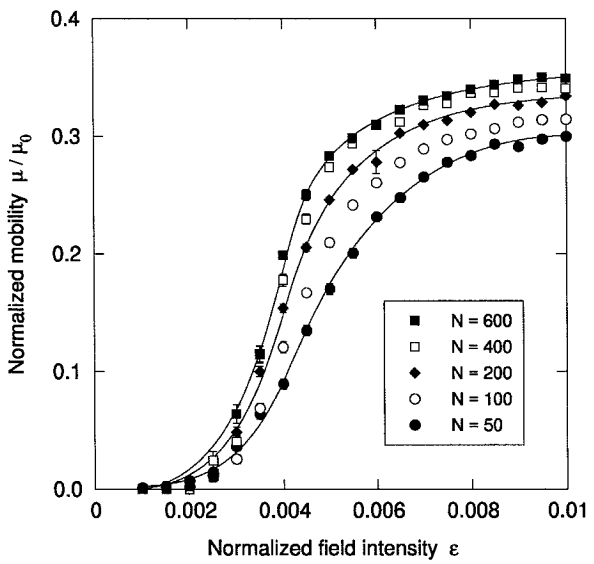

Figure 5. Normalized mobility of a polyelectrolyte in a 3D microchannel as a function of normalized field intensity ϵ, for various molecular sizes N. The plotted values are an average over multiple (10–30) simulations, and error bars represent the standard error on the mean (most are smaller than the size of the points). Solid lines are drawn over the $N = 50$, $N = 200$, and $N = 600$ data to guide the eye.

$\nu = 1$ for an extended chain or $\nu = {}^3/_4$ for a two-dimensional self-avoiding coil.) We therefore write $\Delta F \sim sT - s^{1+\nu}E$, and we find that the critical contour length s_c for the onset of escape satisfies $s_c^{\nu} \sim (T/E)$. Since the span of the inserted coil itself scales as s^{ν}, we have $x_c \sim s_c^{\nu}$, and we recover eq 2 for x_c. Hence, the linear dependence of x_c on $1/\epsilon$ is a robust feature of the system, in the sense that it does not depend on the conformation of the chain inside the gap. On the other hand, these considerations affect the expression for the mean trapping time, since we now obtain a dependence of the form $\tau_{trap} \sim \exp[(\epsilon_0/\epsilon)^{1/\nu}]$ as opposed to eq 3.

IV. Simulation Results

A. Mobility. The mobility of the polyelectrolytes in the microchannel is plotted as a function of the applied electric field in Figure 5. We find that long molecules are faster than shorter ones for practically all field values. Note that the data for small fields ($\epsilon < 0.003$) are not very reliable, as they bear large uncertainties due to very long trapping times. In the region of best separation (around $\epsilon = 0.004$), we find that the mobility increases by about 30% when the chain length is increased by a factor 4, in good agreement with the experimental observations of Han et al.[1] We also note that the shape of the mobility curves qualitatively reproduces that of the experimental ones very well. The separation capability of the device appears to be retained at high fields, which is also consistent with Han's more recent report,[2] although it may be exaggerated in our simulation for reasons we will discuss later. We should recall that, depending on the type of separation one is trying to achieve, the resolution of the device may actually be limited by the diffusion of the molecules inside the device, so that the best separation on the mobility graph does not necessarily correspond to the best resolution regime for an actual separation device (see section IV.E).

B. Molecular Conformation. It follows from the simple theory of trapping and escape reviewed in section III that the fraction of the monomers directly in contact with the well–gap boundary is an important factor in determining the separation capability of the device. Larger molecules escape faster mostly because they expose more monomers to this boundary (along the y direction), favoring multiple hernia nucleations (see Figure 4b), hence increasing the escape probability and therefore the overall electrophoretic mobility. Furthermore, the electric forces deform the molecule during trapping, pressing it against the vertical wall, thus accentuating the difference between small and large molecules. Of course, such deformation along the gap can play a role only if it takes place faster than the escape time of the chain. To investigate this conformational contribution to the separation process, we plot in Figure 6a–c the Cartesian components of the radius of gyration of the polymer (X_g, Y_g, Z_g, with $R_g^2 = X_g^2 + Y_g^2 + Z_g^2$) as a function of the position of the center of mass of the polymer coil inside the channel (mod L), for a field intensity $\epsilon = 0.004$. The graphs are normalized to the values X_{g0}, Y_{g0}, and Z_{g0} obtained for chains in an open channel, i.e., one without constrictions. The radius of gyration of a polymer coil is a highly fluctuating quantity (i.e., $\langle (R_g - \langle R_g \rangle)^2 \rangle \sim \langle R_g^2 \rangle$). Hence, we applied a moving window averaging filter[23] over the raw data to obtain the smooth curves shown in Figure 6; we estimate an uncertainty of 5% for these smoothed curves.

These graphs provide a clear picture of the typical conformations adopted by the molecules as they travel down the channel. At $x = 0$, X_g is large because the molecules have extended while crossing the previous entropic barrier in a slithering motion. This is also clearly observed, for example, in video microscopy movies captured by Han et al.[24] The relative extension of the molecules along the x axis is more important for long chains, although it decreases at some point due to the finite length of the gap. (The two ends of a $N = 600$ molecule can lie in two different wells, and only the middle extended portion of the chain then contributes to the increase in X_g.) At $x = 100$, the molecules leave the narrow gap and undergo rapid compression along x, which can be a consequence of two factors. First, the large gradient of electric field in x at the exit of the gap favors an accumulation of monomers (much like a traffic jam in a region of sudden low velocity). Second, the field lines are diverging in z (see Figure 3) and can thus stretch the chains along that axis, thereby inducing a decrease in X_g. (The plot of Z_g near $x = 100$ shows that

Macromolecules, Vol. 35, No. 12, 2002 Long Polyelectrolytes **4795**

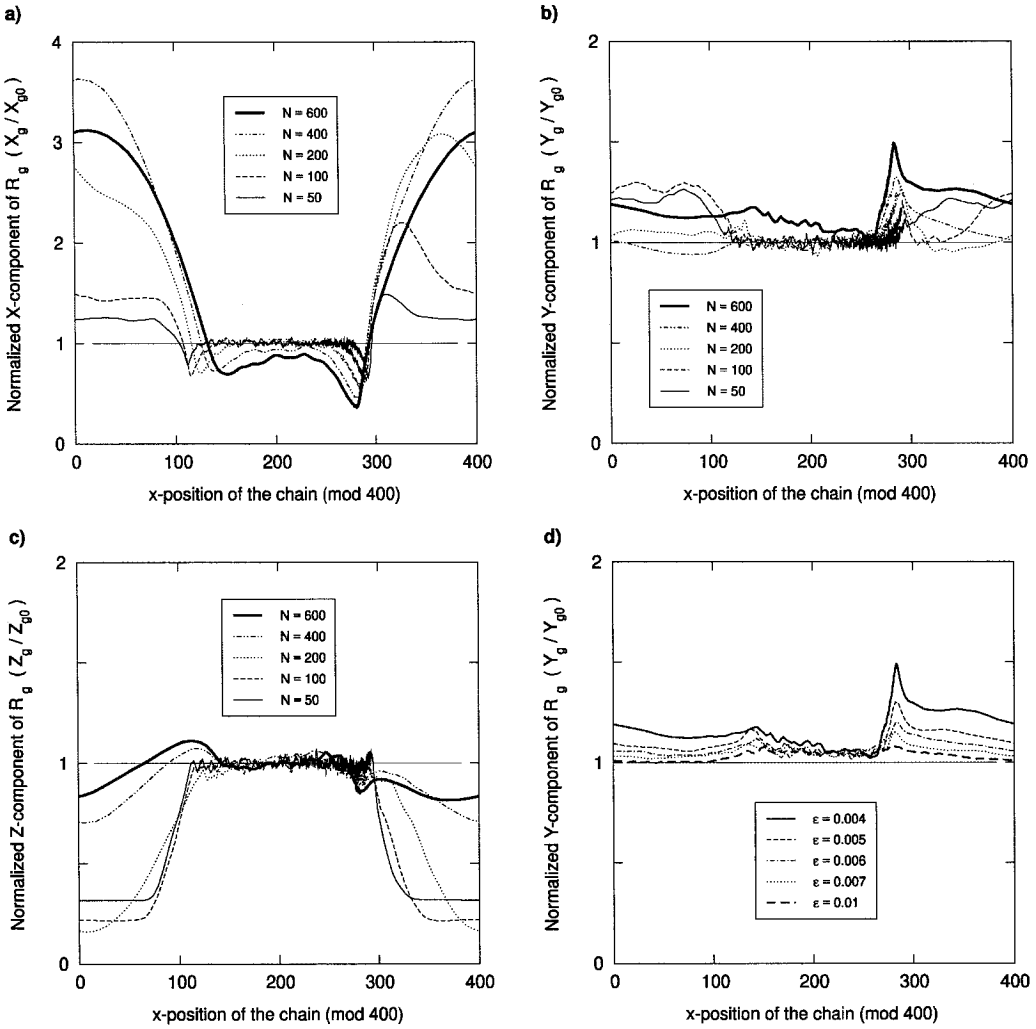

Figure 6. (a), (b), and (c) respectively show the average of the normalized X, Y, and Z component of the radius of gyration R_g as a function of the position (mod $L = 400$) of the center of mass of the polyelectrolyte inside the channel, for a field $\epsilon = 0.004$. The well–gap interface where trapping occurs is located at $x = 300$, and the horizontal line at 1 represents the value for chains in a channel without constrictions. (d) shows another graph for the Y component, but for a single molecular size $N = 600$ and various values of the electric field ϵ. The magnitude of the deformation near the well–gap interface at $x = 300$ is seen to decrease with increasing field strength.

this second process is only significant for the two longest chains.) Further inside the well region, the molecules recover their normal radius of gyration values, except for the $N = 600$ chain which does not have time to relax completely. (For $N = 600$, the top and bottom walls confine the coil slightly and hence may inhibit rotational relaxation modes.)

The actual differentiation of molecular sizes occurs near $x = 300$, as the molecules reach the thin gap through which they must somehow escape. The coils undergo a large compression in the x direction coupled with an important extension along the y direction, as they are pressed against the vertical wall at $x = 300$ (since Z_{g0} is typically larger than the size of the gap). The small dip in the Z_g value at this point for large N indicates that the converging field lines also slightly squeeze large molecules vertically. In Figure 7, we plot the value of Y_g (not normalized) at its peak near the gap entrance as a function of molecular size. For $\epsilon = 0.004$, the size along y scales as $N^{0.75}$ (the scaling law for the size of self-avoiding chain in two dimensions), so the number of monomers available for hernia nucleation also scales as $N^{0.75}$ (since it is just proportional to the length of the coil directly exposed to the gap). The deformation is thus more pronounced for larger molecules. In other words, the molecule adopts the conformation of an "ellipsoidal pancake" near the well–gap interface.

The deformation of the molecule during trapping also depends on the strength of the electric field. One may think that the compression of the molecule against the gap interface (and therefore its extension in y) will increase with field, but this is not so. In fact, we find just the opposite. As the field increases, the probability that any given hernia will actually lead to a complete escape of the molecule also increases, and long molecules simply do not have time to deform before escape is initiated. The situation then resembles Figure 4a. To confirm this, we provide in Figure 6d plots of Y_g for different values of the field strength ϵ. The four curves are similar, but the extension along y near the well–gap interface gradually *fades out* as ϵ rises (and this

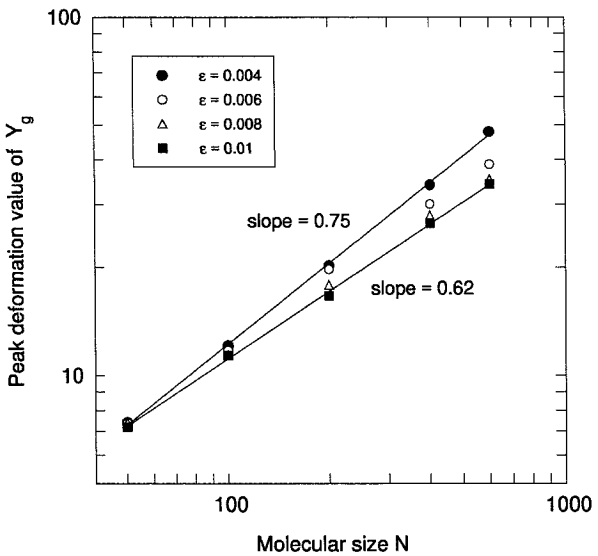

Figure 7. Maximum value of the Y component of the radius of gyration R_g during trapping as a function of molecular size N, for different values of the field ϵ.

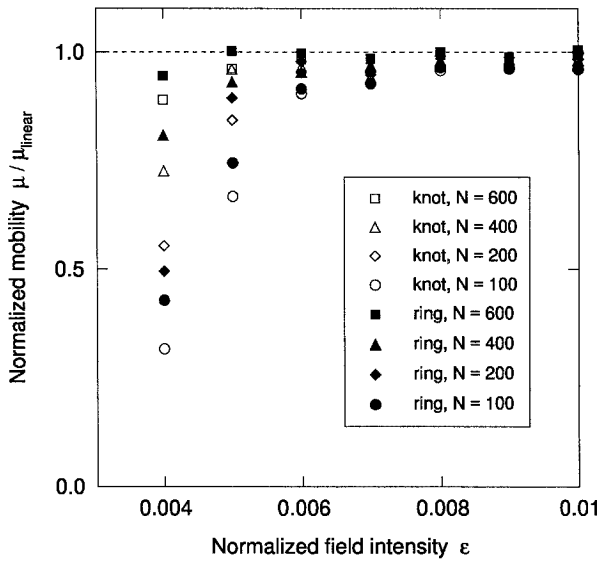

Figure 8. Mobility of ring and trefoil-knotted molecules inside the microfluidic device, normalized to the mobility of a linear chain of the same size. We see an overall downward trend in the mobility as the molecules become more compact. The uncertainties on the plotted values at low field (not shown) are quite large and may account for the crossing of the knot and ring curves for $N = 200$ and $N = 400$.

holds true for the other molecular sizes as well). This effect is also apparent in Figure 7 where the scaling law for the size of the coil gradually returns toward the usual $N^{0.58}$ (for a self-avoiding walk in three-dimensions) as the field increases, indicating that the deformation becomes minimal when the field is very large. On the other hand, we verified that between $\epsilon = 0.001$ and $\epsilon = 0.004$ the field is too weak to induce larger deformations. Hence, there is a tradeoff between the field-driven molecular deformation and the hernia nucleation time: the best separation occurs near $\epsilon = 0.004$, the highest field value for which the average trapping time is at least as long as the deformation time for all molecular sizes N (see section IV.E for more details). This key finding is consistent with the idea that the contact area between the molecule and the well–gap interface plays a determinant role in the separation process. Our results confirm that the size and the deformation of a molecule as a whole control to a large extent its electrophoretic behavior in the microdevice.

C. Topoisomers. As further evidence of the importance of the overall size, shape, and deformation of the molecules in the separation process, we consider topoisomers. By "topoisomer" we mean molecules that have the same number of monomers but different topologies. For example, we can compare the mobility of linear, ring, and trefoil-knotted molecules in the microchannel. Since a change in topology generally implies a change in the overall size R_g of the molecule (rings are smaller than linear chains, and knots are smaller than rings), we expect to see a separation according to topology, the more compact molecules travelling more slowly inside the channel. Indeed, we see in Figure 8 that rings have a smaller mobility than linear chains and that knots, in general, are slower than rings. Moreover, we find that at high fields the topoisomer separation capability vanishes, which is consistent with our assertion that the ratio between the molecular deformation time and the trapping time is a determinant variable in this system.

D. Critical Hernia Nucleation Size. In this section we look at the escape process on a smaller scale, in that we give a measure of the critical insertion length x_c, i.e., the maximum distance a chain can venture inside the gap region without initiating the escape of the whole molecule. We also refer to x_c as the critical hernia nucleation size, since it sets a demarcation between small temporary hernias inside the gap and the ones that continue to grow and eventually lead to the escape of the whole molecule. In fact, this length corresponds to the position of the maximum of the free energy barrier, according to the theory reviewed in section III. The critical length x_c is hardly tractable experimentally but can further validate the theory through the verification of the prediction $x_c \sim 1/E$. Note that the theory also suggests that x_c is independent of the molecular size N, which seems reasonable since hernia nucleation is a local process for long enough chains (for which Z_{g0} is larger than the gap).

To extract the value of x_c from simulations, we periodically record the position of the monomer having the largest x coordinate; we call this monomer the leading monomer, or *leader*, and denote its position by x_{lead}. Small samples of the leading monomer position as a function of time are provided in Figure 9. From these data we determine when the chain is trapped and plot a distribution of the leader's position (mod L) exclusively during trapping. Examples of such distributions are shown in Figure 10. We can describe the tail of the distribution inside the gap (i.e., to the right of the well–gap interface located at $x = 300$) rather well with a number of simple functions, including the exponential $\rho(x_{lead}) = \rho_0 e^{-x_{lead}/x_c}$, where ρ_0 is a normalization factor. We thus extract the value of x_c directly by fitting this function to the data. (We restrict the fit to the middle $^3/_5$ of the points to avoid the slight deviations at the gap entrance and the noisy tail.)

In Figure 11 we show the results of our analysis for all molecular sizes N as a function of $1/\epsilon$. We first observe that for large chains the critical length does exhibit a clear $1/\epsilon$ dependence, as indicated by the

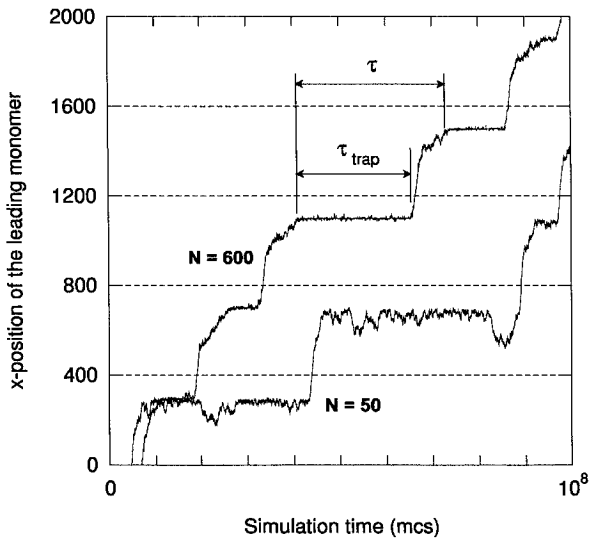

Figure 9. Position of the leading monomer as a function of simulation time (with arbitrary offsets), for two molecular sizes and a field strength of $\epsilon = 0.004$. Labels identify what we define as the trapping time τ_{trap} and the total transit time τ. For the calculation of the critical hernia nucleation size, we only use the data corresponding to trapped configurations. Horizontal dashed lines indicate the periodic boundaries of the channel.

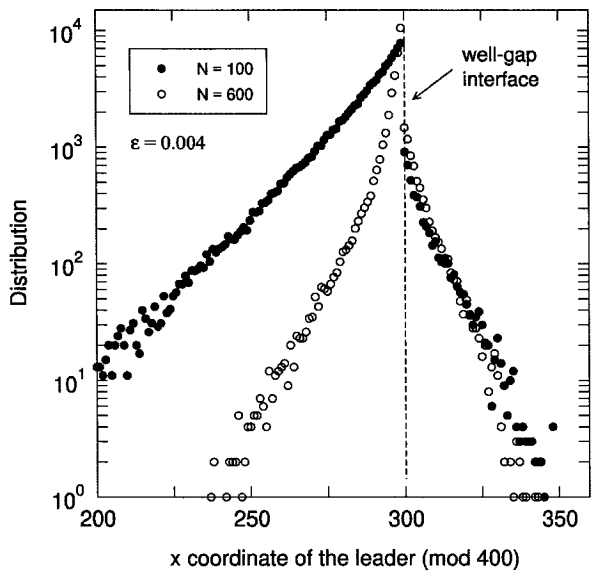

Figure 10. Unnormalized distribution of the position of the leading monomer during trapping events, for two molecular sizes, and $\epsilon = 0.004$. The vertical dashed line indicates the position of the well–gap interface ($x = 300$).

straight line fit over the $N = 600$ data. For the two smallest chains $N = 50$ and $N = 100$, x_c seems to level off at some point, indicating that there is probably a change of regime when there is not enough monomers left in the well to sustain trapping. Another feature apparent in Figure 11 is a slight molecular size dependence, as x_c is slightly larger for the $N = 50$ and $N = 100$ chains. We attribute this size dependence to the fact that small chains more frequently enter the gap head first or tail first, whereas longer chains almost exclusively enter the gap through hernia nucleation. The subtle difference between these two processes is not

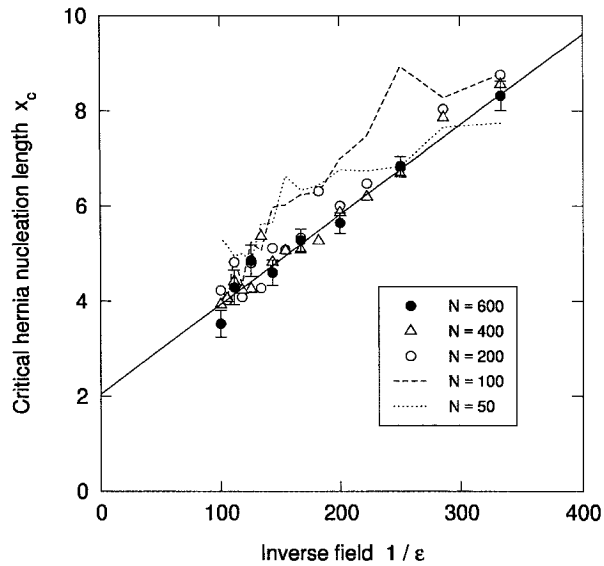

Figure 11. Critical hernia nucleation size x_c as a function of $1/\epsilon$, for five different molecular sizes. Typical error bars, included for the $N = 600$, are calculated using a Monte Carlo regression technique[23] on each point. The solid line is a linear fit for $N = 600$.

captured by the simple free energy model suggested in ref 1, but we verified that for ring molecules, which do not have any dangling ends, this dependence of x_c on N is lost (data not shown). Considering that the ends of a chain have more entropy than other parts of the chain, we do expect the critical length x_c to increase for end insertion because the entropic barrier the polymer has to overcome is then effectively higher.

The position of the leading monomer also provides valuable information about the thermal fluctuations of the center of mass of the molecule during trapping, which are clearly apparent from the distributions at the left of the well–gap interface in Figure 10. On the basis of these distributions, we see that the molecules can backtrack inside the well over an appreciable distance. As a matter of fact, these fluctuations constitute an additional size-separation mechanism favoring higher mobilities for longer chains inside the device. Indeed, smaller molecules carry a smaller total charge and are thus more loosely *bound* to the interface by the electric field. This implies that they can move away from the gap interface and travel backward inside the well after unsuccessfully trying to enter the gap for a while (as seen in Figure 9 for $N = 50$). Consequently, they are more rarely in the vicinity of the well–gap interface, and this contributes to slow them down compared to longer molecules.

E. Trapping Time Statistics. The theory in section III predicts the functional form of the mean trapping time τ_{trap} for the molecules inside the entropic trap array. The trapping time corresponds to the average time the molecules have to wait before their attempts to escape from the trap succeed; it is directly related to the height of the free energy barrier ΔF_{max} for the penetration of the molecule inside the gap region.

For our analysis, we define τ_{trap} as in Figure 9, i.e., as the interval between the first arrival of the leading monomer within $10a$ of the position of the well–gap interface along x and the onset of the escape of the whole molecule, defined as the moment of nucleation of the

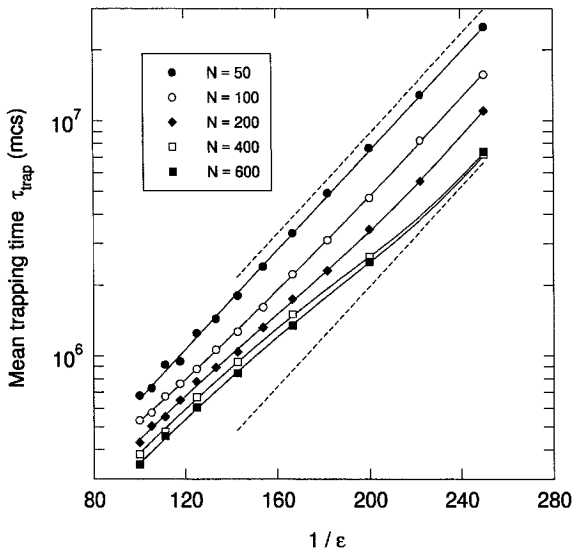

Figure 12. Mean trapping time τ_{trap} as a function of $1/\epsilon$. The dashed lines indicate the slope of the curve for $N = 50$, and solid lines are superimposed on each data set to guide the eye.

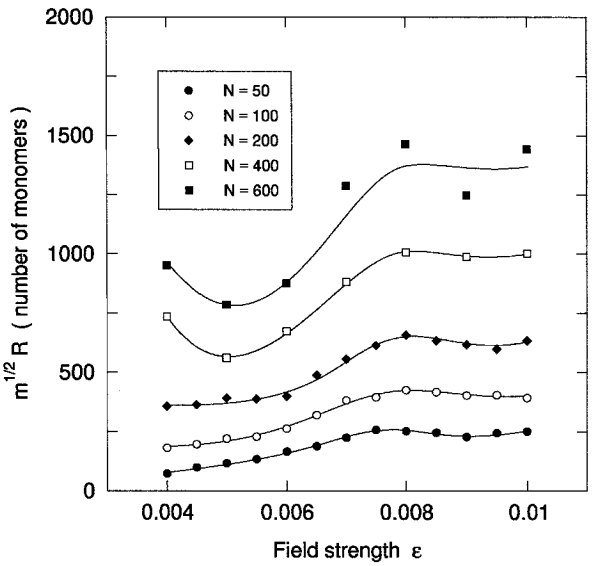

Figure 13. Resolution of the device as a function of the field strength ϵ for different molecular sizes. The values plotted here should be divided by $\sqrt{m}$ to obtain the actual resolution for a channel with m traps. The resolution corresponds to the smallest size difference that can be resolved (measured in number of effective monomers, each of which corresponds to approximately 150 base pairs in the case of dsDNA); the smaller the value, the better the resolution. Solid lines are sketched to guide the eye.

hernia that eventually grows to cross the whole gap region. (We use the threshold $10a$ to compensate for the coarse sampling during the simulation.) In Figure 12 we plot the results for τ_{trap} as a function of $1/\epsilon$, for five different molecular sizes N. We find that for $N = 50$ the data indeed follow the prediction $\tau_{trap} \sim \exp(\epsilon_0/\epsilon)$, as seen from the essentially perfect straight line on the semilog plot. For large molecular sizes, however, the lines exhibit an upward curvature as $1/\epsilon$ decreases, which we explain in terms of our foregoing argument about global molecular deformations. When the field is high, the trapping time becomes very short, so short in fact that molecules do not have time to deform completely before escape is initiated. (The decreased deformation at high fields is shown in Figure 6d.) Hence, long chains tend to behave like shorter ones since only one entrance blob has time to form. The dependence of the mobility on molecular size N thus decreases, and the lines get closer together as at higher fields ϵ in Figure 12.

In fact, the point of departure of the curves from the straigth line in the graph gives a rough estimate of the deformation time τ_d for each molecular size at a given field. We verified that the deformation time estimated in this way is consistent with the approximation $\tau_d(N,\epsilon) \sim R_g/v_{well} \sim R_g/(\mu_0\epsilon) = N^{3/5}/(\mu_0\epsilon)$, where v_{well} is the electrophoretic speed of the molecule inside the well. In other words, the shape and offset of the curves in Figure 12 are controlled by the prefactor τ_0 in eq 3, where τ_0 depends on both the molecular size N and the field strength ϵ. This dependence is different from that derived in ref 22, for example, because of the molecular deformation magnitude and time scale issues. Finally, we also note that in their respective linear portions all the curves in Figure 12 have similar slopes. This is consistent with the Han et al. findings[1] and confirms that ϵ_0 in eq 3 does not depend on the molecular size N. From a fit of the $N = 50$ data we obtain $\epsilon_0 \approx 0.025$.

F. Resolution. From a pratical point of view, and depending on the type of separation one wishes to achieve, the resolution of the separation device might become the limiting factor for reliable detection of the separated species. Thinking in terms of total elution time $t_e(N,\epsilon)$ for the molecules inside the channel (in *finish line mode*, where all molecules travel an equal distance), we can give a measure of the resolution using the ratio of the temporal peak width $w_t(N,\epsilon)$ associated with the population of molecules having a certain molecular size N to the elution time difference between different peaks. Thus, we may express the resolution $R(N,\epsilon)$ as follows:

$$R(N,\epsilon) = \frac{w_t(N,\epsilon)}{\partial t_e/\partial N} \tag{4}$$

Note that according to this definition a decrease in R corresponds to an improvement of the resolution. The value of R also coresponds to the smallest difference in molecular size one can expect to resolve. (Keep in mind, however, that we are here talking about effective monomers which represent, for example, more than 100 base pairs.) It is convenient to rewrite eq 4 in terms of the molecular mean transit time $\tau(N,\epsilon)$ over one period L of the channel, a quantity for which the simulations provide good statistics (given that the molecules visit enough traps, which holds true in our case when $\epsilon \geq 0.004$). Taking $t_e(N,\epsilon) = m\tau(N,\epsilon)$, where m is the number of traps in the device and $\sigma_\tau(N,\epsilon)$ as the standard deviation of τ, and assuming that $w_t = \sigma_\tau\sqrt{m}$ (successive transit times are uncorrelated, so the total variance is the sum of the variance for each trap), we obtain

$$R(N,\epsilon) = \frac{1}{\sqrt{m}}\left(\frac{\sigma_\tau(N,\epsilon)}{\partial\tau(N,\epsilon)/\partial N}\right) \tag{5}$$

In Figure 13 we plot the factor in brackets on the right-hand side of eq 5 as a function of field for different molecular sizes. We find that the optimal resolution

Macromolecules, Vol. 35, No. 12, 2002 Long Polyelectrolytes **4799**

occurs at low field. Only for the two longest chains do we see a shallow minimum near $\epsilon = 0.005$; for the three other chain lengths, we can only say that the optimal resolution lies below $\epsilon = 0.004$. The resolution generally worsens as the field increases but levels off for $\epsilon > 0.008$. Our graph indicates that the value of $\sqrt{mR}$ for molecules with $N = 100$, corresponding roughly to 15 kbp, lies between 165 and 430 bond-fluctuation monomers, i.e., between 25 and 65 kbp. This is consistent with published experimental data[2] from which we can estimate $\sqrt{mR} \approx 50$ kbp for this molecular size in a channel of $m = 3750$ traps. Along those lines, our simulations predict that for molecular sizes of $N = 600$, or nearly 100 kbp, a 1 kbp resolution is achievable with about 15 000 traps.

V. Discussion

The first point we must address is the correspondence between the simulations and the real microchannel device of Han et al.[1,2] As demonstrated throughout the Results section, our simulations reproduce what is found experimentally: an increase in mobility with molecular size, the overall shape of the mobility curves, the simple dependence of the trapping time and the critical hernia nucleation size on the inverse of the field strength, and an optimal resolution near the low field limit of operation. In addition, simulations allowed us to study microscopic details of the molecular conformations, the trapping events, and the escape processes. Such details, not normally accessible experimentally, clarify the fundamental mechanisms behind this first microfluidic separation system based entirely on entropic effects. We have not, however, compared simulation and experimental results on a strictly quantitative basis. Such a correspondence is generally difficult to establish in Monte Carlo work and in our work in particular because of a discrepancy in the values of the electric field strength. Case in point, if we take $q \approx 300e$ (DNA carries two electronic charge per base pair, and one effective monomer represents in very coarse terms 150 base pairs), $a \approx 20$ nm, and $T \approx 300$ K, we find that $\epsilon = 0.005$ corresponds to a global electric field of $E = \Delta V_0/L \approx 20$ V/m, whereas the typical field values in experiments are over 2000 V/m. Three factors can account for this. First, we do not include counterions in our simulations, and thus we do not account for the increased local friction they exert locally on the polyelectrolyte (although the free-draining property of the coil, a consequence of this local friction, is preserved by our Monte Carlo approach). Second, as pointed out in section II.C, the force needed to mechanically pin the polyelectrolyte in the real device is reduced by a factor $\sim N^{2/5}$; hence, the electric force needed to overcome the steric barrier is underestimated by the same factor. Third, the experiments are performed at high ionic strength;[1,2] hence, counterion condensation[25] may come into play, reducing the effective charge of the dsDNA strand. All of these effects suggest that we underestimate the electric field strength in the simulations. Note also that any electroosmotic flow in the device (although reportedly quenched[2]) would reduce the speed of the DNA molecules and demand a stronger field. Despite the offset introduced in our simulations by omitting these effects, our findings remain qualitatively sound.

Our simulation results uphold the idea that the main separation mechanism in the device relies on the size *and* the deformation of the molecule as a whole. Longer molecules move faster through the microchannel simply because they have more opportunities to escape from the entropic traps. We established that the scaling law for the size of the chain along the well–gap interface during trapping is $N^{0.75}$ in the best resolution regime. This lies midway between the assumption of Han et al.[1] for the contact area between the coil and the gap (based on the scaling law for the size of a self-avoiding walk in three dimensions, i.e., $N^{0.58}$) and that of Sebastian's model[22] (in which the number of monomers available for hernia nucleation scales as N^1). We also found that the deformation of the molecule depends on the magnitude of the driving field. When the field is too weak, it cannot deform the coil substantially, and when it is too strong, molecules escape from the trap swiftly and do not have time to deform. Current models fail to take these dynamical phenomena into account, although such effects appear important for the future design and optimization of microdevices that manipulate macromolecules. On the basis of our findings for the mobility of topoisomers, we also predict that the device of Han et al. would be able to fractionate not only rings and simple knots but also a variety of other topological arrangements, such as branched polymers and catenane structures (interlocked rings), provided that they differ in size or in deformability.

As explained at the end of section IV.D, the thermal motion of the center of mass of the molecule inside the well region serves as an additional separation mechanism favoring a higher mobility for longer chains. In fact, this second mechanism is probably the only one remaining at high field, when the contributions of the overall shape and deformation have already vanished (as argued from the topoisomer results above). The magnitude of the molecular-scale thermal motion decreases with increasing field strength. Consider for example a simplified picture in which the whole molecule is represented by a point particle with charge Nq. Taking x_g as the position of the well–gap interface, the probability distribution of the position of this particle for $x < x_g$ would follow a probability density $\sim e^{-N\epsilon(x_g - x)/a}$ (e.g., the left side of the distribution in Figure 10). The magnitude of the thermal fluctuations is then embodied in the factor $1/N\epsilon$, so for a 100-fold increase in ϵ the extent of the fluctuations is reduced 100-fold. Hence, in light of the fact that the real field strength is about 2 orders of magnitude larger than the simulation field strength, this second separation mechanism is probably irrelevant for the current experimental conditions. At such high fields the molecules remain in contact with the well–gap interface practically all the time during trapping, even in what corresponds to our "low-field" regime. Fluorescence video microscopy sequences captured by Han et al.,[24] in which individual dsDNA molecules are never seen moving against the field inside the wells, support this claim.

From the simulation data we extracted the mean trapping time τ_{trap} and the critical hernia nucleation size x_c, two quantities expected to depend in a simple way on $1/\epsilon$ according to a simple free energy model. We find good agreement with this prediction for both τ_{trap} (provided we understand the deviations caused by long deformation time scales) and x_c (given that we acknowledge the limit imposed by a finite chain length). According to our comment at the end of section III, the linear dependence of $\log(\tau_{trap})$ on $1/\epsilon$ identified in Figure 12 suggests that the hernias are indeed well extended

along the field direction inside the gap for $\epsilon \geq 0.004$.

Last, we found that the resolution of the device is generally optimal at low field and that after deteriorating over midrange field strengths, it levels off around $\epsilon = 0.008$. This is interesting at first sight because it suggests that high-field—thus high-speed—separation may be possible without loss of resolution in this microdevice. But we recall that the good resolution calculated at high field stems from the separation caused by the global thermal motion of the center of mass of the molecule, an effect most likely absent in experiments. The plateau in R at high fields may therefore only occur in the simulation context. On the other hand, the trend observed at low field agrees with the general experimental observation that as the field decreases, the improved separation of molecular sizes wins out over the increased dispersion due to longer trapping time,[2] leading to better resolution.

We are currently using our Monte Carlo simulations to explore new regimes of operations and optimize the geometry of this entropic separation device using the information we have gathered on the dominant physical mechanisms at play.

Acknowledgment. We acknowledge the support of the Natural Science and Engineering Research Council of Canada for a Research Grant to GWS and scholarships to F.T. and the University of Ottawa for scholarships to F.T. In addition, we acknowledge J. Han, S. W.Turner, and H. G. Craighead for useful discussions about their microdevice experiments.

References and Notes

(1) Han, J.; Turner, S. W.; Craighead, H. G. *Phys. Rev. Lett.* **1999**, *83*, 1688.
(2) Han, J.; Craighead, H. G. *Science* **2000**, *288*, 1026.
(3) Volkmuth, T. D. W. D.; Wu, M. C.; Austin, R. H.; Szabo, A. *Phys. Rev. Lett.* **1994**, *72*, 2117.
(4) Chou, C.-F.; Austin, R. H.; Bakajin, O.; Tegenfeldt, J. O.; Castelino, J. A.; Chan, S. S.; Cox, E. C.; Craighead, H.; Darnton, N.; Duke, T.; et al. *Electrophoresis* **2000**, *21*, 81.
(5) Turner, S. W.; Perez, A. M.; Lopez, A.; Craighead, H. G. *J. Vac. Sci. Technol. B* **1998**, *16*, 3835.
(6) Ertaş, D. *Phys. Rev. Lett.* **1998**, *80*, 1548.
(7) Duke, T. A. J.; Austin, R. H. *Phys. Rev. Lett.* **1998**, *80*, 1552.
(8) Derényi, I.; Astumian, R. D. *Phys. Rev. E* **1998**, *58*, 7781.
(9) Chou, C.-F.; Bakajin, O.; Turner, S. W. P.; Duke, T. A. J.; Chan, S. S.; Cox, E. C.; Craighead, H. G.; Austin, R. H. *Proc. Natl. Acad. Sci. U.S.A.* **1999**, *96*, 13762.
(10) Hammond, R. W.; Bader, J. S.; Henck, S. A.; Deem, M. W.; McDermott, G. A.; Bustillo, J. M.; Rothberg, J. M. *Electrophoresis* **2000**, *21*, 74.
(11) van Oudenaarden, A.; Boxer, S. G. *Science* **1999**, *285*, 1046.
(12) Griess, G. A.; Rogers, E.; Serwer, P. *Electrophoresis* **2001**, *22*, 981.
(13) Chou, H.-P.; Spence, C.; Scherer, A.; Quake, S. *Proc. Natl. Acad. Sci. U.S.A.* **1999**, 11.
(14) Slater, G. W.; Guo, H. L.; Nixon, G. I. *Phys. Rev. Lett.* **1997**, *78*, 1170.
(15) Carmesin, I.; Kremer, K. *Macromolecules* **1988**, *21*, 2819.
(16) Deutsch, H. P.; Binder, K. *J. Chem. Phys.* **1991**, *94*, 2294.
(17) Allen, M. P.; Tildesley, D. J. *Computer Simulations of Liquids*; Oxford University Press: New York, 1990.
(18) Long, D.; Viovy, J.-L.; Ajdari, A. *Biopolymers* **1996**, *39*, 755.
(19) Long, D.; Viovy, J.-L.; Ajdari, A. *Phys. Rev. Lett.* **1996**, *76*, 3858.
(20) Long, D.; Ajdari, A. *Electrophoresis* **1996**, *17*, 1161.
(21) Long, D.; Dobrynin, A. V.; Rubenstein, M.; Ajdari, A. *J. Chem. Phys.* **1998**, *108*, 1234.
(22) Sebastian, K. L.; Paul, A. K. R. *Phys. Rev. E* **2000**, *62*, 927.
(23) Press, W. H.; et al. *Numerical Recipes in C*; Cambridge University Press: New York, 1992; p 650.
(24) http://www.hgc.cornell.edu/biofab/entropic.htm, 1999.
(25) Manning, G. S. *Q. Rev. Biophys.* **1978**, *11*, 179.

MA0110406

3

Strategies for the separation of polyelectrolytes based on non-linear dynamics and entropic ratchets in a simple microfluidic device

F Tessier, GW Slater. *Applied Physics A* **75**, 285 (2002)

Appl. Phys. A 75, 285–291 (2002)
DOI: 10.1007/s003390201337

Applied Physics A
Materials Science & Processing

F. TESSIER
G.W. SLATER✉

Strategies for the separation of polyelectrolytes based on non-linear dynamics and entropic ratchets in a simple microfluidic device

Department of Physics, University of Ottawa, 150 Louis-Pasteur, Ottawa, Ontario, K1N 6N5, Canada

Received: 16 November 2001/Accepted: 11 February 2002
Published online: 22 April 2002 •

ABSTRACT We perform Monte Carlo simulations of an existing electrophoretic microchannel device used for the size separation of large DNA fragments. This device is normally operated with a constant (dc) driving field. In contrast, we consider the case of a varying (ac) driving field, in the zero-frequency limit. We find that a time-asymmetric pulse can yield interesting migration regimes, in particular bidirectional transport for different molecular sizes. We also study a spatially asymmetric version of the device and show that it can rectify unbiased but non-equilibrium molecular motion, in agreement with previous predictions for entropic ratchets. Finally, at finite frequency we uncover a resonance for the molecular velocity in the channel which could lead to improved performance.

PACS 87.15.Tt; 87.15.Aa; 87.14.Gg

1 Introduction

Experimental and theoretical enthusiasm surrounding ratchets has proliferated rapidly over the last several years. It is generally accepted that ratchets are a useful model description of some molecular motors [1–3], and that they might become useful for manipulating and sorting molecules or particles on the microscopic scale [4–15]. Most investigations on ratchets generally deal with point-like particles, whereas we consider the application of ratchet ideas to the size separation of flexible macromolecules. In the case of point-like or rigid particles, the non-linearities required to obtain ratchet effects must come from an external potential with acceptable properties. Slater et al. [16] suggested in a previous article that in the case of flexible macromolecules, which possess conformational entropy, this potential could be provided by static molecular-size steric constrictions since the conformational entropy of the molecule then becomes position-dependent. Upon entering strictures, the polymer experiences an opposing entropic force (because its internal entropy decreases), which corresponds to an effective potential barrier. The highly non-linear entropic potential thus imposed by geometric means can be used as a basis to construct a ratchet. We call such devices *entropic ratchets* since conformational entropy is necessary for them to function (i.e. point-like particles would not be very affected in such devices). The goal of this article is to explore to what extent similar ratchet effects can improve the performance of some emerging electrophoretic tools. Work on ratchets often remains rather theoretical; in contrast, we propose a practical study based on an existing device.

We focus our attention on the microfluidic channel fabricated by Han et al. [17, 18]. The latter consists of a periodic array of deep and shallow regions etched on a silicon chip. Shallow regions act as entropic barriers to molecular drift and long polyelectrolytes – double-stranded DNA fragments – electrophoresed through this structure by a constant (dc) electric field become sorted by fragment size: long fragments migrate faster than short ones. Note that this elution order is rather counterintuitive, as one would normally expect small molecules to migrate faster through a sieving system made of small openings. The reverse order found here is a non-trivial consequence of the way deformable polymers move across a potential barrier such as a constriction or a hole in a thin wall, a hot topic of theoretical investigation at this time [19–23]. This device is different from traditional electrophoresis sieving media in that it relies exclusively on molecular-scale entropic effects rather than sub-molecular sieving mechanisms.

The device described above is essentially a symmetric version of the funnel system described by Slater et al. [16]. In the funnel case, separation occurs in a time-symmetric pulsed (ac) driving field, as the asymmetry of the channel rectifies the molecular drift. Moreover, molecules of different size can be forced to move in opposite directions by imposing a small bias on the ac pulse. In the microchannel of Han et al., separation is achieved in the dc regime and does not rely on asymmetries or ratchet modes. What we investigate in the current article are the characteristics of this device under various ac driving field conditions. In particular, we study whether strategies based on ratchet-like ideas can lead to increased performance. Since the device has already been built, our findings can readily be tested ex-

✉ Fax: +613-562-5190, E-mail: gslater@science.uottawa.ca

perimentally. In other words, it would be relatively easy to use the current device in the various ac regimes proposed here.

In what follows, we introduce our computational model and our general approach. We then review the simulation results that will form the basis of what we develop in this article. Next we investigate the influence of time asymmetry and spatial asymmetry on the performance of the device, in the zero-frequency limit. Finally, we also study the case of a finite-frequency ac modulation added to a dc driving electric field.

2 Method

We model the behavior of macromolecules inside this microchannel with computer simulations based on the bond-fluctuation (BF) algorithm, a well-known Monte Carlo lattice method for polymer simulations [24, 25]. A side view of the simulation environment is presented in Fig. 1. We construct the macromolecule from N cubic monomers of side a, and we restrict bond lengths and lattice site occupancy to enforce self-avoidance of the polymer chain. We model the interaction between the charged molecule and the driving electric field by adding a charge q to each monomer and associating an appropriate electrostatic potential value to each lattice site. The field lines are realistic in that they curve to follow the non-conducting channel walls. Taking V as the global potential difference applied across the channel period of length L, and k_BT as the unit of thermal energy, we define a dimensionless measure of the field strength $\varepsilon = aqV/Lk_BT$. Monomers attempt to move one at a time in discrete steps by one lattice spacing following a Metropolis test of the change in electrostatic energy. The elementary time unit is given by one Monte Carlo step (mcs), defined as N trial moves. The speed, $v(\varepsilon, N)$, of the molecules and their electrophoretic mobility, $\mu(\varepsilon, N) = v(\varepsilon, N)/\varepsilon$, are the basic quantities we use to assess the separation capability of the device. We denote by μ_0 the mobility of the molecules in free solution (in a channel without constrictions), which is independent of field strength and molecular size.

In another article [19], we describe our technique in more detail and report simulation results for the microchannel in the dc regime, which are in excellent agreement with experimental data published by Han et al. [17, 18]. Investigating the case of an ac driving field via direct Monte Carlo simulation is in our case not practical because the parameter space is too large: in addition to the molecular size and the global field strength, we must consider the pulse frequency, its shape and its amplitude. However, in the limit of low frequencies we can build from our dc results: we fit them to obtain analytical expressions for $\mu(\varepsilon, N)$, which we then combine to express the behavior of the system in the ac regime, in the zero-frequency limit. Only when the pulse frequency approaches other characteristic frequencies of the system (for example, $1/\overline{\tau}$, where $\overline{\tau}$ is the mean trapping time of the molecule near the entrance of the shallow region) do we need to perform explicit simulations. An added benefit of this approach is that it clearly distinguishes effects due to non-linearities in the system's response (e.g. ratchet motion) from other frequency-induced effect (e.g. resonance).

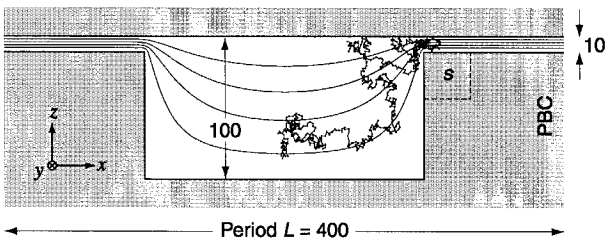

FIGURE 1 A two-dimensional side view of the channel structure used for the simulation. The dimensions are given in terms of the lattice spacing, a. Periodic boundary conditions (PBC) are imposed along x so as to form a periodic array of narrow and deep regions. The driving electric field lines and a sample $N = 600$ molecule are also shown. The *square region* labelled s can be removed to create an asymmetric channel

3 dc simulation results

Simulations of the device in the dc regime are reported and discussed in another article [19]. In Fig. 2 we recall the results for the normalized mobility, $\mu(\varepsilon, N)/\mu_0$, which are consistent with the experimental observation that mobility increases with molecular size. Han et al. suggested a phenomenological model for the mobility of the molecules [17]. Taking $\overline{\tau}$ as the mean trapping time at the entrance of the narrow gap and t_{tr} as the mean time it takes to travel over one period, L, of the channel (in the absence of trapping), they wrote the intuitive relationship as follows:

$$\frac{\mu(\varepsilon, N)}{\mu_0} \sim \frac{1}{1+\overline{\tau}/t_{tr}} . \tag{1}$$

Obviously, the travel time $t_{tr} = L/v = L/\mu_0\varepsilon \sim 1/\varepsilon$ for simple electrophoretic drift. As for the trapping time, Han et al.

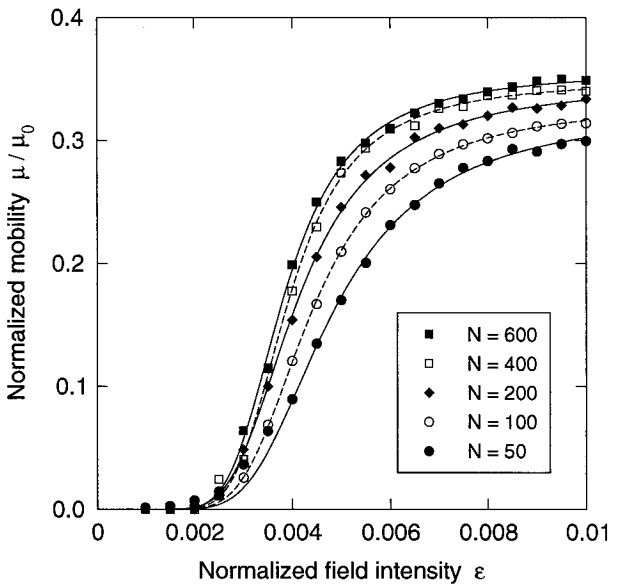

FIGURE 2 Mobility of macromolecules in the symmetric channel as a function of the global applied field, in the dc regime. Long molecules migrate faster than short ones. *Solid and dashed lines* are fits of (2). Uncertainty in the simulation data points is typically covered by the symbol size

derived the approximate relation $\overline{\tau}(\varepsilon, N) \approx \overline{\tau}_0(N)e^{-\kappa/\varepsilon}$ based on entropic trapping arguments. Consequently, we choose to fit our dc mobility simulation data with a function of the form

$$\frac{\mu(\varepsilon, N)}{\mu_0} = \frac{\alpha(N)}{1+\beta(N)\varepsilon e^{\kappa(N)/\varepsilon}} . \tag{2}$$

We numerically fit the mobility curves according to (2), and for each molecular size, N, we extract the coefficients $\alpha(N)$, $\beta(N)$, and $\kappa(N)$. The results of these fits are shown as continuous curves in Fig. 2. In contrast with (1) we find that it is necessary to let the coefficients $\alpha(N)$ and $\kappa(N)$ depend on N in order to obtain reliable fits that match our data closely over the range of fields studied (this dependence is very slight: α and κ vary by less than 1% between $N = 50$ and $N = 600$). We recall that our objective here is to obtain expressions for our data with which we may work analytically. We could have chosen any suitable functional form, our particular choice of (2) being motivated only by its kinship with (1). Note that (2) is only valid up to a certain field strength (in our case up to $\varepsilon \approx 0.01$), since the function eventually decreases at high field, whereas in reality the mobility must plateau. We also point out that our fits do not follow all data points very well for $\varepsilon < 0.0035$ (perhaps because of the large molecular deformations during trapping at low field); therefore we do not study such low field values in the analysis that follows.

4 Temporal asymmetry ratchet

The curves in Fig. 2 show that the velocity of the molecules inside the channel does not increase linearly with field strength (in which case the mobility would be constant). This implies that we can operate the device in a ratchet mode in which we can impart net motion to the molecules with a null time-averaged force. Consider an applied field of the type used in zero-integrated-field electrophoresis (ZIFE) [16, 26, 27]: periodically, a field of strength $\varepsilon_1 > 0$ and duration t_1 is followed by a field of strength $\varepsilon_2 = -r_\varepsilon \varepsilon_1$ and duration $t_2 = t_1/r_\varepsilon$, where $0 < r_\varepsilon < 1$. Such a pulsed field is depicted in Fig. 3a. We verify that the net applied field $\varepsilon_{\text{net}} = (\varepsilon_1 t_1 + \varepsilon_2 t_2)/(t_1 + t_2)$ indeed vanishes.

We can resort to (2) to calculate the velocity of the molecules under such conditions, in the limit of long t_1 and t_2. Using indices 1 and 2 to refer to the first and second part of the pulse, respectively, and realizing that $\mu(\varepsilon, N) = \mu(-\varepsilon, N)$ owing to the symmetry of the channel, we write the velocity of the molecules in the ratchet mode as follows:

$$\begin{aligned} v_r(\varepsilon_1, N, r_\varepsilon) &= \frac{v_1 t_1 + v_2 t_2}{t_1 + t_2} \\ &= \frac{\mu(\varepsilon_1, N)\varepsilon_1 t_1 + \mu(\varepsilon_2, N)\varepsilon_2 t_2}{t_1 + t_2} \\ &= \frac{\varepsilon_1}{1 + 1/r_\varepsilon}\left[\mu(\varepsilon_1, N) - \mu(\varepsilon_1 r_\varepsilon, N)\right] . \end{aligned} \tag{3}$$

In Fig. 4 we plot v_r as a function of r_ε for $\varepsilon_1 = 0.008$ and three values of N. In all our graphs we normalize v_r with respect to $v_0 = 2 \times 10^{-5}$a/mcs, which is a typical velocity of the molecules in the best dc separation region around $\varepsilon = 0.004$. We first observe that the molecules indeed acquire a significant velocity under zero net force and that $v = 0$ when $r_\varepsilon = 1$, as required by symmetry. But the most striking feature of Fig. 4 is that the elution order of the different molecular sizes, or bands, can be reversed compared to the dc case. The exact form of the crossing of the curves in Fig. 4 is not necessar-

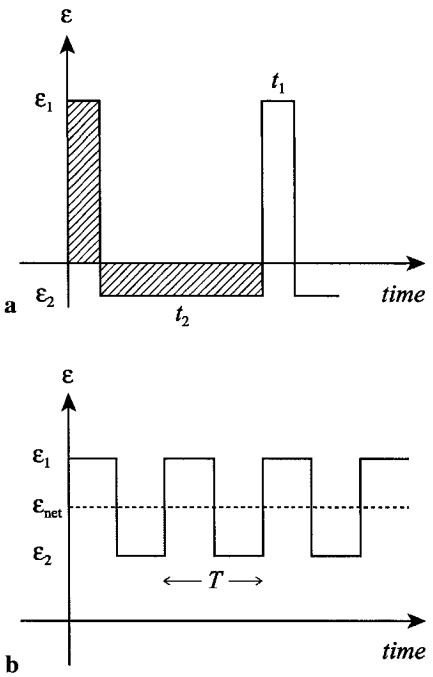

FIGURE 3 **a** The electric field pulse we consider for our time-asymmetric ratchets; in the unbiased (ZIFE) version shown here, the two *hatched regions* have equal area and the mean applied field vanishes. **b** The ac modulation we use to study finite frequency resonance effects

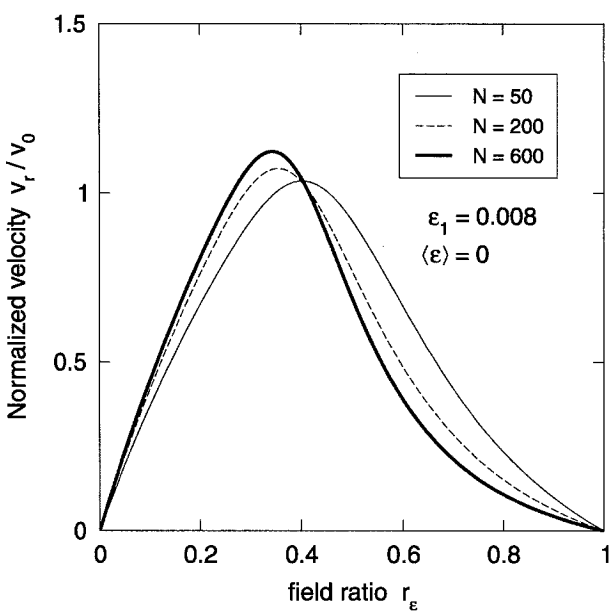

FIGURE 4 Velocity of macromolecules in a symmetric channel with a ZIFE driving field pulse (in the zero-frequency limit), as a function of the field ratio, r_ε, for $\varepsilon_1 = 0.008$. The normalization velocity, $v_0 = 2 \times 10^{-5}$a/mcs, represents the typical velocity of molecules in the dc regime around $\varepsilon = 0.004$

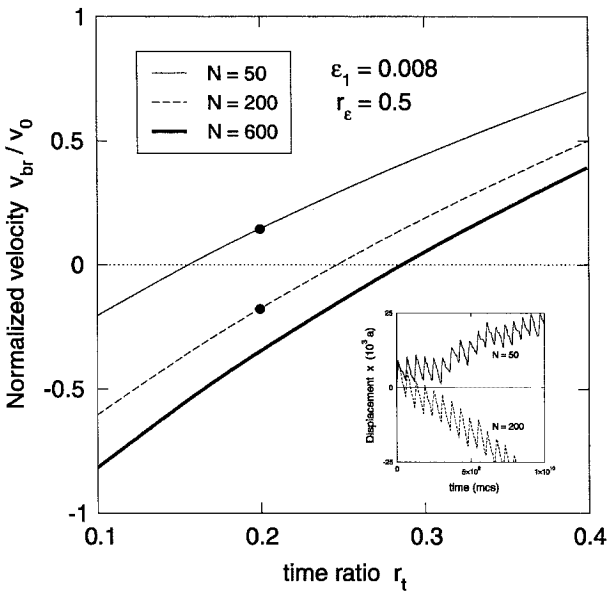

FIGURE 5 Normalized velocity of the macromolecules in a symmetric channel and a biased ratchet driving field, as a function of r_t, for $\varepsilon_1 = 0.008$ and $r_\varepsilon = 0.5$. The *inset*, showing the actual displacement of molecules of sizes 50 and 200 as a function of time during an explicit low-frequency simulation with $r_t = 0.2$ (corresponding to the *black dots* in the main figure), confirms bidirectional transport

ily realistic (since it occurs in a region where the fits may not be entirely accurate), but the reversal itself is sound. Indeed, a quick inspection of (3) reveals that the order of the bands near $r_\varepsilon = 1$ is set by the sign of $\partial^2\mu/\partial N\partial\varepsilon|_{\varepsilon=\varepsilon_1}$, which is negative when $\varepsilon_1 = 0.008$ (see Fig. 2); in the limit $r_\varepsilon \to 0$ it is simply given by the sign of $\partial\mu/\partial N|_{\varepsilon=\varepsilon_1}$, which is positive in our case.

This inversion is most interesting, as we can exploit it in the following way: Suppose we bias the ZIFE pulse slightly in the negative direction (the direction of $\varepsilon_2 < 0$). This bias will reduce the net drift of the molecules, and we therefore expect the curves in Fig. 4 to shift down vertically. Since the dc electrophoretic drift is more important for large molecules than for small ones, the curves will remain separated and will cross zero at different points. Hence the net drift direction will depend on molecular size. One way to impose such a bias is to modify the original ZIFE pulse to take longer strides in the direction of ε_2. Defining a new ratio $r_t = t_1/t_2$ and following a similar derivation as in (3), we obtain an expression for the velocity of the molecules in the biased ratchet:

$$v_{br}(\varepsilon_1, N, r_\varepsilon, r_t) = \frac{\varepsilon_1 r_t}{1+r_t}\left[\mu(\varepsilon_1, N) - \frac{r_\varepsilon}{r_t}\mu(r_\varepsilon\varepsilon_1, N)\right] . \quad (4)$$

In Fig. 5 we plot v_{br} as a function of r_t, for $\varepsilon_1 = 0.008$, $r_\varepsilon = 0.5$, and three values of the molecular size, N. We find that for an appropriate choice of r_t the $N = 50$ and $N = 200$ molecules, for example, move in opposite directions (see figure inset). More significantly, it becomes possible to elute the different bands one by one by sweeping across a range of r_t values during a separation, a feature that may dramatically improve the separation capability of the device especially if the latter is used for preparative electrophoresis. There are of course other ways to impose a bias on the system, such as adding a dc component to the original pulse or alternating between a ratchet pulse and a dc field; in those two cases we can also find a region of parameter space for which we obtain bidirectional transport.

5 Spatial asymmetry ratchet

In the previous section we described a ratchet system based on a symmetric channel and an asymmetric driving electric field. Conversely, we can obtain ratchet motion in an asymmetric device with a symmetric pulse. Consider again the channel in Fig. 1, in which we remove the square region labelled s to create a step. It should then be easier for the molecules to travel in the $+x$ direction compared to the $-x$ direction; hence they should acquire a net positive velocity under a symmetric ac driving field. This steric ratchet is then similar to the asymmetric funnel proposed by Slater et al. in their study of self-modulating entropic ratchets [16].

We use the same technique as in Sect. 3 for our analysis: we extract dc mobility values from simulations in both the positive and negative directions, we fit the data according to (2) and then we combine the resulting functions to obtain the ac characteristics of the device in the zero-frequency limit. In Fig. 6 we show some sample dc mobility curves and the corresponding fit for the two drift directions. (Note that the mobility is higher in the negative direction compared to the symmetric channel case because the dent, s, in the channel wall increases the field strength everywhere in the deep region.) As before, we will not consider field values $\varepsilon < 0.0035$, since our fits are not as reliable in this region. The expression for the net velocity of the molecules in a square driving field

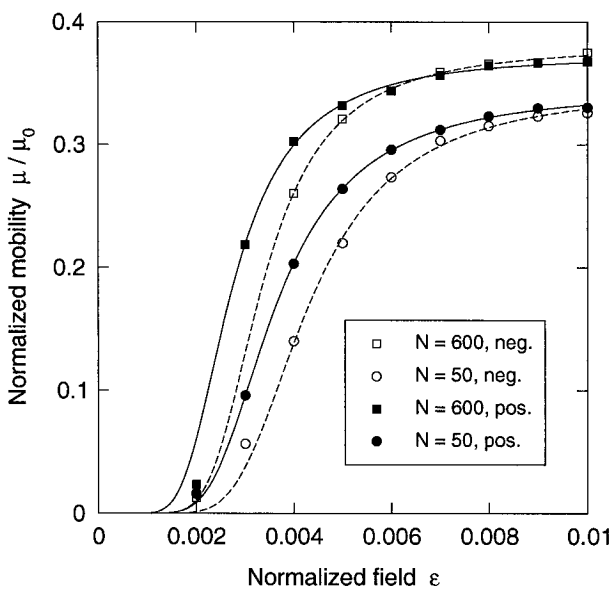

FIGURE 6 Mobility of macromolecules in an asymmetric channel as a function of the global applied field, in the dc regime. *Solid and open symbols* represent the positive and negative direction respectively. *Solid and dashed lines* are fits of the data according to (2). Uncertainty in the simulation data points is typically covered by the symbol size

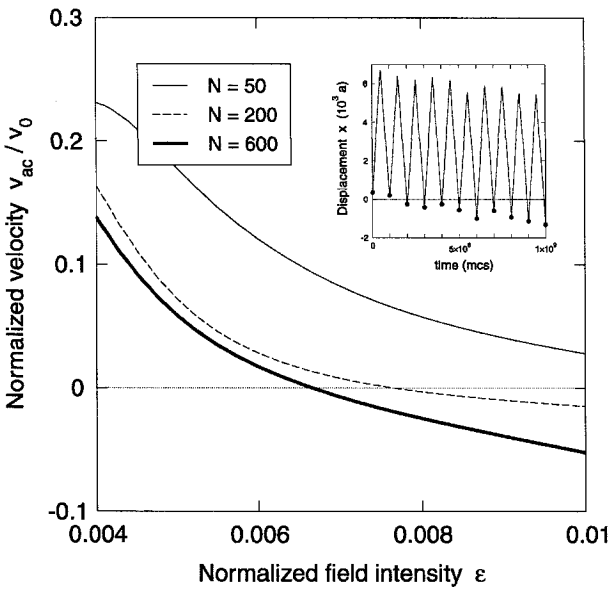

FIGURE 7 Velocity of macromolecules in an asymmetric channel as a function of the global applied field, in the ac regime (*square pulse*), in the zero-frequency limit. The results are normalized to $v_0 = 2 \times 10^{-5}$a/mcs to facilitate comparison. The explicit low-frequency simulation data in the *inset* confirms that the displacement of an $N = 600$ molecule indeed becomes slightly negative at high field intensity

pulse in the zero-frequency limit is calculated as in (3). Letting μ_p and μ_n represent the mobility in the positive and negative directions respectively, we simply obtain

$$v_{ac}(\varepsilon, N) = \frac{\varepsilon}{2}\left[\mu_p(\varepsilon, N) - \mu_n(\varepsilon, N)\right] . \tag{5}$$

In Fig. 7 we plot v_{ac} as a function of ε for three values of N. We observe that under the appropriate conditions, and without any bias, we can reverse the elution order and induce bidirectional transport (although the absolute net velocity is slightly smaller than in the time-asymmetry ratchet). The reversal of the net velocity at high field is somewhat surprising, since it indicates that at some point migration becomes easier in the negative direction (see figure inset). We can rightfully question the accuracy of the simulations and the quality of the numerical fits, but we can also explain this reversal in the following way: We know that molecules normally escape from the deep regions by uncoiling and slithering across the narrow region [17–19]. At low field, the step confines the molecules near the narrow region, which helps the escape process. At high field, however, the time it takes for long molecules to fill the step region (i.e. to overcome the corresponding entropic barrier) becomes larger than their typical trapping time at the constriction, and the step then has a detrimental effect on the molecular drift.

6 Resonance and transport

Up to now we have only considered the zero-frequency limit of various ac driving fields. As mentioned before, this approach allows us to work with analytical functions and quickly extract results from our dc simulation data. It also ensures that the resulting phenomena are solely due to the non-linearities in the molecular velocity. On the other hand, we do expect interesting phenomena to occur when the driving frequency approaches one of the natural frequencies of the device. For completeness, we investigate in this section the finite-frequency (or non-adiabatic) ac response of a symmetric system.

We collect data from simulations (performed in a symmetric channel) in which the electric field explicitly follows a square pulse of period T that oscillates between two positive field values (T is not to be confused with temperature, which in our context only appears in the definition of the dimensionless field intensity, ε). We choose $\varepsilon_1 = 0.007$ and $\varepsilon_2 = 0.003$, for a net global field $\varepsilon_{net} = (\varepsilon_1 + \varepsilon_2)/2 = 0.005$ (see Fig. 3b). Out of the many time scales in the system, the one most likely to harbor a resonance in the drift velocity lies around $2\overline{\tau}(\varepsilon_1, N)$, i.e. twice the mean trapping time at $\varepsilon = \varepsilon_1$. Indeed, if $T/2 < \overline{\tau}$, then the probability that a molecule escapes during the most favorable ε_1 half of the pulse period is greatly reduced. However, if $T/2 > \overline{\tau}$, then the pulse becomes unnecessarily long and the overall drift is reduced (unless of course the pulse is long enough for many barriers to be crossed in a single pulse cycle; since the standard deviation in trapping time $\sigma(\tau) \sim \overline{\tau}$, as derived below, these "harmonics" cannot be seen). Based on these observations, we can build a simple phenomenological equation for the dependence of the drift velocity on the pulse period:

$$v_{ac}(T) \sim \text{Prob}(\tau < T/2)\frac{L}{T} . \tag{6}$$

The first factor in (6) is the probability that the trapping time in any given trap is less than half the period, which increases with T. The second factor is inversely proportional to T and embodies the waste of time due to unnecessarily long pulses. Here we assume that the molecule may only escape from the trap during the ε_1 part of the pulse, and we disregard trapping times longer than T (associated, for example, with additional delays of T, $2T$, $3T$, etc., when the molecules fails to escape repeatedly). In that sense this is a first-order model.

To find the position of the resonance peak from (6), i.e. the value, T_0, for which the velocity is maximized, we must calculate $\text{Prob}(\tau < T/2)$; hence we need to know the probability density function of the trapping time, τ. From dc simulation data (not shown) we find that the distribution of trapping times is generally well approximated by the normalized distribution

$$\varrho(\tau) = 2(\tau/\tau_c^2)e^{-(\tau/\tau_c)^2} , \tag{7}$$

where $\tau_c^2 = 4\overline{\tau}^2/\pi$. From $\varrho(\tau)$ we calculate $\text{Prob}(\tau < T/2) = (1 - e^{-(T/2\tau_c)^2})$ and maximize $v_{ac}(T)$ in (6) to find the resonance condition $T_0^2 \approx 5\tau_c^2$, or

$$T_0 \approx \sqrt{\frac{20}{\pi}}\overline{\tau} \approx 2.5\overline{\tau} . \tag{8}$$

From the distribution in (7) we can also calculate $\sigma(\tau) = \sqrt{(4/\pi - 1)}\overline{\tau} \approx \overline{\tau}/2$; the distribution is thus quite broad. Consequently, we expect the resonance peak to be quite broad as well.

Finally, we can deduce the asymptotic behavior of the velocity far from the resonance region, for very long or very

short periods, T. When $T \gg \overline{\tau}$, we expect the velocity of the molecules to approach the mean of the velocities corresponding to each field intensity; hence we write

$$\lim_{(T/\overline{\tau})\to\infty} \mu_{ac}(\varepsilon_1, \varepsilon_2, N, T) = \frac{\mu(\varepsilon_1, N)\varepsilon_1 + \mu(\varepsilon_2, N)\varepsilon_2}{2\varepsilon_{net}} . \quad (9)$$

On the other hand, when $T \ll \overline{\tau}$, we expect to recover the mobility corresponding to the net global field, ε_{net}:

$$\lim_{(T/\overline{\tau})\to 0} \mu_{ac}(\varepsilon_1, \varepsilon_2, N, T) = \mu(\varepsilon_{net}, N) . \quad (10)$$

Simulation results for the mobility of the molecules in the ac regime are presented in Fig. 8 (the mobility is just proportional to the velocity here). Dashed lines indicate the long and short period limits calculated above, while for each molecular size an arrow points to the value of T_0 calculated from $\overline{\tau}$ (extracted from the dc data) according to (8). We see that the predictions for the asymptotic limits and for the position of the resonance peak are quite good. The separation is best for very short T, which corresponds to the dc case at a field, ε_{net}, which was chosen close to the optimum choice for dc separation. There is no inversion in the order of the bands, which makes sense since the driving field is always applied in the same direction. It is also clear from the graph that one cannot hope to single out a given molecular size by tuning into its resonant frequency, as the peaks for different molecular sizes are very broad.

The most interesting feature of the ac regime is that at resonance the overall drift speed increases significantly (by as much as 30% for $N = 50$), while the separation of the different bands decreases only slightly. Hence it appears possible to increase the operating speed of this device while keeping the separation capability intact by means of an ac modulation of the dc driving field. We should note that we have studied only one amplitude of the ac modulation; the amplitude should also be examined as a variable to isolate the optimal separation scenario. It is quite possible that at optimal field intensity and ac amplitude one might actually obtain a performance exceeding that of the dc regime. Moreover, one might investigate finite-frequency ratchet modes by adding temporal or spatial asymmetry to further optimize the separation.

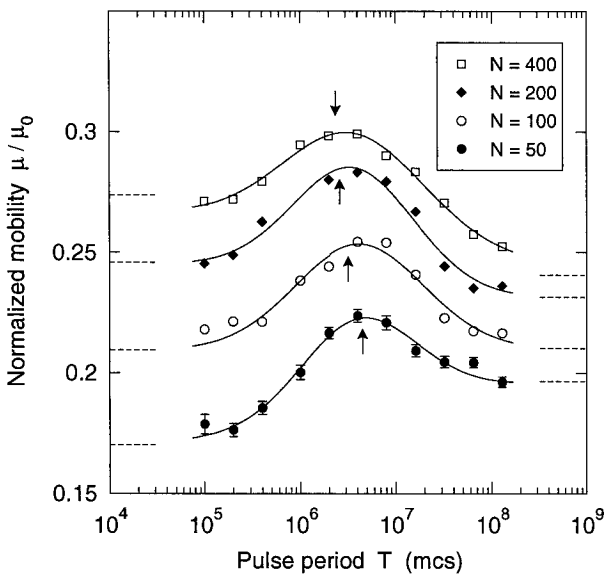

FIGURE 8 Mobility of macromolecules in a symmetric channel in the ac modulation regime, as a function of the driving field pulse period. The field oscillates between $\varepsilon_1 = 0.007$ and $\varepsilon_2 = 0.003$. The low- and high-frequency limits, calculated from (9) and (10), are indicated by *dashed lines* on the right and left sides of the graph, respectively. The value of T_0 is indicated by an *arrow* for each molecular size. *Solid lines* are added to guide the eye

7 Conclusion

Our study focused on an existing microdevice used for dc electrophoresis of DNA fragments. We performed simulations of this device in various dc and ac modes to find interesting operating regimes. Most notably, we found that with a ratchet pulse we can reverse the elution order, while with a biased ratchet pulse we can control bidirectional drift, practically at will. We also considered an asymmetric version of the original device and showed that it also features bidirectional drift properties. Hence we conclude that strategies based on entropic ratchet ideas can find useful applications in existing micro-electrophoretic devices. It would also be interesting to see if we could create two-dimensional structures that could spread molecules in a plane based on two spatially orthogonal modes, e.g. separating molecules based on molecular weight in one direction and on architecture in the orthogonal direction (for instance, we previously showed that the Han et al. device can actually separate linear and ring polymers of the same molecular weight in dc mode). In the finite-frequency domain, we found a resonance peak in the velocity of the molecules that may help improve the operating speed or the separation capability of microdevices. Although our results pertain to a specific system, our findings are relevant in other contexts where large macromolecules are forced through small constrictions. The strategies presented here should be applicable to a wide variety of microfluidic devices handling biological and synthetic macromolecules.

ACKNOWLEDGEMENTS We acknowledge the support of the Natural Science and Engineering Research Council of Canada for a Research Grant to G.W.S. and scholarships to F.T., and the University of Ottawa for scholarships to F.T. In addition, we acknowledge J. Han, S.W. Turner and H.G. Craighead for useful discussions about their microdevice experiments.

REFERENCES

1 R.D. Astumian, M. Bier: Phys. Rev. Lett. **72**, 1766 (1994)
2 F. Jülicher, A. Ajdari, J. Prost: Rev. Mod. Phys. **69**, 1269 (1997)
3 M. Porto, M. Urbakh, J. Klafter: Phys. Rev. Lett. **85**, 491 (2000)
4 M.O. Magnasco: Phys. Rev. Lett. **71**, 1477 (1993)
5 J. Prost, J.-F. Chauwin, L. Peliti, A. Ajdari: Phys. Rev. Lett. **72**, 2652 (1994)
6 J. Rousselet, L. Salome, A. Ajdari, J. Prost: Nature **370**, 446 (1994)
7 S. Leibler: Nature **370**, 412 (1994)
8 M. Bier, R.D. Astumian: Phys. Rev. Lett. **76**, 4277 (1996)
9 R.D. Astumian: Science **276**, 917 (1997)
10 L. Gorre-Talini, S. Jeanjean, P. Silberzan: Phys. Rev. E **56**, 2025 (1997)
11 I. Derényi, R.D. Astumian: Phys. Rev. E **58**, 7781 (1998)
12 J.S. Bader, R.S. Hammond, S.A. Henck, M.W. Deem, G.A. McDermott, J.M. Bustillo, J.W. Simpson, G.T. Mulhern, J.M. Rothberg: Proc. Nat. Acad. Sci. USA **96**, 13 165 (1999)
13 R.W. Hammond, J.S. Bader, S.A. Henck, M.W. Deem, G.A. McDermott, J.M. Bustillo, J.M. Rothberg: Electrophoresis **21**, 74 (2000)

14 C. Kettner, P. Reimann, P. Hänggi, F. Müller: Phys. Rev. E **61**, 312 (2000)
15 G.A. Griess, E. Rogers, P. Serwer: Electrophoresis **22**, 981 (2001)
16 G.W. Slater, H.L. Guo, G.I. Nixon: Phys. Rev. Lett. **78**, 1170 (1997)
17 J. Han, S.W. Turner, H.G. Craighead: Phys. Rev. Lett. **83**, 1688 (1999)
18 J. Han, H.G. Craighead: Science **288**, 1026 (2000)
19 F. Tessier, G.W. Slater: Macromolecules, in press (2002)
20 P.J. Park, W. Sung: J. Chem. Phys. **111**, 5229 (1999)
21 K.L. Sebastian, A.K.R. Paul: Phys. Rev. E **62**, 927 (2000)
22 K.L. Sebastian: Phys. Rev. E **61**, 3245 (2000)
23 M. Muthukumar: J. Chem. Phys. **112**, 10 371 (1999)
24 I. Carmesin, K. Kremer: Macromolecules **21**, 2819 (1988)
25 H.P. Deutsch, K. Binder: J. Chem. Phys. **94**, 2294 (1991)
26 C. Turmel, E. Brassard, R. Forsyth, K. Hood, G.W. Slater, J. Noolandi: In *Electrophoresis of Large DNA Molecules – Theory and applications*, ed. by E. Lai, B.W. Birren (Cold Spring Harbor Laboratory Press, Plainview, NY 1990) pp. 101
27 G.A. Griess, E. Rogers, P. Serwer: Electrophoresis **21**, 859 (2000)

4

Effective Debye length in closed nanoscopic systems: a competition between two length scales

F Tessier, GW Slater. Accepted in *Electrophoresis* (November 9, 2005)

Abstract

The famous Poisson-Boltzmann equation (PBE) is widely employed in fields where the thermal motion of free ions is relevant, in particular in situations involving electrolytes in the vicinity of charged surfaces. The traditional solutions of this non-linear differential equation usually concern open systems (in osmotic equilibrium with an electrolyte reservoir, a semi-grand canonical ensemble), while solutions for closed systems (where the number of ions is fixed, a canonical ensemble) are either not appropriately distinguished from the former or are dismissed as a numerical calculation exercise. However, a closed system can be interpreted as an open one with an effective Debye length determined by conservation conditions. Techniques for solving the PBE in open systems can therefore be brought to bear on closed systems, provided that this effective parameter is known. We show herein that the PBE depends on only two critical lengths (or, equivalently, when combined with the characteristic system size, two dimensionless parameters), and that in first approximation only their combination in a simple ratio is significant for the determination of the effective Debye length. Comparisons with self-consistent numerical results for the non-linear PBE reveal that a simple expression for the value of the effective Debye length, obtained within a crude approximation, remains accurate even as the system size is reduced to nanoscopic dimensions, and well beyond the validity range typically associated with the PBE solution.

Introduction

A particularly elegant and well-recognized theoretical continuum limit description of an electrolyte in thermal equilibrium near a charged body relies on a combination of the Poisson equation for the electrostatic potential and the Boltzmann equation for the distribution of diffusing ions, into the celebrated Poisson-Boltzmann equation (PBE). This mean-field approach is so widely fruitful, in fact, that for historical reasons its various incarnations are known under distinct names in different contexts: Gouy-Chapman theory, Debye-Hückel theory, DLVO theory [1]. Its foundations, applications and limitations are discussed at length in many excellent textbooks [2, 3], hence the short reminder included here will suffice for the purpose of this article. Interest in the PBE is as alive now as ever (seeding more that a thousand research articles in the 1990s, by one account [4]), and progress in its treatment is crucial for advances in colloid science and molecular biophysics.

The PBE is also a workhorse in modern microfluidic device analysis; such devices typically involve electrolytes confined in small channels (the surface of which becomes charged upon contact

with an aqueous medium), and rely on electroosmosis for fluid transport [5–7]. At the microscale a continuum description is certainly appropriate and, moreover, the characteristic length scale associated with electrokinetic phenomena (the so-called Debye length) is typically on the order of the nanometer, much smaller than the device size, thus allowing for simplifications and analytical solutions. But even if we consider emerging nanofluidic devices, for which the PBE is admittedly not the most realistic model (it neglects ion size and correlation effects[2, 8, 9] which can lead to the very interesting phenomenon of charge and flow reversal [10–12]), the ubiquity of the approach rightfully makes it a popular baseline in the interpretation of simulation data [13–15].

Despite the impressive body of publications on electrokinetic phenomena in confined environments, headed by the seminal work of Burgreen and Nakache [16], Rice and Whitehead [17], and Ninham and Parsegian [18], few studies explicitly address the case of a closed system, that is, one where the total number of ions is fixed (a canonical ensemble). Typically, the electrolyte is assumed to be in osmotic equilibrium with a salt reservoir and an open boundary condition is applied (called a semi-grand canonical ensemble in the literature). This important but occasionally overlooked distinction is most clearly expounded on in articles by Dubois *et al.* [19] and by Hansen and Trizac [20]. The relative lack of results for closed systems is hardly surprising: conservation constraints turn the already difficult non-linear PBE into an intractable integro-differential equation that is readily discounted as a problem that can only be solved numerically. Of course, the issue also attracts little attention because in practice devices are usually connected to reservoirs. However, simulations are often conducted in the NVT ensemble, e.g., a slender capillary with periodic boundary conditions along its length [21, 22, 10], hence it is worth considering the PBE in this context, if anything is to be said of the continuum theory in regard to the simulation data. Our own interest in the subject stems from ongoing Molecular Dynamics simulation work of this kind, pertaining to nano-electroosmotic flow.

The purpose of this article is twofold. First, we want to clarify the discussion of the PBE in the case of a closed system by introducing a new inverse length scale κ_1 proportional to the charge density on the solid surface in contact with the electrolyte. We show that the PBE depends solely on this inverse length κ_1 and on the traditional inverse Debye length κ_0 (related to the salt concentration), and thus establish that there are essentially four different regimes for an enclosed electrolyte, corresponding to the vanishing and infinite limits of κ_0 with respect to the characteristic system size, and of κ_1 versus κ_0. Secondly, we show that a closed system is identical to an open one, provided that κ_0 is replaced by an effective parameter, and we suggest a simple approximation for this

effective parameter, the exact value of which can indeed only be obtained numerically. Comparing this approximation with the exact calculation and with the open case then constitutes the bulk of our discussion. Interestingly, we find that the validity of the approximation is not dependent on the presence of a bulk phase, which is typically invoked to treat the PBE in open systems.

The Poisson-Boltzmann equation in a closed system

We directly obtain the PBE by replacing the net charge density in the Poisson equation for the electric potential by appropriate Boltzmann distributions for ions diffusing in that potential. If k refers to one of N ionic species present in the solution, each of valence z_k (including sign), we have

$$\nabla^2\phi(\mathbf{r}) = -\frac{e}{\epsilon}\sum_{k=1}^{N} c_k z_k \exp\{-ez_k\phi(\mathbf{r})/k_\mathrm{B}T\}\,, \tag{4.1}$$

where $\phi(\mathbf{r})$ is the electric potential at position $\mathbf{r}$, e is the elementary charge, ϵ is the permittivity of the solvent (assumed constant throughout the system [8, 9]), k_B is the Boltzmann constant and T is the absolute temperature. The constants c_k are *a priori unknown* and, in general, they must be determined from electroneutrality and ionic equilibrium or conservation constraints [19, 23]. However, they are often taken as the bulk ionic concentrations n_{0k}, which is strictly only correct in an open system (e.g., a capillary connecting electrolyte reservoirs), but also an excellent approximation in a closed system when the dissolved salt concentration n_0 or the distance between charged surfaces are large enough (a statement which we will quantify below). It becomes increasingly problematic, however, as n_0 decreases or as the characteristic system size is reduced, such as in nanofluidic devices, because then there is effectively no bulk electrolyte region: ions released by the surfaces affect the charge distribution everywhere in the system, and the conservation conditions must be solved self-consistently.

In what follows, we are concerned with an electrolyte confined between two uniformly charged walls located at $x = \pm a$, as depicted in Figure 4.1. Note that we choose a planar geometry merely as a matter of convenience; we could consider other geometries with essentially no change to the argument, apart from a change of coordinates. For definitiveness we choose the walls to be negatively charged with a surface density σ (unsigned), hence negative charges are refered to as coions, and positive charges as counterions. It proves useful to cast the PBE equation into a dimensionless form,

using the variables $u \equiv (e\phi/k_{\mathrm{B}}T)$ and $\xi \equiv (x/a)$:

$$\nabla_{\xi}^{2} u(\xi) = -\frac{e^2 a^2}{\epsilon k_{\mathrm{B}} T} \sum_{k=1}^{N} c_k z_k \exp\{-z_k u(\xi)\} \tag{4.2}$$

Furthermore, seeing as we will only consider the case of a symmetric univalent (1–1) electrolyte, we set $N=2$, $z_1=1$, $z_2=-1$, and use superscripts $+$ and $-$ to label quantities relating to the positive and negative ions respectively. Thus Equation 4.2 reduces to:

$$\nabla_{\xi}^{2} u(\xi) = -\frac{(\kappa_0 a)^2}{2n_0} \left\{ c^{+} \mathrm{e}^{-u(\xi)} - c^{-} \mathrm{e}^{u(\xi)} \right\}. \tag{4.3}$$

The important parameter $\kappa_0 \equiv (2n_0 e^2/\epsilon k_{\mathrm{B}} T)^{1/2} \equiv 1/\lambda_{\mathrm{D}}$ introduced here, with n_0 being the concentration of dissolved salt in the solution, is the inverse of the Debye length λ_{D}, a widely-recognized measure of the extent of the diffuse charge layer near the surface [3] (this identification comes from the solution of a linearized version of the PBE for a semi-infinite bulk solution in contact with a charged plane, $\nabla^2 u(x) = \kappa_0^2 u(x)$, the bounded solution of which has the form $u(x) \sim$

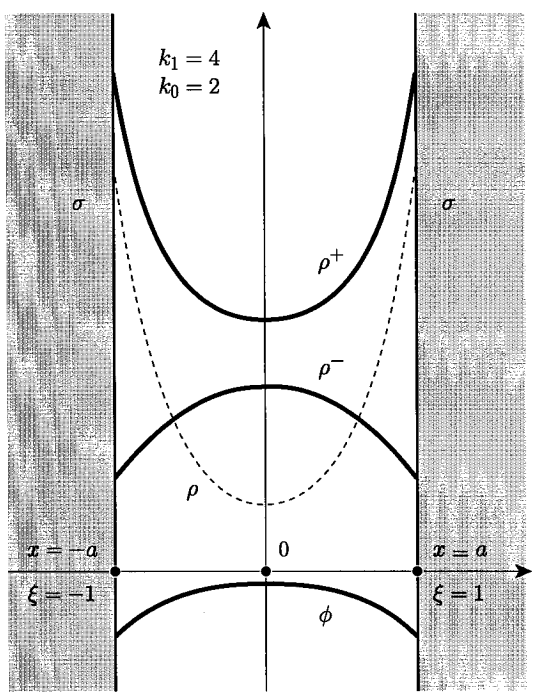

FIGURE 4.1 Diagram of an electrolyte confined between two infinite walls located at $x = \pm a$, or $\xi \equiv x/a = \pm 1$. The walls are negatively charged with a surface charge density σ (unsigned). Also shown in this sketch are numerical solutions for the potential ϕ, the coion density ρ^-, the counterion density ρ^+, and net charge ρ (using arbitrary units), when $k_0 = 2$ and $k_1 = 4$.

$e^{-\kappa_0 x}$). The dimensionless combination $\kappa_0 a$ is called the electrokinetic radius and amounts to the characteristic system size a expressed in units of the Debye layer thickness.

The values of the three quantities c^+, c^- and $u(0)$ are not independent: physically the potential $u(\xi)$ is defined up to a constant and, consequently, c^+ and c^- are defined up to multiplicative factors[19]. To emphasize this point, we now rewrite Equation 4.3 in a way that is more transparent, in terms of the normalized densities of counterions and coions at $\xi = 0$ (the midpoint between the plates), namely

$$m_0^{\pm} \equiv \frac{n_0^{\pm}}{n_0} = \frac{c^{\pm} e^{\mp u(0)}}{n_0} . \tag{4.4}$$

Introducing $u_0 \equiv u(0)$, and dropping the explicit dependence on ξ to simplify notation, we write:

$$\nabla^2 u = \nabla^2 (u - u_0) = -\frac{(\kappa_0 a)^2}{2} \left\{ m_0^+ \, e^{-(u-u_0)} - m_0^- \, e^{(u-u_0)} \right\} . \tag{4.5}$$

With this particular notation it is clear that, while m_0^+ and m_0^- are now fixed by their meaning, the value of u_0 is arbitrary, as expected. The appropriate boundary conditions for solving Equation 4.5 are derived from symmetry and overall electroneutrality:

$$\left. \frac{du}{d\xi} \right|_{\xi=0} = 0 , \tag{4.6}$$

$$\left. \frac{du}{d\xi} \right|_{\xi=1} = -\frac{(2e^2/\epsilon k_B T)\sigma a}{2} = -\frac{\kappa_1 a}{2} , \tag{4.7}$$

where we have defined a new inverse length $\kappa_1 \equiv (2\sigma e^2/\epsilon k_B T)$. It is interesting to note that, from Equations 4.5, 4.6 and 4.7, the solution of the PBE clearly depends only on the two dimensionless parameters $\kappa_0 a$ and $\kappa_1 a$. The first one is the traditional electrokinetic radius, while the second is a similar quantity relating to σ instead of n_0. In the rest of the paper, we will use the shorthand $k_i \equiv \kappa_i a$ to simplify the notation and emphasize the dimensionless character of these parameters. The important dimensionless ratio

$$s \equiv \frac{k_1}{k_0^2} = \frac{\sigma}{n_0 a} \tag{4.8}$$

measures the relative contribution of the wall ionization and the salt dissolution to the total number of counterions in the closed system. When $s = 1$ both phenomena contribute equally, and the limit $s \to 0$ corresponds to the bulk limit usually invoked to treat the PBE. Given that the PBE is completely defined in terms of two dimensionless parameters, it is convenient to conceptually divide the problem in four different regimes, corresponding to the small and the large limits of k_0 and $s = k_1/k_0^2$, as organized in Table 4. The parameter k_0 measures the size of the system in terms of the Debye length

	$k_0 \gg 1$	$k_0 \ll 1$
$s \ll 1$	macro-bulk	nano-bulk
$s \gg 1$	macro-wall	***nano-wall***

TABLE 4.1 Four different regimes that can be associated to the Poisson Boltzmann problem in a closed system, corresponding to the different limits of k_0 (which measures the system size in terms of the Debye length) and $s = k_1/k_0^2$ (which is proportional to the relative mean concentration of counterions contributed by the wall and by the salt).

(typically of the order of 1 nm in water), so we use the prefix *nano* when it is small and *macro* when it is large. The parameter s is the relative mean concentration of counterions contributed by the surface (or wall), as explained above, so we use the suffix *bulk* when this contribution is weak, and *wall* when it dominates. We are here particularly concerned with the nano-wall regime, which corresponds to a system where the Debye length is commensurate or larger than the space between the charged surfaces, and where the wall ionization contributes significantly to the mean counterion concentration. The bulk regimes are handled successfully with an open boundary condition (and with a linear version of the PBE in many cases), while the macro-wall regime corresponds to the less practical case of a macroscopic system where the wall charge nevertheless dominates.

We stress again that m_0^+ and m_0^- in Equation 4.5 are *a priori unknown* constants; they must be determined self-consistently from the *known* total number of counterions and coions in the system, i.e., from the two conservation integrals:

$$m_0^+ \int_0^1 \mathrm{e}^{-(u-u_0)} d\xi = 1 + s \,, \tag{4.9}$$

$$m_0^- \int_0^1 \mathrm{e}^{+(u-u_0)} d\xi = 1 \,. \tag{4.10}$$

The condition in Equation 4.7 is in fact redundant with these two integrals, which, by accounting for all positive and negative ions explicitely, necessarily imply overall electroneutrality (subtract Equation 4.10 from Equation 4.9) [19]. The four equations 4.6–4.10 therefore amount to three independent equations which, along with an arbitrary choice for u_0, are sufficient to fully determine the solution of a second-order differential equation with 2 unknowns (m_0^+ and m_0^-).

Interestingly, the freedom in the choice of u_0 allows us to rewrite Equation 4.5 in a particularly convenient notation. Indeed, let us define the quantity $u_{0\mathrm{eff}} \equiv \ln\{(m_0^+/m_0^-)^{-1/2}\}$. Upon setting

$u_0 = u_{0\text{eff}}$, we have $m_0^+ \mathrm{e}^{u_0} = m_0^- \mathrm{e}^{-u_0} = (m_0^+ m_0^-)^{1/2}$, and we can write the PBE as:

$$\nabla^2 u = k_{\text{eff}}^2 \sinh(u), \tag{4.11}$$

where $k_{\text{eff}}^2 \equiv k_0^2 (m_0^+ m_0^-)^{1/2}$. Equation 4.11 then assumes the same form as, and facilitates comparison with, the PBE for the case where the electrolyte between the plates is in osmotic equilibrium with a salt reservoir of concentration n_0 (implying that $m_0^+ m_0^- = 1$) [19],

$$\nabla^2 u = k_0^2 \sinh(u) \tag{4.12}$$

(subject to the boundary conditions given in Equations 4.6 and 4.7), with k_{eff} replacing k_0. By analogy with the open system case, we call k_{eff} the *effective* electrokinetic radius, and, correspondingly, we have an effective Debye length $\lambda_{\text{Deff}} \equiv a/k_{\text{eff}}$. Standard techniques used to solve the standard PBE given in Equation 4.12 can therefore be employed to solve the closed system problem once the value of k_{eff} is determined (note that the value of $u_{0\text{eff}}$ is not required, but rather provided, by the solution of Equation 4.11). This is by no means trivial at the outset since it amounts to solving the integro-differential problem obtained by combining Equations 4.5–4.10. However, as shown below, even the simplest approximation yields a remarkably accurate value for the value of k_{eff}.

A simple approximation

Given that it is not in general possible to find an analytical solution to the non-linear PBE, a fortiori under conservation constraints, we look for the first-order dependence of the effective electrokinetic radius k_{eff} on the two experimental parameters k_0 and k_1 using a deceptively crude approximation of the conservation integrals 4.9 and 4.10, namely keeping only the zeroth-order terms in the expansion of the exponentials, i.e.,

$$m_0^+ \approx 1 + s\,, \tag{4.13}$$

$$m_0^- \approx 1\,, \tag{4.14}$$

which amounts to replacing the counterion concentrations $m_0^{\pm}$ at the midplane with the mean values $\langle m^{\pm} \rangle$. We thus obtain the following approximate value for the effective electrokinetic radius:

$$k_{\text{eff}}^{\star} = k_0 (1 + s)^{1/4}. \tag{4.15}$$

This expression has been obtained by others [20, 24] by linearizing the PBE around the mean potential in the system, in the slightly different context of colloid suspensions, but under essentially identical considerations. However, this result deserves wider dissemination in the electrophoresis community, especially in light of the current trends in scaling down electrophoretic equipment and in resorting to molecular simulations to gain fundamental insights into electrokinetic phenomena. Our novel derivation, unburdened by concerns surrounding the direct linearization of the PBE, provides an accessible approach. Of course, the approximation 4.15 is only reliable provided that the potential difference $|u - u_0|$ is small compared to unity (so it remains a linear theory), and we can quickly sketch its region of validity as follows. When $k_0 < 2$, the Debye layer starts to bridge the whole gap between the plates, and the potential, given the boundary conditions 4.6 and 4.7, assumes the parabolic profile $u(\xi) \approx u_0 - k_1\xi^2/4$, hence the approximation is fair when $k_1 < 4$. When k_0 increases far beyond unity, on the other hand, the Debye length decreases and the potential profile near the wall approaches the bulk limit exponential form $u(\xi) \approx u_0 - (k_1/2k_0)\mathrm{e}^{-k_0(1-\xi)}$, hence $|u - u_0| < 1$ when $k_1 < 2k_0$. For a more rigorous analysis, we resort to a self-consistent numerical integration of the non-linear PBE in order to determine the real value of k_{eff} as a function of k_0 and k_1. Numerically, of course, the problem is straighforward: we start with an initial guess for m_0^+ and m_0^- (say equal to 1) and solve Equation 4.5 numerically, enforcing the boundary conditions 4.6 and 4.7. We then adjust the values of m_0^+ and m_0^- according to Equations 4.9 and 4.10, using our first solution as an approximation for the potential $u(\xi)$. We solve the PBE again using these new values, and iterate this procedure until m_0^+ and m_0^- converge. We have carried out these calculations with our own integration code, and we have checked our results against independent solutions obtained with the Maple software.

Discussion

The validity limits estimated above are sketched in Figure 4.2 in the (k_0^{-1}, k_1^{-1}) plane, along with the numerical contour lines correspondig to $k_{\mathrm{eff}}^{\star}/k_{\mathrm{eff}} - 1 = 1\%$, 5% and 10%. We see that the sketched limits do indeed provide a rough guide to the validity of approximation 4.15. Furthermore, Figure 4.2 immediately suggests the three following observations: 1) if k_0 is small enough (the Debye length is larger than the plate separation), the validity of Equation 4.15 is indeed practically independent of the salt concentration and in any case, when $k_1 < 4$ it is in practice always quite reliable; 2) approximation 4.15 is valid within, but not limited to the bulk regime ($s < 1$), or to the Debye-Hückel region (delineated in Figure 4.2 by a dashed curve, where the direct linearization

of Equation 4.11 is a good approximation of the full problem); 3) if $k^{\star}_{\text{eff}}$ is accurate for a given combination of salt concentration, wall charge and system size a, then it is increasingly reliable as the system size is reduced, since reducing a corresponds to moving away from the origin in Figure 4.2.

It is possible to carry the approximation further by using higher order series expansions of the exponentials in the integrals 4.6 and 4.7, but of course we must then guess the form for the unkown potential $u(\xi)$, thereby severely limiting the applicability of the calculation. For example, we can calculate higher order terms of the conservation integrals using the Debye-Hückel approximation $u(\xi) \approx -k_1 \cosh(k_{\text{eff}}\xi)/2k_{\text{eff}} \sinh(k_{\text{eff}})$ (found upon linearizing Equation 4.11) and solve for the

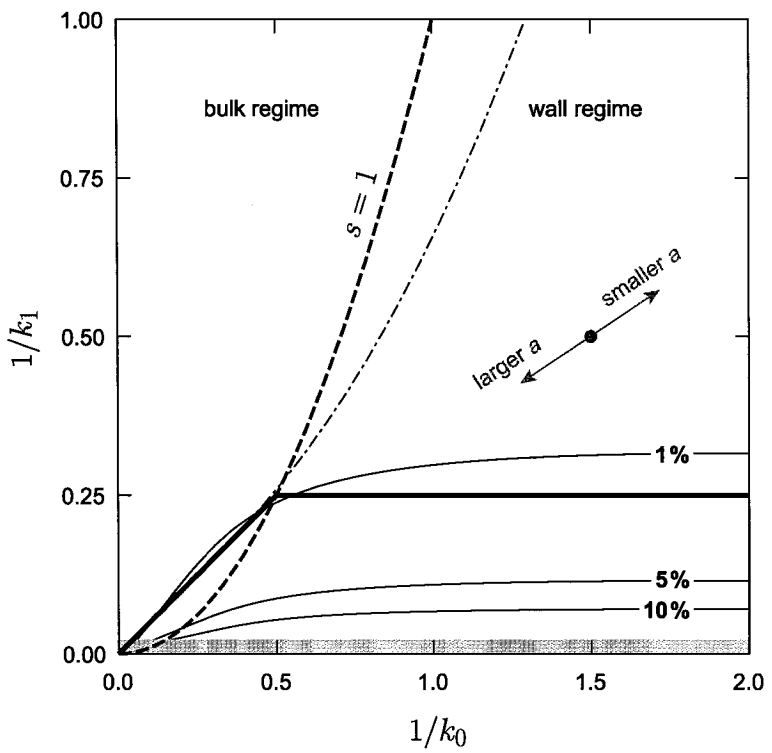

FIGURE 4.2 Three contours (1%, 5% and 10%) of the relative error $(k^{\star}_{\text{eff}}/k_{\text{eff}} - 1)$ incurred by using the $k^{\star}_{\text{eff}}$ approximation, in the (k_0^{-1}, k_1^{-1}) plane (the gray indicates that we have not calculated the error function in that region). The thick solid line represents the validity boundary of $k^{\star}_{\text{eff}}$, estimated by the limiting forms of the PBE solution. The dashed curve shows the boundary $s = 1$ separating the bulk- and wall-dominated regimes (to the left and to the right, respectively). The dot-dashed line corresponds to the linear regime boundary; systems corresponding to points on the left of this line can be handled in good approximation by linearizing the PBE directly. (The gray region indicates that we have not computed the function there.)

value of k_{eff}. The resulting expression then provides a better approximation for k_{eff} in the linear regime, at the expense, however, of its applicability outside of it. The crude approximation $k^{\star}_{\text{eff}}$ given in Equation 4.15, on the other hand, does not presuppose any form for the potential and is therefore amenable to a wider range of (k_0, k_1) values, while already providing of the order of 1% accuracy in the linear regime; a constructive tradeoff in our opinion.

Let us now consider real world parameter values: is $k^{\star}_{\text{eff}}$ useful in a practice? Yes. Take for example a on the order of 1 nm (admittedly the lower bound for anything concerning fluids). For water at room temperature and at physiological salt concentration ~ 0.1 M [25], the Debye length is roughly 1 nm, so that $k_0 \approx 1$. A glass surface in contact with this electrolyte, near neutral pH, bears a surface charge of the order of $0.1e/\text{nm}^2$ (or 0.017 C/m^2) [26], yielding $k_1 \approx 2$, and $s = 2$. Under these conditions, we thus rest in the center of the graph in Figure 4.2; we are outside the bulk regime ($s = 2$), yet we find $k^{\star}_{\text{eff}} = 3^{1/4} k_0 \approx 1.32 k_0$, which is only 0.4% higher than the exact value calculated numerically. Decreasing the ionic concentration n_0 takes us further to the right in the graph, while a reduction in the surface charge density σ takes us up vertically (actually, σ is not completely independent from n_0, so for a given system size we should really think about moving along some curve in the plane [27, 26]). Increasing the system size a amounts to scaling up k_0 and k_1 by an equal amount, thus moving towards the origin in the graph. This quick survey shows that the simple $k^{\star}_{\text{eff}}$ is quite apt at handling the transition to nanoscopic dimensions, especially when n_0 and σ are smaller than the values quoted above. For a more striking example, consider a salt concentration low enough so that the situation is almost completely dominated by counterions from the wall: $a = 10$ nm, $n_0 = 10\ \mu$M and $\sigma = 0.01e/\text{nm}^2$ (0.0017 C/m^2), which translates into $k_0 = 0.1$ and $k_1 = 2$. In this case we lie far in the nano-wall regime ($s = 200$), yet approximation 4.15 still gives an estimate of $k^{\star}_{\text{eff}} = 201^{1/4} k_0 \approx 3.77 k_0$ that is only about 0.5% higher than the exact value.

Of course, the actual physics of the problem rests more on the charge distribution than on the electric potential (which is only defined up to a constant), hence it is interesting to compare the dimensionless net charge densities obtained with three different electrokinetic radii. By order of decreasing accuracy, we have k_{eff}, $k^{\star}_{\text{eff}}$, and k_0, which yield three different solutions for the electric potential via the non-linear PBE (e.g., Equation 4.11), and in turn to different net charge densities, respectively $\rho(\xi)$, $\rho^{\star}(\xi)$ and $\rho_0(\xi)$, via the Poisson equation. The first one is thus the exact numerical solution for the net charge density, the second one corresponds to the simple approximation 4.15, and the last one to the naive open system calculation. The three functions are plotted in Fig-

ure 4.3 for $k_0 = 2$ and $k_1 = 4$. The approximation based on $k^\star_{\text{eff}}$ is quite accurate and cannot be distinguished from the exact solution in the graph. On the other hand, the charge density profile calculated from k_0 is markedly different from the exact one: in the closed system, the net charge is displaced slightly towards the wall, as expected from the fact that the effective Debye length is smaller than the nominal one. Note that the three solutions are constrained by the overall electroneutrality condition 4.7, so for a given value of k_1 they all have the same area under the curve (this implies that they always cross each other at some point). We can quantify the relative error of an approximate solution with its normalized root mean square difference to the exact solution, e.g.,

$$\Delta\rho_0 \equiv \frac{\sqrt{\int_0^1 (\rho_0(\xi) - \rho(\xi))^2 d\xi}}{\int_0^1 \rho(\xi) d\xi}. \tag{4.16}$$

The smaller this quantity, the better the agreement between the tentative charge distribution $\rho_0(\xi)$ and the exact one $\rho(\xi)$. The two relative errors $\Delta\rho_0$ and $\Delta\rho^\star$ are plotted in Figure 4.4 as a function of $1/k_0$, on a semi-log scale, for three values of k_1. We are not surprised to find that for any given k_1,

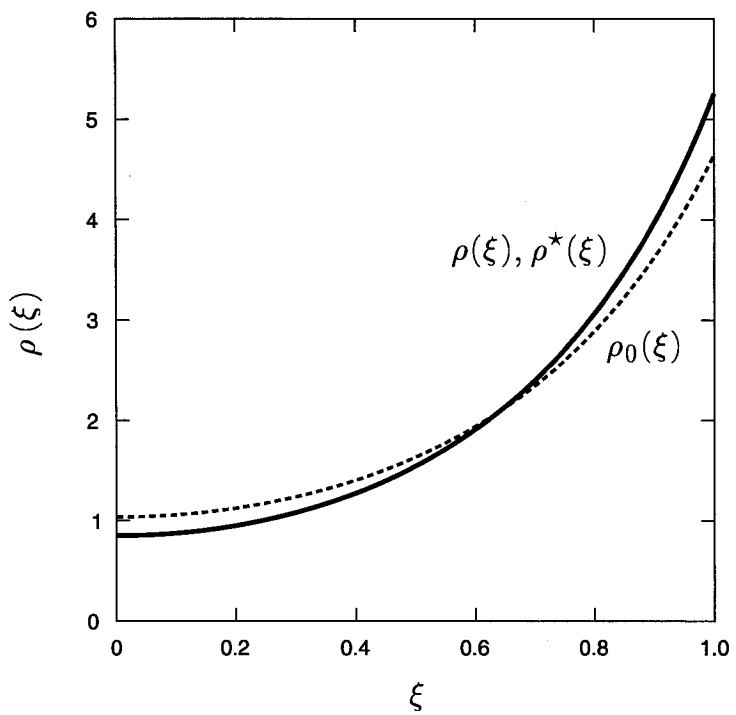

FIGURE 4.3 The three different (dimensionless) net charge densities ρ, $\rho^\star$ and ρ_0 obtained from the exact solution for the electric potential (solid line), the approximate solution obtained with $k^\star_{\text{eff}}$ (solid line, cannot be distinghuised from the former in this graph), and the open system calculation (dashed line). In the closed system the effective Debye length is smaller and the charge is indeed displaced towards the wall.

$\Delta\rho^\star$ is always more accurate than $\Delta\rho_0$ (by a nearly constant factor, greater than 10 when $k_1 < 4$). What is more interesting, however, is that $\Delta\rho_0$ features a maximum near $s = 1$ (identified by a dot on the curves), i.e., near the transition between the bulk-dominated and wall-dominated regimes. For either very large or very small values of s, the open system approach does yield an accurate picture of the net charge density profile (in these limits the potential obtained from k_{eff}, $k^\star_{\text{eff}}$, and k_0 only differ by a constant). The $k^\star_{\text{eff}}$ approximation, on the other hand, does not seem to exhibit such a dependence on s, the maximum occurring instead near a seemingly constant value of $k_0 = 2$, i.e., when the Debye layer just bridges the gap between the walls. In any event, the key advantage of the $k^\star_{\text{eff}}$ calculation here is that it directly provides a reliable estimate of the counterion and coion distributions, *separately*, via

$$\rho^{\pm}(\xi) \approx 0.5(k^\star_{\text{eff}})^2 \mathrm{e}^{\mp u^\star_{\text{eff}}(\xi)} . \tag{4.17}$$

This is not possible with the open system approximation based solely on k_0 because we don't know the appropriate value of $u(0)$; finding it indeed amounts to determining k_{eff}, the whole point of this article.

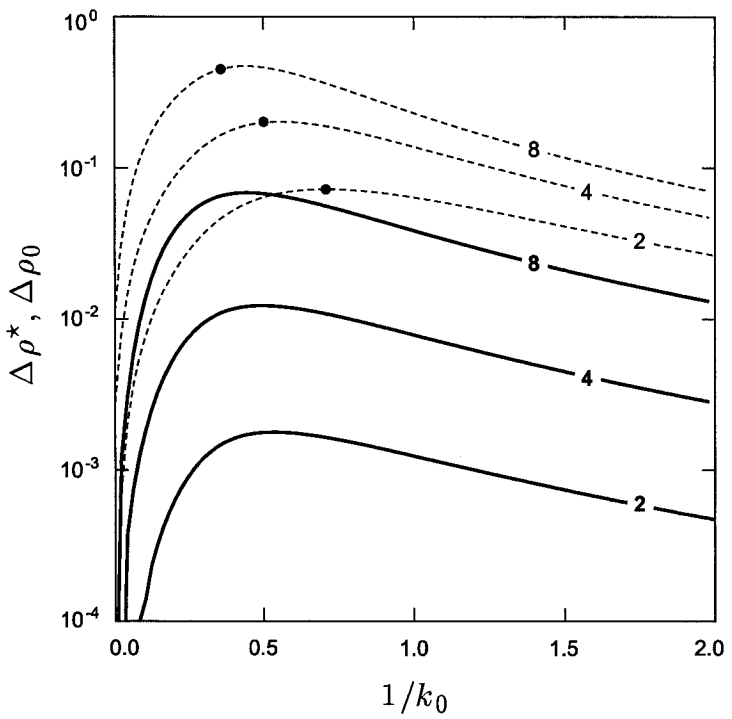

FIGURE 4.4 The error $\Delta\rho^\star$ (solid lines) and $\Delta\rho_0$ (dashed lines), for three different values of k_1 (labeled on the curves). The black dots on the open calculation results correspond to $s = 1$ (the bulk to wall regime transition) and show that the maximum error occurs near that point when the open system calculation is used.

Conclusion

In this article we explored the well posed problem of the distribution of ions in an electrolyte confined by charged surfaces, at the level of Poisson-Boltzmann theory, in a closed system (canonical ensemble). We showed that the solution to this problem depends solely on two dimensionless parameters, k_0 and k_1, pertaining to the salt concentration and the surface charge density, respectively. We also proposed a simple nomenclature to identify the four limiting situations in terms of k_0 and the ratio $s = k_1/k_0^2$: the *macro-bulk*, *macro-wall*, *nano-bulk* and *nano-wall* regimes, the latter being the main focus of this article. In our view, the foregoing treatment clarifies the applicability of the PBE in closed systems where the contribution of counterions from surface dissociation compared to that from the salt cannot be neglected, a situation most relevant to studies of electrolytes in nanofluidic channels.

More importantly, we showed that a closed system is completely equivalent to an open one if the Debye length of the electrolyte is replaced by an effective one. This is significant because it means that techniques for solving the non-linear PBE in open systems can be readily applied in closed ones, provided that this effective parameter is known. Although, strictly speaking, its value is only tractable numerically, we showed that an approximation based on the straighforward quantity $(1+s)^{1/4}$ yields estimates accurate to within 1% over a large portion of parameter space not accesible to a bulk theory (limited to small s values). Two applications of this approximation immediately spring to mind: 1) it can directly replace the original Debye length in calculations relating to closed systems, provided that the incurred relative error landscape sketched in Figure 4.2 is borne in mind; 2) it can serve as an analytical approximant in further calculations, providing insight where previously only numerical results were available.

Comparing the net charge density obtained with the exact, approximated and open-system calculations, we found that discrepancies are not dramatic, and maximum when either $s \approx 1$ (open system solution), or when the Debye length of the electrolyte is commensurate with the characteristic system size (approximated solution). However, only the exact and approximated calculation can provide reliable values for the coion and counterion distributions, *separately*. While many processes only involve the net local charge density (e.g., the body force on fluid elements generated by an external field, as in electroosmosis), other phenomena depend on the local density of a given ion type (e.g., screening of an analyte in electrophoresis) [28, 29]; thus for the latter in particular, it is crucial to take into account the closed nature of the system.

Although some may submit that investigating closed systems is not worthwhile, on grounds that practical systems always involve reservoirs, it is in fact rather important to correctly assess the PBE in the nano-wall regime, in light of the growing interest in canonical ensemble simulations of nanofluidic systems and the ubiquity of Poisson-Boltzmann-based analysis in the interpretation of simulation data.

References

[1] Boda, D., Fawcett, W. R., Henderson, D., Sokolowski, S., *J. Chem. Phys.* 2002, *116*, 7170–7176.

[2] Israelachvili, J., *Intermolecular & surface forces, 2nd ed.*, Academic Press, London 1992.

[3] Russel, W. B., Saville, D. A., Schowalter, W. R., *Colloidal dispersions*, Cambridge University Press, Cambridge 1989.

[4] Shkel, I. A., Tsodikov, O. V., M. T. Record, J., *J. Phys. Chem. B* 2000, *104*, 5161–5170.

[5] Li, D., *Electrokinetics in microfluidics*, Elzevier, London 2004.

[6] Conlisk, A. T., McFerran, J., Zheng, Z., Hansford, D., *Anal. Chem.* 2002, *74*, 2139–2150.

[7] Karniadakis, G., Beskok, A., *Microflows: fundamentals and simulation*, Springer-Verlag, New York 2001.

[8] Attard, P., Mitchell, D. J., Ninham, B. W., *J. Chem. Phys.* 1988, *88*, 4987–4996.

[9] Attard, P., Mitchell, D. J., Ninham, B. W., *J. Chem. Phys.* 1988, *89*, 4358–4367.

[10] Qiao, R., Aluru, N. R., *Phys. Rev. Lett.* 2004, p. 198301.

[11] Greberg, H., Kjellander, R., *J. Chem. Phys.* 1998, *108*, 2940–2953.

[12] Kjellander, R., Greberg, H., *J. Electroanalyt. Chem.* 1998, *450*, 233–251.

[13] Freund, J. B., *J. Chem. Phys.* 2002, *116*, 2194–2200.

[14] Cui, S. T., Cochran, H. D., *J. Chem. Phys.* 2002, *117*, 5850–5854.

[15] Qiao, R., Aluru, N. R., *J. Chem. Phys.* 2003, *118*, 4692–4701.

[16] Burgreen, D., Nakache, F. R., *J. Phys. Chem.* 1964, *68*, 1084–1091.

[17] Rice, C. L., Whitehead, R., *J. Phys. Chem.* 1965, *69*, 4017–4024.

[18] Ninham, B. W., Parsegian, V. A., *J. Theor. Biol.* 1971, *31*, 405–428.

[19] Dubois, M., Zemb, T., Belloni, L., Delville, A., Levitz, P., Setton, R., *J. Chem. Phys.* 1992, *96*, 2278–2286.

[20] Hansen, J. P., Trizac, E., *Physica A* 1997, *235*, 257–268.

[21] Thompson, A. P., *J. Chem. Phys.* 2003, *119*, 7503–7511.

[22] Qiao, R., Aluru, N. R., *Nano Letters* 2003, *3*, 1013–1017.

[23] de Carvalho, R. J. F. L., Trizac, E., Hansen, J.-P., *Phys. Rev. E* 2000, *61*, 1634–1647.

[24] Deserno, M., von Grünberg, H., *Phys. Rev. E* 2002, *66*, 011401.

[25] Alberts, B., Bray, D., Lewis, J., Raff, M., Roberts, K., Watson, J. D., *Molecular biology of the cell, 2nd ed.*, Garland Publishing, New York 1989.

[26] Behrens, S. H., Grier, D. G., *J. Chem. Phys.* 2001, *115*, 6716–6721.

[27] Behrens, S. H., Borkovec, M., *J. Phys. Chem. B* 1999, *103*, 2918–2928.

[28] Zheng, J. J., Yeung, E. S., *Anal. Chem.* 2002, *74*, 4536–4547.

[29] Iki, N., Kim, Y., Yeung, E. S., *Anal. Chem.* 1996, *68*, 4321–4325.

5

Control and quenching of electroosmotic flow with end-grafted polymer chains

F Tessier, GW Slater. *Macromolecules* **38**, 6752–6754 (2005)

Control and Quenching of Electroosmotic Flow with End-Grafted Polymer Chains

Frédéric Tessier and Gary W. Slater*

Department of Physics, University of Ottawa, 150 Louis-Pasteur, Ottawa, Ontario, Canada K4A 2E7

Received April 20, 2005

Revised Manuscript Received June 21, 2005

Electroosmotic flow (EOF) refers to a fluid flow induced by an external electric field applied parallel to a solid surface and occurs when a space charge builds up in the fluid near the surface (e.g., the deprotonation of silanol groups at a silica–water interface leaves a net negative surface charge bound to the silica and positive solvated counterions in a diffuse layer near the surface, called the Debye layer). When an external electric field is applied, the mobile counterions are set in motion and, through viscous coupling with the uncharged fluid, eventually drag the bulk of the solution in a uniform flow. EOF is an efficient mode of fluid transport at small scale, and for microfluidic applications it is strongly preferred over Poiseuille flow because (1) it does not require large pressure gradients and (2) it exhibits a flat velocity profile which helps maintain the integrity of material samples transported in solution.[1–3] Ways in which the EOF can be tuned, or eventually quenched, are of immediate pratical relevance,[4–7] to decouple electrosmotic and electrophoretic motion of analytes in order to optimize the separation of biomolecules, to cite one example. Polymer coatings are routinely employed to modulate the EOF or to reduce the adsorption of analytes in capillary electrophoresis, and they exercise their control by either regulating the capillary surface charge or enhancing viscosity near the capillary surface (and therefore reducing the ion mobility in the Debye layer), or both.[8] Despite the wealth of empirical knowledge about the chemistry, processing, and performance of a large number of coatings, a fundamental understanding of the way in which adsorbed (dynamic coatings) or grafted (covalent coatings) polymer molecules modulate the EOF is still lacking. In particular, the relative merit of charge regulation and viscosity enhancement is hardly tractable experimentally. In our opinion, Harden, Long, and Ajdari provided the best theoretical account of the problem to date,[9] extracting insightful scaling laws for the EOF mobility in the presence of end-grafted neutral polymers, as a function of the grafting density and field strength.

The goal of this short communication is straightforward. We report on the first molecular dynamics simulation study of EOF control with grafted polymer chains. We show evidence that momentum absorption by neutral grafted macromolecules is, alone, capable of modulating the EOF strength, eventually to a point of where the bulk flow rate vanishes. The simulations are coarse-grained, typically involve on the order of 10^5 individual particles, and explicitly account for hydrodynamic and electrostatic interactions. Our generic approach is not chemically specific and allows us to model relatively small Debye length systems, thereby extending the scope of our conclusions to the microfluidic regime.

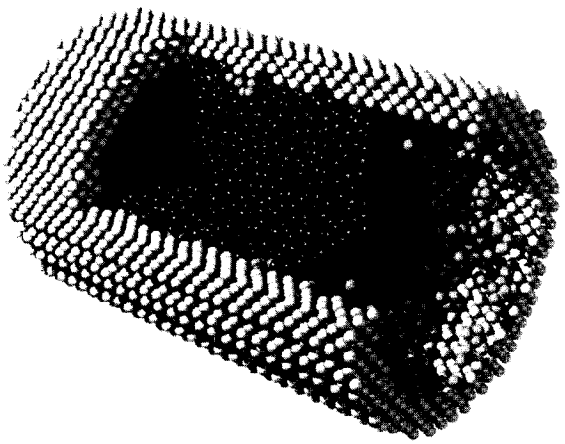

Figure 1. A cut view of a section of the capillary, captured from a simulation of EOF control via end-grafted polymer chains (with some particles removed to reveal the interior of the system). Shown here are the wall (gray), the fluid (blue), positive ions (red), negative ions (black), monomers (yellow), and grafting sites (orange). The diameter of the beads in the figure corresponds to the LJ interaction range, the unit of length in this paper. In this particular picture, the inner capillary wall bears a negative surface charge density $\sigma = -0.1$, the salt density is $n_0 = 0.02$, and the grafted polymer chains have a length $N = 5$ (instead of $N = 10$, for clarity).

We choose to tackle this problem with united-atom molecular dynamics (MD) simulations,[10,11] an ubiquitous technique for discrete fluid simulation. All particles in our simulations interact with a pairwise purely repulsive (truncated) Lennard-Jones (LJ) potential. We confine the fluid inside a cylindrical shell extruded from an fcc lattice, with periodic boundary conditions along the capillary axis, to model a narrow, infinitely long capillary (see Figure 1). Wall particles differ from fluid ones in that they are anchored to fixed lattice sites via a harmonic potential. We model self-avoiding grafted polymer chains of length N by stringing together N particles with a finitely extensible nonlinear elastic (FENE) potential and further binding the first monomer of the chain to a wall site using the same potential.

To introduce the electrostatic aspect of EOF, we endow some particles (randomly selected in the fluid or on the inner surface of the capillary wall, respecting overall neutrality) with an electric charge and add between all charged pairs a Coulomb interaction, truncated at distances beyond a third of the capillary length. It is generally incorrect in 3 dimensions to impose a cutoff on the long-ranging Coulomb interaction, but in our case the system only extends along one direction so we may consider the interaction as short-ranged[10] for distances larger than twice the capillary radius a. By varying the cutoff length r_c from $1a$ to $8a$, we verified that simulation results are independent of the cutoff value when it is above $3a$, and we chose a safe $r_c \approx 5a$ in producing our final data. We control the temperature of the system by periodically rescaling the velocity of the particles in the outer layers of the capillary wall to keep their mean kinetic energy consistent with the target temperature. We thus effectively only couple the outside of the capillary to a heat sink, ensuring that our thermostat does not bias the net fluid velocity or the hydrodynamic effects during EOF.

10.1021/ma0508404 CCC: $30.25
Published on Web 00/00/0000 PAGE EST: 2.3

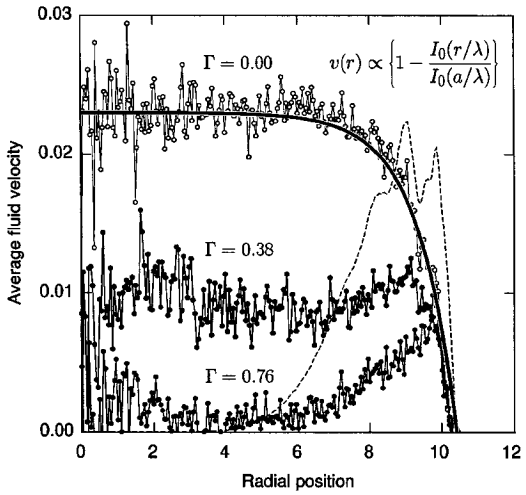

Figure 2. Molecular dynamics EOF velocity profiles in a capillary of radius $a \approx 10.4$, without a polymer coating (open circles) and for two polymer grafting densities $\Gamma = 0.38$ and $\Gamma = 0.76$ (filled circles). The wall charge density is $\sigma = -0.1$, the salt density is $n_0 = 0.02$, and the external field is $E = 1$. The grafted polymers have length $N = 10$, and the normalized monomer distribution is shown as a dashed line (using an arbitrary scale); it is the same for both values of Γ. The thick line is a fit of the polymer-free EOF flow profile to the continuum theory prediction, given in the top right of the figure.

Physical quantities herein are quoted as dimensionless numbers and are understood to be multiplied by an appropriate combination of the natural MD units: the LJ range parameter σ for length, the LJ energy scale ϵ for energy, and the mass m_f of fluid particles. Together these three units determine the natural MD unit of time $\tau = \sqrt{m_f\sigma^2/\epsilon}$. The system is initialized in a random state, and the particle trajectories are integrated using the velocity-Verlet algorithm with a time increment $\Delta\tau = 0.001\tau$, for more than 10^6 steps. All simulations reported here are carried out with the same mean fluid density $\tilde{\rho}_f = 0.8$, mean wall density $\tilde{\rho}_w = 1.0$, temperature $k_BT = 1.0$, capillary radius $a = 10.4$, capillary length $L = 158.7$, Coulomb cutoff length $r_c = 50$, and the same Bjerrum length $\lambda_B = 2$ (corresponding to that of water, a fluid with a high dielectric constant).

The EOF arises naturally in our simulations when we apply an external electric force on all the charged particles. We choose a surface charge density of −0.1 for the inside capillary wall (with compensating positive counterions in the fluid) and a fluid salt density of 0.02. This yields a Debye length $\lambda \approx 1$, and as expected, the flow initially arises in this layer, near the wall, where there is a net charge. However, the bulk of the fluid is rather quickly dragged into a steady-state flow, which exhibits a uniform velocity outside the Debye layer, as shown in Figure 2, where the open circles show simulation results for the steady-state EOF velocity profile when an external field $E = 1$ is applied. The thick solid line corresponds to the velocity profile expected from continuum electrostatics and hydrodynamics: $v(r) \propto [1 - I_0(r/\lambda)/I_0(a/\lambda)]$ (where I_0 is the modified Bessel function of the first kind);[12] the proportionality constant is the only fitted parameter. Our simulation technique thus reproduces the known qualities of EOF faithfully. The measured velocities exhibit relatively large fluctuations because we are limited to small external fields; larger fields generate to much Joule heating inside the fluid for the wall thermostat to regulate the temperature effectively. Note that the magnitude of the EOF is inversely proportional to viscosity and that our fluid, in the bulk, has about a fourth of the viscosity of water (this is not surprising, given the absence of the attractive part in the LJ interaction and the absence of hydrogen bonds).

We now arrive at the central question of this communication: in what measure can neutral polymer chains grafted on the capillary surface reduce the magnitude of the EOF flow, and can they quench it altogether? We consider the impact of chains of length $N = 10$ grafted on the inside surface of the capillary, for two surface grafting densities $\gamma = 0.05$ and $\gamma = 0.10$. It is convenient to cast γ into the dimensionless coverage parameter $\Gamma = \gamma\pi R_g^2$ (where R_g is the radius of gyration of the polymer) to give a sense of whether we are in a "mushroom" regime ($\Gamma < 1$) or a "brush" regime ($\Gamma > 1$).[9] For grafted chains of length $N = 10$, we have extracted $R_g = 1.56 \pm 0.07$, so the two grafting densities studied correspond to $\Gamma \approx 0.38$ and $\Gamma \approx 0.76$; both cases thus correspond to a mushroom regime. The steady-state results for the corresponding flow profiles are shown in Figure 2, where they can be compared to the situation where there is no polymer coating on the capillary wall. The dashed line in Figure 2 gives the shape of the normalized monomer distribution as a function of radial position to show that the coating thickness is commensurate with the Debye length (the distribution is essentially the same for both grafting densities, supporting the idea that we are in a mushroom regime rather than a brush regime).[9,13] The results in Figure 2 clearly indicate that the grafted chains significantly reduce the ability of the drifting ions in the Debye layer to drag the bulk of the fluid into a uniform flow. At $\Gamma = 0.76$, the flow velocity in the central part of the channel has practically vanished, even though the flow generation has not relented in the immediate vicinity of the wall. We should point out that the net charge density is practically unaffected by the presence of the polymers, so the shear plane does not move away from the wall in the coated situation (the zeta potential is the same). We also note that the field is small enough that both the monomer and the net charge distributions are not affected significantly during flow; hence, there is no charge regulation at work here. The only mechanism of EOF control is a transfer of energy from the fluid adrift inside the Debye layer to the grafted chains by collisions, and in turn to the wall particles, where it is evacuated as heat.

To our knowledge, this is the first simulation work that confirms the operation of a viscosity-only quenching of EOF. Although it is not surprising that EOF is reduced by anchored flexible molecules, it is unexpected to find that it is completely quenched at a coverage value well below the brush regime threshold and without any shift in the position of the shear plane. These first results compel us to investigate more closely the dependence of EOF mobility on the chain length N and the coverage parameter Γ. We will report on these simulations in a future, more detailed publication and compare our results directly with the theory of Harden, Long, and Ajdari, valid in the limit of vanishing Debye length.[9] Other critical parameters definitely include the chain stiffness and the field strength (we have implemented a new profile-unbiased thermostat derived from

dissipative particle dynamics,[14] which can be applied to the whole fluid, allowing us to study regimes where the conformation of the grafted chains is affected by the flow). Finally, our approach is also geared toward the study of adsorbed polymer coatings, and we think it will provide some fundamental insight into the peculiar mode of operation of adsorbed coatings conjectured from experimental evidence.[7]

Acknowledgment. The authors gratefully acknowledge the support of the Natural Sciences and Engineering Research Council of Canada (NSERC) and of the National Institutes of Health (NIH) of the USA (Grant NHGRI R01 HG002918-01).

References and Notes

(1) Israelachvili, J. *Intermolecular and Surface Forces*; Academic Press: San Diego, 1992.
(2) Russel, W. B.; Saville, D. A.; Schowalter, W. R. *Colloidal Dispersions*; Cambridge University Press: Cambridge, 1989.
(3) Li, D. *Electrokinetics in Microfluidics*; Elsevier: London, 2004.
(4) Horvath, J.; Dolnik, V. *Electrophoresis* **2001**, *22*, 644–655.
(5) Dolnik, V. *Electrophoresis* **2004**, *25*, 3589–3601.
(6) Doherty, E. A. S.; Meagher, R. J.; Albarghouthi, M. N.; Barron, A. E. *Electrophoresis* **2003**, *24*, 34–54.
(7) Doherty, E. A. S.; Berglund, K. D.; Buchholz, B. A.; Kourkine, I. V.; Przybycien, T. M.; Tilton, R. D.; Barron, A. E. *Electrophoresis* **2002**, *23*, 2766–2776.
(8) Steiner, F.; Hassel, M. *Electrophoresis* **2003**, *24*, 399–407.
(9) Harden, J. L.; Long, D.; Ajdari, A. *Langmuir* **2001**, *17*, 705–715.
(10) Allen, M. P.; Tildesley, D. J. *Computer Simulation of Liquids*; Clarendon Press: Oxford, 1992.
(11) Rapaport, D. C. *The Art of Molecular Dynamics Simulation*; Cambridge University Press: Cambridge, 1995.
(12) Rice, C. L.; Whitehead, R. *J. Phys. Chem.* **1965**, *69*, 4017–4024.
(13) De Gennes, P. G. *Macromolecules* **1980**, *13*, 1069–1075.
(14) Soddeman, T.; Dunweg, B.; Kremer, K. *Phys. Rev. Lett.* **2003**, *68*, 046702.

MA0508404

6

Modulation of electroosmotic flow strength with end-grafted polymer chains

F Tessier, GW Slater. *Macromolecules* **38**, ASAP article (2006)

Modulation of Electroosmotic Flow Strength with End-Grafted Polymer Chains

Frédéric Tessier and Gary W. Slater*

Department of Physics, University of Ottawa, Ottawa, Ontario K1N 6N5, Canada

Received October 13, 2005; Revised Manuscript Received November 29, 2005

ABSTRACT: We report on coarse-grained molecular dynamics simulations of the electroosmotic flow (EOF) of an electrolyte confined in a cylindrical, nanoscopic pore. We present results for the equilibrium distribution of fluid particles and ions in the electrolyte, and we show that our computational model reproduces the well-known characteristics of EOF in the steady-state regime, in particular the well-known pluglike character of this type of flow when the Debye length is small compared to the characteristic channel size. Upon adding a number of neutral, grafted polymer chains on the interior capillary surface, we find a significant reduction of the magnitude of the EOF. We characterize the polymer coatings and further show that the observed reduction in flow strength, as a function of polymer surface coverage, is in quantitative agreement with recent theoretical scaling predictions regarding the coupling of EOF and polymer coatings in small Debye length systems. As far as we know, our results constitute the first independent, quantitative verification of these predictions.

1. Introduction

Electroosmotic flow (EOF) refers to a fluid flow induced by an external electric field applied parallel to a solid surface and occurs when a space charge builds up in the fluid near the surface. This interfacial charge may arise for different reasons, a common one being the ionization of chemical groups attached to the surface and the ensuing accumulation of counterions in an electric double-layer (EDL) near the interface (e.g., the deprotonation of silanol groups at a silica−water interface results in a net negative surface charge bound to the silica and positive counterions in solution). The EDL is often conceptually divided into an adsorbed layer (the Stern layer) and a diffuse layer of counterions; when an external electric field is applied parallel to the surface, the mobile charges in the diffuse layer are set in motion and, through viscous coupling with the uncharged fluid, eventually drag the bulk of the solution in a uniform flow.[1−5]

EOF is an efficient mode of fluid transport at small scale. Although it poses its own set of challenges, mainly regarding the control of surface chemistry, EOF is often preferred over Poiseuille (pressure-induced) flow for two main reasons: (1) The velocity of a Poiseuille flow is proportional to the square of the capillary radius; hence, the pressure gradient required to obtain decent flow rates often becomes impractical as the system size is reduced. For example, generating a 1 mm/s flow of an aqueous buffer in a 1 μm wide capillary (or 1 pL/s) already demands a pressure gradient of nearly 100 atm/cm! (2) Poiseuille flow exhibits a parabolic velocity profile, which unduly disperses material samples transported in solution. In contrast, electroosmosis generally produces a rather flat velocity profile (often called a plug flow), and for typical experimental conditions, a modest applied electric field of about 100 V/cm can reproduce the flow conditions quoted above.

A renewed interest in EOF, especially in the context of microfluidic technology, is manifest in recent publications extending EOF theory to handle time-dependent regimes[6−10] and treat completely new ideas[11,12] or proposing numerical schemes aimed at solving the constitutive equations of EOF in specific geometries.[13−15] Of a different character, in that they do not rely a priori on a continuum hydrodynamic model, molecular dynamics (MD) simulations, in which the flow emerges naturally from the integrated equations of motion of a large number of particles (representing solvent molecules, ions, etc.), have also attracted attention lately.[16−24] MD simulations provide a fundamental picture of fluid flow at the molecular scale and are likely to play a critical role in the development of nanofluidic technologies. In this article, we report on coarse-grained MD simulations of EOF in a nanoscopic cylindrical pore (or capillary), which explicitly account for the discrete nature of fluid molecules as well as hydrodynamic and electrostatic interactions; our generic approach (detailed in section 3) allows us to model large systems with nearly 5×10^4 individual particles. In contrast to some other recent EOF simulations performed in atomistic detail, we are able within our coarse-grained approach to model an electrolyte with a Debye length significantly smaller than the capillary radius; hence, the scope of our conclusions extends in part to the case of macroscopic channels.

We show in this paper that our MD model reproduces the basic characteristics of electrolytes and EOF very well, and then we consider the modification of the capillary surface with grafted polymer chains to investigate in what measure the latter is able to modulate and eventually quench the EOF altogether. This is of immediate technological relevance,[25−28] e.g., to decouple electroosmotic and electrophoretic motion of analytes in order to optimize the separation of biomolecules. Polymer coatings are routinely employed to modulate the EOF and/or to reduce the adsorption of analytes in capillary electrophoresis. These coatings exercise their control either by regulating the capillary surface charge or by enhancing viscosity near the capillary surface, or both.[29] Despite the wealth of empirical knowledge about the chemistry, processing, and performance of a large number of coatings, a fundamental understanding of the way in which adsorbed (dynamic coatings) or grafted (covalent coatings) polymer molecules modulate the EOF is still lacking. While there is considerable interest and a number of recent reports on the deformation of grafted polymers in flows near solid surfaces, we could only find one theoretical article, albeit an exceptional one, by Harden, Long, and Ajdari,[30] dedicated entirely to the coupling between the electroosmotic flow and the deformation of grafted polymer chains and the consequence

10.1021/ma0522211 CCC: $33.50
Published on Web 00/00/0000 PAGE EST: 10.6

of this coupling on the far-field solvent flow, self-consistently. Therein the authors establish some clear predictions for the deformation of polymers and for the effective bulk EOF velocity as a function of the polymer grafting density, the polymer size, and the field strength. At the end of section 2, we review the simplest limits of their theory, which serve as a baseline in the interpretation of our simulation data. As announced in our short Communication published recently,[24] this article provides elaborate details on methodology, equilibrium results for a confined electrolyte, and steady-state EOF data and ultimately offers a systematic and quantitative account of EOF modulation as a function of the coverage fraction of the polymer coating.

2. Theory

2.1. Continuum Theory of Electroosmotic Flow. Before describing our computational model and presenting our simulations results, we briefly recall the continuum theory of EOF, which relies on a combination of the Poisson equation for the electrostatic potential and the Boltzmann equation for the distribution of charges inside the diffuse layer. In general, if k refers to one of N_s ionic species present in the solution, each of valence z_k (including sign), we obtain the well-known Poisson–Boltzmann (PB) equation

$$\nabla^2\phi(\mathbf{r}) = -\frac{e}{\epsilon}\sum_{k=1}^{N_s} z_k n_{0k} \exp\{-ez_k\phi(\mathbf{r})/k_BT\} \quad (1)$$

where $\phi(\mathbf{r})$ is the potential at position $\mathbf{r}$, e is the elementary charge, ϵ is the permittivity of the solvent (we assume it is a constant), k_B is the Boltzmann constant, and T is the absolute temperature. The n_{0k} factors are the ionic concentrations of each species in the bulk (far away from the charged wall). For the case of a symmetric univalent (1:1) electrolyte of bulk concentration n_0 confined in a system of characteristic size a, we often find eq 1 written as (in terms of the dimensionless potential $\phi^* = e\phi/k_BT$)

$$\nabla^2\phi^*(\mathbf{r}) = \frac{2e^2n_0}{\epsilon k_BT}\sinh\phi^*(\mathbf{r}) = \kappa^2\sinh\phi^*(\mathbf{r}) \quad (2)$$

The important parameter $\kappa \equiv (2n_0e^2/\epsilon k_BT)^{1/2}$ introduced here is the inverse of the Debye length λ_D, a widely recognized measure of the extent of the diffuse charge layer (also called the Debye layer). The dimensionless combination κa is called the electrokinetic radius and amounts to the system size expressed in terms of the Debye length. The linear or Debye–Hückel (DH) approximation of eq 2, namely $\nabla^2\phi^*(\mathbf{r}) \approx \kappa^2\phi^*(\mathbf{r})$, can be invoked when $|\phi^*| < 1$ everywhere in the system. It is in this linear context that, in 1965, Rice and Whitehead (RW) first derived the properties of EOF in a cylindrical pore,[31] and their solution for the net charge density is given in terms of Bessel functions as

$$\rho(r) = -\epsilon\kappa^2\zeta\frac{I_0(\kappa r)}{I_0(\kappa a)} \quad (3)$$

where r is the distance from the capillary axis, a is the radial position of the boundary of the diffuse layer, and $\zeta \equiv \phi(a)$ is the value of the electric potential at $r = a$. In dimensionless form, in terms of $\rho^* = \rho/n_0e$ and $\zeta^* = e\zeta/k_BT$, eq 3 becomes

$$\rho^*(r) = -2\zeta^*\frac{I_0(\kappa r)}{I_0(\kappa a)} \quad (4)$$

If we further consider continuum hydrodynamics, we can substitute expression 3 for the charge density $\rho(r)$ into the electric body force term in the Navier–Stokes (NS) equation and solve for the fluid velocity field. Assuming that the flow is in steady state under the action of an external field E oriented along the axis of the capillary, that there are no pressure gradients, and that the fluid viscosity η is constant, the NS equation reduces to

$$\nabla^2 v(r) = -\frac{E\rho(r)}{\eta} \quad (5)$$

Upon substituting the DH solution for $\rho(r)$ and integrating, we find

$$v(r) = -\frac{\epsilon\zeta E}{\eta}\left(1 - \frac{I_0(\kappa r)}{I_0(\kappa a)}\right) \equiv v_0\left(1 - \frac{I_0(\kappa r)}{I_0(\kappa a)}\right) \quad (6)$$

where we have defined $v_0 \equiv \epsilon\zeta E/\eta$, the so-called "Helmholtz–Smoluchowski" velocity for the fluid far away from the charged surface (beyond the Debye layer). Note that when the ratio $I_0(\kappa r)/I_0(\kappa a)$ is replaced by $e^{-\kappa x}$ in eqs 3 and 6, we recover the appropriate solutions for a planar geometry (with x the distance from an infinite plane).

Apart from the DH linearization itself which is only reliable when $|\phi^*| < 1$, the assumption that $n_{0k} = n_0$ for all ionic species, implicit in going from eq 1 to eq 2, is in fact only valid when either the diffuse layer thickness is small compared to the characteristic system size ($\kappa a \gg 1$) or when the system is in equilibrium with a bulk electrolyte reservoir of concentration n_0. The first condition is easily violated in nanoscale capillaries, where the surface-to-volume ratio is large (i.e., there is no bulk phase inside the capillary), and although the second condition is usually met in practical settings, it is typically not enforced in simulation work, in which the total number of ions is usually fixed (NVT ensemble). In a closed nanoscale system, counterions ionized from the surface affect the ionic concentrations significantly across the entire system, and we must resort to numerical solutions of the PB equation, with values of n_{0k} determined from a self-consistent numerical solution of eq 1 under ionic conservation constraints. This point is often overlooked in the EOF literature, although it has been addressed in the context of cell models in colloid science.[32–36] We have recently presented a treatment of the issue that is both more concise and more amenable to the study of EOF in small κa systems.[37] The gist of the matter is that the PB equation for a 1:1 electrolyte can be casted in a form that resembles eq 2

$$\nabla^2 u(\mathbf{r}) = \kappa_{\text{eff}}^2\sinh u(\mathbf{r}) \quad (7)$$

where u is simply the dimensionless electric potential ϕ^* shifted by a constant, and $k_{\text{eff}} \equiv (2n_{\text{eff}}e^2/\epsilon k_BT)^{1/2}$ is the inverse of an effective Debye length that can only be determined numerically (from boundary conditions and charge conservation integrals) and that depends on the salt concentration n_0, the wall charge density σ, and the system size a via the dimensionless combination $s \equiv |\sigma|/n_0a$. The quantity s measures the importance of the counterions dissociated from the wall, compared to that from the dissolved salt. When $s \ll 1$, the contribution of wall counterions is negligible, and we expect a bulk situation, where the effective ionic concentration away from the wall is essentially the same as the nominal salt concentration. In the opposite regime, when $s \gg 1$, the situation is dominated by the wall counterions, and both the ionic concentration and the net charge can increase well above that of the bulk approximation

values, across the whole system. It turns out that there exists a simple approximation for k_{eff}

$$\kappa_{eff} \approx \kappa (1+s)^{1/4} \quad \text{or} \quad n_{eff} \approx n_0 (1+s)^{1/2} \tag{8}$$

where n_{eff} is then an effective salt concentration. This approximation is reliable when the wall charge σ is small enough and, most notably, even outside the linear DH regime.

2.2. Coupling between EOF and Polymer Coatings. In their self-consistent theory for the interaction between the EOF and grafted polymer chains,[30] Harden, Long, and Ajdari explore the limits of both the "mushroom" regime, in which the grafted chains are essentially isolated from one another, and the "brush" regime, in which the chains are closely packed and swell in the direction perpendicular to the surface.[38] To quantify these limits, it is customary to define a dimensionless coverage parameter $\gamma^* \equiv \gamma\pi R_g^2$, where γ is the surface polymer grafting density (the number of chains per unit area) and $R_g \equiv \langle R_g^2 \rangle^{1/2}$ is the equilibrium radius of gyration of the polymers (the angled brackets denote an ensemble average). This quantity is then proportional to the fraction of the wall surface area that is covered by polymer molecules; typically, the mushroom regime corresponds to $\gamma^* \ll 1$ and the brush regime to $\gamma^* \gg 1$. We draw specific attention to the predictions of Harden et al. for the effective bulk EOF velocity v_{eff}, which can be directly extracted from simulation data. In the mushroom regime, they consider that the chains act as isolated obstacles to EOF flow generation and therefore predict, to first order, a linear decrease in the fluid velocity with γ^*:

$$v_{eff} = v_0(1 - K_m\gamma^*) \quad (\gamma^* \ll 1) \tag{9}$$

where $K_m = K_m(N,E)$ is a proportionality factor which depends on the chain length N and the electric field strength E in nontrivial ways—detailed in the original paper—to account for the possible deformation of the chain in the flow field. In the brush regime, the argument relies on an analogy with the exponential screening $e^{-H/d}$ of the flow by a porous medium of height H and mean pore size d. A blob picture yields $H/d \sim \gamma^{*5/6}$, hence the scaling prediction

$$v_{eff} = \frac{v_0 K_b}{\cosh \gamma^{*5/6}} \approx v_0 K_b \exp(-\gamma^{*5/6}) \quad (\gamma^* \gg 1) \tag{10}$$

Here K_b is akin to K_m and also exhibits highly nontrivial dependencies on the polymer length and the field strength, to account for the perturbation of the brush in the flow field. These dependencies are carefully scrutinized by Harden et al., but for our purpose we only need to contemplate the undeformed brush limit, in which $K_b = 1$.

We should point out that eqs 9 and 10 above are derived under the assumption that the Debye length is much smaller than other characteristic lengths in the system, such as the polymer coil size, the channel radius a, or the spacing between grafting sites, so that the diffuse charge layers are considered to be infinitely thin. Interestingly, this approximation allows one to cast the problem of grafted polyelectrolytes into a simpler one involving only neutral chains.[30] At any rate, we are curious to compare the results of our simulations, in which the Debye length is finite, against the foregoing theoretical predictions.

3. Simulation Method

Our generic model of the full electrohydrodynamic aspect of EOF is based on united-atom molecular dynamics (MD), a ubiquitous technique in the field of discrete fluid simulation (especially when macromolecules are involved, given the prohibitive computational costs of an atomistic approach when relaxation times are very long). Our system consists of about 5 $\times$ 10^4 spherical particles interacting via the Weeks–Chandler–Andersen (WCA) pair potential (i.e., a truncated and shifted Lennard-Jones potential, so that only the repulsive part remains):

$$U_{WCA}(r) = \begin{cases} 4\epsilon\left[\left(\frac{b}{r}\right)^{12} - \left(\frac{b}{r}\right)^{6}\right] + \epsilon & r \le r_c \\ 0 & r > r_c \end{cases} \tag{11}$$

with $r_c = 2^{1/6}b$. Physical quantities in this article are quoted as dimensionless numbers and are understood to be multiplied by an appropriate combination of the natural MD units of b for length, ϵ for energy, m_f for the mass of fluid particles, and e for the elementary charge. The three first units determine the natural MD unit of time $\tau = \sqrt{m_f b^2/\epsilon}$. Because of the coarse-grained nature of the simulation, we should not attach to much importance to the interpretation of the fundamental units in terms of a specific physical system (e.g., a silica capillary filled with water at room temperature, etc.). However, to set things concretely, we can imagine that each fluid bead represents a molecule of water and that $\epsilon = k_BT$ (with $T = 300$ K), thereby establishing the rough correspondence $b \approx 0.3$ nm, $m_f \approx 18$ atomic mass units, and $\tau \approx 25$ ps. The trajectory of the particles is integrated using the velocity–Verlet algorithm with a time increment $\Delta\tau = 0.01\tau$. Most of the simulations are carried out with the same set of physical parameters, summarized in Table 1, along with corresponding approximate values in SI units according to the rough mapping established above, to provide a sense of scale. To aid in the description of our model, a snapshot of the simulation system is also provided in Figure 1.

Table 1. Simulation Parameters[a]

parameter	symbol	value (MD units)	~ value (SI units)
WCA interaction range	b	1	0.3 nm
WCA interaction strength	ϵ	1	$k_BT = 300$ K
fluid particle mass	m_f	1	3×10^{-26} kg
elementary charge	e	1	1.6×10^{-19} C
wall particle mass	m_w	3	9×10^{-26} kg
mean fluid number density	$\tilde{\rho}_f$	0.8	50 mol L^{-1}
mean wall number density	$\tilde{\rho}_w$	1.0	62 mol L^{-1}
wall spring constant	k_w	300	14 N m^{-1}
thermal energy	k_BT	1.0	300 K
bjerrum length	λ_B	2	0.6 nm
salt concentration	n_0	0.02	1 mol L^{-1}
surface charge density	σ	−0.1	−0.2 C m^{-2}
external electric field	E	3	3×10^6 V cm^{-1}
capillary radius	a	10.4	3 nm
periodic box length	L	127	38 nm
MD unit of time	τ	1	25 ps
MD integration time step	$\Delta\tau$	0.01	0.25 ps
total simulation time	t_{sim}	10^4–10^5	0.25–2.5 μs
coulomb interaction cutoff	r_{cc}	40	12 nm
FENE interaction strength	k	30	1.4 N m^{-1}
FENE interaction range	r_0	1.5	4.5 nm
DPD thermostat friction	η_{dpd}	1.5	10^{-14} g s^{-1}
total no. of particles	-	$\approx 5 \times 10^4$	$\approx 5 \times 10^4$
polymer grafting density	γ	0.01–0.15	10^{13}–10^{15} cm^{-2}
monomers per chain	M	2–20	2–20

[a] The values in MD units are understood to be multiplied by the appropriate combination of the four independent fundamental units of length (b), energy (ϵ), mass (m_f), and elementary charge (e). As an example, corresponding values in SI units are derived from the loose correspondence established for the four fundamental quantities. The polymer grafting density and the polymerization index are the parameters of most significance in this work.

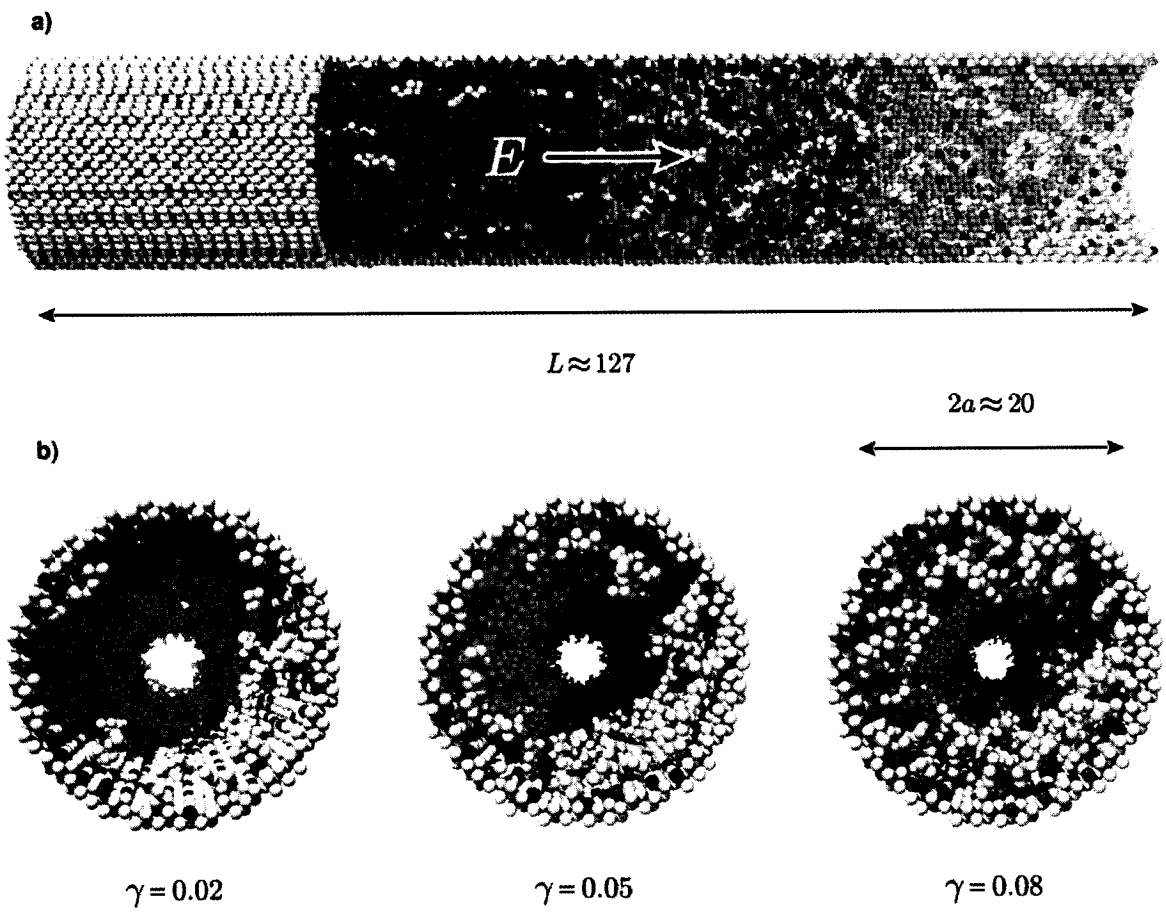

Figure 1. Visual snapshots from MD simulations of EOF control via grafted polymer chains. (a) The full length of the capillary, with some particles progressively hidden to reveal the different components of the system. Wall particles are shown in gray, fluid particles in blue, positive ions in red, negative ions in black, polymers chains in yellow, and polymer grafting sites in green. The diameter of the beads corresponds to b, the fundamental MD unit of length. Periodic boundary conditions are applied along the capillary axis, and the external field $E = 3$ is oriented toward the right. In this particular image, the grafting density is $\gamma = 0.02$, and each polymer chain comprises 10 monomers. (b) Axial snapshots, with fluid particles hidden, for three coatings of increasing polymer grafting density γ, for chains of length $M = 10$ (monomers that appear disjointed belong to chains partly outside the scope of the image). In these images, the external field is oriented out of the page.

3.1. The Capillary Wall. The capillary wall consists of a cylindrical shell extruded from an fcc lattice of mean density $\tilde{\rho}_w = 1.0$ with periodic boundary condition along the capillary axis, which models a narrow, infinitely long tube. Wall particles differ from fluid particles only in their mass m_w and in the fact that they are anchored to fixed lattice sites by simple harmonic springs with force constant k_w. We choose $m_w = 3$ and $k_w = 300$, ensuring that (1) the fundamental vibrational frequency of the wall ($\omega_w = \sqrt{k_w/m_w} = 10$) is comparable to the Einstein frequency of the fluid ($\omega_f \approx 7.8$, upon expanding the LJ potential around its minimum), so that the MD time step $\Delta\tau$ is appropriate for both; (2) the wall qualitatively behaves like a solid, in that the root-mean-square displacement of the wall particles remains below $0.1d$ (where d is the nearest-neighbor distance of the lattice; $d = (\sqrt{2}/\rho_w)^{1/3}$ in the fcc case), an empirical Lindemann criterion for melting,[39] which becomes $k_w > 3k_BT/(0.1d)^2 \approx 238$ in the current context; (3) the wall efficiently transports heat generated in the fluid by the Joule effect (i.e., we choose a small mass m_w within the limits imposed by the first two conditions). Any number of other combinations are possible, and the specific choice has little impact on the simulation outcome provided, of course, that the wall density is high enough to prevent fluid molecules from leaking out of the capillary. Given the capillary volume V (which is just the number of wall atoms removed to create the bore, divided by $\tilde{\rho}_w$) and the axial length L of the periodic box, the geometric inner capillary radius a is unambiguously determined from $V = \pi a^2 L$.

3.2. Electrostatic Interactions. To model the electrostatic aspect of EOF, we simply endow some particles with an electric charge and add between all charge pairs a truncated Coulomb interaction potential U_C, given here in dimensionless form:

$$\frac{U_C(r_{ij})}{k_BT} = \begin{cases} \dfrac{\lambda_B q_i q_j}{r_{ij}} & r \le r_{cc} \\ 0 & r > r_{cc} \end{cases} \qquad (12)$$

where r_{ij} is the distance between particles i and j, carrying charges q_i and q_j, respectively; we limit our study to univalent ions, i.e., we take $|q_i| = 1$. The Bjerrum length $\lambda_B \equiv e^2/4\pi\epsilon k_BT$ determines the relative strength of the electrostatic interaction (it corresponds to the distance at which the Coulomb energy between two unit charges is equal to the mean thermal energy). In all the simulations reported here we have set $\lambda_B = 2$, a value appropriate for water at room temperature. It is widely known that it is incorrect in 3 dimensions to impose a cutoff on the long-ranging Coulomb interaction, and Ewald summation

methods are required to take into account the contribution of the periodic images of the charges. In our case, however, the system only extends along one direction so we may consider the Coulomb interaction as short-ranged[40] for distances larger than the capillary diameter $2a$. By varying the cutoff length r_{cc} from $1a$ up to $8a$ (and increasing the periodic box length accordingly), we indeed verified that simulation results are independent of r_{cc} when it is beyond $3a$, and for the production of our final data, we chose $r_{cc} \approx 4a$, a very safe value.

The initial choice for which particles are charged is random, with the provision that the bound charges on the inner capillary surface are constrained to lie at a minimal distance from each other, so that the distribution remains more or less uniform. Pairs of opposite charges are thus applied randomly to fluid particles to model dissociated salt, and counterions opposite in charge but equal in number to the surface-bound charges are also introduced, to achieve overall electroneutrality. For all simulations we use the same salt concentration $n_0 = 0.02$ and the same surface charge density $\sigma = -0.1$ (the wall charges are negative; hence the counterions are positive). In terms of the Debye length introduced in section 2, for the largest capillary of radius $a = 10.4$ we have $\lambda_D = (8\pi n_0 \lambda_B)^{-1/2} \approx 1$, and according to eq 8, the effective Debye length is then $k_{eff}^{-1} \approx 0.91$. Thus, we expect that there will be a net positive charge and that the EOF will arise within a distance of one or two molecular diameters from the wall. Note that we do not expect to see a Stern layer of ions adsorbed on the solid surface because we use the same interaction parameters for fluid–wall and fluid–fluid interactions; at the level of our molecular-primitive model, a Stern layer would simply renormalizes the capillary radius and surface charge.

3.3. The Polymer Molecules. We model linear polymer molecules by stringing together M beads, or monomers, binding them with a finitely extensible nonlinear elastic (FENE) potential

$$U_{FENE} = \frac{1}{2}k \ln\left(1 - \frac{r^2}{r_0^2}\right) \tag{13}$$

where k and r_0 determine the stiffness and maximum extension of the bonds, respectively. We choose $k = 30$ and $r_0 = 1.5$, a widespread choice and an appropriate one to model a self-avoiding chain.[41] Another advantage of this potential over a simple harmonic one is that the polymer chain exhibits a physically realistic finite length, even under strong shear forces. In our simulations we tracked the intermonomer distance and found it to remain in the narrow range 0.97 ± 0.04. We graft each polymer to the interior capillary wall by attaching one of its ends to a random neutral wall particle with the same FENE interaction potential, and we also constrain grafting points to lie at a minimum distance from each other to limit fluctuations in the local grafting density. The polymers are initially "grown" from the grafting point in a random conformation, and in an attempt to keep the fluid density constant, we remove as many fluid particles as we add monomers (note that monomer pairs along the chain lie on average slightly closer than fluid particle pairs, so this actually implies a slight decrease in the mean fluid density). An important quantity in the analysis of the coupling between the EOF and the polymer coatings is the dimensionless coverage parameter $\gamma^* = \gamma\pi R_g^2$, which involves the equilibrium radius of gyration R_g of the chains. We have performed independent simulations to determine R_g for free chains (in bulk solution) and for isolated chains grafted on the interior capillary surface, as a function of the number of intermonomer bonds N in the molecule, with $N = M - 1$. The results are shown in

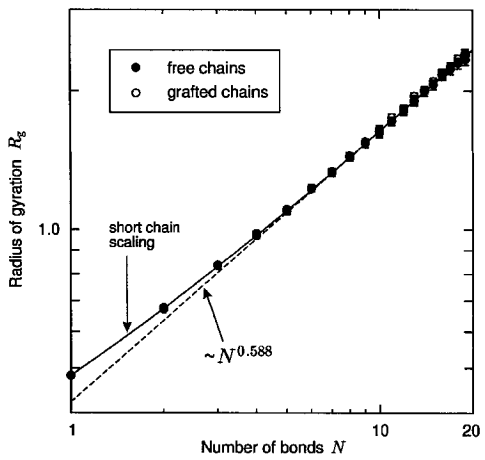

Figure 2. MD simulation results for the equilibrium radius of gyration of free and grafted FENE polymer molecules, as a function of the number of bonds N. The dashed line indicates the large N scaling relation $R_g \sim N^{\nu}$, where $\nu = 0.588$. The solid line is a nonlinear fit of a function which includes scaling corrections for small chains: $R_g = N^{0.588}(a_0 + a_1 N^{-1/2} + a_2 N^{-1} + a_3 N^{-2})$. The values we find for the expansion coefficients a_0, a_1, a_2, and a_3 are all within 25% of published, precise values for self-avoiding walks on a cubic lattice.[42] Where visible, the error bars indicate the standard deviation in the measured R_g values.

Figure 2, and it is nice to see that they are consistent with the large N scaling behavior $R_g \sim N^{0.588}$ (dashed line), as well as the known scaling corrections for small N (solid line; details in the figure caption).[42] The results also indicate that, for the small chain lengths considered here, grafting has little influence on the radius of gyration of the polymer coil, and in our analysis we use the free chain R_g values.

3.4. Temperature Control. Since we are preforming non-equilibrium electrokinetic flow simulations, energy is imparted to the system by the external electric field, and in steady state this energy is converted to heat, mostly through the friction between drifting ions and the surrounding fluid and wall (Joule heating). It is therefore essential that we extract this heat from the capillary to control the temperature of our system, and to this end we combine two strategies. First, the velocity of the wall particles are rescaled periodically (typically at every 100 steps of the velocity–Verlet integration, i.e., at every τ) to keep their average kinetic energy consistent with the target temperature $k_B T = 1$. However, this is found to be insufficient (unless really small field intensities are considered, but then the flow rates become intractable in realistic simulation times), and we therefore also need to couple the fluid particles directly to a heat bath, in a way that does not bias the fluid flow and that does not require a priori knowledge of the flow profile. There exists a number of "profile-unbiased" thermostats for nonequilibrium simulations, and in our simulations we resorted to the DPD thermostat (so-called because its formulation emerged from the dissipative particle dynamics simulation method). This novel and ingenious approach boils down to rescaling the relative velocities of neighboring particles, so as to leave intact hydrodynamic interactions and the overall fluid velocity field.[43] We apply this thermostat between pairs of fluid particles, at every integration step. Finally, no thermostat is applied to the grafted polymer molecules, but their temperature is well controlled by the surrounding fluid and by their direct coupling with the wall.

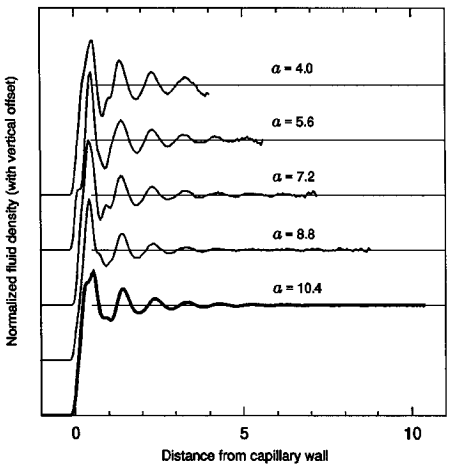

Figure 3. Normalized local fluid density $\rho_f/\tilde{\rho}_f$ as a function of the distance from the capillary wall (defined as $a - r$), for different capillary radii a, in equilibrium ($E = 0$ and $\gamma^* = 0$). The curves are offset from each other for clarity, and the horizontal lines correspond in each case to the value of the mean fluid density $\tilde{\rho}_f = 0.8$; their vertical separation of 0.5 provides a vertical scale.

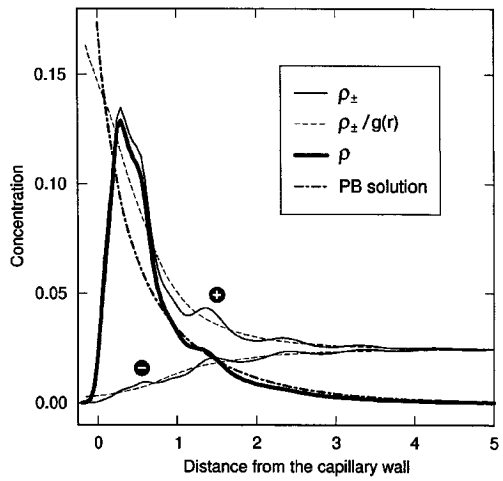

Figure 4. Details of the concentration profile for positive ions and negative ions (thin solid lines, as labeled on the graph) and for the net charge (bold solid line) near the capillary wall as a function of the distance from the wall ($a - r$), in equilibrium ($E = 0$ and $\gamma^* = 0$). The dashed curves show the ionic concentration data normalized by the local relative fluid density. The dash–dotted curve shows the net charge density predicted by the self-consistent numerical integration of the nonlinear PB eq 1 and compares favorably with the simulation results, except in the first fluid layer, where steric effects dominate.

4. Simulation Results

4.1. Equilibrium State. We first present equilibrium simulation results when there is no external field and no grafted polymers ($E = 0$, $\gamma^* = 0$). Figure 3 shows the normalized equilibrium distribution $g(r)$ of fluid particles across the capillary as a function of the distance to the capillary wall ($a - r$). The density of fluid particles shows decaying oscillations around the mean fluid density $\tilde{\rho}_f$ in the vicinity of the wall. The oscillations are very similar irrespective of the capillary radius, except for small changes in the fine structure due to the slightly different fcc lattice artifacts for different capillary radii. The values for the oscillation period (0.96 ± 0.01) and the decay length (1.2 ± 0.2) are both close to the characteristic separation of fluid particles ($\tilde{\rho}_f^{-1/3} \approx 1.08$). This layering phenomenon, due to the packing of fluid particles into layers near a solid surface, is well recognized both theoretically and experimentally.[1] Within our model it is not practical to study capillaries with a radius smaller than $a = 4.0$ because positional correlations between particles then become so strong across the whole bore as to induce intermittent crystallization of the fluid, akin to the stick–slip motion and the wall-induced glass transition observed in simulations by others.[44,45] For the rest of this work we focus on capillaries of radius $a = 10.4$ to obtain decent fluid phase in the center of the capillary and to clearly resolve the Debye length. We should reiterate here that the length of our periodic box along the capillary axis is $L = 127$, which is large enough to alleviate concerns about hydrodynamic and electrostatic self-interaction artifacts.

In Figure 4, we present results for the equilibrium charge distribution as a function of the distance to the capillary wall ($a - r$). The thick solid curve shows the net charge density ρ, obtained directly by summing the separate ionic densities ρ_+ and ρ_-, represented by thin solid lines and as labeled on the graph. The thin dashed curves give a view of the ionic concentrations $\rho_\pm$ normalized by the density oscillations $g(r)$, and the smooth profiles thus rendered show that the electrostatic and steric aspects are in first approximation separable. The PB equation therefore remains useful in predicting the charge distribution in small capillaries on a length scale smaller than the decay of density oscillations. This is confirmed most clearly by the thick dot–dashed curve, which corresponds to the net charge density profile calculated from the self-consistent solution of the nonlinear PB eq 1 (we cannot use the linear DH approximation here because $\zeta^* \approx 1.5$). The agreement with the MD simulation results is remarkable, except within one molecular diameter b of the capillary wall, as expected since the theory does not account for the finite size of the ions. The theory therefore overestimates the charge concentration in the immediate vicinity of the wall and underestimates it in the first molecular layer; however, beyond the first solvent layer the PB prediction is already quite accurate. We should note that dividing the charge density by $g(r)$ is not strictly correct because this operation does not conserve the total charge. More rigorously, we could account for packing effects in the theory by including an effective chemical potential $\mu_{pack} = \ln(g(r))$ in both exponentials in eq 1.[20] Of course, the function $g(r)$ is generally not known a priori, but it is easily extracted from a single simulation.

Beyond the right edge of the graph, toward the center of the capillary, the net charge density vanishes, and the positive and negative ionic number densities both tend toward the value $n_{eff} = 0.0247 \pm 0.0001$, which is higher than the initial salt concentration $n_0 = 0.02$. This increase is due to the absence of a bulk ionic reservoir in our system, as discussed in the paragraph leading to eq 7 in the theory above. Note that the net charge density does not necessarily vanish at $r = 0$. It does here, within the measurement uncertainty, because the Debye length is sufficiently small compared to the capillary radius. The simulation value for n_{eff} compares favorably with that prescribed by eq 8, i.e., $n_{eff} \approx n_0(1 + s)^{1/2} \approx 0.0243$, but this is partly fortuitous because the full numerical integration of the PB equation in fact predicts $n_{eff} \approx 0.0226$, which is about 10% lower. Perhaps we can attribute the discrepancy between the measured and theoretical values of n_{eff} to the structure of the fluid near the wall. According to Figure 4, ions are displaced away from the wall compared to the continuum theory prediction because of steric interactions, and it is certainly reasonable to

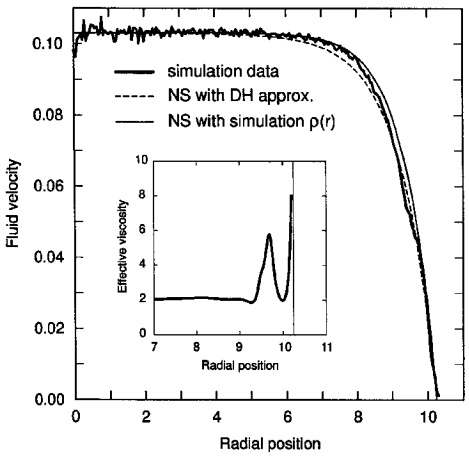

Figure 5. Steady-state EOF axial velocity $v(r)$ of fluid particles as a function of the radial position in the capillary, for an external field $E = 3$ (thick solid curve). Also shown are the prediction of the Rice and Whitehead formula based on a combination of the DH approximation for the charge density and the NS equation (dashed curve) and the numerical integration of the NS equation using the charge density determined directly from simulation data (thin solid curve). Inset: the position-dependent viscosity, as calculated from the NS equation, the charge distribution and the EOF velocity profile. The thin vertical line shows the position of the capillary wall.

expect that this has an impact on the charge density at $r = 0$, at least for the capillary size we are considering.

4.2. Steady-State EOF. We now turn to nonequilibrium simulations, in which we apply an external electric field to generate EOF, but in which the capillary walls are still free of grafted polymers. These "free-flow" results will serve as our reference scenario to calculate the reduction in the EOF strength when we consider polymer coatings in the next subsection. The electric field is included in the simulation in the form of an additional axial force qE acting on all charged particles. There is a compromise in choosing for the field strength; i.e., it must be large enough so that the velocity profiles can be resolved in a realistic computational time, yet if it is too strong it becomes difficult to control the temperature of the fluid effectively; we settle for the value $E = 3$, and we verified that under these conditions the thermostat can keep the temperature of the fluid constant across the bore and within about 1.5% of the target temperature $k_BT = 1$; the temperature gradient is located almost entirely within the capillary wall.

In Figure 5, we present the steady-state velocity profiles $v(r)$ of the fluid during EOF. The transient between the equilibrium state and the fully developed flow typically lasts about 100τ after the onset of the external field, and we only consider data points beyond 500τ in the calculation of fluid velocity profile, to ensure that they correspond to the steady-state regime. We immediately notice that we recover the expected plug-flow-like character of EOF: the profile is quite flat in the center of the capillary, and the shear is located mostly within a couple of Debye lengths from the capillary wall. We also see that our model produces a no-slip boundary condition since the fluid velocity vanishes at $r = a$. Actually, careful inspection reveals that the velocity vanishes at $r = 10.25 \pm 0.05$, which is slightly smaller than the geometrical capillary radius, and we will therefore use this reduced value in our analysis of velocity profiles. It is remarkable that, despite the irregularities in the interior wall due to the fcc lattice structure, the capillary radius inferred from geometry and from electrokinetic data agree to within 2%. The small fluctuations in the velocity profile are due to thermal noise: the typical flow velocity here is 0.1, compared to a nominal thermal velocity of $\sqrt{3k_BT/m_f} \approx 1.73$. We are thus extracting a 5% signal from the thermal motion background, and we manage to reduce fluctuations below 5% by averaging over 10^3-10^4 velocity profiles collected every 10τ during long simulations (lasting anywhere between $10^4\tau$ and $10^5\tau$).

Table 2. Three Data Sets Used in the Analysis of EOF Control with Polymer Coatings[a]

data set label	no. of data points	grafting density γ	monomers per chain M
M10	10	0.010−0.100	10
G025	10	0.025	2−20
G100	10	0.100	2−20

[a] Each set contains 10 data points, in most cases obtained from two independent simulations with the same parameters. In the text, the data sets are referred to by labels M10, G025, and G100.

We include in Figure 5 the expression derived by Rice and Whitehead for the velocity, quoted in eq 6, replacing κ by $k_{eff} \approx 1.06$, using $a = 10.25$ and taking v_0 as a fitting parameter (dashed curve; the fitted value $v_0 = 0.103 \pm 0.001$ implies a small Reynolds number $Re \approx 1$, and we are thus in a laminar flow regime). It is somewhat surprising to find that the velocity profile shape is predicted rather well by the linearized theory with adjusted parameters (it is important to note that k_{eff}, which determines the shape of the curve, is not a fitting parameter here; its value is calculated independently). We can also integrate the NS eq 5 numerically using the net charge density data $\rho(r)$ measured during EOF (different from that shown in Figure 4 because the net charge is slightly displaced away from the wall during flow) to obtain the prediction of continuum hydrodynamics without a predefined model for the distribution of charges. The predicted profile is included in Figure 5, as a thin solid line, and we see that it also describes the simulation data very well. At any rate, we cannot assess the accuracy of the predictions categorically because of possible fcc ordering artifacts and because we do not have an independent value for v_0 in the theoretical models. The variation in viscosity due to steric constraints near the wall also probably play a role. In fact, assuming continuum hydrodynamics to be valid at the molecular scale, we can estimate the local viscosity $\eta(r)$ of the fluid from electrokinetic data by writing the NS equation in cylindrical coordinates as

$$\eta(r)\nabla^2 v(r) + \frac{d\eta}{dr}\frac{dv}{dr} + \rho(r)E = 0 \qquad (14)$$

where both the charge density $\rho(r)$ and the fluid velocity $v(r)$ are directly available from simulation data (although we have to smooth the velocity profile by fitting it with a combination of a modified Bessel function and a 10th-order polynomial; FFT and running average filters do not yield curves amenable to second-order differentiation). The result of the numerical integration for $\eta(r)$ is shown in the inset of Figure 5. According to this calculation, the viscosity indeed exhibits notable variations near the wall, probably on account of the strong layering confinement of particles in the first fluid layer.

4.3. Characterization of Polymer Coatings. Given the foregoing simulation results, we are satisfied that our simulation method reproduces the features of equilibrium electrolytes and steady-state EOF very well. We now present the central point of this article, namely, a quantitative investigation of the coupling between polymer coatings and EOF, especially in light of the predictions of Harden et al. presented in the Theory section. We first summarize in Table 2 the three data sets on which we base our analysis; M10 corresponds to a data set in

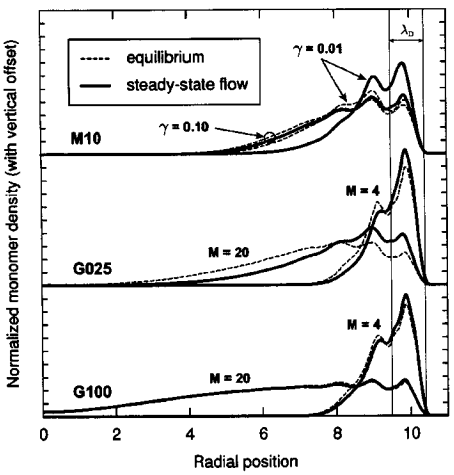

Figure 6. Radial monomer distribution in the capillary for two representative cases taken from each of the three data sets M10, G025, and G100, as labeled on the graph. We normalized the density values by γM (i.e., by the total number of monomers divided by the capillary surface) to resolve all the curves on the same scale, and we added a vertical offset between different data sets for clarity. Tick marks on the vertical axis are separated by 0.1, and the baseline for each set is evident from the curves themselves. The dash line show the equilibrium distribution when $E = 0$, i.e., when there is no flow, and the thick solid lines show the profiles during steady-state EOF, for $E = 3$. The Debye length λ_D is also indicated on the figure.

which only the grafting density is varied, for a fixed chain length, while G025 and G100 correspond to sets in which M, the number of monomers per chain, is varied, for two different grafting densities. All the other physical parameters, in particular the field strength E, assume the constant values indicated in Table 1.

The curves in Figure 6 show the normalized density of monomers as a function of radial position inside the capillary for various values of γ and M. For each data set, we show two curves: small and large values of grafting density for M10, short and long chains for G025 and G100; the curves for intermediate parameter values (not shown) interpolate well between the ones presented here. These plots characterize the polymer coating in the radial direction. The difference in profiles between the equilibrium situation ($E = 0$, dashed curves) and the steady-state flow situation ($E = 3$, solid curves) provides valuable information about the deformation of the polymers under the action of the EOF. The G100 data set indicates that for the high grafting density $\gamma = 0.1$ the monomer distribution is practically unaffected by the EOF, irrespective of chain length; the flow is not strong enough to deform these tight brushes (note that the EOF strength itself depends on the coating density, of course). On the other hand, the G025 set shows that for the small grafting density $\gamma = 0.025$ large chains incur significant deformation; the EOF pulls on the grafted chains and thus displaces the monomers toward the capillary surface. Finally, the set M10 shows a transition as the grafting density increases, for a fixed chain length: the $\gamma = 0.01$ case exhibits deformation, but the $\gamma = 0.1$ case practically none. It also clearly shows a transition from a mushroom regime to a brush regime: monomers in chains of equal lengths lie further from the surface as the grafting density increases. Assessing the flow-induced deformation of the polymer coating is important because the theoretical predictions of Harden et al. for the reduction in EOF strength due to grafted polymer chains depend on chain deformation via the numerical factors K_m and K_b in eqs 9 and 10, respectively.

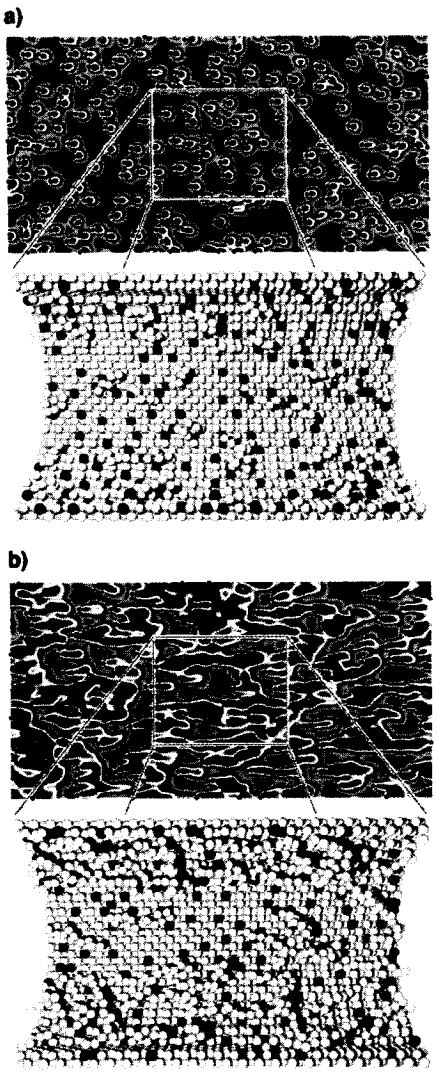

Figure 7. Visual representations of the polymer surface coatings at low grafting density $\gamma = 0.025$ (from the G100 data set), during steady-state electroosmotic flow, oriented toward the right. In the density plots, red indicates a mean monomer density of 0.5, blue represents a density of zero, and the black contours a density of 0.25. The small black points represent the anchor point of each polymer. The simulation snapshot images represent a small portion of the wall, as indicated. Wall particles are shown in gray, the wall-bound negative ions in black, the grafted chains in yellow, and the grafting sites in green; other components are hidden to reveal the structure of the coating. (a) Chains composed of six monomers are displaced from their grafting position, but they adopt conformations that are not atypical of the equilibrium state. (b) Chains composed of 14 monomers, on the other hand, incur large deformations in the direction of the flow.

A more compelling representation of the polymer coverage is provided by surface density plots such as those in Figure 7. These images show the monomer coverage density, i.e., the average number of monomers observed per unit area "above" each point of the interior capillary surface (the monomer positions are projected radially onto the surface). The red represents a mean coverage density of 0.5 or more, blue corresponds to a coverage density of zero, and the black dots show the position of the grafting sites. We show two steady-state EOF cases taken from the G025 data set: in panel Figure 7a, the chains are short and thus not affected much by the EOF. They are displaced slightly from their respective grafting points in the direction of the flow (toward the right in the figure), but

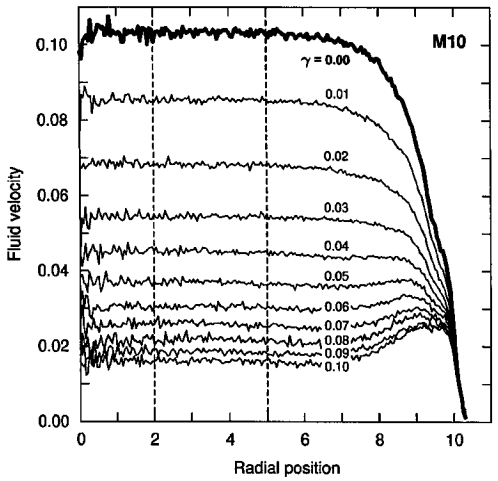

Figure 8. Molecular dynamics data of fluid velocity profiles used to determine the impact of polymer coatings on the magnitude of the EOF. We show here the data from the M10 set, with one curve for each value of the grafting density γ, as labeled on the graph. The effective bulk fluid velocity is obtained in each case from the 60 data points that lie between the vertical dashed lines.

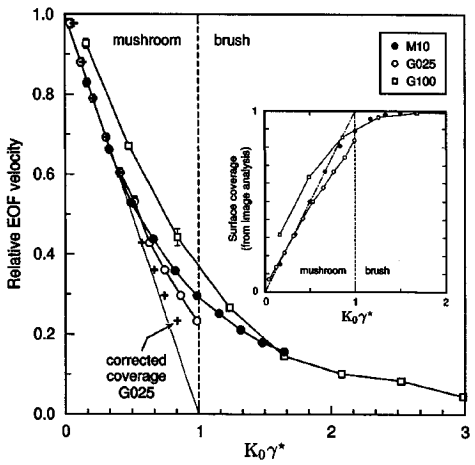

Figure 9. Relative bulk EOF velocity v_{eff}/v_0 as a function of the nominal polymer coverage density $K_0\gamma^*$, for all three data sets M10, G025, and G100. The value $K_0\gamma^* = 1$ (dashed line) divides the mushroom regime from the brush regime. The inset shows the actual coverage, obtained from the image analysis of monomer density plots (see Figure 7), as a function of the nominal coverage. Crosses on the graph show the G025 data replotted as a function of the corrected coverage values, which are more reliable in cases where the grafted polymers are deformed by the flow.

they adopt conformations that are not atypical of undeformed coils. In Figure 7b, we see how long chains are elongated in the direction of the flow by the EOF. We also remark that there is significant overlap of the chains, so that coverage fractions calculated from an isolated chain approximation are certainly overestimated. In fact, we can obtain a more reliable estimate of the polymer coating coverage fraction from a direct analysis of the density plots in Figure 7. The black contours in the images correspond to a mean monomer coverage density of 0.25; we choose to count all sites (or pixels) above this threshold as occupied (inside the contours), and the fraction of occupied sites thus yields a value for the surface coverage fraction of the coating (the choice of the value 0.25 will be motivated in the next subsection). According to this method, the situations in parts a and b of Figure 7 correspond to coverage fractions of about 0.22 and 0.65, compared to nominal γ^* values of 0.22 and 0.58, respectively. We also include in Figure 7 three-dimensional snapshots from a small section of the wall (as indicated on the figure) from the corresponding MD simulations, with fluid and solvated ions removed, to show what each coating actually looks like during steady-state EOF.

4.4. EOF Modulation with Polymer Coatings. We now present results for the reduction of the EOF due to grafted, neutral polymer chains. As our initial data, we take the average velocity profiles of the fluid as a function of the radial position r in the capillary, such as those presented in Figure 8 for the data set M10, i.e., for different values of γ at fixed chain length $M = 10$. Right away we see that there is indeed screening of the flow by the polymer coating at high grafting density: the fluid velocity is higher in the Debye layer, where the flow is generated, than in the bulk, away from the wall and the coating. We compute the effective bulk EOF velocity v_{eff} in each case by averaging over the velocity profile between $r = 2$ and $r = 5$ (to avoid the large fluctuations at small r and the shear layer near the wall), and we divide this value by the reference free-flow EOF velocity v_0 to obtain the relative EOF velocity. In Figure 9, we plot this relative velocity, v_{eff}/v_0, as a function of the dimensionless parameter $K_0\gamma^*$, where K_0 is the small deformation limit of K_m. We determine the value $K_0 = 2.20 \pm 0.05$ from eq 9 and from two data points in set G025 corresponding to $M = 4$ and $M = 6$. By comparing radial monomer density profiles with and without flow (see Figure 6), we found that these were the two mushroom regime cases that featured the least deformation of the grafted chains during EOF. The value of $K_0\gamma^*$ is thus a good measure of the surface coverage of the polymer coating for isolated chains, and accordingly, the vertical dashed line at $K_0\gamma^* = 1$ indicates the onset of the brush regime, wherein the polymer coating effectively covers the entire surface.

This is corroborated by the graph inset, in which we plot, as a function of the nominal coverage value $K_0\gamma^*$, the coating coverage fraction obtained independently from the analysis of monomer coverage density images, as detailed in the previous subsection (the only adjusted parameter in the image analysis procedure is the threshold 0.25, chosen so that the image analysis yields the same coverage as $K_0\gamma^*$ for the small deformation case $\gamma = 0.025$ and $M = 6$). Points to the right of the dash–dotted line of unit slope correspond to cases for which $K_0\gamma^*$ overestimates the value of the coating coverage (and conversely), on account of the deformation of the chains (in the sparse grafting G025 case) or because of steric interactions between chains and the emergence of the brushlike character (in the dense grafting G100 case). Fortuitously, chain deformation and steric interactions seem to compensate for each other up to a coverage fraction of about 0.8 for data in the M10 set. We remark that all the data points for which $K_0\gamma^* > 1$ correspond to coverage fractions above 0.9; hence, this threshold is indeed a good predictor of the brush regime. As mentioned above in the discussion of the radial monomer density profiles, the coatings in the M10 data set clearly show a transition from a mushroomlike regime to a brushlike one, whereas in G025 they retain a mushroom character for all chain lengths, and in G100 they mostly correspond to brushes.

On the basis of these data, let us consider the theoretical predictions of Harden et al., starting with eq 9 for the mushroom regime. We disregard the G100 data set here because the high grafting density $\gamma = 0.1$ implies that it does not include any mushroom regime data points (except perhaps for the shortest chain, but in that case the coating thickness barely spans the Debye length and the relative EOF velocity is then obviously

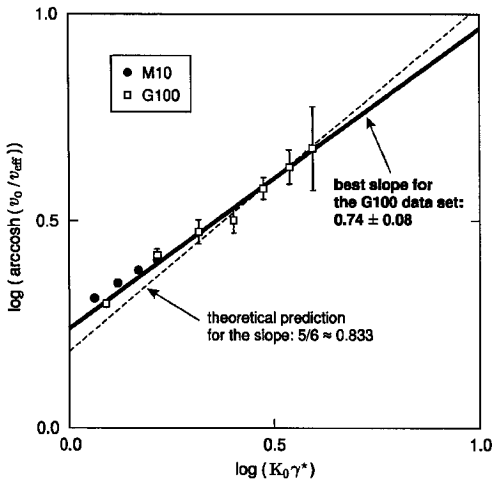

Figure 10. A plot of the brush regime data points from the M10 and G100 data sets, in a form appropriate to extract the exponent of γ^* in eq 10. The bold curve shows the best fit to the values from the G100 set, with a slope of 0.74 ± 0.08. However, as indicated by the dashed line, the highest coverage data points are certainly not inconsistent with the slope 5/6 = 0.83 predicted from a hydrodynamic screening argument.

biased upward). Our simulation results for v_{eff}/v_0 as a function of $K_0\gamma^*$, shown in Figure 9, support the prediction that the magnitude of the EOF in the mushroom regime decreases linearly with the fraction of the surface that is covered by the polymers. Indeed, data from both the M10 and G025 sets show the same linear decrease with surface coverage. Furthermore, if we correct the coverage fraction values according to the inset, to take into account flow-induced polymer deformation of the grafted chains, we improve the agreement between data points from the G025 data set and the linear decrease of unit slope, as indicated by crosses in Figure 9.

For the analysis of the brush regime, we focus our attention on the high coverage data points of the G100 set, i.e., points for which $K_0\gamma^* > 1$. In Figure 10, we replot the relative EOF velocity so as to isolate the value of the exponent of γ^*, following the form of eq 10 (we recall that, according to the radial monomer profiles in Figure 6, brushes are essentially undeformed in the G100 data set, so we take $K_b = 1$). Upon fitting the brush regime data points with a linear function on the logarithmic graph, we find that the simulation results are best described by the equation

$$\frac{v_{eff}}{v_0} = \cosh^{-1}\{(1.74 \pm 0.08)\gamma^{*0.74\pm0.08}\} \qquad (15)$$

Thus, we find that the value of the exponent of γ^* is just beyond one standard deviation from the scaling prediction $^5/_6 = 0.8\overline{3}$ derived from the hydrodynamic screening argument. For comparison, a line of slope $^5/_6$ is also shown on the graph, and we see that the data points are qualitatively consistent with it, especially if we consider the highest coverage values. The points from the M10 set are also included in Figure 10; they do not seem to follow exactly the same trend, possibly because the brushes in M10 do incur some deformation for moderate grafting densities. In any event, the M10 curve does not extend high enough beyond $K_0\gamma^* = 1$ to be conclusive in regards to the brush regime exponent.

5. Conclusion

We carried out large-scale molecular dynamics simulations of EOF inside a nanoscale cylindrical pore and reproduced, in a quantitative way, the distribution of ions similar to what is expected from continuum theory. The oscillations of the fluid density, although manifest near the solid wall, do not appear to have a critical impact, in the sense that we can treat them separately with reasonable accuracy (provided they do not span the whole capillary pore); this is in agreement with what others have reported.[46] Classical continuum equations should not be discounted, even at the nanoscale, on the sole fact that they overlook the discrete nature of solvent molecules. The distribution of ions in the pore is predicted quite successfully by the nonlinear PB equation, provided that the effective electrolyte concentration is determined in a self-consistent way. We also considered the case where an external electric field is applied to the ions, and we reproduced an EOF velocity profile which is consistent with the predictions of continuum hydrodynamics. Note that we considered a Debye length that is about one-tenth of the capillary radius, so our findings are not necessarily specific to nanoscopic capillaries. Evidently, the scope of our conclusions is modulated by the choice of a particular simulation model. Others have performed simulations of EOF with atomistic resolution[17−20] and have reported dramatic effects pertaining, e.g., to ionic sizes and species, hydration effects, and Stern layers. The advantage of a more generic approach is precisely that it isolates the physical aspects of the problem from chemical specificity. It is also computationally more efficient, allowing for the simulation of larger length and time scales and of more complex situations that involve, case in point, polymer chains.

The main goal of this paper was to investigate the modulation of the EOF by static polymer coatings. Upon including neutral chains grafted to the interior capillary surface in our simulations, we find that the reduction of the EOF follows the theoretical predictions of Harden et al. quite well, in both the mushroom and the brush regimes (even though the theory is derived in the limit of an infinitely small Debye length). When the chains are isolated from each other, the EOF decreases linearly with γR_g^2 (with a proportionality constant $K_0 = 2.2 \pm 0.2$; it is interesting to note that we have $K_0\gamma\pi R_g^2 \approx \gamma(^3/_2R_g)^2 \approx \gamma(2R_H)^2$, where R_H is the hydrodynamic radius of the coil). In the brush regime, the coating screens the EOF generated near the surface, and the characteristic scaling exponent 0.74 ± 0.08 that we extract from simulation data is just short of the theoretical value $^5/_6$. However, our results certainly do not rule out the value $^5/_6$, and we need to consider higher density brushes to conclude more definitely on this matter. This will require significantly larger capillaries because the longest chains considered in this work already extend close to the center of the capillary (moreover, the brush height scales linearly with N), and increasing the grafting density beyond $\gamma = 0.1$ is not practical within our model (it becomes difficult to grow the chains and the fluid density near the wall decreases significantly).

There are many directions in which to pursue this research further. In particular, we could attempt to verify more precisely the detailed predictions of Harden et al., including dependencies on the polymer length and the field strength, although we are limited in varying these two parameters by the size of the capillary and by issues with temperature control during the simulation. We could vary the Debye length to determine the behavior of the EOF in terms of λ_D/R_g and consider the case of polyelectrolyte coatings by adding charges to the monomers. We could also investigate the transient between the equilibrium state and the fully developed flow after the onset of the external field to see how polymer coatings affect the establishment of the flow in the first place. On a side note, we would maybe pay attention to the very small but systematic dip in the EOF

velocity profile at the interface of the fluid and the polymer brush (consider Figure 8, for $\gamma \geq 0.05$). Finally, our model is readily amenable to the study of dynamic coatings, which consist of adsorbed, rather than grafted, polymer chains. Intriguing experimental observations[28] concerning the magnified action of dynamic polymer coatings with reduced adsorption still lack a definitive explanation.

Acknowledgment. The authors gratefully acknowledge the support of the Natural Sciences and Engineering Research Council of Canada (NSERC) and of the National Institutes of Health (NIH) of the USA (Grant NHGRI R01 HG002918-01). F.T. also extends his gratitude to colleagues Michel Gauthier, Martin Kenward, and Jean-François Mercier for fruitful discussions. The authors are grateful to HPCVL, SHARCNET, and Westgrid for high-performance computational resources.

References and Notes

(1) Israelachvili, J. *Intermolecular and Surface Forces;* Academic Press: San Diego, 1992.
(2) Russel, W. B.; Saville, D. A.; Schowalter, W. R. *Colloidal Dispersions;* Cambridge University Press: Cambridge, 1989.
(3) Behrens, S. H.; Borkovec, M. *J. Chem. Phys.* **1999**, *103*, 2918−2928.
(4) Viovy, J. L. *Rev. Mod. Phys.* **2000**, *72*, 813−872.
(5) Karniadakis, G.; Beskok, A. *Microflows: Fundamentals and Simulation;* Springer-Verlag: New York, 2001.
(6) Erickson, D.; Li, D. Q. *Langmuir* **2003**, *19*, 5421−5430.
(7) Yang, C.; Ng, C. B.; Chan, V. *J. Colloid Interface Sci.* **2002**, *248*, 524−527.
(8) Kang, Y. J.; Yang, C.; Huang, X. Y. *Int. J. Eng. Sci.* **2002**, *40*, 2203−2221.
(9) Ren, L. Q.; Li, D. Q. *J. Colloid Interface Sci.* **2001**, *243*, 255−261.
(10) Dutta, P.; Beskok, A. *Anal. Chem.* **2001**, *73*, 5097−5102.
(11) Gitlin, I.; Stroock, A. D.; Whitesides, G. M.; Ajdari, A. *App. Phys. Lett.* **2003**, *83*, 1486−1488.
(12) Ajdari, A. *Phys. Rev. E* **2000**, *61*, R45−R48.
(13) Ren, L. Q.; Sinton, D.; Li, D. Q. *J. Micromech. Microeng.* **2003**, *13*, 739−747.
(14) Jin, Y.; Luo, G. A. *Electrophoresis* **2003**, *24*, 1242−1252.
(15) Patankar, N. A.; Hu, H. H. *Anal. Chem.* **1998**, *70*, 1870−1881.
(16) Thompson, A. P. *J. Chem. Phys.* **2003**, *119*, 7503−7511.
(17) Qiao, R.; Aluru, N. R. *App. Phys. Lett.* **2005**, *86*,.
(18) Qiao, R.; Aluru, N. R. *Phys. Rev. Lett.* **2004**, *92*,.
(19) Qiao, R.; Aluru, N. R. *Nano Lett.* **2003**, *3*, 1013−1017.
(20) Qiao, R.; Aluru, N. R. *J. Chem. Phys.* **2003**, *118*, 4692−4701.
(21) Zhou, J. D.; Cui, S. T.; Cochran, H. D. *Mol. Phys.* **2003**, *101*, 1089−1094.
(22) Cui, S. T.; Cochran, H. D. *J. Chem. Phys.* **2002**, *117*, 5850−5854.
(23) Lo, W. Y.; Chan, K. Y.; Lee, M.; Mok, K. L. *J. Electroanal. Chem.* **1998**, *450*, 265−272.
(24) Tessier, F.; Slater, G. W. *Macromolecules* **2005**, *38*, 6752−6754.
(25) Horvath, J.; Dolnik, V. *Electrophoresis* **2001**, *22*, 644−655.
(26) Dolnik, V. *Electrophoresis* **2004**, *25*, 3589−3601.
(27) Doherty, E. A. S.; Meagher, R. J.; Albarghouthi, M. N.; Barron, A. E. *Electrophoresis* **2003**, *24*, 34−54.
(28) Doherty, E. A. S.; Berglund, K. D.; Buchholz, B. A.; Kourkine, I. V.; Przybycien, T. M.; Tilton, R. D.; Barron, A. E. *Electrophoresis* **2002**, *23*, 2766−2776.
(29) Steiner, F.; Hassel, M. *Electrophoresis* **2003**, *24*, 399−407.
(30) Harden, J. L.; Long, D.; Ajdari, A. *Langmuir* **2001**, *17*, 705−715.
(31) Rice, C. L.; Whitehead, R. *J. Chem. Phys.* **1965**, *69*, 4017−4024.
(32) Dubois, M.; Zemb, T.; Belloni, L.; Delville, A.; Levitz, P.; Setton, R. *J. Chem. Phys.* **1992**, *96*, 2278−2286.
(33) Attard, P.; Mitchell, D. J.; Ninham, B. W. *J. Chem. Phys.* **1988**, *88*, 4987−4996.
(34) Attard, P.; Mitchell, D. J.; Ninham, B. W. *J. Chem. Phys.* **1988**, *89*, 4358−4367.
(35) Hansen, J. P.; Trizac, E. *Physica A* **1997**, *235*, 257−268.
(36) de Carvalho, R. J. F. L.; Trizac, E.; Hansen, J.-P. *Phys. Rev. E* **2000**, *61*, 1634−1647.
(37) Tessier, F.; Slater, G. W., submitted for publication.
(38) De Gennes, P. G. *Macromolecules* **1980**, *13*, 1069−1075.
(39) Ubbelohde, A. R. *The Molten State of Matter;* John Wiley & Sons: Chichester, 1978.
(40) Allen, M. P.; Tildesley, D. J. *Computer Simulation of liquids;* Oxford University Press: New York, 1987.
(41) Kremer, K.; Grest, G. S. *J. Chem. Phys.* **1990**, *92*, 5057−5086.
(42) Dayantis, J.; Palierne, J. **1994**, *49*, 3217−3225.
(43) Soddemann, T.; Dunweg, B.; Kremer, K. *Phys. Rev. E* **2003**, *68*, 046702.
(44) Thompson, P. A.; Robbins, M. O. *Science* **1990**, *250*, 792−794.
(45) Thompson, P. A.; Grest, G. S.; Robbins, M. O. *Phys. Rev. Lett.* **1992**, *68*, 3448−3451.
(46) Freund, J. B. *J. Chem. Phys.* **2002**, *116*, 2194−2200.

MA0522211

7

Conclusion

According to a popular saying, "a conclusion is the place where you got tired of thinking". I hope, therefore, that this chapter will not be considered as a shortage of research interests, but merely as the necessary epilogue to the collection of articles presented in this thesis. The unifying theme throughout this work has been the use of computer models to study electrokinetic phenomena involving confined polymers, with specific, practical applications. We implemented both Monte Carlo and Molecular Dynamics methods, two pillars of modern computer simulation, to test theoretical predictions and uncover new phenomena in two systems of a rather different nature. We first considered a microfluidic device for the electrophoretic length-separation of DNA, and implemented a lattice Bond-Fluctuation algorithm to verify the validity of the proposed mode of operation. We then turned our attention to a nanofluidic capillary, and performed simulations with explicit hydrodynamic and electrostatic interactions, to investigate the coupling between static polymer coatings and the electroosmotic flow. As a tribute to the versatility of computer simulations, I will mention that other members of our research group are currently using essentially identical computer models to investigate such diverse problems as the nanopore translocation of polymers, the electrophoresis of polyelectrolytes and their collision with posts and other polymers in free-solution, microfluidic mixing, the diffusion of small globules through a matrix of obstacles, the growth of bacterial colonies, and the optimization of capsule drug-delivery. Computer models may in some cases seem unrealistic, but in polymer physics we usually strive to determine physical properties that are independent of the underlying local, chemical structure; generic models allow us to isolate such universal characteristics. Since my thesis is composed of a series of articles, a proper conclusion to each part of

the work is, of course, already found in the respective chapters. In what follows, I will nevertheless summarize the highlight of my research, and offer a few additional thoughts.

Our Monte Carlo simulations of the entropic trap array device, in Chapter 2, model the motion of long macromolecules in a periodic array of square wells linked by narrow constrictions. The results offer compelling evidence to uphold the idea that the electrophoretic migration of the molecules is well predicted by a simple free-energy model, derived from a balance between electric and entropic forces, in which we take the nucleation hernia length as the reaction coordinate. In particular, we reproduced the experimental observation that long molecules migrate faster than short ones in the microchannel, and quantitatively obtained an inverse field dependence of both the characteristic trapping time and the critical hernia nucleation size. Furthermore, simulations allowed us to investigate in detail the local dynamics and the conformation of the molecule as a function of its position in the device, and we clearly resolved the contribution of global deformation of the polymer coil to the separation process. We also showed that, by the same token, it would be possible to separate molecules according to topology, e.g., ring and trefoil-knot molecules, a prediction that for the moment awaits experimental confirmation. We were the first group to carry out a computational study of this microfluidic electrophoresis system, and our work has inspired others to work in the same direction (our article has up to now been cited by six other publications independent from our own). Streek *et al.*, from Bielefeld University in Germany, decided to tackle the problem using an off-lattice, Brownian Dynamics approach, another simulation method akin to Molecular Dynamics, but in which the solvent molecules are replaced by friction and random thermal fluctuations. They reported findings generally consistent with our own, as well as other possible separation mechanisms (Streek *et al.*, *J. Biotech.* **112**, 79–86, 2004; Streek *et al.*, *Physical Review E* **71**, 011905, 2005). The success of our approach also encouraged researchers at the University of California at Berkeley to consider the Bond Fluctuation algorithm as an efficient model to study the electrophoretic stretching of DNA around posts (Feree and Blanch, *Biophys. J.* **85**, 2539–2546, 2003). We should also note that the generic problem of a polymer translocating between two potential wells, over a potential barrier, has also been the subject of theoretical investigations, in particular by Park and Sung, and by Paul and Sebastian, with one particular approach by the latter group reviewed in Appendix C.

In our contribution to the special issue of *Applied Physics A* on the topic of ratchets, presented in Chapter 3, we showed that the electrophoresis device built by the Craighead group could very easily be turned into a ratchet system, wherein, notably, DNA molecules can be forced to move in opposite directions, depending on their length; obviously an optimal scenario as far as separation

resolution is concerned. The entropic ratchet effect which motivated this work was first reported by Slater *et al.* in 1997 in *Physical Review Letters*, and supported at the time with simulations in a two-dimensional asymmetric channel. Our new implementation demonstrated the practical reality of the phenomenon in an existing, three-dimensional system. However, the scope of our conclusions can probably be extended to a large class of systems in which macromolecules undergo entropic trapping (because the process rests largely on the non-linearity of the mobility as a function of the applied field). Given that it would be very easy to operate the entropic trap device in a ratchet mode, e.g., by simply driving the molecules with an alternating electric field, in the temporal asymmetry implementation, we are very surprised that it has not yet been tried experimentally — or at least not reported —, although we have personally discussed such opportunities with Han and Craighead! In fact, their original design was inspired in part by the discovery of Slater *et al.*, so they must be have been aware of the advantages of a ratcheting scheme. Our calculations of the various ratchet regimes relied on an analytical description of simulation data, which limited our calculations to the low-frequency response of the system. For the sake of completeness, we performed additional simulations to study a case in which the driving field frequency is commensurate with a natural timescale of the system (e.g., the translocation time). We thus uncovered a previously unreported "resonance" effect in the migration of intermittently trapped macromolecules: for a given modulation amplitude, the mobility of long chains through entropic traps can be increased significantly by tuning the driving field frequency. Our results demonstrate that this resonance, while broad in frequency, and thus not very useful to enhance separation directly, can nevertheless lead to an effective mobility that is higher than that observed for the average value of the driving field, without adversely affecting resolution of the separation process. Hence this strategy could find applications in optimizing the throughput of entropic trapping electrophoresis systems.

The only work in this thesis that did not involve simulation work *per se* is reported in Chapter 4, and consists of a theoretical and numerical investigation of the distribution of ions in an electrolyte confined within a closed, nanofluidic environment. We found a simple approximation to determine the effective salt density in systems where the surface-to-volume ratio is large enough that the ionic contribution of the surface is significant compared to that of the dissolved salt. This work actually derived from original attempts to solve the full Poisson-Boltzmann equation analytically, a project which unfortunately did not come to fruition. However, during this research we found that there existed a simple and useful expression that could describe ionic distributions in nanoscopic, closed systems. The approximation we proposed had in fact already been reported in other forms in the

context of the cell model in colloid science (a model which treats each colloidal particle as enclosed in its own electrolyte cell, with appropriate boundary conditions). However, upon finding that the existing literature on the subject was typically complicated by issues not relevant to the matter at hand, we decided to present a more concise treatment of the problem, one that is unburdened at the outset by linearization concerns, and that is more accessible to the electrophoresis community. With the advent of micro- and nanoscale devices, it becomes critical to pay attention to surface effects, which are often overlooked because, in traditional electrophoresis contexts, the presence of a bulk phase is usually a valid assumption.

My most recent research venture, and incidentally the first one considered at the beginning of this Ph.D. program, consisted of a Molecular Dynamics investigation of electrokinetic phenomena in confined geometries, a broad topic which we eventually narrowed down to the study of electroosmotic flow (EOF) modulation by polymer coatings in a cylindrical, nanofluidic capillary. As the results presented in Chapters 5 and 6 clearly demonstrate, grafted polymer chains can effectively reduce, even practically quench EOF. Most significantly, our simulations reproduced, quantitatively, the known features of EOF and the theoretical scaling prediction of flow modulation by a coating of neutral polymers. In the mushroom regime (isolated chains), the EOF reduction is proportional to the polymer surface coverage, and in the brush regime (full coverage), the flow strength exhibits an exponential decrease related to the thickness of the coating. To our knowledge, this work represents the first independent verification of these scaling predictions. Our most recent results are not yet published, but considering the positive comments regarding our short Communication (Chapter 5) and the manifest curiosity for the subject at various conferences, we are confident that this final publication will find a receptive readership. We should mention that our Molecular Dynamics program is amenable to the study of adsorbed, rather than grafted, polymer coatings (by simply inserting chains in the solution and adding a favourable interaction between monomers and wall particles). This is probably the most pressing and interesting research avenue in extending our work on this topic, because such dynamic polymer coatings are widely used, on an empirical basis, to control EOF or reduce analyte adsorption in capillary electrophoresis. A recent, experimental study by the Barron group at the University of Chicago has revealed a systematic reduction of the EOF as the affinity of the polymers for the wall *decreases* (Doherty *et al.*, *Electrophoresis* 23, 2766–2776, 2002). This is qualitatively understood in terms of the formation of a more diffuse coating layer, but experimental measurements cannot, at this time, resolve the onset of EOF reduction at small adsorption strength. We strongly believe that a simulation approach such as our own could address this issue.

A

Theory of DNA electrophoresis: a look at some current challenges

Slater GW, et al. *Electrophoresis* **21**, 3873 (2000)

Electrophoresis 2000, *21*, 3873–3887

Review

Gary W. Slater
Claude Desruisseaux
Sylvain J. Hubert
Jean-François Mercier
Josée Labrie
Justin Bolleau
Frédéric Tessier
Marc P. Pépin

Department of Physics,
University of Ottawa,
Ottawa, Canada

Theory of DNA electrophoresis: A look at some current challenges

Although electrophoresis is one of the basic methods of the modern molecular biology laboratory, new ideas are being suggested at an accelerated rate, in large part because of the pressing demands of the biomedical community. Although we now have, at least for some methods, a fairly good theoretical understanding of the physical mechanisms that lead to the observed peak spacings, widths and shapes, this knowledge is often too qualitative to be used to guide further technical developments and improvements. In this article, we review some selected elements of the current state of our theoretical ignorance, focusing mostly on DNA electrophoresis, and we offer several suggestions for further theoretical investigations.

Keywords: Gel electrophoresis theory / DNA separation and sequencing / Capillary electrophoresis / Free-flow electrophoresis / Ratchet separation systems / Simulations / Review

EL 4137

Contents

Correspondence: Dr. Gary W. Slater, Department of Physics, University of Ottawa, 150 Louis-Pasteur, Ottawa, Ontario, Canada K1N 6N5
E-mail: gslater@science.uottawa.ca
Fax: +613-562-5190

Abbreviations: **BD**, Brownian dynamics; **BRF**, biased reptation with fluctuation model; **BRM**, biased reptation model; **ELFSE**, end-labeled free-solution electrophoresis; **LPA**, linear polyacrylamide; **MC**, Monte-Carlo; **MD**, Molecular Dynamics; **PA**, polyacrylamide

1 Introduction

The development of automated capillary electrophoresis (CE) and capillary array electrophoresis (CAE) are the most recent technological advances that have made possible the completion of the sequencing of the human genome years ahead of the original estimates [1]. Besides sequencing further genomes for comparison and other applications (for example in the agricultural sciences), genetic testing and diagnostic will now represent the major pressure for the development of even higher throughput and more robust DNA analysis technologies. Electrophoretic technologies are likely to remain an important tool for years to come, although we are now seeing a clear evolution in the way electrophoresis is being used. For instance, the recent microchannel systems based on various entropic and ratchet concepts represent drastic departures from standard sieving-based electrophoretic processes. These novel ideas will be discussed in this review.

 0173-0835/00/1818-3873 $17.50+.50/0

We have published a review article covering some of the new, innovative separation ideas in 1998 [2]. Obviously, much progress has been made in most of these directions since then. Instead of updating our review, however, we decided to choose a different path. Standard review articles typically discuss the progress made over the last several years, showing the successes and predicting the probable course of the research for the next little while. Werner von Braun once said: "Fundamental science is what I do when I don't know what I am doing". Based on this unique philosophy, our review will actually focus on the state of our ignorance. A review of some of the theoretical questions that remain to be answered, is a useful first step towards designing new fundamental research programs (combining both experimental and theoretical investigations). We hope that this original approach will be useful to experimentalists wishing to carry out fundamental studies of electrophoretic processes, and to theoreticians who are looking for new challenges.

The plan of the article is simple: each section covers a different technological or theoretical topic. The sections typically describe several key questions, why they remain unanswered, what (if anything) has been done recently about it, and in some cases which path research might take. We thus offer questions, not answers. These questions apply to a variety of separation modes (CE, slabs, ratchets, free-flow, microchannels, *etc.*; Fig. 1 presents a schematic picture of the different CE and microchip separation modes that will be covered in this review) and uses (mapping, sequencing, preparative, sizing). Similarly, they are related to a number of fundamental theoretical issues (ionic effects, CE and microchannel walls, sieving mechanisms, diffusion and band broadening, resolution, and read length, entropic effects) and they may require a range of theoretical methods (scaling analysis, simple analytical models, complex computer simulations). Obviously, it is impossible to cover all aspects of DNA electrophoresis in a single review article. As many of us know, it is even hard to keep track of the evolution of the discipline! This is why *Electrophoresis's* excellent annual review articles are so important. Our reference list is by no mean complete. Our choice of questions is also far from being complete: the choice we made is certainly biased by our very own interests, as one would expect. We can assure the reader, however, that the scientific community ignores a lot more than what we discuss in this review!

2 How can we design a sieving matrix for DNA CE sequencing?

Polyacrylamide (PA) gels are no longer the electrophoretic sieving matrices of choice for small DNA fragments, especially for sequencing applications, since CE methods now dominate the technology. Although entangled solutions of very long polymers behave roughly like cross-linked gels (compare, *e.g.*, Figs. 1d and 1f), there are differences. Moreover, the larger number of parameters related to the polymer solution (the chemical composition, the molecular size and its polydispersity, the stiffness, the hydrophilicity or -phobicity, the polymer architecture, *etc.*) makes it more difficult to narrow the search for the optimal choice. Among the (numerous) factors that we must take into account, we find: (i) the possibility of using uncoated capillaries if the polymer self-coats the walls and kills the EOF [3]; (ii) the viscosity of the solution must be such that injection is mechanically doable; (iii) the entanglements must be long-lived compared to the relevant time scales [4]; (iv) the effective pore size of the solution must optimize the resolution [4]. In some cases, the polymer solution is self-organizing into microphases [5, 6]; the periodicity and geometry of these structures are then additional factors.

Perhaps the best studied sieving polymer is polydimethylacrylamide (pDMA) [3]. Heller [7–9] published a superb analysis of the performance of pDMA. His results show that the biased reptation model with fluctuations (BRF) [10–15], the best model that we currently have for understanding the electrophoresis of DNA fragments in dense porous systems, does not quite explain all the observations. Cottet *et al.* [4], on the other hand, described how theoretical concepts can be used to compare the performance of different polymers. Together, these studies provide a systematic methodology to characterize the sieving properties of polymer solutions. Unfortunately, most studies use less-than-optimal and hard-to-compare methodologies and data analysis approaches.

Perhaps the key questions where theory is lacking in predictive power are: (i) Is it preferable to have microstructures or homogeneous (nonassociating) polymer solutions? (ii) Is it preferable to have linear or branched polymers? (iii) How can we mix different polymers to optimize the resolution/read length? (iv) What length scales and time scales must be optimized when designing the polymer solution? (v) What happens when the concentration c of the solution is close to the overlap concentration c^*? (vi) what is the role of the polymer dynamics, especially on band broadening/diffusion processes? (vii) Can we use extremely high-fields in spite of the fact that the gel is elastic and compliant?

The best reported results appear to come from linear polyacrylamides (LPAs) [16], although there is no fundamental reason why PA should remain the leading polymer sieving matrix for DNA CE sequencing. There is certainly a lot of room for theoretical studies and computer model-

ing. Our knowledge of the physics of electrophoresis in polymer solutions is quite limited compared to what we previously achieved for gel electrophoresis. We believe that computer simulations will play an important role in the next few years since it is now possible to do realistic simulations of very detailed analyte-gel systems using a variety of computational tools.

3 Can end-labeled free-solution electrophoresis (ELFSE) be developed for sequencing applications?

Our group started developing a new method for DNA separation, which we called ELFSE, in 1994 [17]. ELFSE goes against intuition since it is usually taken for granted that separation of DNA fragments in the absence of a sieving matrix is impossible (indeed, the DNA free solution mobility μ_0 is normally molecular size-independent [15, 18]). ELFSE is based on the idea that one can create an "hydrodynamic asymmetry" by attaching a neutral object (a buoy!) at one end of the DNA molecules (see Fig. 1a). This object breaks the charge-to-friction symmetry and the mobility of a DNA molecule with M bases is then given by

$$\mu(M) = \mu_0 \frac{M}{M + \alpha} \qquad (1)$$

where α is the effective friction coefficient in the "buoy" (measured in number of equivalent DNA bases). Recently, we reported the separation of dsDNA fragments [19] and the sequencing of about 100 bases in $\approx$ 18 min [20]. This method would be perfect for CE and microchip technologies since it does not require the injection of viscous polymer solutions in small ID channels. Equation (1) clearly indicates that the number of DNA bases that we can sequence with ELFSE, is directly proportional to the "size" α of the buoy. Larger buoys would lead to increased read lengths [20]. However, it is not trivial to find a large monodisperse object that could act as an efficient ELFSE label. Although larger labels would considerably slow down the separation, previous experimental work demonstrated that high fields can be used with ELFSE since biased reptation does not take place in free solution [19]. With a streptavidin buoy ($\alpha \approx 30$), about 100 bases could be sequenced. To achieve 500–600 bases, we probably need a value as large as $\alpha \approx 250$ [17, 20]. If you add to this that this label must be perfectly monodisperse, uncharged and hydrophilic, you have quite a challenge!

On the theoretical side, many fundamental issues need further clarification, including: (i) What is the diffusion coefficient (and the relevant band broadening processes) of the labeled DNA molecule during ELFSE? (ii) What kind of molecular architecture would optimize the performance of an ELFSE label? (iii) In particular, what would be the effect of a deformable label [21, 22]? (iv) Since one applies both electric and mechanical forces to the DNA molecules during ELFSE, the free-draining nature of the polyelectrolyte is modified in a fundamental way [22–26]. What is the impact of this breakdown of the free-draining concept on the performance of ELFSE? Our group is currently making progress in most of these directions, but the lack of experimental or numerical systems to test the predictions of the new theoretical framework that we are developing is a problem.

4 Are artificial electrophoresis "sieving" structures better?

The development of artificial electrophoresis sieving media is certainly a major step towards optimizing DNA separation methods and integrating them on chip within complete microanalysis environments. These novel sieving structures typically consist in arrays of obstacles etched on the surface of a silicon wafer using lithographic technologies. Precise control over the geometry of the sieving matrix is therefore possible, and this design flexibility probably constitutes a key advantage of artificial structures over traditional separation media. Examples of artificial separation microstructures include matrices of posts that mimic gel fibers (shown schematically in Fig. 1h) [27–30], channels with alternating deep and shallow regions that form entropic trap arrays (Fig. 1i) [31, 32], and asymmetric arrays of obstacles that act as Brownian motion rectifiers [28, 33–35] (see also the Brownian ratchet Section 1.1 herein).

The challenges brought about by these devices are at the outset practical ones. With resolution and operation speed already approaching those of leading separation technologies for DNAs in the kbp range [28, 34, 36], question concerning their scalability arise. One may thus ask: Will artificial structures ever reach sequencing resolution or fractionate multimegabase strands? Chou *et al.* [28] anticipate that sequencing will indeed be possible in arrays of sub-μm posts with ultrahigh (and pulsed) electric fields, but this has yet to be demonstrated. Channel structures are best suited for the separation of very long DNA molecules since they contain no small scale obstacle that inhibit chain relaxation, but Mbp molecules have not been tested so far. As for Brownian rectifiers, they have the advantages of sorting globular objects of practically any type (possibly even cells) and operating continuously [34]. It thus seems likely that various structures will eventually cooperate in a single chip environment to allow preparation and analysis of molecules over a wide range of sizes and types. We should also note that band-broad-

ening remains an important practical limitation to high resolution and reliable detection in artificial sieving structures.

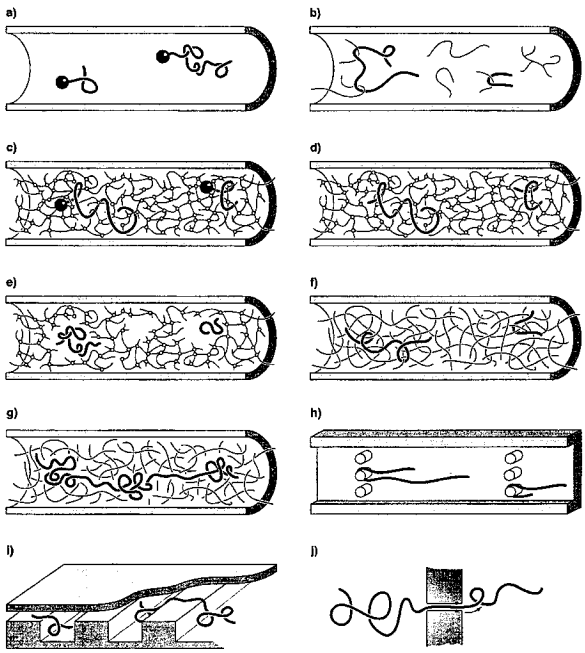

Figure 1. Schematic pucture showing some of the DNA separation mechanisms and ideas discussed in this article. (a) In ELFSE, a neutral buoy slows down the smaller DNA molecules during free-flow CE; (b) collisons between long DNA molecules and the polymer chains of an ultradilute (unentangled) polymer solution provide very fast CE separations; (c) in trapping electrophoresis, the large particle attached at the end of the DNA molecules gets stuck when the leading DNA strand chooses too narrow a passage; (d) gel electrophoretic separation of DNA molecules *via* a reptation process; (e) entropic trapping dominates the migration of smaller DNA molecules that jump between the larger pores inside a disordered gel; (f) the CE separation of DNA molecules in entangled polymer solutions resembles the situation observed in gels (see d), except for the fact that the polymer matrix is dynamic; (g) in very dense polymer solutions, megabase DNA molecules migrate in an elongated conformation that seems to fill large "lakes" in an almost periodic manner; (h) artificial arrays of post can be designed at will using modern techniques; here, two DNA molecules escape from the collision with apost; in the process, they go through a U→J→I sequence of conformations; (i) artificially constructed entropic trapping system; the DNA molecules must squeeze to go through the narrower parts of the channel, and this process leads to size separation; (j) in nanopore technologies, a ssDNA molecule is pulled through a nm-size hole, one monomer at a time, and information about the sequence can be inferred from various physical measurements.

The availability of simple and regular geometries also presents unique opportunities from the standpoint of electrophoresis theory and modeling, as it alleviates difficulties associated with the intricate pseudorandom and irreproducible architecture of polymer gels. Simple models already seem to explain the dynamics of molecules through microfabricated arrays quite well. Not to mention that direct observation of DNA strands in artificial structures can reveal some of their fundamental properties and how these are related to the local geometry. Theoretical investigations can now adopt a more quantitative point of view and revisit issues such as the impact of molecular size, type, and topology on separation efficiency. Detailed mechanisms of electrophoretic separation can be uncovered, the effect of order and disorder in the disposition of sieving elements can readily be studied, and new ideas can be tested in conclusive ways on new custom-made devices. Given the dimensions of microfabricated arrays and the processing involved in their fabrication, the dynamics of biomolecules and their interactions with surfaces also suggest new challenges on the road to integrated systems.

Lastly, while microfabricated sieving structures clearly offer many advantages over polymer gels, we should question whether sieving altogether is the optimal technique for macromolecular sizing. After all, on-chip arrays and channels often reproduce structural features found in gels (albeit in a controlled and orderly fashion) and size information is still extracted indirectly through mobility measurements. But given that we can design structures of molecular dimensions practically at will, perhaps we can tackle the problem in a more straightforward way. The single molecule DNA sizing device constructed by Chou *et al.* [36], which allows an absolute measure of strand length *via* fluorescence detection, stands as a superb example of a direct sizing approach. Advances in separation science based on refined lithographic methods are thus not limited to the design of more efficient sieving media, but also include the research for alternative ways to sort, identify and size biomolecules.

Some of the questions that require further theoretical investigation thus include: (i) Is it possible to design a sieving structure or imagine a mode of operation that limits dispersion? (ii) Can we take advantage of different sieve geometries, perhaps more elaborate ones, to optimize separation? There is currently no theory that can guide the development of such sieves. (iii) Can EOF be used, together with geometrical constraints, to separate biomolecules? Of course, the work on ratchet-like systems will remain heavily influenced by theory since their operation depends on very subtle thermodynamic effects that would be hard to optimize in a purely empirical way.

B

Theory of DNA electrophoresis (~1999–2002 1/2)

GW Slater, et al. *Electrophoresis* **23**, 3791 (2002)

Electrophoresis 2002, 23, 3791–3816

Review

Gary W. Slater
Steve Guillouzic
Michel G. Gauthier
Jean-François Mercier
Martin Kenward
Laurette C. McCormick
Frédéric Tessier

University of Ottawa,
Ottawa, Canada

Theory of DNA electrophoresis (~1999–2002½)

Over the last two decades, the introduction of new methods such as pulsed-field gel electrophoresis and capillary array electrophoresis has made it possible to map and sequence entire genomes, including our own. The development of these experimental methods has been helped by the progress of theoretical and computational sciences, and the interactions between these three *modi operandi* of modern science are still pushing the limits of our technologies. We now see a clear trend towards proteomics and microfluidic (even nanofluidic!) devices. In this review, we take a look at the progress of the field over the last 3 years using the glasses of the theoretical scientist and focusing mostly on new ideas and concepts. About a dozen different subfields are discussed and reviewed. We conclude by giving a commented list of some of the best review articles published over the last 2–3 years.

Keywords: Capillary electrophoresis / Computer simulations / Entropic trapping / Microfluidics / Review / Theory of electrophoresis EL 5176

Contents

Correspondence: Professor Gary W. Slater, Département de Physique, Université d'Ottawa, 150 Louis-Pasteur, Ottawa, Ontario K1N 6N5, Canada
E-mail: gslater@science.uottawa.ca
Fax: +613-562-5190

Abbreviations: BD, Brownian dynamics; **FENE**, finitely extensible nonlinear elastic; **SNP**, single-nucleotide polymorphism

1 Introduction

Clearly, microfluidic devices are on the verge of creating a whole new family of technologies and industries (indeed, it is already happening). Although the main interest in these systems is due to the fact that we can make macroscopic systems more efficient (and more robust) by reducing their scale, we should not forget that microfluidic systems also allow us to use new separation and physicochemical processes unknown on a macroscopic scale. An example is that of entropy-based separation systems where one of the dimensions of a channel is smaller than the normal geometric size (*e.g.*, the radius of gyration) of a polymeric analyte [1, 2]. Understandably, the theoretical work has been somewhat biased towards the micro- and even nanofluidic world over the last 5 years or so. Although this review will not focus entirely on the theoretical issues surrounding this new technological paradigm, it will itself suffer from this bias.

Of course, we had to make a selection of topics. This selection is certainly driven to some extent by what the authors find stimulating and promising these days. Two of the exciting topics that we nevertheless chose to ignore are the problems related to sample injection in microfluidic devices and the phenomenon of dielectrophoresis. Injection is an extremely important issue for the optimization of separation devices and even represents one of the most remarkable difference between CE and microfluidic systems; however, injection is not a separation process as such and is thus slightly beyond the scope of the present review. Dielectrophoresis, on the

 0173-0835/02/22-2312–3791 $17.50+.50/0

other hand, can be used as a separation tool, even for DNA, but it does not rely on the same transport properties that make electrophoretic separations possible; therefore, we decided to avoid this topic for the present review.

We also decided not to include a specific section about the development of new separation matrices for DNA separations. Although the development of new polymeric sieving matrices remains an active field, the benefits appear to have become largely technical (lower viscosities for easier injection, *etc.*). Indeed, no major improvements in either sequencing readlength or elution times have been reported that can be directly related to a revolution in sieving matrices. We must add, however, that in some cases, the separation process is probably novel and remains to be investigated [3, 4].

We do not cover the fields of electroosmotic flow (EOF) and capillary coatings. This is truly a remarkably dynamic field of investigation, both theoretically and experimentally. Although the fundamentals of EOF are well-understood, we still have no clear understanding of the effects of dynamic polymer coating agents (*e.g.*, polydimethylacrylamide) on the EOF. Would it be better to use branched or monodisperse polymers? Can we coat the capillary walls to avoid analyte-wall interactions while retaining a uniform and strong EOF for fluid pumping purposes? What kind of covalent polymer brushes would better control the EOF? Beside these standard CE issues, others are more directly related to microfluidics: *e.g.*, can we use inhomogeneous EOF flows to mix liquids in μm-size devices? These are immensely interesting topics, but we had to make a selection of topics for this review.

On a similar note, we do not review the recent progress in our understanding of the effect of curves in microfluidic devices. Modeling has led to an excellent understanding of the race-track effects inherent to such devices, and several clever new designs have been suggested. However, the subject matter is yet to be fully understood. Indeed, essentially all current models apply to free-flow electrophoresis where both the mobility (μ) and the diffusion coefficient (D) of the analyte are independent of the local field intensity (E). This is clearly not the case for DNA separation in sieving polymer matrices. Strangely, the impact of these nonlinear field effects has never been studied in this context.

The next fourteen sections present different topics related to the separation of DNA molecules. In each case, we discuss some of the main outstanding issues and the progress made over the last 2–3 years. The last section concludes with a commented list of some of the best relevant reviews published over that period of time.

2 Nanopore technologies

While microfluidics is still in its infancy, recent developments suggest that it may be rendered obsolete by nanofluidics before it even had a chance to become a success story! Indeed, as noted in our previous review [5], *in vitro* polymer translocation through nanopores has emerged as a promising technique for DNA analysis and sequencing. Experimental articles published since that review have furthered our knowledge about this process. For instance, Kasianowicz' group [6] has determined that the rate of entry of ssDNA into an α-hemolysin channel increases linearly with DNA concentration and exponentially with the voltage difference applied along the channel. They also found that the rate of entry is higher when the DNA enters the channel through the protein's larger vestibule rather than through the other end. Meller and co-workers [7] also studied this particular system in the presence of a voltage difference along the channel. They found that the translocation speed of long ssDNA strands, *i.e.*, longer than the channel, is independent of the polymer length. However, for polymers shorter than the channel, the translocation speed increases as the polymer length decreases. They also found that the translocation speed depends nonlinearly on the driving voltage. It thus appears that the confined geometry within the pore plays a nontrivial role in the translocation dynamics.

It is believed that a single nanopore could eventually allow a ssDNA strand to be read at a rate of several thousand bases per second [8]. Two key requirements for this to become reality are: (i) A reproducible and heavy-duty nanopore. In this respect, recent work on ion-sculpting promises to yield solid-state pores that could replace the currently used α-hemolysin channel [9]. (ii) A process to sequentially read the individual bases as the polymer threads through the pore, which may require the ssDNA strand to be threaded relatively slowly and the stochastic movement due to thermal motion to be minimized. This has yet to be accomplished.

Although DNA cannot yet be sequentially read using translocation, alternate ways of analysing DNA with the help of nanopores and ionic currents have recently been designed. In one case, Howorka and co-workers [10, 11] have shown that a given sequence of ssDNA can be detected using an α-hemolysin channel in which the complementary DNA sequence has been attached. Indeed, the target DNA binds to its complementary sequence and takes longer to translocate than the other chains. Another analysis method has been implemented by Kasianowicz' group [12]. In this case, DNA sequences are first designed to bind with a given analyte and are then allowed to translocate. In the absence of the analyte,

Electrophoresis 2002, *23*, 3791–3816

the DNA strands translocate normally across the nanopore. However, when the analyte of interest is present and binds to the DNA, two phenomena occur: (i) the rate of DNA entry into the pore decreases and (ii) once the DNA has entered the pore, the analyte prevents the DNA strand from getting through. Designing different signatures for different analytes could allow the simultaneous detection of various types of analytes using a single nanopore. Finally, Vercoutere and co-workers [13] have succeeded in distinguishing among various hairpins in ssDNA, down to a single-nucleotide resolution. Indeed, the hairpin must unfold during the translocation in order for the DNA strand to cross the channel, and the different sequences yield different signatures of ionic current.

Over the years, several theoretical papers have attempted to capture the dynamics of polymer translocation [14–27]. In almost all cases, however, the dynamics is being projected onto a quantity known as the translocation coordinate and defined as the length (or the fractional length) of the polymer on one side of the pore. In order for this approximation to be valid, the polymer on each side of the membrane is implicitly assumed to relax on a time scale much smaller than the one on which the translocation process is taking place. Even if experimental results do support some of the conclusions arising from current models, the separation of time scales assumption is probably not valid in the general case [28]. To our knowledge, [19] is the only theoretical paper to forgo this assumption. In addition, all current models neglect the effect of hydrodynamic interactions. The contribution of these interactions is likely to be nontrivial because of the presence of an obstruction, namely the membrane across which the translocation is taking place, and the nonequilibrium nature of the process. Consequently, although the basics of polymer translocation are now well understood, a lot of work remains to be done at the theoretical level before the intricacies of this process have been fully explored. In this context, we are currently studying this phenomenon using Molecular Dynamics simulations with explicit solvent, in which the excluded volume and the hydrodynamic interactions are explicitly taken into account (see Fig. 1). This approach should allow us to determine under what experimental conditions, if any, the separation of time scales assumption is valid.

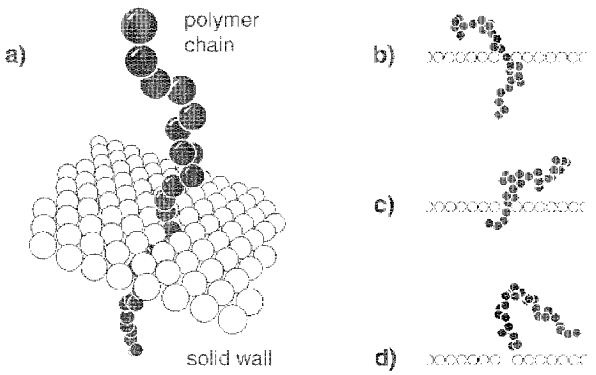

Figure 1. (a) In our current Molecular Dynamics simulations of polymer translocation, we study the unbiased translocation of a polymer chain through a pore in a thin membrane. The polymer (black beads), the membrane (white beads) and the solvent (not shown) are represented by identical point-like particles interacting through a purely repulsive Lennard-Jones interaction. In addition, the monomers of the polymer chain are held together by a FENE interaction and the membrane particles are simply kept immobile. The explicit inclusion of the solvent particles allows the hydrodynamic interactions to be taken into account. A schematic representation of actual simulation data is shown in (b)–(d): (b) the polymer is initially placed midway through the pore and the mid-monomer is held in place for a given relaxation period; (c) the mid-monomer is then released and the polymer is allowed to move back and forth freely through the pore; (d) the polymer eventually exits on either side of the membrane.

3 Surface electrophoresis

Pernodet and co-workers [29] recently proposed and tested a novel method for the separation of DNA fragments based on the strikingly simple process of inducing electrophoretic migration near a smooth surface. Using this approach, DNA strands migrate across a planar substrate, and the interactions between the DNA molecule and the substrate apparently act as a source of friction. In their proposed picture of the process, this friction is more significant for longer fragments than for shorter ones, hence the mobility becomes length dependent and separation is achieved. In some sense, this new idea lies somewhere between conventional electrophoresis and chromatography: an electric field drives molecules across the device, but the length dependence of the mobility arises due to surface interactions, rather than topological constraints. This research group has studied surface electrophoresis experimentally as well as with computer simulations, and they have updated their findings in two articles published this year [30, 31].

The experimental procedure is as follows. First, a SiOH-rich oxide layer about 2 nm thick is grown on a rectangular, flat and clean silicon substrate. A droplet containing a solution of fluorescently dyed dsDNA is then deposited at one end of the substrate and allowed to air-dry. Differential evaporation within the droplet focuses DNA fragments into a very thin band on the rim of the droplet, and these fragments bind (electrostatically) with the surface. The

substrate is then placed in a buffer-filled electrophoresis cell and an electric field is applied parallel to the surface. Finally, the fluorescence of the migrating molecules is detected as a function of time at a fixed distance from the injection point. Results indicate that the mobility (μ) scales with molecular size (M) as

$$\mu \sim 1/M^{0.25} \quad (1)$$

over an impressive range of molecular sizes spanning 3 orders of magnitude [30], from 125 bp to (at least) 164 kbp. The resolution (R) follows the predicted scaling law $R \sim M^{0.75}$, and appears to be mainly limited by the initial loading width, thus indicating that thermal diffusion is of a lesser importance under these conditions [30]. This new separation method offers three clear advantages: (i) the device fabrication and the mode of operation are very simple; (ii) there are no topological constraints, hence very long fragments can be separated (in fact, it is still not known if there is a maximum molecular size which can be separated); (iii) it can be readily integrated into emerging silicon-based microfluidic systems.

In order to better understand the separation mechanisms at work in surface electrophoresis, Luo and Gersappe [29, 31] performed Brownian Dynamics simulations of adsorbed chains subjected to a low intensity electric field. They used a standard coarse-grained approach in which all monomers interact *via* a Lennard-Jones (LJ) potential while adjacent ones interact *via* a finitely-extensible non-linear elastic (FENE) potential [32]. The chain monomers and the surface atoms interact *via* an LJ potential with a tunable interaction strength, to mimic the surface interactions in the experiments. The simulation results confirm that the weakly and the strongly adsorbed cases correspond, respectively, to a 3-D and a 2-D free-draining regime, and that consequently no separation is possible in either of these limits. For intermediate interaction strengths, however, separation is observed and is attributed to the length-dependent chain conformations and to the formation of "trains" of adsorbed monomers and unbound loops extending in solution (see Fig. 2).

As with any new separation method, surface electrophoresis raises its share of new questions. However, owing to the simplicity of the design, it is reasonable to hope that these will be addressed and answered over the next few years. In particular, understanding the precise nature of DNA-surface interactions and finding ways to control them are issues calling for immediate attention. Some polymer coatings have already been studied [30], and current work focuses on the possibility of using surface nano-patterns to amplify and optimize the separation [31]. Roughening of the surface with a deposited film of microscopic beads has also been cleverly used to

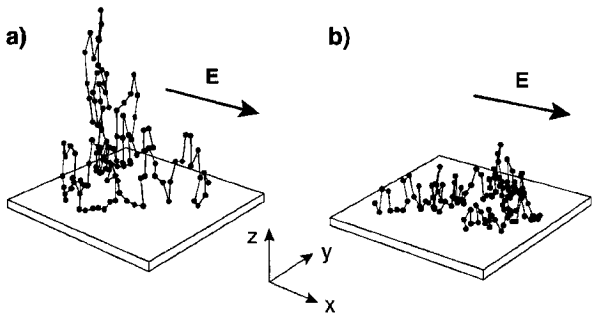

Figure 2. Snapshot of a polymer chain during computer simulations of surface electrophoresis performed by Luo and Gersappe. The chain is attracted to a planar substrate and is driven parallel to the surface by the electric field E. In (a) the surface interaction is weak and the chain behaves as a free-draining coil. In (b), the surface interaction is strong, hence the chain is tighly bound to the surface and apparently behaves as a 2-D free-draining coil. Separation according to molecular size is obtained for an intermediate attraction strength between these two limits. Reprinted from [31], with permission.

show that separation is indeed due to surface friction rather than topological constraints [30]. The design of a new loading mechanism amenable to integration on-chip is also needed for this method to find applications in microscopic analytic devices. Finally, as the exact nature of the separation mechanism remains elusive at this point, there is a pressing need for a more elaborate theory that includes electrostatic and hydrodynamic effects, both of which play a major role when DNA approaches a solid-liquid interface. Similarly, the computational model could be extended to explicitly include solvent molecules, electrostatic interactions and counter-ions (and the Debye layer near the surface) so as to continue to steer research on this topic towards a more realistic model.

To summarize, it appears worthwhile to follow developments in surface electrophoresis. Not only can it potentially serve as a simple and more efficient separation mechanism, but a better understanding of polymer-surface interactions has direct applications in microfluidic devices where polymers travel in highly confined environments.

4 Ratchets

A ratchet is a device that can induce directional motion of particles or molecules without a net external force or gradient. The operating principle of ratchets relies on the rectification of the effects of either thermal motion or a zero-average external field [33, 34]. This fascinating concept continues to permeate many fields, from quantum

Electrophoresis 2002, *23*, 3791–3816

mechanics to biophysics, and perhaps the current level of enthusiasm for ratchets is best illustrated by the special issue on the subject published recently in *Applied Physics A* [35]. From our standpoint, ratchets are interesting for three main reasons: (i) they can operate as novel separation systems, or enhance the performance of existing ones; (ii) they can serve as a transport mechanism for particles or molecules on the microscopic scale, a task pertinent to the integration of electrophoresis technologies on chip; (iii) because of the first two points, they may be used as complementary and orthogonal techniques for the separation of complex mixtures of analytes.

The development of theoretical and computational models of ratchet systems flourishes [35–44] and is essential for the design of new separation methods and the interpretation of experimental observations. One of the challenges encountered in describing the operation of real electrophoresis-based ratchets is the faithful representation of the field lines in microfabricated electrophoretic devices. A vivid example of this difficulty is given in a recent article by Austin *et al.* [45] where they consider the curved field lines present in an asymmetric array of insulating deflectors; Austin's group [46] has successfully used this type of array to separate DNA molecules in a continuous mode. They show that if the obstacles are perfect insulators and if the particle density is symmetric, then there can be no deflection of particles on average, so no separation should be observed. The fact that separation does occur experimentally can be attributed to various factors (such as partly conducting obstacles or the deformation of the macromolecules), but this example illustrates that a realistic representation of the field lines can become crucial in the interpretation of experimental results. On the other hand, the curvature of the field lines around obstacles does not always affect the dynamics; indeed, our group has shown that in general, in the zero-field limit, the electrophoretic mobility and the diffusion coefficient of a point-particle is independent of both the field lines curvature and the obstacle shape [47].

Computer simulations of ratchet systems are useful for the optimization of separation techniques. Since the quality of separation is mostly affected by diffusion, it is important that new models of ratchets take into account the dispersion of particles in addition to their average dynamical properties. This question is addressed by Keller *et al.* [36] in a paper where they calculate not only the macroscopic drift velocity, but also the diffusion tensor of particles in a 2-D geometric ratchet, *via* a lattice Monte Carlo simulation. This allows them to evaluate the quality of the angular separation Q of two different kinds of particles using both their average position $\langle x \rangle$ and their dispersion σ:

$$Q = \frac{|\langle x_1 \rangle - \langle x_2 \rangle|}{\max(\sigma_1, \sigma_2)} \quad (2)$$

Their calculation reveals that the quality of a separation does not rely solely on the magnitude of the ratchet effect (which is often considered a measure of the quality of ratchets). The diffusion process resulting from the ratcheting effect obviously plays a major role in determining the value of Q and should not be overlooked in future models.

Current models of ratchets often impose other restrictions that should be overcome in the forthcoming years. One example is the adiabatic approximation in which the frequency (ω) of the applied force is supposed small compared to the relaxation time of the analyte. In 2002, Fistul [37] calculated the motion of an overdamped Brownian particle in a ratchet beyond this approximation. His derivation offers an explanation for the sign reversal of the velocity function $v(\omega)$ with increasing ω, previously found in numerical studies. This illustrates the fact that unexpected and useful dynamical properties of ratchets can be uncovered if we extend current models to higher frequency regimes. Finally, we want to point out that most of the theoretical studies still deal with point-like particles. However, one of the most interesting applications in separation technologies – the sorting of DNA or polymers – involves macromolecules, which possess a large conformational entropy that can be used as a separation parameter. An example of a ratchet exploiting molecular entropy was first described by Slater *et al.* [2] and we think that efforts should continue in this direction, both theoretically and experimentally.

It is by now well established that ratchet devices work in practice, and ongoing work focuses on exploiting them for separation purposes. Marquet and co-workers [48] designed a promising ratchet system which exploits both dielectrophoresis and electrophoresis effects. Their system induces directed motion of latex beads (1–6 μm in diameter) using an oscillating electric field (of zero mean value) in a microfabricated channel with an asymmetrically modulated diameter. Another prime example of a successful Brownian rectifier is the one built by Bader and co-workers [49–51] for DNA oligomer separation in free solution. Their device consists of interdigitated electrodes which produce a simple asymmetric sawtooth potential (see Fig. 3). During the field-on periods, DNA molecules drift to the bottom of the potential wells, while during field-off periods, they undergo free diffusion. Owing to the asymmetry of the potential profile, the molecules tend, on average, to drift in a given direction. In a recent report, the application of this device to fast genotyping of single-nucleotide polymorphisms (SNPs) is discussed [49]. Another type of functional ratchet is the field-rectifying device conceived by Griess and Serwer [34, 52,

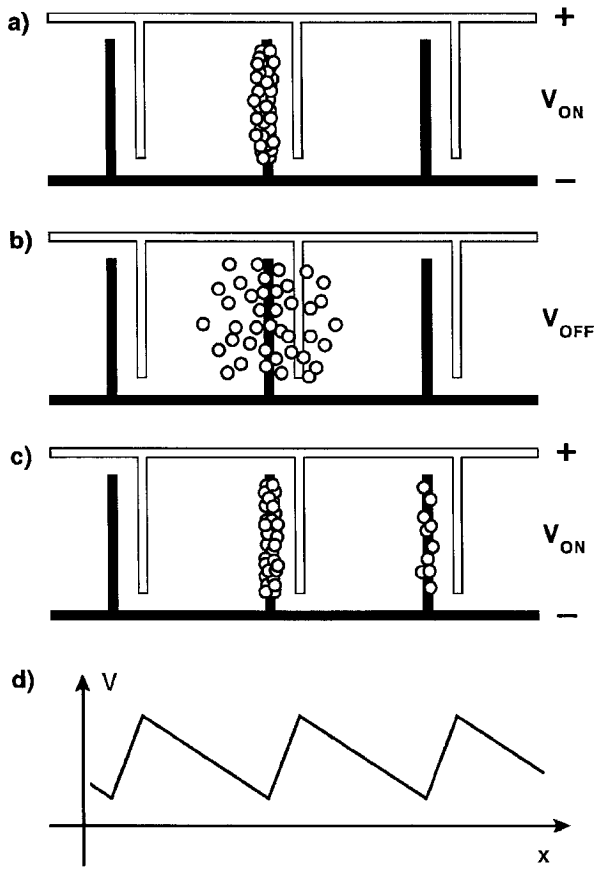

Figure 3. A simple Brownian ratchet device. An asymmetric saw-tooth potential $V(x)$ is created using interdigitated electrodes (d). When the field is on, the positively charged particles are trapped near the negative electrode (a). When the field is turned off, the particles (with a diffusion coefficient D) diffuse symmetrically around this electrode (b). When the field is turned back on again, the particles that have diffused beyond the neighboring positive electrodes are trapped by the next negative electrodes (c). Since these electrodes are asymmetrically distributed in the space, it results a net motion of the particles with a velocity directly related to D (inspired by Fig. 1 of [51]).

53] for the separation of DNA. They use a standard gel matrix as the separation media, but drive the molecules with an electric field E that slowly alternates between long low-intensity strides in the forward direction, and short high-intensity steps in the reverse direction (with an average force over time of zero). Since the mobility of DNA in the gel is both E-dependent and size-dependent, net motion is induced and interesting migration regimes arise. Most notably, by alternating between a ratchet mode and a continuous mode, the resolution can be increased to a limit set only (at least in principle) by the detection sensitivity [53]. Griess and Serwer [34] also describe a circular preparative electrophoretic cell in which strands of different lengths could migrate at different angles. Other applied work includes a computer simulation of an existing microfluidic separation system by our group. We modeled the microfluidic device fabricated by the Craighead group [1, 54] and found that, in the ratchet regime, the drift of the macromolecules is rectified, and that strands of different lengths can be forced to migrate in opposite directions when a small field bias is applied [55]. Moreover, we studied an asymmetric version of the Craighead channel and showed that it can rectify the motion of molecules subjected to an unbiased square-pulse driving field; this is an example of the entropic ratchet concept introduced by Slater *et al.* [2] a few years ago.

As bioanalytical tools are integrated on-chip, transport of fluids in μm-size channels becomes a challenge. Ajdari [56, 57] has proposed a clever way to combine electroosmotic and ratchet effects to build a pump that relies exclusively on small local oscillations of the electric field. The idea is to create small electroosmotic vortices with electrodes on the channel walls. When the electrodes are placed in some asymmetric fashion, the vortices themselves become asymmetric and net momentum is transferred to the bulk fluid. Interestingly, this method allows for the transport of small droplets since everything occurs locally. A prototype of such a pump has been built [58] and appears to operate as predicted. Another experiment exploiting a ratchet effect to control microdrops is based on a channel whose diameter is modulated with an asymmetric saw-tooth shape [59]. Applying an oscillating electric field or even a mechanical vibration disrupts the contact lines between the fluid and the walls, and the asymmetry of the structured surface rectifies the motion of the drop. Along similar lines, functional drift ratchets in which the fluid in pumped back and forth in asymmetric pores in order to separate suspended particles have been built [60].

Overall, the fundamental questions about ratchets we asked in our previous review continue to hold [5]. Band broadening remains an issue for Brownian ratchets, which are based on diffusion and are thus inherently stochastic. Perhaps resorting instead to strategies without a diffusive step proper, as in shifted ratchets [61] or field-rectifying ratchets [62] can help to address this problem. Ratchets are also still limited in the molecular size range they can handle, because of the physical size of their features. However, field-rectifying ratchets offer the possibility to work with traditional media, amenable to a broad size range, or perhaps with surface electrophoresis where there are simply no obstacles and therefore no preferred length scale (see Section 3 herein). Finally, no

Electrophoresis 2002, *23*, 3791–3816

ratchet separation scheme based on substantially new molecular properties has been proposed. On the other hand, potent new ratchet mechanisms, involving EOF and surface tension effects, have been devised for the control and transport of fluids in microscopic channels.

5 Entropy-based separation systems

Internal conformational entropy is certainly one of the dominant properties of flexible macromolecules such as DNA. Moreover, internal entropy is directly proportional to the molecular contour length (*i.e.*, it is an extensive property), so it only seems natural to devise schemes that utilize entropic effects to achieve size-separation of macromolecular objects, such as DNA fragments. Such schemes are typically rooted in the process of entropic trapping (ET), which consists in trapping molecules in regions where their conformational entropy is maximized (*e.g.*, voids inside a cross-linked gel). ET was first introduced as a generic concept over a decade ago by Baumgärtner and Muthukumar [63–65], and has since been the object of numerous experimental and computational studies [66–72]. In one recent article, Liu, Li and Asher [73] report on a novel way to construct sieving gels comprising a periodic array of voids by selective etching out of self-assembled silica beads (~100 nm in diameter) included during gelation. The regularity of the void spacing has made the direct experimental verification of ET possible *via* diffraction measurements. At a recent American Physical Society meeting, Hoagland [74] reported using a somewhat similar approach to template a 2-D gel with close-packed spherical beads, and observing the discrete "hopping" of DNA molecules between traps directly *via* fluorescence microscopy. It will be most interesting to see the properties of these gels when used as sieving media for electrophoresis.

At the risk of giving the reader more reasons to believe that we suffer from the bias acknowledged in the introduction of this article, we think that the most striking demonstrations of entropic effects lie in recent experiments performed in microfluidic channels. Members of the Craighead research group from Cornell have built and tested microfabricated devices for the separation of DNA which exploit entropic effects. This group's most recent experimental system consists in a quasi-2-D channel in which some regions are populated with a dense array of nanopillars (35 nm diameter) [75]. Long DNA molecules can be driven trough the pillared region with an electric field, but since the pillars are closely spaced (160 nm apart), the DNA must elongate in order to migrate downfield, at a great cost in conformational entropy (see Fig. 4). When the field is turned off, molecules that have

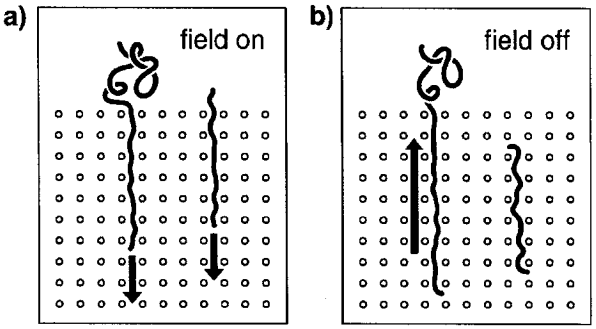

Figure 4. A schematic top view of the recent microfluidic separation device built on chip by the Craighead research group. The pillars, shown as small circles, are approximately 35 nm in diameter and 160 nm apart. In (a), the electric field pulls DNA fragments in the low-entropy pillared region. In (b), the field is turned off, and molecules that straddle the interface rapidly recoil to return in the open region. Molecules that have completely entered the pillared region, however, have no impetus to recoil and simply relax locally (inspired by [75]).

only partially entered this region quickly recoil in the pillar-free region in order to maximize their conformational entropy. Not only can this device be developed into a functional separation tool (for instance, because longer DNA molecules take more time to enter the pillared region), but it also allows first-hand observation, *via* fluorescence microscopy, of the recoiling DNA molecules. This can certainly improve our understanding of the dynamics induced by entropic effects.

Earlier, the same group built another separation device that also relies on entropic effects. It consists of a periodic array of alternating deep and shallow regions [1, 54]. DNA in the 10–100 kbp range is electrophoresed through the structure and becomes trapped at the entrance of the shallow constrictions, before it manages to escape in a slithering motion. The typical trapping time of the molecules is length-dependent and, surprisingly, long molecules migrate faster than shorter ones (it turns out that this a geometric effect: bigger coils expose more monomers to the shallow region entrance and thus increase their chances of escape per unit time). In a recent paper, Han and Craighead [76] further developed a theoretical model of this device, identified the optimal conditions for enhancing resolution, and discussed ways to scale the method to smaller fragments or even megabase strands. Monte Carlo simulations of this device by our group [77] largely support the proposed scaling relationship for the mean trapping time τ in the low field regime,

$$\tau \sim \frac{1}{\sqrt{M}} \exp\left(\frac{\alpha}{E_S k_B T}\right) \tag{3}$$

where M is the number of monomers in the chain, E_s is the field strength in the constriction, T is the absolute temperature and α is a constant. The simulations also highlight some finer aspects of the geometric and relaxation effects and also suggest the possibility of resolving topological objects such as rings and knots. When extended to the case of alternating driving fields [55], our simulations indicate that the system could operate in various low-frequency ratchet regimes, and reveal an interesting resonance effect occurring when the frequency of the driving pulse is commensurate with the mean trapping time of the molecules.

We should also mention that microfabricated separation systems typically demand fairly long channels, so having them curve back and forth on the chip surface is sometimes required for proper packaging. Incidently, this curvature itself gives rise to subtle entropic effects, because there is more volume per arc length (hence more entropy) along a curved channel section. This phenomenon has been addressed analytically before [78], and is currently under experimental investigation by Ueda and co-workers [79], along with interesting and potentially useful electric field gradients and polymer stretching effects in curved geometries.

While it is true that there has been significant progress on the experimental aspects of ET brought about by microfluidic technologies, strides have also been taken on the theoretical front. The reason behind the vigorous development of theory in this area is that ET is ultimately related to the problem of barrier crossing for macromolecules. In order to understand ET, one must also understand how flexible objects escape from potential wells. This fundamental problem is very generic (equivalent to the Kramers problem for Brownian particles [80]) and fosters a unified perspective on the behavior of macromolecules in constrained environments. Current models mainly attempt to describe how flexible chains stretch to reduce the effective height of potential barriers. Following the work of Park and Sung [81], Sebastian and Paul [61, 62] studied the Kramers problem for macromolecules using a Rouse model, in the case where the barrier width is smaller than the polymer contour length. They identified two escape mechanisms, namely end-crossing and hairpin formation, and derived expressions for the activation energy, the crossing time and the net crossing rate. Lee and Sung [82, 83] studied the same problem from the point of view of a coil-stretch transition of polymer chains and rings, and explained how conformational fluctuations also participate in lowering the barrier. Muthukumar [22] developed the theory for the translocation of a confined polymer through a small pore, by analogy with a nucleation and growth process. Of note, his Brownian Dynamics simulations uphold his prediction that the mean escape time τ scales as

$$\tau \sim M(M/\rho)^{1/3\upsilon} \quad (4)$$

where M represents the number of monomers, ρ is the initial density in the vesicle and $\nu = 3/5$ is the Flory exponent in 3-D. Finally, Reguera and Rubí [84] have developed a kinetic model for the diffusion of particles in the presence of entropic barriers based on a Ficks-Jacob equation. If their formalism can be extended to deformable objects and to cases where trapping occurs (non-ergodicity), it could provide a very general framework to analyze the dynamics of macromolecules in the presence of entropic barriers.

6 Magnetic self-assembling sieves

Microlithographically fabricated devices such as quasi-periodic arrays of fixed obstacles etched on a silicon surface have been employed as a separation medium for DNA [85]. The production of these devices is a sophisticated and costly procedure with little tunability after construction. A promising new alternative [86, 87] is the use of quasi-regular arrays of columns, formed by the application of a homogeneous magnetic field (> 10 mT) to a suspension of superparamagnetic particles (with a diameter on the order of a few micrometers) confined between two parallel flat plates. Doyle *et al.* [86] have employed such a medium composed of self-assembled posts of a Fe_2O_3 ferrofluid with inter-post spacing of 5 μm to effectively separate 48.5 kbp λ-DNA and associated fragments of 15 and 33.5 kbp in 10–15 min, see Fig. 5. The λ-DNA electropherograms were reproducible within approximately 6% with each subsequent replacement of the sieving medium. The resolution ranged from 5.5 kbp for the 15–33.5 kbp samples to 11.6 kbp for the 33.5–48.5 kbp samples. Size separation in these systems is achieved due to polymer post entrapment [88]. The polymer forms a pulley like structure, where the two downfield arms of the polymer compete to release the molecule. The time it takes to disentangle from the post is a function of the molecular contour length and hence separation is possible [87–90]. This is unlike gel electrophoresis where a long DNA molecule is actually colliding with many gel fibers simultaneously.

Earlier work by Liu *et al.* [91] provided the initial impetus for the possible application of self-assembled ferrofluids as separation media. By comparing experiments and results from a mean field model, they indicated that the average post separation, d^*, can be controlled by varying the height of the microchannel, L, and the ferrofluid volume fraction, and that in particular, post spacing is related to channel height *via* a power law of the form

$$d^* \propto L^{0.37} \quad (5)$$

C

Deformation, stretching and relaxation of single polymer chains: fundamentals and examples

GW Slater, et al. In *Soft Materials: structure and dynamics*, Dutcher JR and Marangoni AG (Eds.), CRC Press, 424 p. (2004)

Slater GW, et al. *Soft Materials* **1**, 365 (2003)

SOFT MATERIALS
Vol. 2, Nos. 2&3, pp. 155–182, 2004

Deformation, Stretching, and Relaxation of Single-Polymer Chains: Fundamentals and Examples[#]

Gary W. Slater,[*] Yannick Gratton, Martin Kenward, Laurette McCormick, and Frédéric Tessier

Department of Physics, University of Ottawa, Ottawa, Ontario, Canada

ABSTRACT

We review the basic theory for the static and dynamic properties of ideal and real chains. We describe the stretching of single ideal chains in both the strain and the stress ensembles, give scaling arguments for the deformation of real chains, and also consider the impact of chain rigidity by discussing the stretching of worm-like chains. We complement this theoretical outlook with specific examples that highlight the relevance of the single-molecule deformation in a practical perspective: the translocation of a macromolecule over a potential barrier, the collision of a single chain with fixed obstacles or other chains, the dynamics of a thethered chain in a strong shear flow, and some remarkable predictions concerning the deformation of composite chain molecules during free-solution electrophoresis.

Key Words: Polymer dynamics; Polymer stretching; Separation science; Microfluidics.

[#]This article is a corrected version of a paper which has already appeared in *Soft Materials* [C.W. Slater, Y. Gratton, M. Kenward, L. McCormick, F. Tessier, *Soft Materials* 1, 365 (2003)]. Due to problems in the publishing process at the time, the original publication contained an excess of errors. This was not the fault of the authors. The editors wish to apologise to authors and readers. Florian Müller-Plathe, Editor-in-Chief.

[*]Correspondence: Gary W. Slater, Department of Physics, University of Ottawa, 150 Louis-Pasteur, Ottawa, Ontario, Canada, K1N 6N5. E-mail: gslater@science.uottawa.ca.

DOI: 10.1081/SMTS-200056264
1539-445X (Print); 1539-4468 (Online)

POLYMER STRETCHING OVER POTENTIAL BARRIERS

The theoretical concepts introduced above have significant practical applications. Indeed, the deformation of single macromolecules can often improve—or in some cases lie at the very heart of—the operation of analytical devices. In particular, recent leaps in the designability of fluidic systems at the microscopic or even nanoscopic level offer unprecedented opportunities to modulate the conformation of individual macromolecules by means of molecular-scale obstacles and confinement. The induced conformational changes give rise to significant "entropic forces" that can be brought to serve a useful purpose, for example, sorting biopolymers according to size or topology (linear chain, ring, knot, etc.). The perspective adopted here is slightly different compared to the previous section, in that we are not actively deforming the polymer by pulling on its ends. Rather, we consider how a polymer deforms when it encounters a potential barrier, and how this deformation, in turn, affects how the polymer may escape from the potential well.

A striking example of the relevance of conformational entropy for the design of analytical tools is the entropic trap array built by the Craighead group.[19–23] Schematically represented in Fig. 2a, it consists of a microfluidic channel with alternating deep wells, where the polymer molecule sits comfortably, and shallow constrictions, which the molecule can only cross by adopting an elongated shape. Elongation incurs a large entropy cost, thus at equilibrium, the molecule is, in fact, confined to a given well (hence the name *entropic trap*). With an external force oriented along the channel direction, however, the molecule is encouraged to travel from one trap to the next by slithering across the constriction. The rate at which this *translocation* process occurs is determined by the balance between the external and the entropic forces.

The prevailing model for this system simply considers scaling relations for the change in free energy ΔF when a coil section of length x—a hernia—stretches out inside the constriction. For the case at hand, an electric field of strength E is pulling on a DNA

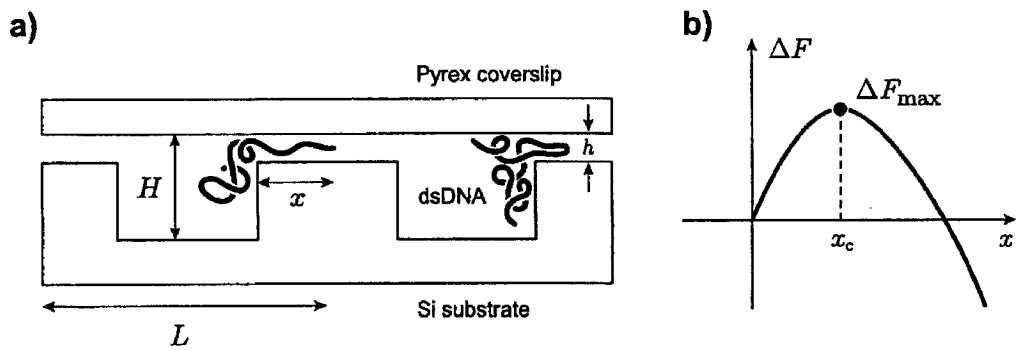

Figure 2. a) The microfluidic channel built by the Craighead research group to separate double-stranded DNA (dsDNA) according to size. In the actual devices, $H \approx 1$ μm, $h \approx 0.1$ μm, and the period L can range from a few microns to a few tens of microns. The molecules are pulled towards the right by an external electric field, but their migration is hindered by the shallow constrictions. b) A sketch of the change in the free energy ΔF of the molecules as a function of the hernia length x. The effective activation energy corresponds to the maximum of ΔF, which occurs at a critical hernia length x_c.

strand (a polyelectrolyte) inside the channel, so we have $\Delta F_{\text{entropic}} \sim x$ (because conformational entropy is an extensive molecular variable) and $\Delta F_{\text{electric}} \sim -x^2 E$ (because both the charge and the span of the hernia are proportional to x). Hence the total change in the free energy of the polymer as a function of hernia size follows

$$\Delta F \sim (x - x^2 E). \tag{28}$$

Eq. (28) reveals the presence of a potential barrier (see Fig. 2b), and differentiation predicts that both the critical hernia length x_c and the corresponding barrier height $\Delta F_{\max}$ scale like $1/E$. The net rate of crossing, κ, thus takes the Arrhenius form:

$$\kappa = \kappa_0 e^{-\Delta F_{\max}/k_B T} = \kappa_0 e^{-E_0/E}, \tag{29}$$

where κ_0 and $E_0 \sim 1/k_B T$ are independent of the field intensity E. In Eq. (29), there is no explicit dependence of the rate κ on the total number of monomers N, because we have overlooked the three-dimensional aspect of the system (going *into* the page in Fig. 2a). In reality, larger coils expose more monomers to the constriction than smaller ones, thus generate more herniae per unit time, and therefore increase their chances of escaping from the well. This contribution turns up as an N-dependence of the pre-factor κ_0, making size separation possible. Furthermore, the field E pushes the coil against the constriction, which enhances this effect. Note that although they lose more entropy in the narrow channel, longer molecules move faster here!

The system discussed above is, of course, but one example of a microdevice intended to manipulate and analyze macromolecules, and recent literature abounds in clever designs that exploit conformational behavior (stretching and relaxation) of single molecules. The kind of model presented above is generic and thus generally helpful to describe the operation of devices that rely on similar principles. However, it is possible to further refine our understanding by considering not only the dynamics of the polymer chain as a whole, but of each of its segments explicitly. The fundamental question here is: *How does a polymer chain cross a potential barrier?* This is a generalization of the well-known Kramers problem for Brownian particles to the case of string-like objects, and Sebastian and Paul have published instructive accounts of the solution for the case of long chains, i.e., chains with a contour length much larger than the barrier width.[24–28] The mathematical derivation of the translocation rates and the total crossing time are rather involved, extending beyond the scope of this short account, so we only review here the simple calculation of the activation energy.

The approach is based on the Rouse model,[8] introduced in the first section I, considered here in the continuum limit (i.e., we treat the bead index n as a continuous variable ranging from 0 to N), a reasonable approximation for long chains. The polymer is placed in a potential double-well, such as the one shown in Fig. 3, and we investigate how it may overcome the potential barrier. Taking $\boldsymbol{R}(n, t)$ as the position of bead n at time t, and $V(\boldsymbol{R}(n, t))$ as its potential energy, we can write Newton's equation of motion for the (massless) beads:

$$\zeta \frac{\partial \boldsymbol{R}(n, t)}{\partial t} = K \frac{\partial^2 \boldsymbol{R}(n, t)}{\partial n^2} - \nabla V(\boldsymbol{R}(n, t)) + \boldsymbol{\Phi}(n, t), \tag{30}$$

where ζ is the friction coefficient of a bead, and $\boldsymbol{\Phi}(n, t)$ is a random force. The spring constant K accounts for entropic effects; as before, $K = 3k_B T/\langle h^2 \rangle$, with $\langle h^2 \rangle$ the mean

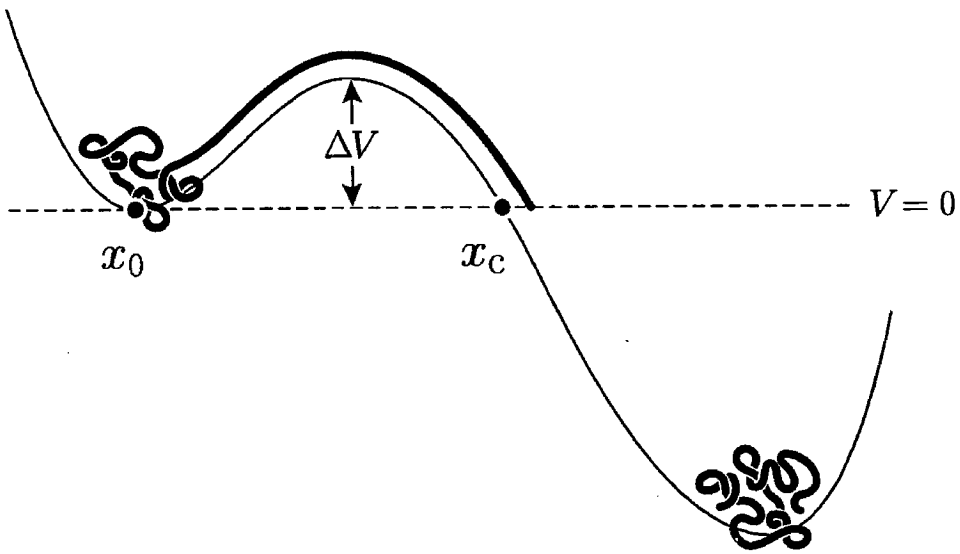

Figure 3. Schematic representation of a polymer coil crossing a potential barrier. The coil is initially localized around the potential minimum at x_0, and initiates translocation by stretching over the potential barrier ΔV up to a point x_c where $V(x_c) = V(x_0)$.

square length of the springs. In addition, we impose the boundary conditions $(\partial \boldsymbol{R}/\partial n)|_{n=0} = (\partial \boldsymbol{R}/\partial n)|_{n=N}=0$ to reflect the fact that the two ends of the chain are free.[8]

For our purpose, it suffices to restrict the analysis to a one-dimensional case and to the deterministic part of Eq. (30) (i.e., $\boldsymbol{R} = x$ and $\Phi = 0$). We are primarily interested in the situations of static equilibrium, where the positions of the beads are independent of time. In this case, the equation of motion reduces to

$$K\frac{d^2x(n)}{dn^2} = \frac{dV(x(n))}{dx} \tag{31}$$

An obvious solution of this equation is when the beads are localized in one potential well, for then both sides of Eq. (31) vanish. But there is another solution where a portion of the chain just straddles the potential barrier, as depicted in Fig. 3. The total free energy of the chain is then most interesting, as it gives the activation energy for the onset of translocation, i.e., the effective barrier height seen by the polymer. Indeed, following,[24] we notice that Eq. (31) is, in fact, Newton's equation of motion for a particle of mass k moving in a potential $-V$, where n plays the role of time. By analogy with conservation of energy, we at once have that the quantity

$$U = \frac{k}{2}\left(\frac{dx}{dn}\right)^2 - V(x) \tag{32}$$

is conserved as one moves along the chain contour, from $n = 0$ to $n = N$. Recalling that $(dx/dn) = 0$ at either end of the chain, we have $U = 0$, because the tail of the chain lies at a point where we chose $V = 0$, hence, the equality

$$\frac{k}{2}\left(\frac{dx}{dn}\right)^2 = V(x) \tag{33}$$

holds everywhere along the chain. In particular, the head of the straddling portion of the chain must also lie at the point (denoted x_c in Fig. 3 where $V=0$ on the other side of the barrier. This state of unstable equilibrium is intuitively correct when one thinks, for example, of a frictionless rope resting over a bump. To calculate the activation energy for translocation, we introduce the free energy density along the chain contour, i.e.,

$$\mathcal{F}(n) = \frac{k}{2}\left(\frac{dx}{dn}\right)^2 + V, \tag{34}$$

where the first term on the right is the contribution from the local stretching around bead n, while the second term is simply the potential energy of bead n. The total free energy of the chain may then be expressed as

$$F = \int_0^N \mathcal{F}(n)\, dn. \tag{35}$$

Combining Eqs. (33) to (35) and assuming that $x(n)$ is an increasing function of n, we find the activation free-energy for the crossing process to be

$$\Delta F_a = \int_0^N 2V\, dn = \int_{x(0)}^{x(N)} 2V\left(\frac{dn}{dx}\right)dx = \int_{x_0}^{x_c} \sqrt{2kV}\, dx. \tag{36}$$

This result is independent of the total length of the polymer: *the extension of the head of the chain across the barrier is sufficient to initiate translocation.* When compared with the energy $N\Delta V$ that would be required to move the N beads across the barrier *all at once*, it becomes clear that the effective height of the barrier is greatly reduced by stretching for long chains. There is yet a third solution of Eq. (31) corresponding to a chain hairpin, instead of a chain end, resting atop the potential barrier. This translocation mechanism is increasingly probable as N grows, and its activation energy is easily seen to be twice that of the end-activated crossing. Such results can be applied to situations of practical interest and, in the case of the Craighead device discussed above, they agree in character with Eq. (29) and with experimental data.

Park, Lee and Sung have also published a thorough analysis of the Kramers problem for a Rouse chain, for polymer contour lengths that are not necessarily large compared to the barrier width.[29–31] They showed that the stretching induced by a convex barrier *always* reduces the activation energy for chain translocation. Therefore, the rate of crossing is always larger than in the globular limit where N beads rigidly cross the barrier simultaneously. This conformational effect is stronger for longer chains, while it becomes insignificant for small polymers crossing wide barriers. Most interesting, there is a maximum in the effective barrier height at intermediate values of N, i.e., there is a critical chain length at which the crossing rate is minimized, because of the competition between surmounting the barrier and stretching at the barrier top.

From this short overview, we gather that molecular deformations play a determining role in the escape dynamics of polymer chains from potential wells, including those arising for entropic reasons. Qualitatively, the key point to bear in mind regarding this kind of process is that only a fraction of a long flexible macromolecule needs to overcome the potential barrier in order to initiate the directed translocation of the whole chain. The analogy with a siphon, wherein a relatively small amount of energy is required to

trigger fluid to flow naturally over a gravitational potential barrier, provides a helpful picture to remember this aspect of the polymer translocation process.

POLYMER–OBSTACLE COLLISIONS

As mentioned in the previous section, polymer deformation, stretching, and relaxation play a crucial role in the separation of biological macromolecules. Many separation microdevices, such as those utilized to analyze biological macromolecules (including DNA), often exploit molecular collisions between a moving analyte and various obstacles. These collisions, and the molecular deformation they generate, slow the analyte in such a way that useful separation can be achieved. The importance of these devices in the biosciences (e.g., it is the invention of powerful DNA separation methods that allowed the human genome to be mapped and sequenced years ahead of schedule) has spurred a renewed interest in the dynamical behavior of single isolated polymers.[32–36] Two excellent model systems for examining single-chain dynamics and the effects of hydrodynamics are either microscopic obstacles (or arrays of obstacles) fabricated using microlithography[32] or magnetically self-assembled super paramagnetic ferro-fluid particles[33,37] that can form quasi–regular arrays of posts.

Electrophoresis uses an electric field to move charged analytes through a sieving system. When a DNA molecule collides with an obstacle, it generally deforms and slides around it in order to continue its migration. During the collision, the presence of both electric and mechanical forces may lead to subtle effects that will be briefly discussed in the next section. Here, we will neglect these combined effects and examine polymer–obstacle collisions from a purely mechanical point of view. Several authors have looked at different aspects of this problem, because these single-polymer systems represent, in some sense, the fundamental unit of separation in such devices.[32,34,36]

We can, in fact, think of two, apparently analogous, methods of moving a polymer through a microfluidic device. One can either apply a uniform mechanical force directly on each monomer (e.g., a sedimentation force), or alternatively, one can use a low Reynold's number fluid flow with velocity v_s to force the molecule through the device. Although these approaches lead to nearly identical molecular behavior, there is a subtle difference related to the hydrodynamic properties of deformed polymer chains. It is on this interesting difference that we will focus our attention.

Mechanical Forces

First consider a quiescent isotropic viscous fluid in which a polymer is moving under the influence of a uniform external field (this corresponds to Fig. 4a). Thus, each of the N monomers experiences an identical external force f_0 regardless of the chain conformation. The simplest such example is a rope moving in a gravitational potential. In the case of a polymer moving in a viscous liquid, this uniform external force alone is unable to deform the polymer. Without obstacles, the motion of the chain is dictated by the retarding effect of the friction between the polymer and the solvent.

The chain friction can be described by two different models, the local hydrodynamically permeable (Rouse) and nonlocal hydrodynamically impermeable (Zimm)